Fracture mechanics of volcanic eruptions

This thesis is submitted for the degree of Doctor of Philosophy at

University College London

Clare Matthews

January 2009

Department of Earth Sciences

University College London

Gower Street

London

WC1E 6BT

Declaration

I, Clare Matthews, confirm that the work presented in this thesis is my own. Where information has been derived from other sources, I confirm that this has been indicated in the thesis.

Signed .....

Date .....

Abstract

Seismology is a key tool in the forecasting of volcanic eruptions. The onset of an eruption is often preceded and accompanied by an increase in local seismic activity, driven by fracturing within the edifice. For closed systems, with a repose interval of the order of a century or more, this fracturing must occur in order to create a pathway for the magma to reach the surface. Time-to-failure forecasting models have been shown to be consistent with seismic acceleration patterns prior to eruptions at volcanoes in subduction zone settings. The aim of this research is to investigate the patterns in seismic activity produced by a failure model based on fundamental fracture mechanics, applied to a volcanic setting. In addition to the time series of earthquake activity, statistical measures such as seismic *b*-value are also analysed and compared with corresponding data from the field and laboratory studies. A greater understanding of the physical factors controlling fracture development and volcano-tectonic activity is required to enhance our forecasting capability.

The one dimensional, fracture mechanics grid model developed in this work is consistent with the theory of growth and coalescence of multi-scale fractures as a controlling factor on magma ascent. The multi-scale fracture model predicts an initial exponential increase in the rate of seismicity, progressing to a hyperbolic increase that leads to eruption. The proposed model is run with variations in material and load properties, and produces exponential accelerations in activity with further development to a hyperbolic increase in some instances. In particular, the model reproduces patterns of acceleration in seismicity observed prior to eruptions at Mt. Pinatubo (1991) and Soufriere Hills (1995). The emergence of hyperbolic activity is associated with a mechanism of crack growth dominated by interaction and coalescence of neighbouring cracks, again consistent with the multi-scale fracture model. The model can also produce increasing sequences of activity that do not culminate in an eruption; an occurrence often observed in the field.

Scaling properties of propagating fractures are also considered. The seismic *b*-value reaches a minimum at the time of failure, similar to observations from the field and measurements of acoustic emissions in the laboratory. Similarly, the fractal dimension describing the fracture magnitude distribution follows trends consistent with other observations for failing materials. The spatial distribution of activity in the model emerges as a fractal distribution, even with an initially random location of fractures

along the grid. Significant shifts in the temporal or spatial scaling parameters have been proposed as an indication of change in controlling factors on a volcanic system, and therefore represent a relatively unexplored approach in the art of eruption forecasting.

Acknowledgements

Firstly and foremost I thank my supervisors Prof. Peter Sammonds and Dr. Christopher Kilburn for their invaluable assistance and support over the course of my research. I am also extremely grateful for the additional advice and encouragement from my CASE supervisor, Dr. Gordon Woo. I acknowledge funding for this research from NERC and RMS Ltd.

My research has benefited from the interest and feedback received from members of the Earth Sciences department at UCL, in particular Prof. Phil Meredith and Dr. Rosanna Smith.

I am grateful to Prof. Hashida for hosting an enjoyable three-month visit to the Fracture and Reliability Institute at Tohoku University, Japan, and to the fellow students of the Institute for making me feel so welcome. Prof. Nishimura provided numerous fascinating discussions on Japanese volcanology. I acknowledge JSPS for funding this fellowship.

I would like to thank members of the Benfield UCL Hazard Research Centre for their friendship and advice over the course of my research, in particular Judy Woo, Andy Bell, Bob Robertson, Carina Fearnley, Catherine Lowe and Wendy Austin-Giddings.

Finally, I would like to thank my parents, for their unconditional support in all I choose to do, and Jed, for his patient technical support.

Table of contents

List of figures

Fig. 4.3 The stress intensity at a distance x_1 from a crack of length $2a_1$, and distance x_2 from a crack of length $2a_2$, is calculated by summing the effects of each of the two cracks interacting with a notional crack of equal length (grey cracks), as described in Equation (4.8). The distance between the modeled and notional cracks is the same as that between the original cracks (i.e. $x_1 + x_2$). The centre-to-centre distances between the two modeled cracks and the modeled and notional cracks are given by c, c_1 and c_2 respectively, and are related by $2c = c_1 + c_2$.

Fig. 4.4 Typical outputs from the one dimensional model under a constant stress, showing seismic event rate with time. (a) Exponential growth is often recorded. Inset shows the natural log of event rate, with a good linear fit ($R^2 = 0.99$). A drop-off in event rate is often seen immediately prior to failure due to a limited number of cells remaining intact. (b) A trend which becomes hyperbolic is also observed. Inset shows the initial linear log event rate ($R^2 = 0.99$), followed by a linear inverse rate, signifying the onset of hyperbolic growth ($R^2 = 0.99$).

Fig. 4.5 Progression of the one dimensional array with time. Intact cells are grey, failed cells red. (a) Failure dominated by one primary fracture produced the exponential trend in seismicity shown in Fig. 4.4a. (b) Event rate produced is exponential initially, but becomes hyperbolic prior to failure (Fig. 4.4b). Results represent typical examples from multiple runs of the model.

Fig. 4.6 Progression of one-dimensional array with time, showing simultaneous growth and interaction of multiple cracks, and the resulting event-rate and inverse-rate trends. This represents a typical such result from multiple runs of the model.

Fig. 4.7 Progression of cracks with time for three simulations of the one-dimensional model, with identical fracture toughness distribution. Each run has 20 initially failed cells, with a different spatial distribution of the failed cells in each case. (a) Failed cells are distributed uniformally along the array, as 10 cracks of length 2 with an inter-crack

distance of 98 cells. (b) Failed cells produce one single, central crack of length 20. (c) Failed cells are distributed at random along the array.

Fig. 4.8 Progression of a one dimensional array with uniform fracture toughness. The largest initial crack dominates activity entirely and growth spreads evenly while the model boundaries allow. Growth rate slows slightly once the dominating crack can grow in one direction only.

Fig. 4.9 Event rate and log event rate with time for four runs of the model with an identical distribution of initial flaws, and fracture toughness values assigned from different distributions. Fracture toughness values are selected at random from a rectangular distribution with a range of (a) 5 (b) 20 and (c) 10 units. Values are assigned randomly along the array. (d) The final run has toughness values selected at random from a rectangular distribution with a range of 20 units, which are applied to the array with clusters of similar magnitude values. All runs produce a roughly exponential increase in event rate. The exponential rate constant reduces with the increase in range of the fracture toughness distribution, λ = 0.4, 0.24, 0.28 respectively for ranges 5, 20 and 10 (Figs. (a) to (c)) respectively. A clustered distribution produced the rate λ = 0.39. For the case of a constant fracture toughness (Fig. 4.8) λ = 0.57.

Fig. 4.10 Event rate with time for 200 individual runs of the one dimensional model under increasing stress. Input parameters are chosen at random from the distributions described in Table 4.1. Time is measured from the start of each model run.

Fig. 4.11 Cumulative probability function for (a) the exponential rate constants from 138 Monte Carlo runs producing an expoential increase in event rate, and (b) the gradient of inverse seismic event rate for the 4 Monte Carlo runs producing an exponential followed by hyperbolic increase in event rate. The peak event distributions describe the exponential rate constants and inverse gradients for the Monte Carlo runs when only the local peaks in event rate were used in analysis, as described in Section 3.2.2. When only peak events are included, 29 of the Monte Carlo runs produce an

exponential event rate that becomes hyperbolic prior to failure (b), and 7 produce a purely hyperbolic increase. Figure (c) shows the cumulative probability function for the gradient of the inverse event rate in these 7 cases. Event rate trends are the output from 200 individual runs of the one dimensional model subjected to increasing stress.

Fig. 4.12 Event rate with time for 100 individual runs of the one dimensional model under constant load. Input parameters are chosen at random from a range of possible values and distributions. Time is measured from the start of each model run.

Fig. 4.13 Cumulative probability function for (a) the exponential rate constant from the 77 Monte Carlo runs producing an exponential increase in event rate prior to failure, and (b) the gradient of inverse number of events with time for the 9 Monte Carlo runs producing an exponential trend that becomes hyperbolic prior to failure. The peak event distributions describe the exponential rate constants and inverse gradients for the Monte Carlo runs when only the local peaks in event rate were used in analysis, as described in Section 3.2.2. When only peak events are included, 27 of the Monte Carlo runs produce an exponential event rate that becomes hyperbolic prior to failure (b). Event rate trends are the output from 100 individual runs of the one dimensional model under constant load.

Fig. 4.14 Examples of alternative event rate trends, produced by the Monte Carlo run, which do not show an exponential or hyperbolic growth.

Fig. 4.15 Event rate with time for 550 individual runs of the one dimensional model. Varying input parameters are fracture toughness and initial flaw distributions, as well as external loading conditions.

Fig. 5.1 Exponential rate constant for 77 Type I (blue diamonds) and 8 Type II (red squares) exponential trends recorded in 100 runs of the 1D model, for varying distributions of fracture toughness and initial flaws.

Fig. 5.2 Duration against characteristic timescale of Type II exponential sequences produced in Monte Carlo simulation.

Fig. 5.3 Duration of exponential sequence t_f normalised against total length of pre-failure sequence, *T*, for Type I sequences produced by the Monte Carlo run, as a function of characteristic timescale.

Fig. 5.4 Duration against characteristic timescale for 21 sequences prior to eruptions or intrusions at Mauna Loa, Kilauea and Mt. Etna (Bell, 2007).

Fig. 5.5 Number of newly activated cracks per time step for model run 1 (a) and run 2 (b), Type I and Type II precursory trends respectively. The dashed lines show the best-fit exponential trends prior to the observed drop-off, and the arrow indicates the point at which the Type II trend becomes hyperbolic.

Fig. 5.6 Log plot of the number of newly activated cracks, before the pre-failure drop-off. Both Type I (red and black squares) and Type II (blue and grey diamonds) precursors show mean exponential activation rates, although each type may show second-order fluctuations about the mean (red squares and grey diamonds). The rate constants for both types cover a similar range of values (0.31 and 0.18 for blue and grey diamonds; 0.29 and 0.22 for black and red squares). The red squares and blue diamonds correspond to model runs 1 and 2 respectively, shown in Fig 5.5. The second Type I (black squares) and Type II (grey diamonds) trends were produced from model runs 3 and 4 respectively.

Fig. 5.7 (a) Number of active existing cracks (blue diamonds) and the resulting total number of cracks (red squares) with time, for a Type I trend (model run 1). An active existing crack is one that grows during a time step, but has also been active during the previous time step. The total number of cracks includes those that are present in the

array but have not yet grown. (b) The proportion of the total number of cracks that grow during a time step.

Fig. 5.8 (a) Number active existing cracks (blue diamonds) and the resulting total number of cracks (red squares) with time, for a Type II trend (model run 2). An active existing crack is one that grows during a time step, but has also been active during the previous time step. The total number of cracks includes those that are present in the array but have not yet grown. (b) The proportion of the total number of cracks that grow during a time step. Arrow indicates the point at which the event rate trend becomes hyperbolic.

Fig. 5.9 Total number of cracks for model runs 3 (blue diamonds) and 4 (red squares), Type I and Type II precursory trends respectively. Arrow indicates the point at which the Type II trend becomes hyperbolic.

Fig. 5.10 Proportion of cells that have failed at the point of exponential-hyperbolic transition in nine runs from the Monte Carlo simulation.

Fig. 5.11 Mean crack length with time, normalised for maximum length (equal to array size) and sequence duration respectively. The two cases show Type I (blue diamonds) and Type II (red squares) precursory trends. Arrow indicates the point at which the event rate trend becomes hyperbolic. Note the logarithmic scale for the vertical axis.

Fig. 5.12 Inverse mean crack length with time, for model runs 1 (a) and 2 (b), producing Type I and Type II precursory trends respectively.

Fig. 5.13 Mean inter-crack distance with time, normalised for initial mean inter-crack distance and duration of sequence respectively. The two examples show a Type I (blue

diamonds) and Type II (red squares) precursory trend. Arrow indicates the point at which the Type II trend becomes hyperbolic.

Fig. 5.14 Cumulative distribution function for the inter-crack distance at the (a) outset of the model run and (b) approximately three quarters through the total run time of the model for Type I (blue diamonds) Type II event-rate trends (red squares).

Fig. 5.15 Snapshots of the array at progressive time steps, from a model producing a Type II trend (model run 5). Cells that have failed are coloured red, intact cells are black. The hyperbolic trend emerged at t = 15.

Fig. 5.16 New failures at progressive time steps in model run 5 (Fig. 5.15). Cells that have failed during the previous time step are coloured yellow.

Fig. 5.17 Length of the active region ahead of advancing crack tips for model run 5, as shown in Figures 5.15 and 5.16. Length is measured as the total number of cells spanned. Plot (a) describes the upper region in Figure 5.16, 500 < cells < 1,000; plot (b) describes the lower region, 0 < cells < 500. Note the logarithmic scale for the vertical axis. Arrows indicate the point at which the event-rate trend becomes hyperbolic.

Fig. 5.18 Density of failed cells in the regions of activity ahead of advancing cracks for model run 5, as described in Figures 5.15 – 5.17. Plot (a) describes the upper region in Figure 5.16, 500 < cells < 1,000; plot (b) describes the lower region 0 < cells < 500.

Fig. 5.19 Cumulative distribution function *F* for stress intensity factor, normalised for maximum stress intensity, over all cells at (a) the start of the model run and (b) approximately two thirds through the total run time of the model. $F(K/K_{max})$ describes the probability that the normalised stress intensity is less than or equal to the specified ratio. The two examples shown are for model run 1 (blue diamonds) and model run 2

(red squares), producing Type I and Type II event-rate trends respectively. Plot (b) shows *F* at the point at which the Type II trend becomes hyperbolic. The dashed lines show the value of the remotely applied stress, normalised for maximum stress intensity, and therefore represent the minimum stress intensity for each example. Note the logarithmic scale for the horizontal axis in plot (b).

Fig. 5.20 Cumulative distribution function for the ratio of stress intensity to fracture toughness over all intact cells of the one-dimensional array for model runs 1 (blue diamonds) and two (red squares), producing Type I and Type II event-rate trends respectively. The distribution function is shown at: (a) the start of the run, (b) approximately two thirds through the total run time of the model, and (c) approximately 85% through the total run time of the model. Dashed lines show the range of linearity of the cumulative distribution function for each example. Plot (b) shows the point at which the Type II example switches to a hyperbolic event rate.

Fig. 5.21 Event rate plots from two model runs showing faster than exponential, step like increases in rate prior to failure.

Fig. 5.22 The intensity of earthquakes per day prior to eruption (t_u) at Shiveluch, 1964 (1), Bezymianny, 1956 (2), and Mt. St. Helens, 1980 (3) (Tokarev, 1985). Intensity is measured as the average number of daily earthquakes.

Fig. 6.1 Frequencies of global earthquakes in 2007 (www.usgs.com). *N* is the number of events with a magnitude greater than m. The linear log relationship for $m \geq 5$ is that described by the Gutenberg-Richter Law. Below $m = 5$ the catalogue of earthquakes is incomplete as the magnitudes become too low for observation.

Fig. 6.2 Typical frequency-magnitude distribution for the one-dimensional model. N is the number of events with a magnitude greater than m. Lower magnitudes provide a good fit to the Gutenberg-Richter Law, with a deviation from a linear fit for $m > 1.7$.

Fig. 6.3 Variation of *b*-value with time, under increasing stress conditions. A sliding window of 500 events is used for each calculation, advancing 50 events at a time. Vertical bars indicate the standard error.

Fig. 6.4 Variation of *b*-value with time, under constant stress conditions. A sliding window of 500 events is used for each calculation, advancing 50 events at a time. Vertical bars indicate the standard error. Fluctuations occur in the gradual decline of *b*-value with time.

Fig. 6.5 Variation of *b*-value with time (blue diamonds) under increasing stress conditions. Red triangles show the average stress intensity over all intact cells, normalised for fracture toughness.

Fig. 6.6 Variation of *b*-value (blue diamonds) with time under constant stress conditions. 500 events were used for each calculation. The maximum (red squares) and minimum (red triangles) recorded magnitude for each window of events is also shown. Magnitudes are calculated using the total length of active cracks.

Fig. 6.7 Variation of *b*-value (blue diamonds) with time. Re triangles show applied stress, normalised by the maximum applied stress. The model reached equilibrium after the drop in stress with intact cells remaining.

Fig. 6.8 (a) Spatial variation in *b*-value over an array of 2,000 cells, under increasing stress conditions. Vertical bars show the standard error. (b) Evolution of the array with time.

Fig. 6.9 (a) Spatial variation in *b*-value over an array of 2,000 cells, under constant stress conditions. Vertical bars show the standard error. (b) Evolution of the array with time.

Fig. 6.10 (a)Average time interval between successive events of equal magnitude, for a typical run of the one-dimensional model. Events are grouped into nearest magnitude bins for the analysis in (b).

Fig. 6.11 Fracture networks with equal fractal dimension ($D = 2$), but with different fault length distributions. (After Bonnet et al., 2001). Sets with identical fractal dimension can exhibit very different fracture densities.

Fig. 6.12 (a) Variation of the fractal dimension D_F with time leading to failure, under increasing stress conditions. D_F will naturally tend to one as the failed cells eventually form a continuous line. The acceleration in D_F shortly before failure correlates with the exponential acceleration in event rate (b).

Fig. 6.13 Box-counting results used to calculate D_F. The fractal dimension is given by the negative gradient of the log-log plot of the number N(l) of boxes of size l needed to cover all failed cells.

Fig. 6.14 Distribution of failed cells (red) used in the box-counting calculation plotted in figure 6.13. This shows a clear variety of crack densities along the array.

Fig. 6.15 Variation of fractal dimension D_E with time, under increasing stress conditions. A sliding window of 300 events is used for each calculation, advancing 50 events at a time. Vertical bars indicate the standard error.

Fig. 6.16 Variation of fractal dimension D_E with time, under increasing stress conditions. A sliding window of 300 events is used for each calculation, advancing 50 events at a time. Events are defined as the central cell of adjacent simultaneously failing cells. Vertical bars indicate the standard error.

Fig. 6.17 Variation of fractal dimension D_E with time, under increasing stress conditions. A sliding window of equal time period is used for each calculation. Time periods of (a) 20 units and (b) 5 units advance (a) 5 and (b) 3 time steps each calculation. Vertical bars indicate the standard error.

Fig. 6.18 Variation of fractal dimension with time, under constant stress conditions. A sliding window of 500 events is used for each calculation, advancing 50 events at a time. Events are defined as the central cell of adjacent simultaneously failing cells. Vertical bars indicate the standard error.

Fig. 6.19 Location of events (red) in windows used for calculation of fractal dimensions in Figure 6.18.

Fig. 6.20 Variation in correlation dimension with time (as described in (6.13)), under constant stress conditions. A sliding window of 300 events is used for each calculation, advancing 50 events at a time. All failed cells are included as event locations.

Fig. 6.21 Log-log plot of the proportion of data points within linear distance *r* of each other. The negative gradient gives the correlation dimension.

Fig. 6.22 Evolution of a one-dimensional array of 1,000 cells with time. (a) Failure is dominated by the growth of a single, primary fracture. (b) Multiple cracks grow simultaneously.

Fig. 6.23 Variation in fractal dimension D_E with time, under increasing stress conditions. The two data sets compare D_E for the growth of a single, dominant crack (blue diamonds) and multiple cracks (red squares). Vertical bars show standard errors.

Fig. 6.24 Variation in fractal dimension D_E with time, under increasing stress conditions and a fractal geometry of initial cracks. Vertical bars show standard errors.

Fig. 6.25 Log-log plot of crack length distribution in a one-dimensional array subject to an increasing applied stress. $N(l)$ is the number of cracks greater than length l. The fractal dimension D_l is given by the negative gradient of the linear trend and is calculated over data points where linearity holds (blue diamonds). $D_l = 0.99$.

Fig. 6.26 Variation in seismic b-value (blue diamonds) and fractal dimension D_l (red squares) with time, under increasing stress conditions. Magnitude values used to calculate b are derived from (a) the number of adjacent simultaneously failing cells and (b) the number of adjacent current and existing failed cells. Note the change in scale for b.

Fig. 7.1 Event rate with time for a one-dimensional array subjected initially to an increasing stress, which is then reduced by 50% and held constant. The dashed line shows the point at which stress is reduced. The event rate continues increasing until bulk failure of the array is reached.

Fig. 7.2 Event rate with time for two separate runs of the one-dimensional model. The models are subjected initially to an increasing stress, which is then reduced by 50% and held constant. The dashed line indicates the point at which stress is reduced. After this drop, fracturing continued in one run of the model until bulk failure of the array (blue diamonds), while in the second run the event rate eventually died down and the model remained in an intact state (red triangles).

Fig. 7.3 (a) Four characteristic exponential trends and (b) the frequency of exponential sequences from the Monte Carlo simulation described in Chapter 4 when grouped with the closest characteristic trend.

1. Introduction

1.1 Fracturing at volcanoes

The study of volcanoes covers a vast range of very different research fields, with work being done in areas from geology and chemistry, to health science and disaster management. Research can be broadly divided in terms of two distinct objectives; understanding the mechanisms within a volcano, and identifying the impact of volcanic activity. This thesis concentrates on the former problem and attempts to apply well developed fracture mechanics tools for this aim. Investigations into the workings of an active volcano are becoming increasingly sophisticated with continuing developments in engineering and technological capabilities. Drilling projects, thermal imaging, GIS and interferometry tools are just a few methods that have been applied in attempts to understand activity inside of a volcano. With increasing computer power it is also possible to run increasingly complex numerical simulations of fracture or flow within the Earth's crust. Combining these models with observed field data such as seismic activity, gas emissions or deformation, it is possible to identify the mechanisms and interactions of volcanic processes; for example, the interactions between magma movement and rock fracture. To fully understand the workings of a volcano it is necessary to develop understanding of each of these processes. An increased knowledge of the processes occurring within a volcano may also consequentially improve the ability to forecast the onset and style of eruptive activity.

1.2 Volcanic hazards and forecasting eruptions

An estimated 10% of the world's population live within an area potentially threatened by a volcanic eruption (Peterson, 1986). In order for populations to be safely evacuated from these areas prior to an eruption, there must be a timely warning of not only the expected time and location of an eruption, but also the size and style of activity. Slow moving lava flows create a very different hazard to rapidly moving, devastating pyroclastic flows.

No two volcanoes behave in the same way and even successive eruptions at the same volcano can exhibit very different patterns of activity. In addition, few volcanoes are extensively monitored and knowledge of previous eruptions often relies on geological evidence rather than first-hand experience.

Although frequently erupting basaltic volcanoes like Kilauea in the USA are now relatively well understood and activity can be accurately forecast, it is the less active volcanoes that most endanger local populations. It is not uncommon for a volcano to be at rest for intervals on the order of a century or more. In the case of many long repose volcanoes there will be little detail known of previous activity and local communities may not even recognise the volcano as active and as a threat. For this reason they are also less likely to be adequately, if at all, monitored. However, some significant progress has been made in the past few decades regarding eruption forecasting.

Beginning several months prior to the catastrophic May 1980 eruption at Mt. St. Helens in the USA there were reports of seismicity, ground deformation and steam emissions at the volcano. It was recognised that an eruption was both likely and imminent, and local residents and tourists had been warned of the risks. However, the suddenness and intensity of the activity on May 18th were totally unexpected and many important aspects of the eruption were not forecast. The extensive monitoring of seismicity was maintained following the first cataclysmic eruption and much of the continuing activity was anticipated. Several of the explosive eruptions in the summer of 1980 were successfully forecast and the following dome building eruptions were all forecast within time periods ranging from just hours, up to 3 weeks prior to activity (Swanson et al, 1983).

Lessons learned at Mt. St. Helens are thought to have played a vital role in the successful forecasting and evacuation of Pinatubo in the Philippines in 1991. Pinatubo erupted violently after around 500 years quiescence. Very little was known about the volcano prior to initial signs of unrest leading up to the eruption, but a timely forecast of expected events saved thousands and maybe even tens of thousands of lives, as well as allowing for the movement of millions of dollars worth of military equipment from nearby US airbases (Newhall and Punongbayan, 1996). There has also been forecasting success at volcanoes with a shorter repose time. For example, by closely monitoring the activity that preceded the 2000 eruption at Mt. Usu, Japan, local experts were able to advise the evacuation of nearby communities in the days before the eruption. There were no reported fatalities or injuries despite the damage and destruction of over 450 homes and businesses.

For each success story though, there are many more examples of events that have not been adequately forecast, and for which the cost to human lives and property has been great. The largest, most destructive eruptions, such as that at Pinatubo in 1991, thankfully occur infrequently. This does however mean that the data and observations so vital for increasing understanding of such eruptions are very limited.

1.3 Precursory seismicity

Seismicity is generally recognised as the most significant and reliable precursor to a volcanic eruption. Some level of increased seismicity precedes almost all eruptions, particularly those ending a long repose interval. Seismicity is also one of the more practical precursors to monitor as it can be done relatively cheaply and remotely without the necessity for entering potentially dangerous areas. Clearly, leveraging the forecasting potential of these precursors relies on the necessary monitoring equipment being in place, and only a third of the volcanoes that have erupted historically are seismically monitored to some extent (McNutt, 2000). A network of seismometers placed around a volcano can record not only the frequency of events but also enables the location and possible source mechanism of an event to be identified. Through studying the frequency, type, size and migration of seismic events an image of what is occurring beneath the volcano can be pieced together.

Earthquakes observed in volcanic settings can be broadly divided into two different types by their frequency characterisation. Low frequency, long period events are typically associated with the movement or pressurisation of fluids such as magma and the resulting deformation (Chouet, 1996). High frequency events resemble classic tectonic earthquakes, in both mechanism and spectral components and are therefore labelled volcano-tectonic (VT) (McNutt 2000). The shear faulting or tensile fracture of brittle rock provides a similar source mechanism for both tectonic and VT earthquakes, but for VT events this process is driven by the stresses induced by magma movement or overpressure rather than the movement of tectonic plates. The two also differ in their temporal distribution. High frequency earthquakes around a volcano tend to occur in swarms, increasing towards the onset of an eruption rather than the classic, well documented foreshock-aftershock sequences of tectonic events.

In practice, there exists a continuous range of events between the characteristic high and low frequency earthquakes. Volcanic tremor is a continuous, low frequency signal with a duration of minutes to days. Tremor is recorded both prior to and accompanying eruptions and is linked to the continuous ground movement caused by injection and interaction of magma with the surrounding rock (Konstantinou and Schlindwein, 2003). Hybrid events contain a mixture of high and low frequency signals. So-called very-long-period events have also been recorded during eruptions, caused by resonance of the conduit-reservoir system (Nishimura & Chouet, 2003).

Identifying the source mechanism for different observed signals allows a sequence of seismic events to be translated into a picture of what is occurring within a volcano. High frequency events are often the first sign of unrest and can be recorded months (Pinatubo 1991) or even years (Unzen 1991) before an eruption. Stress induced fracturing indicates the movement of magma at depth, and the resulting VT events therefore have the potential to provide a relatively long-term indicator to an approaching eruption. Hypocentres of the high frequency events can be well distributed throughout and around the volcano, often with no obvious migration of events with time, as fracturing occurs throughout the edifice (Scandone et al., 2007). Long period and tremor events are more likely to appear in the days to hours before the onset of magmatic activity, and tend to be more spatially clustered, giving a clearer indication to the location and movement of fluids (e.g. Burlini et al., 2007). Tremor may therefore provide a useful short-term warning of rapidly approaching eruptive activity. However, it is unlikely to supply the required length of time to successfully evacuate a sizable local community.

Following the onset of eruptive activity, seismicity tends to be dominated by tremor or explosive earthquakes, depending on the nature of the eruption, with the frequency of VT events rapidly declining. Both the driving force of the build up of magma and the favourable environment for brittle rock fracture are diminished once magma has found a pathway to the surface.

1.4 Fracture mechanics

Fracturing is the source of many dynamic processes studied in Earth and planetary sciences. Earthquakes, volcanic eruptions, avalanches, landslides and ice-shelf calving all occur in part due to the formation and propagation of fractures. Theoretical fracture mechanics can be applied to each of these materials in much the same way and therefore provides an essential tool in identifying conditions under which these processes may occur and the dynamics of their propagation. Brittle, linear-elastic fracture mechanics can be applied likewise to a stressed block of rock, snow or ice. Fracture models are then governed by parameters such as friction coefficients and fracture thresholds and can be described by local stress or strain distributions. For example, Åström and Timonen (2001) used a statistical fracture mechanics approach in exploring the potential of forecasting avalanches. Petley (2004) analysed the relationship between stresses and strains to understand the formation and the propagation of fractures in a slope causing large landslides. Sammis (2001) provides an insight into the applications of material science to the mechanisms of earthquakes and faulting within the crust. Fracture mechanics has also been applied to crustal faulting on Venus (Balme et al., 2004), where a model was produced to estimate the temperature and stress conditions necessary to produce observed parallel fractures. Rist et al. (2002) incorporated both experimental and modelling work to investigate effects of material properties and temperature on the stability of ice crevasses. Fracture mechanics is a useful tool in both calculating local environmental conditions such as stress or temperature and also in predicting future behaviour of a body of material. An additional advantage of the approach is the ability to produce data in laboratory experiments that can then be applied to field based models.

Due to its vital role in structural engineering, the field of fracture mechanics is well advanced with analytical and numerical results. High temperature and pressure work carried out in laboratories has also supported much of the theory in applications of fracture within the Earth's crust (e.g. Rocchi et al., 2003; Tuffen et al., 2008). Applying theoretical models to observable processes can greatly improve the understanding of the physical mechanisms behind it. For example, the theory of creep mechanisms has been used to provide physical meaning to empirical constants in laws describing the rates of earthquake foreshocks and aftershocks (Main, 2000). Starting from a fracture mechanics approach can lead to a greater understanding of the physical processes producing the observations.

1.5 Mathematical approach

Probabilistic and statistical tools are an important feature in forecasting natural hazards. Whether looking at mean recurrence times of earthquakes or the increased probability of an eruption following a significant stress trigger, many forecasts have to be worded in terms of probability rather than certainty. Woo (1999) describes how natural phenomena from volcanic eruptions to floods can be described using theoretical concepts such as Poisson or Markov processes.

Over recent decades Earth scientists have also increasingly turned to new theoretical, mathematical concepts in an attempt to describe and explain the apparent disorder of nature. The theories of fractals, percolation and networks, and terms such as self-similarity, scale invariance and power-law are now often to be found in geological literature. These concepts are described briefly below.

Although others before him had touched on the subject, Mandelbrot was the first to formally identify, and name, the geometric object known as a fractal. He recognised the need for a descriptive tool for the shapes and forms abundantly seen in nature that are too irregular to be illustrated by traditional Euclidean geometry:

> *Clouds are not spheres, mountains are not cones, coastlines are not circles, and bark is not smooth, nor does lightning travel in a straight line.*
>
> Mandelbrot, The fractal geometry of nature 1982

Mandelbrot defined a fractal to be a set with Hausdorff dimension strictly greater than its topological dimension. A more familiar perception is that of a self-similar object with a fine structure at increasingly small scales (Falconer 1990). A geometrical example is the Sierpiński triangle (Fig. 1.1). The property of self-similarity describes an object whose form as a whole is repeated as one or more parts of the whole, and it is this characteristic of the same shape being observed on all scales that is the image so often recognised in nature. Indeed it is this attribute that necessitates the use of a scale reference in many geological photographs. In recent years fractal distributions have been identified in phenomena such as fracture networks within the crust (Bonnet et al., 2001), earthquake epicentres and recurrence times (Saichev & Sornette, 2007) and size of pyroclastic fragments (Kueppers et al., 2006). Identifying a fractal processes can provide information on the state of a system, as described below, and offers forecasting

capabilities such as potential fluid flow through a network, earthquake statistics or explosivity of a volcanic eruption.

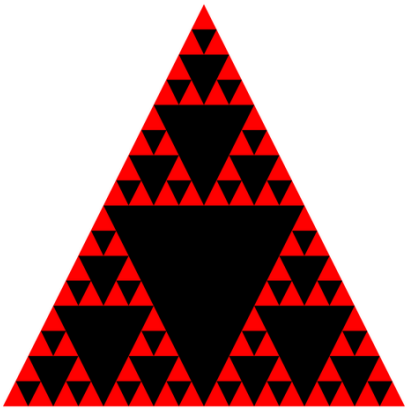

Fig. 1.1 Sierpiński triangle. A fractal formed by the iterative removal of triangles.

Fractals commonly identified in nature, for example mountain ranges, river networks and fault systems, are all approximate as their self-similarity exists over only a finite, all be it an extensive, scale range. For example the scale of the repeating pattern observed in a mountain range cannot extend above the dimensions of the Earth itself or below the grain size of the rock making up the Earth's crust.

Scale invariance is a more exact form of self-similarity. An object or relation that remains unchanged in form and statistically identical under magnification is said to be scale invariant. One of the most widely cited examples of scale invariance in Earth sciences is the empirical Gutenberg-Richter law for the frequency-magnitude distribution of earthquakes:

$$N = 10^{a-bM}$$

N is the number of earthquakes with a magnitude greater than M, and the exponent b, known as the seismic b-value, is an indicator of the relative frequency of large to small earthquakes. Scale invariance yields a power law relationship, another ubiquitous form found in nature. In addition to the obvious use of the Gutenberg-Richter law in estimating the frequency of damaging earthquakes, the b-value itself has proved a useful

tool in seismic analysis. For example, changes in local b-value have been suggested as an indication of the onset of volcanic activity (e.g. McNutt, 2005).

In addition to the obvious illustrations seen all around us in nature, fractal theory was also advanced through its emergence in the area of statistical mechanics and the self-organised criticality of dynamical systems. Self-organised criticality is a phenomenon identified by Bak et al. (1987) around the same time as the advent of fractal geometry, and formally describes the property of a dynamical system that has a critical point as an attractor. A critical point in a system represents a significant change in structure or state and a self-organised system will always naturally evolve to this point no matter what its initial state. Much of the original study into such systems focused on a sandpile model. Adding an extra grain of sand can cause an avalanche of a range of scales from no grains to the entire sandpile. The frequency distribution of these avalanches shows fractal, power law properties. Independent of the starting size of the sandpile, or the number of grains added, the pile will always be attracted to and evolve back to a stationary critical point.

Self-organised criticality has been proposed as a procedure creating complexity in nature. The Earth's crust and the seismicity produced by tectonic stresses have been modelled as a self-organised, critical process (Chen et al, 1991; Barriere and Turcotte, 1994). The fractal nature of several seismic and eruptive processes at Vesuvius has been cited as an indication of a self-organised, critical system (Luongo et al., 1996).

Percolation theory is another increasingly popular branch of statistical mechanics and dynamical systems. The classic idea of percolation is that of a fluid passing through a medium via interconnected channels. An open network is formed once a continuous pathway is created form one side of the medium to the other. At the critical threshold where this fully connected channel is created there is again a change of structure, or state of the system. Networks of fractures within the Earth form a fractal distribution (Hirata 1989). The networks will have a self-similar appearance whether viewed on a micrometre scale, as an arrangement of microcracks in a rock sample or on a kilometre scale, as a network of faults in the Earth's crust. Fracture networks and even the distribution and clustering of earthquakes have been linked to percolation networks (Sahimi, 1994).

Recent research into the form of fracture networks themselves suggests they can be represented by a class of networks known as small-world networks (Valentini et al.,

2007). Watts and Strogatz (1998) have identified many examples of small-world networks in nature and society. In the classical view of networks containing a number of nodes, each of which can be connected to any number of other nodes, a small-world network is identified as one in which most nodes are not directly connected to each other, but conversely most nodes can be reached from every other node in a relatively small number of steps via intermediary nodes. An important feature of small-world networks is that their degree distribution, where the degree of a node is the number of connections going into that node, fits a power law. These types of networks are therefore also scale invariant networks and have the same statistical properties regardless of the size of the network.

Significant advances have been made in the field of seismology under the study of frequency-magnitude b-values and the self-organised criticality of faults. Applying the theories of percolation and networks, fractal and power law distributions, scale invariance and self-organised criticality, introduces many powerful, theoretical tools for analysing the complex processes and interactions occurring within the Earth's crust.

1.6 Aims of research

The ultimate aim of this research is to improve the basic, physical understanding of precursory patterns of seismicity observed prior to volcanic eruptions. A greater understanding of the physical processes producing such observations will aid the analysis and interpretation of seismic sequences and ultimately the probabilistic assessment of an onset of eruptive activity.

The research concentrates on the role of rock fracturing within volcanic systems and therefore focuses on long repose volcanoes where a certain degree of fracturing will be necessary to create a pathway to the surface for magma. A percolation fracture model is used, similar to the cellular automata style model developed by Henderson and Main (1992) to observe the evolution of scaling and fractal parameters with failure. This model is based on fundamental fracture mechanics results and recreates aspects of crack interaction. Beginning with a simple model can highlight the importance of basic physical principles on the observations recorded at a volcano. Further complexities can then be introduced where necessary, and this process allows for a greater appreciation of the main factors controlling edifice failure and eruptions. Initially material properties, crack density and surrounding stress conditions are varied, with their effect on the failure process measured by the seismic sequences produced. This will allow different volcanic and geological settings to be correlated with differences in observable seismic activity.

Numerous simulations of the model can be used to identify additional potential forecasting methods. Parameters such as seismic *b*-value, fractal dimension of percolation thresholds can be calculated to look for distinct pre-failure trends or significant changes at the point of failure. Where an observable parameter is used, such as *b*-value, this would lead directly to a useful forecasting tool. In the case of a non-observable parameter, a failure indication may still point to an underlying cause that may itself be monitorable, or at the very least would improve understanding of the failure process.

In attempting to explain the mechanisms for failure in a volcano, it is also essential to address the question of why failure doesn't always occur and therefore why a volcano doesn't erupt. False alarms of volcanic activity can cause serious problems for scientists and civil authorities. Seismic unrest at volcanoes does not always result in an eruption and it is of vital importance to be able to distinguish between an isolated

seismic swarm and precursory seismic activity. By focusing this research on the fundamental physics of the fracturing process, it is hoped that it may also identify and address this issue of the arrest of fractures and failure.

Little field data exists for seismic precursors to eruptions at long repose volcanoes. It is impossible to know whether the examples already observed represent the typical pattern that will always be produced, or are merely one type out of many possibilities. If a model based on fundamental, physical rules can reproduce the patterns already observed before eruptions it may also explain why these particular sequences have been produced as well as identifying others which could be expected at future eruptions.

1.7 Thesis outline

Following the introduction this thesis contains seven chapters covering the following:

- A brief introduction to the fracture mechanics of rocks and applications to research into the Earth's crust.
- A description of field observations of fracture, and a literature review of the current models of fracturing at volcanoes.
- A description of and observations from a one-dimensional model of rock fracture and pre-eruptive seismicity.
- A discussion of the observed accelerations to failure in the 1-dimensional model and in the field, and the role of crack interaction in the failure of rock.
- A discussion of the statistics of the spatial and temporal distribution of seismicity produced by the 1-dimensonal model and in the field.
- A discussion of the ability to produce and explain precursory seismicity through a simple fracture mechanics model, applications to forecasting and decision making, as well as conclusions and thoughts for future research.

2. Fracture mechanics

2.1 Introduction to the theory of fracture mechanics

Volcano tectonic earthquakes provide one of the best potential tools for medium to long term forecasts of approaching eruptions. These events are generally produced by a similar mechanism to tectonic earthquakes, by brittle shear failure or slip on fault, or as has recently been shown, by the shear failure of magma in the conduit (McNutt, 2005; Tuffen et al., 2008). An application of fracture mechanics is therefore of benefit to consider the processes producing the signals in addition to the resulting patterns of seismic sequences observed.

For an eruption to occur a magma body must find an open network of fractures to the surface. Although many fractures will already exist throughout the volcano, it is likely that a significant amount of further fracturing will be required to create a fully open pathway, particularly in the case of long repose volcanoes. During the weeks to days before an eruption high-frequency earthquakes are typically detected throughout the edifice, with no obvious migration with time (Kilburn, 2003; Scandone, 2007). This supports the assumption that these brittle, stress-induced events create an open network eventually linking magma at depth to the surface, rather than a single, magma-filled crack forcing its way through the host rock. Fracturing of the surrounding volcanic edifice therefore provides a control on the movement and ascent of magma (Kilburn, 2003). Fracture mechanics applies the physics of stress and strain to predict when fractured solids will fail, and as a result can be used to explore the necessary conditions for a connected conduit to form in a tensile stress-field within a volcanic edifice (Kilburn & Sammonds, 2005).

2.1.1 Stress and strain

From a start point of the analysis of stress and strain (Sneddon, 1958), stress, σ, is the measure per unit area of a force applied to a body:

$$\sigma = \frac{F}{A} \tag{2.1}$$

F is the force applied over a cross-sectional area A. Stress is commonly described by two components, one acting normal to the surface of the body and one acting parallel. Normal stresses change the volume of the body they are acting on; compressive stress reduces the volume while tensile stress increases the volume. Parallel or shear stresses change the shape of the body. Strain, ε, is the measure of the resulting change in shape or volume of the loaded body and is defined as the ratio between the change in dimensions, δv and the original dimensions v_0:

$$\varepsilon = \frac{\delta v}{v_0} \tag{2.2}$$

Hooke's law describes the approximately linear relationship between applied stress and resulting strain observed when a material deforms elastically:

$$\sigma = E\varepsilon \tag{2.3}$$

E is known as the Young's modulus and is a measure of the stiffness of a material. The rheological behaviour of rock can vary between elastic and plastic deformation depending on temperature, pressure and strain rate as well as the rock type (Rudnicki & Rice, 1975). However, for modelling the interior of a volcano it is often assumed that rocks will deform and fail following an elastic-brittle regime (Kilburn & Voight, 1998; Pinel & Jaupart, 2003). Results from laboratory rock fracture experiments carried out at

a range of temperatures and confining pressures support this assumption (Rocchi et al., 2003; Smith, 2007).

2.1.2 Fracture criterion

Griffith Energy Balance

Much of today's theory on the fracture of solids stems from the pioneering work of Griffith in the 1920s on the stress and strain of brittle materials. Griffith observed that under loading, elastic materials rarely reached even close to their theoretical strength of $E/10$ before failing, where E is the Young's modulus of the material. The true critical strength of loaded specimens could be as much as 1,000 times less than the value predicted by theory. Prior to Griffith's work, Inglis (1913) had recognised the damaging effect of flaws in a solid body and calculated the distribution of stresses in a uniformly stressed plate containing an elliptical hole. Inglis showed that a remotely applied stress could be magnified several times over at the sharp notch of a thin ellipse. A crack can be modelled as an increasingly narrow ellipse, and Inglis' work demonstrates how any stress applied to a cracked body will be concentrated around the tips of the crack. Griffith (1920) hypothesised that this concentration of stress around sharp cracks was the physical explanation for the decreased critical strength of materials. He argued that loaded specimens would contain numerous flaws or cracks and that even the smallest microcrack could sufficiently enhance local stresses to cause a material to fail far below the anticipated strength. Although this explained the apparent discrepancy between the actual and theoretical strength of a brittle solid, there remained the problem of adequately predicting under what conditions it would fail.

Griffith proposed a theoretical criterion of rupture (1920) that was based on the total change of energy in a cracked body as the crack length increases. He viewed the cracked body as a reversible thermodynamic system and using the first law of thermodynamics described a balance between a crack driving force, resulting from the applied load and strain potential energy stored in the body, and a crack resisting force, due to the free surface energy U_s required to create a new crack surface. The total energy U of the system is the sum of these opposing forces:

$$U = U_m + U_s \tag{2.4}$$

U_m is the mechanical energy provided by the work of the load and the strain potential energy and will decrease as the crack extends. The surface energy U_s will increase with crack length c. At equilibrium, the driving and resistive forces will exactly balance:

$$\frac{dU}{dc} = 0 \tag{2.5}$$

For the case of a thin plate under a constant load, the mechanical energy per unit width of a crack length c, can be calculated using the strain energy per volume U_e (Lawn & Wilshaw, 1975) yielding:

$$U_m = -U_e = \frac{-\pi c^2 \sigma_r^2}{4E} \tag{2.6}$$

where σ_r is the remote stress applied normal to the crack surface.

Taking into account each surface of the crack, the surface energy per unit thickness is given by (Griffith, 1920):

$$U_s = 2c\gamma \tag{2.7}$$

Substituting (2.6) and (2.7) into (2.4) and applying the equilibrium condition gives a critical failure stress for the applied load σ_r:

$$\sigma_r = \left(\frac{4E\gamma}{\pi c}\right)^{1/2} \tag{2.8}$$

Griffith supported his theoretical findings with convincing experimental results on the failure strength of glass. He had therefore not only shown that the presence of cracks could drastically reduce the critical strength of a body to an extent dependent on the crack length itself, but had provided a new theory of fracture criterion. For a given crack length, in a given material, Griffith's criterion predicts a critical stress level which if exceeded allows the crack to propagate freely.

Griffith's energy balance theory has since provided the basis for much work into the brittle fracture of solids. However, the theory only considers the energy change as a crack grows and therefore accounts only for the initial and resulting state of a system rather than the fracture process itself. For example, a stressed body may contain a flaw that under Griffith's theory would be energetically favourable to extend, but if the tip of the flaw is not sharp enough to concentrate the applied stress and exceed the fracture strength of the material the atomic bonds at the tip will not be broken and the flaw will not propagate. As a result Griffith's ideas provide a necessary but not a sufficient condition for fracturing.

Stress Intensity Factor

Sneddon (1946) and Irwin (1958) produced further work on stress concentration and the stress field around a crack tip in an elastic body under load. The stress close to a crack

tip is a function of θ and $r^{-1/2}$ where r and θ are the angular coordinates from an origin at the crack tip, and a scaling factor K.

$$\sigma_{ij} = \frac{K}{(2\pi r)^{1/2}} f_{ij}(\theta) \tag{2.9}$$

σ_{ij} is the stress acting on the i plane in the j direction. This produces a stress singularity at the crack tip ($r = 0$), which highlights the breakdown of linear elastic behaviour in this area and the transition to plastic deformation (Irwin 1958). Provided this plastic zone remains small relative to the crack length, the approximation to a linear elastic body is satisfactory. Irwin formalised the concept of the scaling parameter K as a stress intensity factor, which depends on the crack geometry and loading conditions. Loading can be one of three basic modes, or a mixture of the three; mode I fracturing describes an opening or tensional action, mode II in-plane shear or sliding, and mode III describes anti-plane shearing or tearing. Under a homogeneous load, the general form for K in the vicinity of a crack tip is:

$$K = \sigma_r(\pi a)^{1/2} \tag{2.10}$$

The stress intensity factor is a measure of the stress singularity at a crack tip and provides a necessary and sufficient criterion for fracture propagation. Unstable crack propagation will occur if $K > K_c$ where K_c is the critical stress intensity value, known as the fracture toughness of a material.

The stress based parameter K can be linked with Griffith's energy based argument via the strain energy release rate G. From (2.6):

$$G = \frac{dU_e}{dc} = \frac{\pi c \sigma_r^2}{2E} \tag{2.11}$$

Comparing (2.10) and (2.11), the point at which the stress intensity factor attains the critical value K_c can be associated with a critical strain energy release rate G_c:

$$K_c = (EG_c)^{1/2} \tag{2.12}$$

Rice's J-Integral (1968) bridges the thermodynamic and mechanistic approaches and accounts for the crack-tip plastic region. The J-Integral is a path independent line integral surrounding the crack tip and represents the averaged strain energy release rate. J_c defines a critical point at which plastic yielding will occur and is analogous to G_c for linear elastic materials. This approach deals neatly with the problem of the crack-tip stress singularity arising from assuming purely linear deformation but again it only holds if the plastic region surrounding the crack tip is small relative to the crack size. It also loses any detail of the actual fracture mechanism at work, looking only at energy available for propagation. Advances in technology have allowed the development of many numerical techniques for modelling crack tip stress fields and crack propagation. Approaches using finite element and boundary element methods can deal with difficulties such as crack-tip stress concentrations, crack propagation and the opening or closing of fractures (e.g. Chan et al., 1989).

The linear elastic, stress intensity approach allows insight to the actual mechanisms for the propagation of a crack, taking into account the surrounding stress field, crack geometry and material properties. Considering fracture networks within a volcano, it is necessary to understand something of the distribution, direction and connectivity of individual cracks as well the overall energy state and fracture potential of the system. While rock under high temperature and confining pressure surrounding a magma chamber or along conduit walls may exhibit brittle-ductile behaviour, it is reasonable to assume that the condition of a small plastic region relative to fracture length will still largely hold. The source mechanism of high-frequency earthquakes recorded at volcanoes suggests that they are largely produced by brittle failure of rock.

2.2 Fracturing of the Earth's crust

While much of the early fracture mechanics theory was developed to predict the behaviour and failure of metals, glass or other commonly used engineering materials, the same ideas can be applied to the largely elastic, brittle rock making up the Earth's crust. Forces resulting from tectonic movement or the flow of fluids and gases beneath the ground exert a stress on the crust. The distribution of fractures throughout the crust can relieve or concentrate these stresses in much the same way as a scratch on the surface of a glass rod or metal plate in the lab.

However, the scale of fracture processes within the crust is vastly different to anything that can be reproduced in the laboratory under experimental conditions. This includes temperature and pressure conditions as well as large-scale faults, or low strain rates and long time-scales. In addition experiments will often be conducted under homogeneous loading conditions, whereas the stress conditions in the field will not be so uniform. With the difficulty of observing any crustal fracture process directly, scaling up results produced in the lab is nevertheless a useful insight into how stresses and strains are distributed throughout the crust to cause large scale failure and deformation. The benefit in the application of fracture mechanics to geological processes is the simple fracture criteria available, allowing for an understanding of the necessary conditions for the propagation of cracks.

Faulting associated with seismic activity is thought to involve mainly shearing processes. However, shear faulting on the macroscopic scale is the result of incremental tensile action at the microscopic scale of the fault tip and a tensile stress field can exist even if all principal external loads are compressive (Cox & Scholz, 1988). Mode I fracture is therefore often assumed for the determination of critical stress intensity and strain energy release parameters. In addition to stress-dependent faulting, time-dependent fracture and creep are also important aspects in the failure of rock and mechanism of earthquakes. Costin (1983) describes both time-independent and time-dependent crack growth in rock samples in the laboratory. Subcritical crack growth describes the propagation of a crack tip at a stress intensity below its critical value. Subcritical crack growth in the Earth's crust is associated with long-term loading, or fatigue, and the corrosive effects of chemicals and fluids (Atkinson, 1984). Rudnicki (1980) gives a detailed review of the use as well as the limitations of fracture mechanics for research into fault propagation. Failure within the crust occurs on a vast range of

scales, from the microscopic to rupture of faults thousands of kilometres in length (e.g. Nalbant et al., 2005). Measures of the distribution of failure magnitudes, such as seismic *b*-value, can be related to fracture mechanics parameters, such as energy release rate (Main et al., 1993). The magnitude of events above a certain threshold can be monitored both in the field, and in the laboratory by means of acoustic emissions, and therefore provides information on the fracture mechanisms occurring within the crust, or rock sample.

The ascent pathway of magma through a volcanic edifice will also be controlled somewhat by the regional tectonic stresses. Geological features of a volcano can serve as an indication to the ambient, tectonic stress field (Shaw, 1980). Magmatic overpressure provides another loading source in a volcano and the magma chamber itself can act as a stress concentrator. Anderson (1936) used stress trajectories and the idea of effective stress (the total stress minus pore fluid pressure) to describe the conditions under which magma intrusion from a chamber will form cone-sheets or ring-dykes. Gudmundsson (1990) described criteria for the rupture of a magma chamber and injection of a dyke based too on the magma pressure within the chamber and the local principal stresses, and also the tensile strength of the surrounding rock. Fracture models often idealise the crust as a homogeneous and isotropic material. While a general idea of a stress field distribution can be achieved, fracture criteria depend on material properties. Gudmundsson (2006) also studied dyke emplacement and arrest in a heterogeneous, anisotropic volcanic setting.

Kilburn (2003) considered the mechanical effects of a fluctuating stress field in a closed, but pre-fractured volcanic edifice and applied a time-dependent, energy based argument for propagation and coalescence of cracks. Similarly to Griffith's energy balance theory this approach has the advantage that for a given population of cracks only the proportion supplied with sufficient energy for propagation is required rather than detailed knowledge of the fracture mechanism at each crack tip. However, this model therefore describes only the growth of a population of cracks as a whole without providing any criteria for the coalescence of a network and therefore for the creation of an open pathway for ascending magma.

An accurate description of fracture and faulting within a volcanic system requires input factors such as magmatic and non-magmatic loadings, the geometric distribution of pre-existing cracks, and material and environmental properties of the

rock. At each given volcano these parameters can be described in terms of probabilistic distributions, based on prior knowledge from field or experimental data. Analytical results for stress concentrations and propagation exist for only specific geometrical configurations of cracks, and beyond this scope models must incorporate numerical techniques. Confining the model to a regular geometry allows the application of fundamental fracture mechanics and can highlight aspects of failure at volcanoes that either have a significant effect on the process or that are particularly sensitive to an input factor, or similarly any interactions that may exist. It can then be investigated whether adding further complexities to the model in order to more accurately represent these factors would significantly improve the model's utility. Cause and effect, interactions and relationships can be identified much more readily in a model based on fundamental physical equations, whereas complex numerical models can become something of a black-box in terms of correlating inputs to observed results.

3 Fracture mechanics as a forecasting tool for volcanic eruptions

3.1 Field observations of fracture

While faults are often observed at the surface of volcanoes (Gudmundsson et al., 1997; Corazzato & Tibaldi, 2006), it is clearly difficult to directly observe fracturing within a volcanic edifice. However, by considering the waveform and frequencies of detected seismicity and results from fracture experiments in the laboratory it is possible to infer some facts and characteristics about the failure process which must occur for a volcano to erupt.

Direct evidence of fracturing is occasionally seen due to erosion or collapse of the edifice (Fig. 3.1), or in erupted material. Exposed dykes can reveal information about the mechanical properties of host rock, for example in regard to layers that the dyke has propagated through or where it has become arrested at the boundary (Gudmundsson, 2006). In addition to fracturing of country rock there is also evidence for the brittle failure of lava flows (Rocchi et al., 2003) and viscous magma in the conduit (Dingwell, 1996). Tuffen et al. (2003) identified evidence of repeated failure and healing in an exposed rhyolite conduit in Torfajökull, Iceland. This process is described as repeated tectonic-like shear fracture and then subsequent healing of rising viscous magma, and shows similarities with other seismogenic faults in the crust (Tuffen et al., 2003; Tuffen and Dingwell, 2005). The shear fracture of magma produces sequences of long-period and hybrid earthquakes, concentrated along the conduit walls (Tuffen and Dingwell, 2005). Deformation at the surface has also been used to infer shear stresses along the walls of the conduit at Soufrière Hills, Montserrat (Green et al., 2006). Green at al. (2006) develop a numerical model based on realistic stress and material parameters from the volcano, which reproduces the observed deformation. A combination of field observations and the scaling up of laboratory results can be used to both develop and test models of fracturing within a volcano.

Fig. 3.1 An exposed, terminated dyke in the Reykjanes Peninsula, Iceland. The dyke tip becomes arrested as it approaches the boundary between a tuff layer and lava flow (Gudmundsson & Loetveit, 2005).

3.2 Models of fracturing at volcanoes

Factors such as tectonic setting, past activity and repose interval mean that each volcano is very different in terms of the distribution of stress and the level of fracturing within its edifice and the surrounding crust. However despite these differences the failure mechanisms within the volcano that will precede an eruption are the same, and can be modelled by linear elastic fracture mechanics. Varying stress conditions or the degree of initial damage in such a model may then highlight differences in the precursory activity that may be expected at different volcanoes. Long repose volcanoes in a subduction zone setting, such as Mt. Pinatubo in the Philippines and Mt. Fuji in Japan, will provide a relatively un-fractured body of rock for magma to ascend through (Kilburn, 2003; Scandone, 2007) in a largely compressional field. In addition, distinct patterns of precursory seismicity have been previously identified at subduction zone volcanoes (Kilburn & Sammonds, 2005). This setting therefore provides good potential for the use of fracturing to forecast eruptions.

Faulting and fracturing within a volcano may occur through the combination of stress induced by magma intrusion exceeding the strength of surrounding host rock, and time-dependent weakening of the host rock. In the limiting cases, once a magma chamber has ruptured, it is either magma overpressure and rheology or weakening of rock that controls the ascent of magma through a volcano. Magma may ascend either by following cracks and faults already formed through the edifice, or as a magma-driven extension fracture. In the latter case, a migration of seismic activity would be expected, which followed the propagation of magma. If fracturing was solely occurring ahead of a propagating magma intrusion then seismic activity would be expected to show a systematic migration with the movement of this failure zone. However, observations show no such pattern. Roman and Cashman (2006) study a number of eruptions, several of which follow a long repose interval, and the spatial distribution of their precursory, volcano-tectonic seismicity. A random pattern is observed prior to the eruptions at Soufrière Hills, Mt. Unzen and Mt. St Helens. The lack of migration of events suggests either that failure throughout the edifice has occurred prior to the ascent of magma, or in the event of a magma-driven fracture, that this is not the direct cause of high-frequency seismicity recorded prior to eruptions. The overpressure causing the injection of magma from a chamber can also lead to shear faulting throughout the edifice, which although may not be an ascent path for magma still represents a progressive failure of the edifice. For either scenario of the formation of an open

conduit for magma ascent, or the progressive failure of the edifice in the form of shear faulting due to magmatic pressures, the process can be modelled through the use of fracture mechanics, crack propagation and crack interaction.

The slow fracture hypothesis is supported by the period of time over which precursory seismicity is observed and the spatial distribution of activity. Volcano-tectonic events have been recorded months (eg. Mt. St. Helens; Malone, 1983) to years (eg. Unzen; Umakoshi et al., 2001) before the onset of activity, apparently independent of the size of the eruption (Scandone, 2007). Rock weakening and slow fracture as a control on magma ascent would also explain the observation of eruptions beginning some weeks to months after the detection of magma near the surface of a volcano (McGuire & Kilburn, 1997).

3.2.1 Failure forecasting method

McGuire and Kilburn (1997) suggest that the injection of new magma has two effects on the surrounding edifice. Initially, deformation will relieve the resulting stress to some extent, leaving a constant level of stress causing gradual deformation and failure prior to eruption. Assuming a constant load and temperature, Voight's relation for rate-dependent material failure (1989) can be applied to the stressed crust surrounding a magma source. The empirical formula:

$$\left(\frac{d\Omega}{dt}\right)^{-\alpha}\frac{d^2\Omega}{dt^2} - A = 0 \tag{3.1}$$

was first recognised by Fukuzono (1985) in a study of large scale slope failure. α and A are empirical constants and Ω represents an observable quantity such as fault slip, strain or energy release, whose rate $d\Omega/dt$ can be described in terms of the change in that rate, $d^2\Omega/dt^2$. For positive constants α and A, this relationship implies an acceleration of the deformation process measured by Ω, and if a failure rate, $(d\Omega/dt)_f$ is defined, yields a time of failure of the material, t_f:

$$t_f - t_0 = \frac{1}{A(\alpha - 1)}\left[\left(\frac{d\Omega}{dt}\right)_0^{1-\alpha} - \left(\frac{d\Omega}{dt}\right)_f^{1-\alpha}\right] \tag{3.2}$$

where $(d\Omega/dt)_0$ is the rate at time t_0. To explore its function in eruption forecasting, the relationship in (3.1) has been applied to various precursors such as tilt measurements at Mt. St. Helens (Voight, 1988), cumulative strain release at Bezymyanny Volcano (Voight, 1988), seismic event rate at Soufriere Hills (Kilburn & Voight, 1998) and line measurements at Colima (Murray & Ramirez Ruiz, 2002).

In applications the value of the constant α has generally been found to lie between the limits $1 < \alpha < 2$, often closer to 2 (Voight, 1989; Cornelius & Scott, 1993). Although values outside of this range are also possible, the clustering of these values suggests a physical interpretation of the parameter, which keeps it within these limits. The special case of $\alpha = 1$ reduces (3.1) to a linear differential equation, resulting in the simple exponential relationship:

$$\frac{d\Omega}{dt} = \left(\frac{d\Omega}{dt}\right)_0 e^{A(t-t_0)} \tag{3.3}$$

Alternatively $\alpha = 2$ gives a hyperbolic increase where the exponent of increase of the process is now the value of the process itself:

$$\frac{d\Omega}{dt} = e^{A\Omega} \tag{3.4}$$

This leads to a linear decrease of the inverse rate with time:

$$\left(\frac{d\Omega}{dt}\right)^{-1} = \left(\frac{d\Omega}{dt}\right)_0^{-1} - A(t - t_0) \tag{3.5}$$

As a forecasting tool, a linear relationship has the advantage of being easy to identify and extrapolate. Despite the numerous studies showing good agreement, Voight's material failure relationship can only be used as a successful forecasting tool with prior knowledge of the value of α and therefore of the nature of the acceleration to failure. In order to be able to make real-time forecasts a link must be developed between this empirical parameter and measurable physical quantities.

A link was formally made between subcritical crack growth and the material failure relationship by Cornelius & Scott (1993) and Main (1999). Under a constant load, Charles' Law for sub-critical crack growth (Charles, 1958) can be reduced to an equation of the form:

$$\Omega = A + B\left(1 - \frac{t}{t_f}\right)^m \tag{3.6}$$

where in this case Ω represents crack length and the time of failure, t_f is defined at the point $\Omega(t) \rightarrow \infty$ (Main, 1999). Equation (3.6) provides a finite failure time only when $m < 0$. The exponent m is related to the stress corrosion index p by $p = 2(m-1)/m$, implying that a finite value for t_f exists when $p > 2$. Similarly to α in (3.1), p is a measure of the non-linearity of the crack growth rate in Charles' Law. Voight's relationship can also be written in the form of (3.6) where Ω is now the measure of deformation being observed and m is related to α in (3.1) by $\alpha = (m-2)/(m-1)$. This provides the finite failure time requirement of $1 < \alpha < 2$ which is the range found by application to field and laboratory data. Cornelius and Scott (1993) used the direct relationship between the material failure and stress corrosion parameters, $\alpha = (2p-2)/p$ and experimental results for typical values of p to produce the expected range of values $1.92 < \alpha < 1.99$. This fits within the finite

failure time limits and shows good agreement with many of the hind cast applications (Voight, 1989; Kilburn & Voight, 1998).

Charles' Law for subcritical crack growth incorporates the stress intensity factor at the crack tip and therefore relates the empirical quantity α to a theoretical fracture mechanics process and provides a physical meaning to the parameter. However, Charles' Law is still semi-empirical, incorporating an experimentally determined barrier to crack growth (Cornelius & Scott, 1993). Main (1999) also arrived at an equation of the form (3.6) describing the non-linear behaviour of the size of connected clusters in a simple percolation model.

Voight's failure forecasting relation applied to seismic event rate prior to eruptions following long repose (Kilburn & Voight, 1998; Kilburn & Sammonds 2005), finds acceleration parameters consistent with slow fracture under a constant load (McGuire & Kilburn, 1997), and provides well-constrained forecast windows (Kilburn, 2003; De la Cruz-Reyna & Reyes-Davila, 2001). This method of time-to-failure analysis is less well defined for non-constant stress or dynamic fracture (Smith et al., 2007).

All forecasting potential of the material time-to-failure model depends on prior knowledge of the parameter α and there are very few cases of the material time-to-failure model being used to issue a real-time forecast (De la Cruz-Reyna & Reyes-Davila, 2001). Introducing subcritical crack growth relates Voight's failure forecasting model to deterministic fracturing laws, however this considers only the growth of a single, isolated crack. In the heavily fractured crust surrounding a volcano there will be many cracks, on multiple scales, growing simultaneously. Even under the conditions of a constant load, proximity of neighbouring fractures will alter the stress field around a growing crack, to either enhance or diminish the likelihood of further propagation. Modelling crack growth and failure as an isolated process is therefore discounting a potentially influential variable in the development of bulk failure.

3.2.2 Multi-scale crack interaction

The failure forecasting relation (3.1) has also been applied to a population of cracks. Under a constant load the nature of deformation within a fractured body will evolve from the initial increase of newly active cracks within a fixed volume, to the extension of a fixed number of active cracks (McGuire & Kilburn, 1997). In terms of Voight's

material failure relation, this corresponds to the acceleration parameter increasing from $\alpha = 1$ to $\alpha = 2$ as the dominant mode of failure progresses from crack initiation to crack propagation (Kilburn & Voight, 1998; McGuire & Kilburn, 1997). Growth and coalescence of fractures will prevail during the final stages of bulk failure and therefore an increase towards $\alpha = 2$ is expected in the days prior to an eruption.

Kilburn (2003) considered the growth, interaction and coalescence of fractures on multiple scales, equating a step increase in crack length with a seismic event. The entire process of growth and coalescence of cracks on one scale can be viewed as the extension of a crack on a larger scale, which on extending and joining up with neighbouring cracks will constitute the extension of a fracture on an even greater scale, and so on. While remaining consistent with Voight's material failure model, this multi-scale fracture model forecasts an $\alpha = 2$ acceleration for peak seismic event rate, with intermediary, non-peak events representing fracturing on a smaller scale. Again assuming a constant far-field load, Kilburn (2003) considered the role of random energy fluctuations on a population of multi-scale cracks. A statistical physics approach means that only the distribution of energy among a population of cracks needs to be considered, rather than the energy supplied to each individual crack. Following similar analysis to Boltzmann's work on the movement of gas molecules (Ruhla, 1992), the distribution of energy states describes the probability of cracks being supplied with sufficient energy for propagation. This leads to an expression for the expected rate of cracking, and therefore seismicity:

$$\frac{dN}{dt} \propto e^{-\varepsilon_i} \tag{3.7}$$

with ε_i the extra energy required by crack i for propagation. The rate of cracking is directly dependent on the energy supplied and following the Boltzmann distribution for statistical equilibrium (Ruhla, 1992; Kilburn, 2003) there is a much greater probability of a small amount of energy being supplied than a large amount. From (3.7), as the energy required for propagation decreases linearly the probability of that energy being supplied, and therefore the crack rate, increases exponentially.

The energy required for crack propagation is the difference between the energy required to create new crack surfaces and the strain energy released by surrounding rock by the process of propagation (Griffith, 1920). This can be written in terms of an initial crack length c_0 and increase in crack length per fracture step Δc and decreases linearly with the number N of previous fracture steps:

$$\varepsilon = A - B\frac{c_0}{\Delta c} - BN \tag{3.8}$$

where constants A and B are functions of the surface energy and strain energy for crack extension Δc and total internal energy (Kilburn, 2003). Substituting the above energy equation into the expected crack rate (3.7) gives Voight's material failure relation for the special case of $\alpha = 2$:

$$\frac{dN}{dt} \propto e^N \tag{3.9}$$

The multi-scale fracture model again gives physical reasons for the empirical laws based on observed patterns before eruptions at long repose volcanoes. Although this method has never been used in a real time forecasting situation, the model produces relatively well-constrained forecasts for and is consistent with precursory seismicity to the eruptions at Pinatubo in 1991 and Soufrière Hills in 1995. As the model itself predicts a value for the acceleration parameter α, a forecast only requires sufficient data points to identify a linear inverse trend. The statistical approach requires no detailed knowledge of the stress field or level of fracture damage in the crust. However, due to the infrequent occurrence of eruptions at long repose volcanoes, precursory seismic data prior to these eruptions is very scarce. While the hyperbolic acceleration to failure is consistent with data sets currently available, there is no way to know if this same trend is always to be expected or is just one pattern out of many possibilities.

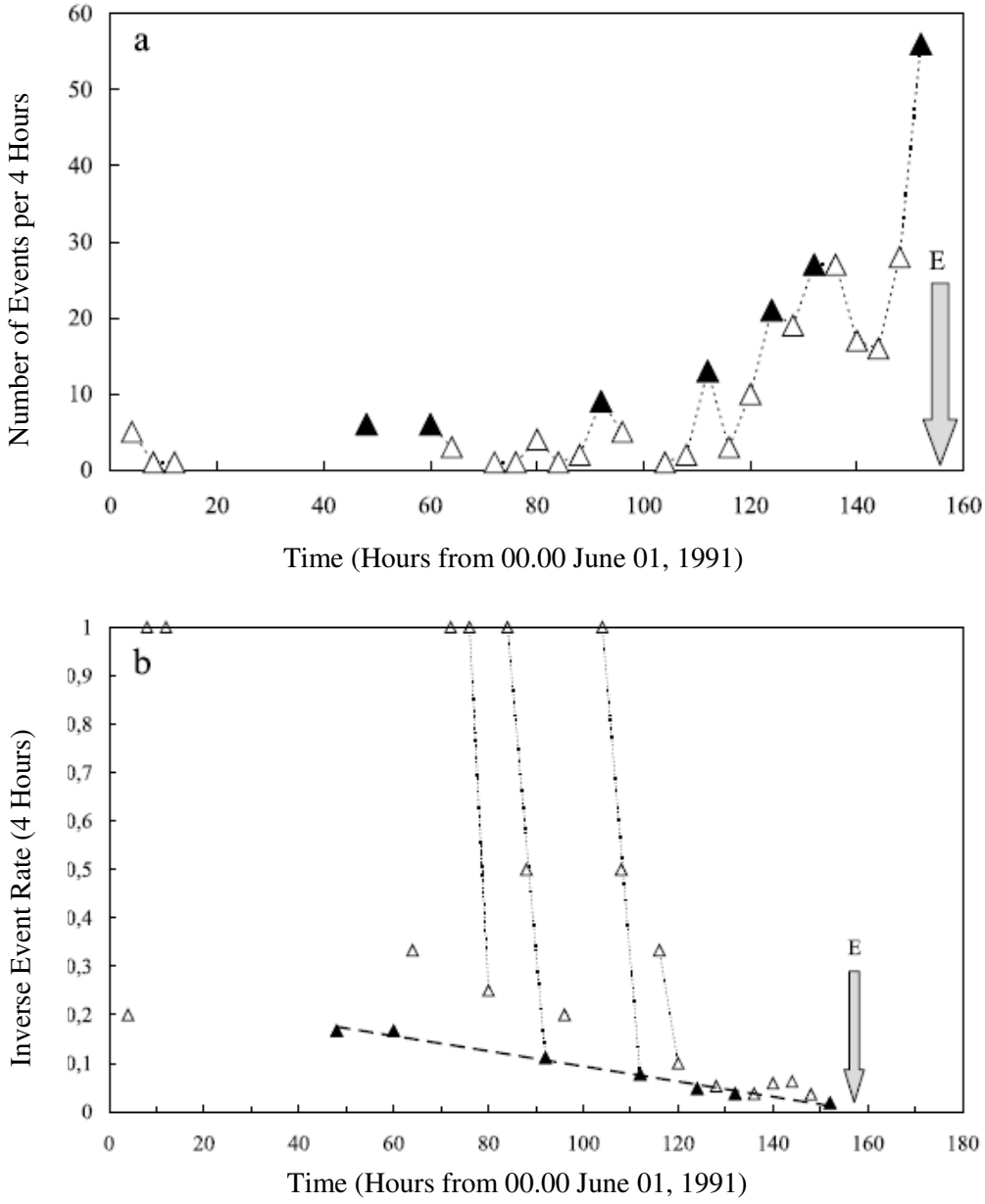

Fig. 3.2 (a) Seismic event rate, per 4 hours, prior to the 1991 eruption at Pinatubo. Filled triangles highlight the peaks in event rate, associated with failure on the largest scale in Kilburn's multiscale fracture model (Kilburn, 2003). The linear trend produced by the inverse of event rate peaks (b) is used to produce a failure forecast time, with failure expected when the trend equals zero. The arrow indicates time of eruption.

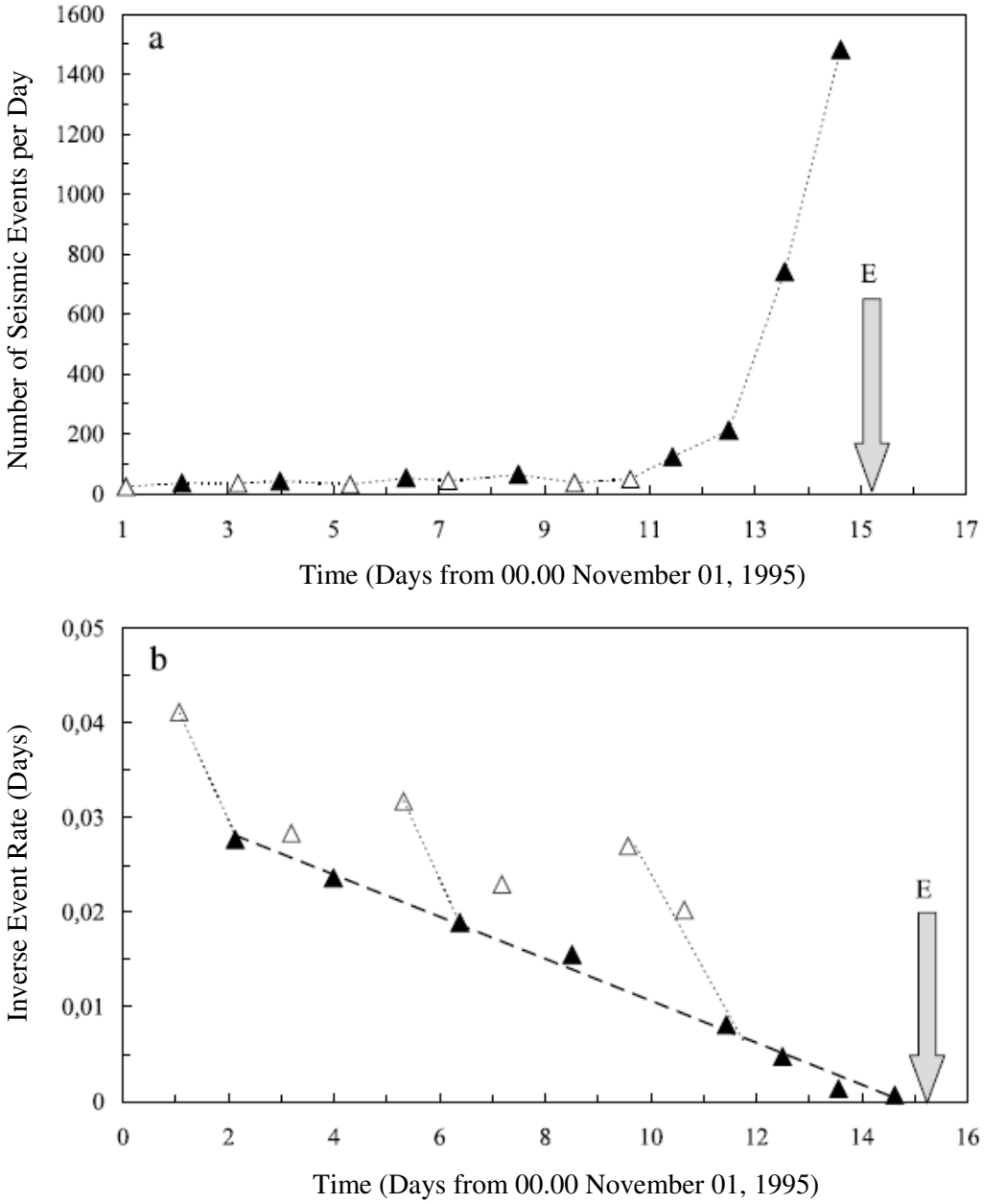

Fig. 3.3 (a) Daily seismic event rate prior to the 1995 eruption at Soufrière Hills. Filled triangles highlight the peaks in event rate, associated with failure on the largest scale in Kilburn's multiscale fracture model (Kilburn, 2003). The linear trend produced by the inverse of event rate peaks (b) is used to produce a failure forecast time, with failure expected when the trend equals zero. The arrow indicates time of eruption.

3.2.3 Propagation and arrest of dykes in a heterogeneous crust

The material failure based models described above predict an acceleration of seismic activity or fracture length suggesting that the process, once begun is uncontrollable. Bulk-failure or eruption is inevitable, the only uncertainty being the time of this event. This runaway style procedure does not explain the occurrence of seismic unrest at

volcanoes or evidence of intruded dykes that never reach the surface (Pinel & Jaupart, 2000). Gudmundsson (2006; 2002) and Gudmundsson and Loetveit (2005) address this issue with a deterministic view of dyke propagation and arrest.

Gudmundsson and Loetveit (2005) considered dyke injection and dyke fed eruptions in rift zones and found that mechanically soft layers of pyroclastic material at shallow depth favour the arrest of propagating dykes. Extensional dyke formation is not confined to rift zones but can occur even in a compressional setting, where dykes will form parallel to the maximum and normal to the minimum compressional stresses. Equally, the action of layers of unfavourable stress conditions acting as barriers to the propagation of extensional dykes applies in various volcanic settings (Gudmundsson, 2002; Gudmundsson, 2006). However, the successive emplacement of arrested dykes gradually homogenises the crust between a magma chamber and the surface, making conditions for eruption more favourable (Gudmundsson, 2002). The relative favouring of dyke propagation or arrest depends only on the mechanical properties of the host rock and the necessary conditions for chamber rupture being supplied by the local stress field, whether this is dominated by the far-field tectonic regime or local effects of magma-induced loading. This mechanism for dyke arrest should therefore apply equally well to any volcanic setting (Gudmundsson, 2006). These models consider the propagation of a magma filled dyke and not the formation and propagation of fractures due to rock weakening and crack interaction, as addressed in this research. However, it is instructive to consider the mechanisms proposed for the suppression of a fracturing process to understand how an accelerating seismic swarm may pass without bulk failure and eruption. The simulation of a layered material made up of varying critical toughness is a simple concept to build into a fracture model based on material properties, and also reproduces an important aspect of a volcanic edifice.

A molten magma chamber can be modelled as a cavity or hole in an elastic solid that disturbs the remote stress field, such that stress concentrates around the magma chamber. Analytical models exist for the behaviour of such a magma chamber in a homogeneous, isotropic crust (Pinel & Jaupart, 2003). Similarly to the runaway, slow fracturing process, injected dykes in a homogeneous model will meet little resistance and will generally propagate to the surface (Gudmundsson, 2006). Typically however, the crust surrounding a magma chamber will be highly heterogeneous and anisotropic and simple, analytical solutions of stress field perturbation are not accurate. Composite volcanoes especially, will often be made of alternating layers of stiff lava flows and soft

pyroclastic material (Gudmundsson, 2006). Gudmundsson (2006) models the effects of layering in the crust on the trajectories of principal compressive stresses, which depend also on the depth, size and geometry of the magma chamber. Boundaries between layers can cause the trajectory of maximum compressive stress to become horizontal, favouring dyke arrest over further propagation. This layering is therefore one possible mechanism to explain the prevalence of injected dykes that never reach the surface.

The dyke propagation model considers only an isolated, magma filled fracture and the effects of the mechanical properties of host rock on the growth of this fracture. Just as stress will concentrate around the magma chamber itself, other faults and fractures within the crust will also alter the local stress field. The magnitude of magmatic pressure decreases with distance from the magma chamber, and at distances on the order of the chamber diameter becomes negligible (Gudmundsson, 2006), but slow fracturing can occur even under a constant load due to rock weakening (McGuire & Kilburn, 1997). The distribution of pre-eruptive, fracture induced seismicity suggests scattered failure rather than a purely magma-driven fracturing.

Gudmundsson's dyke emplacement model and Kilburn's slow fracture model need not be mutually exclusive, but can describe the effects of stress concentrations around cracks, holes or inclusions both immediately surrounding a magma chamber, and throughout the surrounding host rock. Gudmundsson's model also predicts the gradual homogenisation of the crust (Gudmundsson, 2002) and therefore an evolution towards conditions under which Kilburn's multi-scale fracture process explains the rock weakening generated, seismic acceleration to failure and eruption. Gargani et al. (2006) combine the theories of magma-driven failure and fault interaction. They use Coulomb stress change in a finite element model to identify the effect of magma-induced stress perturbations around a molten chamber on pre-existing faults throughout the edifice. Local stresses may create further fracturing of the host rock that in turn influences the magma's pathway from the chamber to the surface. This style of interaction between local stresses and developing fracture networks is one of the key focuses of this research. The finite element model produces surface deformation consistent with field observations, and also indicates regions where seismogenic faulting is most likely to occur. However Coulomb stress transfer shows only where the probability of, or proximity to failure has increased or decreased. With a strict failure criterion it is possible to model directly the formation of a network of fractures and also to incorporate into the model the effects of material properties.

3.3 Fracture mechanics and crack interaction model

In the previous chapter Griffith's energy balance was seen to provide a necessary criterion for fracture, while a critical crack tip stress intensity factor was both a necessary and sufficient condition for crack propagation. The model developed here will represent the evolution of a fractured rock mass and will require the deterministic approach of crack tip characterisation, rather than an energy based structure. The aim is a model based on fundamental fracture mechanics results that will produce an observable output for forecasting purposes. Gudmundsson's deterministic model is based on stress field analysis but offers no observational forecasting tool. An accurate forecast of dyke propagation and arrest requires detailed knowledge of local loading and geometrical form of the volcanic system. Voight's failure forecasting method on the other hand is developed directly from observations. However, in this case producing a forecast requires knowledge of, or an assumption of the value for acceleration parameter α. Kilburn (2003) derived specific values of this parameter that should be expected if failure occurs by slow, multi-scale fracturing under a constant load, and which is consistent with observations. This offers a physical explanation of observable precursors, but has the limitation that it offers no insight into any other mechanisms of pre-eruptive fracturing (Smith et al., 2007), or into different observations that may occur in the future.

The prospective approach taken here requires no prior assumption on the style of fracture rate or acceleration, and therefore places no explicit restriction on the patterns of fracture rate observed, although implicit restrictions may exist due to the very nature of the process being modelled. As well as potentially highlighting any alternative precursory sequences to those that have previously been analysed and modelled, this may also demonstrate necessary conditions under which particular sequences are observed. In addition, the model will not be limited to accelerating sequences only and may therefore be able to reproduce, and hence underline possible causes of seismic swarms that do not result in bulk failure and eruption. In terms of a recordable observation, rates of fracturing in the crust can be correlated with high frequency seismicity, similarly to acoustic emissions measured during fracture experiments in the laboratory (Lockner et al., 1991). Long period or hybrid events may also represent fracture processes within a volcano (Tuffen & Dingwell, 2005; Tuffen et al., 2003). However, these are thought to be produced by fracturing of conduit walls and magma rather than in the process of edifice failure and conduit formation, and the majority of

long period signals are related to the movement of fluids (McNutt, 2005). The bulk of pre-eruptive, conduit forming failure will occur in the brittle elastic regime and allows reasonable use of well established linear elastic fracture results.

Fracture mechanisms can be affected by numerous factors such as pressure, temperature, humidity and material properties. The model produced here will attempt to capture the most important of these factors on the parameters of interest, namely crack propagation and coalescence. The mechanical properties of host rock have been shown to have significant consequences when the same fracture processes have been modelled in a homogeneous and heterogeneous setting (Gudmundsson, 2006; Liu et al., 2007). A heterogeneous crust can present stress barriers or areas of weakness that will have a considerable effect on the growth and coalescence of a population of cracks. The interaction of cracks on a stressed body has also been highlighted as a crucial element of failure. Laboratory experiments suggest that coalescence of micro-cracks is the major process leading to eventual bulk failure of a sample (Amitrano, 2006; Tang, 1997). Ashby and Hallam (1986) described the significance of crack interaction in the fracturing and failing of a brittle material loaded in compression. Crack interaction affects the stress field surrounding close neighbouring cracks and therefore plays an important role in evaluating crack tip characterisation (Lam & Phua, 1991) and subcritical crack growth (Kamaya & Totsuka, 2002). As a result, it is important to consider a population of cracks as a whole rather than just the combined contributions of each individual fracture.

3.4 Chapter summary

Fracture mechanics and failure forecasting have been successfully applied to various areas of volcanology as well as Earth Sciences as a whole. A model of failure mechanisms within a volcanic edifice must incorporate variations in material properties and damage of rock, two important characteristics of individual volcanoes that have a significant effect on fracturing. Even in the absence of precise data it is possible to describe the influence of factors such as remotely applied load, crack geometry, crack interaction and host rock heterogeneity on the development of a fracture network. Both a constant applied load, assuming rock weakening as the sole controlling factor on fracture and magma ascent, and a variable remote stress, due to failure related processes such as deformation or magma degassing can be modelled. Comparison of these results along with those from different distributions for host rock fracture toughness and initial crack network geometry can give indication to the relative importance of these variables on the outcome of a loaded, fractured volcanic edifice.

4. One dimensional model of pre-eruptive seismicity

4.1 Introduction

As described in the previous chapter, evidence for fracturing at volcanoes exists in the form of direct field observations and the development of seismic activity throughout the surrounding crust. The model developed here is based on failure mechanisms preceding an eruption at a long repose volcano and therefore assumes a closed system in which rock weakening is the driving force behind fracturing.

The effects on a volcanic system of rock mechanical properties and the surrounding stress field are described by a one-dimensional array representing the progression of failure throughout a volcano. The initial, intact structure is made up of a number of individual cells, which fail if the local stress intensity exceeds their critical fracture toughness. Stress intensity is a function of neighbouring crack geometry, as well as applied stresses. Cells exist in one of two states, either intact or failed, and once a cell has failed it remains in that state. The number of adjacent failed cells corresponds to the crack length. A connected network of failed cells, extending through the full height of the array, represents a fully connected conduit (Fig. 4.1). A one-dimensional representation is clearly a highly simplified view of the process of crack extension and interaction. Cracks are unlikely to extend and coalesce in a purely tip-to-tip nature, but instead will join through the formation of shear cracks between non-aligned sub-vertical cracks or in some cases will tend to avoid neighbouring cracks leading to arrest of propagation. For this simplified 1D representation, this process has essentially been collapsed down to allow failure in one direction only. For the model it is therefore assumed that cracks will tend to propagate in a tensile mode, in a plane perpendicular to applied stress. In this representation shear stresses cannot exist. Crack arrest can still occur within this model, by the propagation of the crack into an area of greater fracture thoughness.

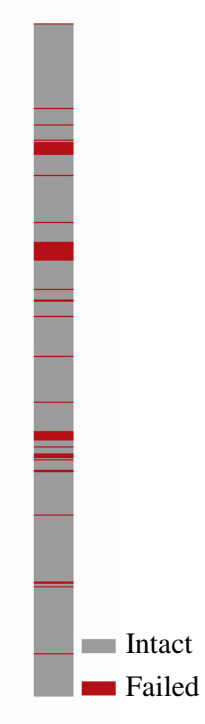

Fig. 4.1 One dimensional array representing a potential pathway to the surface. The array contains a fixed number of cells, each assigned a fracture toughness value. Stress is applied to the array and each cell experinces a stress intensity dependent on the applied stress and location of surrounding cracks. Cells fail once the stress intensity exceeds its fracture toughness. The failure of cells corresponds to seismic events. Grey cells are intact, red cells have failed.

4.2 Physical basis of model

As significant factors in the fracture process, heterogeneous mechanical properties of the host rock and crack interaction are both incorporated into the model. It is assumed that conditions controlling micro-fracturing observed in the laboratory can be applied to macroscopic failure of the scale occurring within the Earth's crust. Statistics of acoustic emissions and scaling parameters from laboratory experiments on rock samples show similarities to those observed in a natural setting. Behaviour of fractures also shows self-similarity over a range of scales (Lockner & Madden, 1991; Xie, 1993). Therefore it is assumed reasonable to apply fracture mechanisms at multiple scales.

4.2.1 Fracture toughness

Heterogeneity of the fracture toughness of rock between a magma chamber and the surface can be introduced into the model using a statistical approach. The Weibull distribution is widely used for representing the distribution of strengths and lifetimes (Weibull, 1951; Tang, 1997; Abaimov et al., 2007). The distribution is based on the concept of a weakest link, and uses the multiplication of the probability of failure of single elements to model failure of the whole (Weibull, 1951). The basic distribution function has the form:

$$F(x) = 1 - e^{-cx^{\gamma}} \tag{4.1}$$

where c and γ are scale and shape parameters respectively. The Weibull distribution is an extreme value distribution, with the shape parameter γ controlling the tail of the distribution. Its utility also stems from its flexibility. The Weibull distribution approximates a normal distribution when the parameter $\gamma = 3.4$, and reduces to an exponential distribution when $\gamma = 1$.

Although the strength and toughness of a material are two different parameters, under various distributions, including Weibull, they may both be described by the same statistical distribution (Xing et al., 1993; Emmerich, 2007). However, it has been suggested that the theoretical basis for the use of the Weibull distribution no longer holds when considering a material's resistance to crack propagation, and that fracture toughness data exhibits a systematic deviation from what is otherwise a reasonable fit by the distribution (Neville & Knott, 1986). Neville (1987) suggests an alternative distribution, based on the theory of stress concentration at crack tips:

$$F(S) = \frac{(S/B)^D}{1 + (S/B)^D} \tag{4.2}$$

"Sampling" S is defined as a power of the stress intensity factor, $S = K^4$, B is the scale parameter and D is the shape parameter. Hazzard et al. (2000) assign bond strengths following a Gaussian distribution in their micromechanical rock failure model, using the variance to control the degree of heterogeneity. Due to its flexibility a Weibull distribution is used to assign cell fracture toughness in the one-dimensional model. By varied selection of parameters, alternative proposed distributions, such as Gaussian can also be accounted for.

Spatial distribution and variability of fracture toughness must also be considered, as along with the statistical distribution, they determine the degree of heterogeneity in the model. A random spatial design can be achieved through a random walk process. A random walk is a sequence of discrete steps, with the magnitude and direction of each step being selected at random from the specified distribution.

Henderson and Main (1992) refer to the abundance of examples of random walks in nature and assign toughness values to their fracture model using a random walk on a Gaussian distribution. A layered structure can represent heterogeneous strata making up a volcanic edifice whilst assuming broad homogeneity of mechanical properties within these strata (Gudmundsson, 2005). For any statistical distribution selected, appropriate experimental data can provide suitable range limits or scale parameter values. In the one-dimensional model both random and layered distributions are applied.

Experimental data exists for fracture toughness measurements over a variety of temperature and pressure conditions for both intrusive and extrusive rock. Meredith and Atkinson (1985) measured the fracture toughness for intrusive rocks, at temperatures from 20 to 400°C and found values between 1.7 and 3.1 MPa$\sqrt{m}$ for Westerly granite and Black gabbro. Balme et al (2004) conducted high-pressure and high-temperature experiments on Icelandic, Vesuvian and Etnean basalts and measured fracture toughness values between 1.4 and 3.8 MPa$\sqrt{m}$. In laboratory experiments, Smith (2007) measured fracture toughness at pressure and temperature conditions consistent with different regions within a volcano, including material close to a conduit, close to a magma source, and rock at depths of 1.5-2.5 km beneath the summit of a volcano. Experiments were carried out on ancestral Mt Shasta andesite and over the various conditions the fracture toughness measured remained consistent around 2.5±0.5 MPa$\sqrt{m}$.

4.2.2 Flaw distribution

Applied stress will concentrate at crack tips and therefore the number, location and size of initial cracks will also affect the progression of the model. In assigning a geometry for initial flaws, both crack length distribution and crack density must be considered. Steacy and Sammis (1992) assume a fractal distribution for starter flaws in their damage mechanics model. Under this assumption, crack size frequency will follow a power law relation between limits of a maximum and a minimum flaw size, where the latter may be dependent on the observation scale, and for modelling will be limited by grid size. Power law trends have been found for crack length populations from the laboratory scale to the field scale (Wong et al., 2006; Hatton et al., 1993).

Renshaw and Pollard (1994) use a uniform probability distribution to assign initial flaw geometry in their numerical fracture set model. Altering the critical probability value in their model, above which a network node fails, creates different

starting distributions. On comparison of the numerical fracture sets with experimental results, "invisible" flaws were added to the numerical distribution to allow for the growth of cracks initially smaller than the model grid size. In the model presented here, the initial location of cracks or flaws can be related to the specified fracture toughness distribution. Fracture toughness measures resistance to propagation of an existing crack and therefore a low value of this property at the grid scale can be associated with the presence of a microcrack at the smaller, invisible scale. In other words, as soon as stress is applied to the model, the weakest areas will fail first, producing an initial distribution of cracks in a similar fashion to the critical probability threshold described above. The spatial and statistical distributions of fracture toughness can then also control the initial crack length statistics.

The pre-existing distribution of flaws or cracks within the crust is highly heterogeneous, depending greatly on the rock and stress history (Wong et al., 2006; Kranz, 1983). Even in the case of a long repose volcano, host rock within and below a volcanic edifice may be heavily fractured (Kilburn, 2003; Scandone et al., 2007) and it will therefore be instructive to also consider the effects of larger scale faults and cracks within an interacting fracture network.

4.2.3 Stress field

In addition to the regional stress field within which a volcano lies, the local stress field can also be affected by topographic loading, and magma and hydrothermal processes (Roman et al., 2004). Topographic loading of the crust has been identified as a major influence on the stress field and resulting seismicity at Mt. Spurr, Alaska and Mt. Vesuvius, Italy (Jolly et al., 1994; De Natale et al., 2000). Roman et al. have looked at the evolution of local stress fields both before and during eruptions at Mt. Spurr (2004) and episodes during the ongoing activity at Soufrière Hills, Montserrat (2008), using detailed analysis of seismic data. Analysis of fault plane solutions of VT events in the weeks to days prior to renewed activity at Soufrière Hills, suggests that the local stress-field undergoes a 90° reorientation during this period. This is correlated with the inflation of a dyke located beneath the vent, and is proposed as a forecasting tool for future activity. However, few sufficiently detailed earthquake data sets exist to enable this method to be used to provide a general picture of local stress fields within a volcano.

Experimental data is largely produced under constant strain rate or constant load testing, modelling rock deformation response to either a regional strain or fixed stress field (e.g. Mavko et al., 1998). The influence of both constant and variable stress conditions on the development of fracture networks has been highlighted by numerical models (Renshaw & Pollard, 1994; Tuckwell, 2003), and fracture patterns in geological materials can be used to interpret the local stress history. In particular, failure of the crust has been modelled under both constant and increasing stresses. Modelling earthquake recurrence times, Main (1988) considered a time dependent remote stress with a constant load rate $\dot{\sigma}$:

$$\sigma(t) = \sigma_0 + \dot{\sigma}t \tag{4.3}$$

De la Cruz-Reyna and Reyes-Davila (2001) developed a visco-elastic model for material failure, with applications to eruption forecasting, and considered a constant load, a linearly increasing load, and an initially increasing load which is then held constant at σ_0 after time t_c:

$$\sigma(t) = \frac{\sigma_0}{t_c} tH(t_c - t) + \sigma_0 H(t - t_c) \tag{4.4}$$

Non-linear increases in stress have generally been associated with magma induced pressure changes, for example in relation to lava-dome eruptions (Sparks, 1997).

The time scale involved when considering medium-term precursory activity is relatively short compared with that for magma induced pressure changes. The lack of migration of VT seismicity prior to eruption suggests that magma intrusion is not a source of stress variation during this process. Slow rock fracture as a control on magma ascent also requires no magma generated increase in pressure (Kilburn & Voight, 1998). Therefore in the one-dimensional model of precursory fracture, an assumption of a temporally constant local stress field is also a reasonable model parameter.

4.2.4 Stress intensity

Stress applied to a body will concentrate at the tips of cracks and flaws within the material, as described in Chapter 2. The remote stress applied to the model is adjusted locally according to the geometry of surrounding cracks. For an isolated, two-dimensional crack the stress intensity factor at each of its tip is given by:

$$K = \sigma\sqrt{\pi a} \tag{4.5}$$

where a is the crack semi-length and σ the applied stress (Lawn & Wilshaw, 1975). In the crack tip region, stresses decrease with the inverse square root of distance from the crack tip (Atkinson, 1987). The stress intensity factor deals with the magnitude of crack-tip stress concentration and the likelihood of a fracture to propagate. Here it is also assumed that the stress intensity factor determines the extent of crack propagation. The greater the crack length, the greater the degree of stress concentration, and the greater the expected increase in crack length (Tuckwell et al., 2003). The crack-tip stress intensity is reduced with distance from the crack, within the range of half the crack length. The extent of propagation will then depend on both crack length and local fracture toughness, with failure occurring a distance x from an isolated crack if local toughness is exceeded by:

$$K = \sigma\sqrt{\frac{\pi a}{x}} \tag{4.6}$$

As cracks form closer together they will interact mechanically and therefore no longer act as isolated cracks. Tuckwell et al. (2003) allow for crack interaction by defining a non-linear process zone around propagating crack tips, the extent of which is dependent on the crack tip stress intensity. Neighbouring cracks will join up if their respective process zones overlap. This method allows only for the coalescence of cracks due to mechanical interaction and not individual crack growth as a result of stress intensity increase in the presence of a neighbouring crack (Sammonds & Ohnaka, 1998). Kachanov (1987) proposes a superposition technique for approximating linear elastic stress fields surrounding an arbitrary distribution of cracks. The integral based

technique produces good approximations to known analytical results until the distance between cracks becomes small relative to crack length, in which case the effects of crack interaction are underestimated.

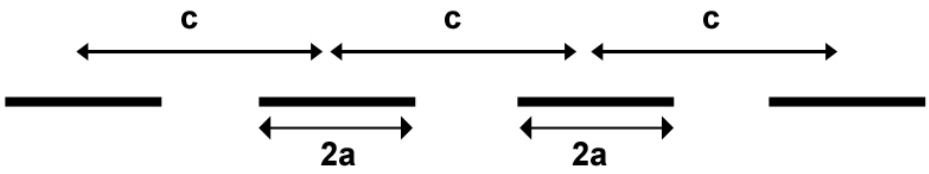

Fig. 4.2 Crack length and spacing measurements used in Rudnicki and Kanamori's stress intensity calculations for an infinite array.

Analytical solutions for crack-tip stress fields exist for only a small number of, generally uniform, geometries of neighbouring, interacting cracks (Tada et al., 1973). As described by Rudnicki and Kanamori (1981), the crack-tip stress intensity factor for an infinite periodic array of cracks is:

$$K = \sigma \left[c \tan\left(\frac{\pi a}{c}\right) \right]^{1/2} \tag{4.7}$$

where c is the distance from one crack centre to the next (Fig. 4.2). When cracks are a great enough distance apart to behave as isolated cracks, Equation (4.7) reduces to (4.6) by the property $\tan\theta \approx \theta$ for small values of θ. Following Henderson and Main (1992), the effects of crack interaction on stress intensity at crack tips and the region between neighbouring cracks is assigned using Equation (4.7), adjusted to allow for unequal crack lengths and inter-crack distances. For a cell in the one-dimensional array, a distance x_1 and x_2 respectively from adjacent cracks of length $2a_1$ and $2a_2$, the stress intensity is calculated by summing the effects of each crack interacting with a notional crack of the same size. This sum is adjusted by a factor dependent on the crack lengths $2a_i$ and the point's distance from each crack x_i, also allowing for attenuation of the concentration away from crack-tips:

$$K = f[a_i, x_i]\,\sigma \sum_{i=1,2} \left[c_i \tan\left(\frac{\pi a_i}{c_i}\right)\right]^{1/2} \tag{4.8}$$

$$f = \frac{1}{c}\left(1 - \delta_{ij}\right)\frac{x_i a_j}{\sqrt{x_j}} \tag{4.9}$$

c is the actual centre to centre distance, while c_i represents the centre to centre distance between crack i and the notional crack of the same length (Fig. 4.3). δ_{ij} is the Kronecker delta function.

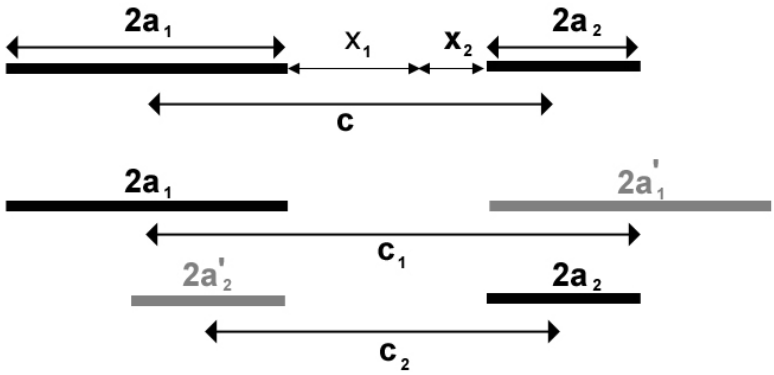

Fig. 4.3 The stress intensity at a distance x_1 from a crack of length $2a_1$, and distance x_2 from a crack of length $2a_2$ (top), is calculated by summing the effects of each of the two cracks interacting with a notional crack of equal length (grey cracks), as described in Equation (4.8). The distance between the modeled and notional cracks is the same as that between the original cracks (i.e. $x_1 + x_2$). The centre-to-centre distances between the two modeled cracks and the modeled and notional cracks are given by c, c_1 and c_2 respectively, and are related by $2c = c_1 + c_2$.

Again, this term for stress intensity concentration tends back to (4.6) when the inter-crack distance is large. For example, when two identical cracks are separated by a distance equal to their length, the effect of interaction on the crack tips increases the stress intensity by just 10% (Rudnicki & Kanamori, 1981).

This interaction effect creates a positive feedback process. As cracks form close together the surrounding stress intensity is increased, causing new cracks to form, which further increases the stress; thus, under certain conditions, a runaway fracturing process is established, and the system rapidly runs to failure.

4.3 Description of model

4.3.1 Initial conditions

In the one dimensional array, a fully connected pathway can arise only when all cells have failed. Model sizes up to 7,000 cells were tested. Results remained statistically consistent for sizes above 1,000 cells and therefore model sizes of 1,000 - 2,000 cells were generally used, in order to reduce long computational running times.

Following the discussion in Section 4.2.1, a fracture toughness value is assigned to each cell by generating a random walk on a Weibull distribution. Initially the shape parameter of the Weibull distribution has a normal distribution with mean 3.4. Values are arranged spatially according to the number of homogeneous layers to be modelled, and the degree of local homogeneity within these layers. For example, for complete heterogeneity a number of layers equal to the number of cells can be selected. The series of fracture toughness values produced by the random walk process are sorted into ascending order and distributed over the cells according to the number of layers and homogeneity within each layer. For a homogeneous layer, consecutive values from the ordered list are selected. For a layer with a greater degree of heterongeneity, values are selected from a larger range within the list of toughness values.

As described in Section 4.2.2, flaws are naturally introduced into the array when the initial stress is applied and cells with a fracture toughness value less than the applied stress fail immediately. For model runs where a specified distribution of flaws is being tested, for example a set of cracks with a power law frequency-length distribution, this distribution is then also assigned. If a greater number of initial flaws are required than those that naturally fail due their fracture toughness, these extra flaws are added by randomly selecting intact cells and assigning a state of failure. Table 4.1 contains each of the input parameters and their respective ranges.

Input parameter	Distribution/Range
Fracture toughness	Weibull$[a, b]$ $a \sim$ N $[3.4, 1]$, $b \sim$ N $[1, 1]$
Number of layers for fracture toughness homogeneity	R $[1, n]$ (n = number of cells)
Homogeneity within layers	R$[0, 1]$ (a value of 0 implies toughness values are assigned at random within the layer, a value of 1 implies toughness values are assigned in numerical order within the layer.
Number of initial flaws	R$[0, n/50]$ (n = number of cells)

Table 4.1 Distributions for input parameters to the one-dimensional model.

4.3.2 Running the model

An initial stress is applied uniformly to the model and a stress intensity value is calculated for each cell, dependent on the geometry of neighbouring flaws, by Equations (4.6) and (4.8). After checking for failing cells the stress intensity values are then re-calculated, taking into account any newly failed cells and adjustment of the remote stress level. Cells are then again checked for failure. These iterations continue until either all cells have failed and a connected pathway is formed, or until no further failures will occur under the prescribed loading conditions. The model is generally run under one of two conditions: constant stress or constant load rate.

Under constant stress, the remotely applied stress remains the same during each iteration of the model and changes to stress intensity arise solely due to the failure of new cells. The model need not always fail under this condition, but can instead reach a state of stability where no further cells are caused to fail. To simulate a constant load rate, some measure of time must be introduced into the model. Each iteration in the running of the model provides a natural measurement of time, as the static stress transfer involved can generally be assumed to occur on a time-scale independent of the size or location of the failure event. A constant load rate is therefore modelled by a regular increase in the remote stress with each iteration of the model.

4.3.3 Seismic event rate

The failure of a cell is considered as representing a seismic event and the event rate is therefore simply the number of cells failing during each iteration of the model. This is recorded along with the location of events, to enable a picture of the spatial development of cracks. An approximate magnitude of events is measured by the length l of adjacent cells failing simultaneously, via a logarithmic relation:

$$m = 4 - n \log l \tag{4.10}$$

The constant n takes a value between 3 and 4 (Kanamori & Anderson, 1975) and A is selected to scale the magnitude. For example, if $n = 4$ and $A = 10$ the failure of a single isolated cell will produce a magnitude zero event. If $n = 3$, $A = 10$ results in a single failure producing a magnitude one event.

By altering the initial variables in the model it is possible to investigate the effects of mechanical inhomogeneities, the extent of damage, and the local stress conditions on the development of a fracture network.

4.4 Observations and sensitivity analysis

4.4.1 Exponential acceleration and linear inverse trend

When run under constant stress or constant load rate, with input parameters taken randomly from the distributions described in Table 4.1, the prevailing patterns of seismic event rate observed are comprised of exponential increase with time, and linear inverse event rate with time. A linear inverse rate can be extrapolated towards a singularity point of infinite event rate and describes hyperbolic growth. A continuous exponential growth or an initial exponential growth that becomes hyperbolic prior to failure, are patterns observed in the model. Representative results are shown in this section, and are typical of the output distibutions produced by random simulations of the one-dimensional model. Figure 4.4 contains two examples of model outputs, showing a good fit ($R^2 > 0.9$) to each of these growth patterns respectively. Figure 4.5 shows the progression of the array for each example.

A drop-off in the event rate is often seen immediately prior to failure. In the case where this coincides with the time of failure, as in the example in Figure 4.4a, it is assumed that this is due to the closed nature of a one dimensional model. During the final loop of the process, there will be a limited number of cells that remain intact and are subsequently available to fail and produce a seismic event.

(a)

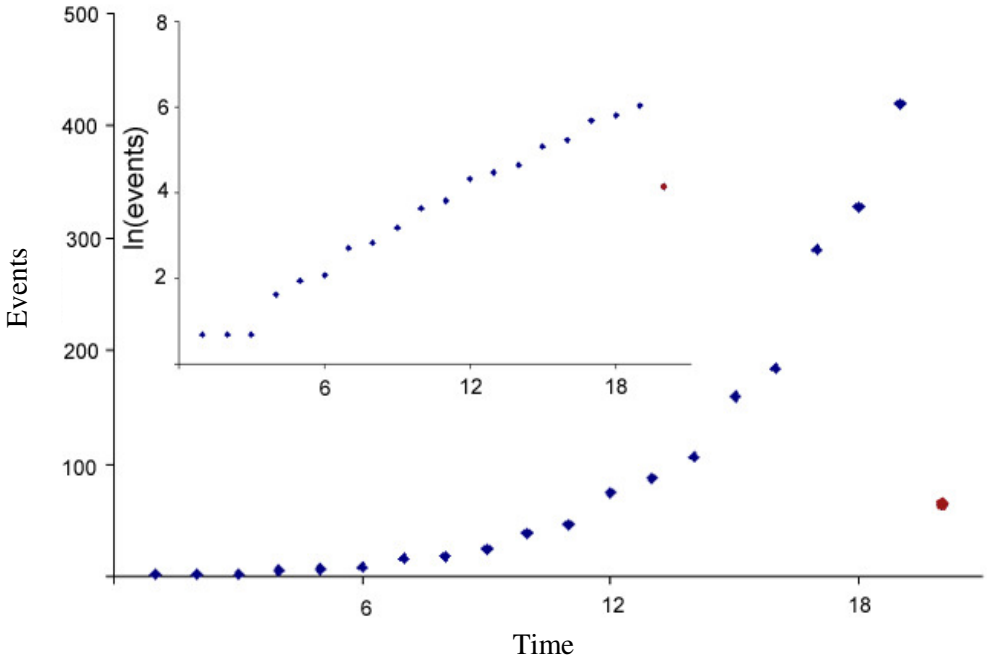

(b)

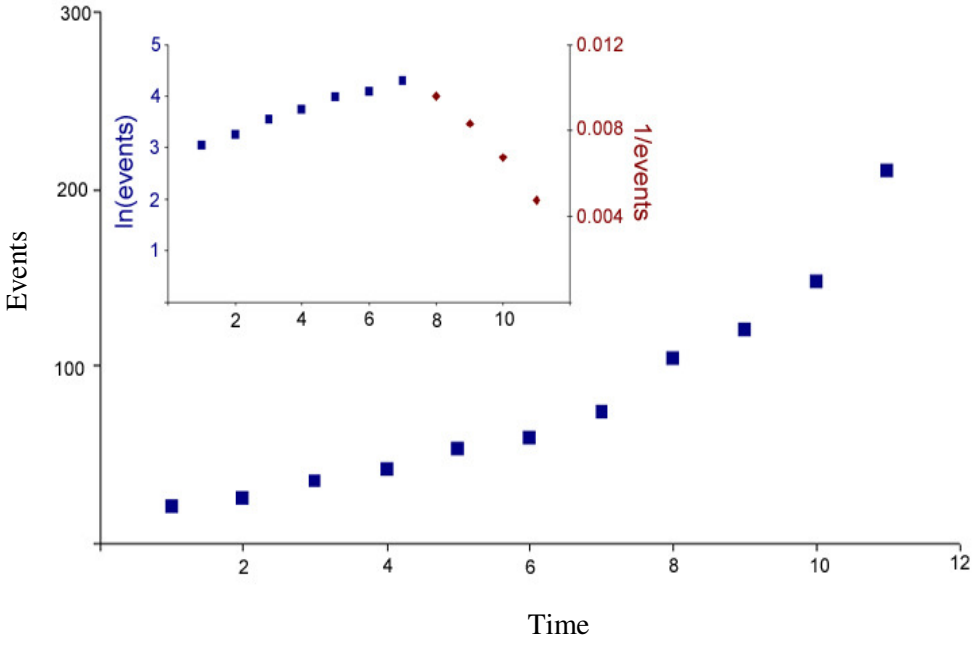

Fig. 4.4 Typical outputs from the one dimensional model under a constant stress, showing seismic event rate with time. (a) Exponential growth is often recorded. Inset shows the natural log of event rate, with a good linear fit ($R^2 = 0.99$). A drop-off in event rate is often seen immediately prior to failure due to a limited number of cells remaining intact. (b) A trend which becomes hyperbolic is also observed. Inset shows the initial linear log event rate ($R^2 = 0.99$), followed by a linear inverse rate, signifying the onset of hyperbolic growth ($R^2 = 0.99$).

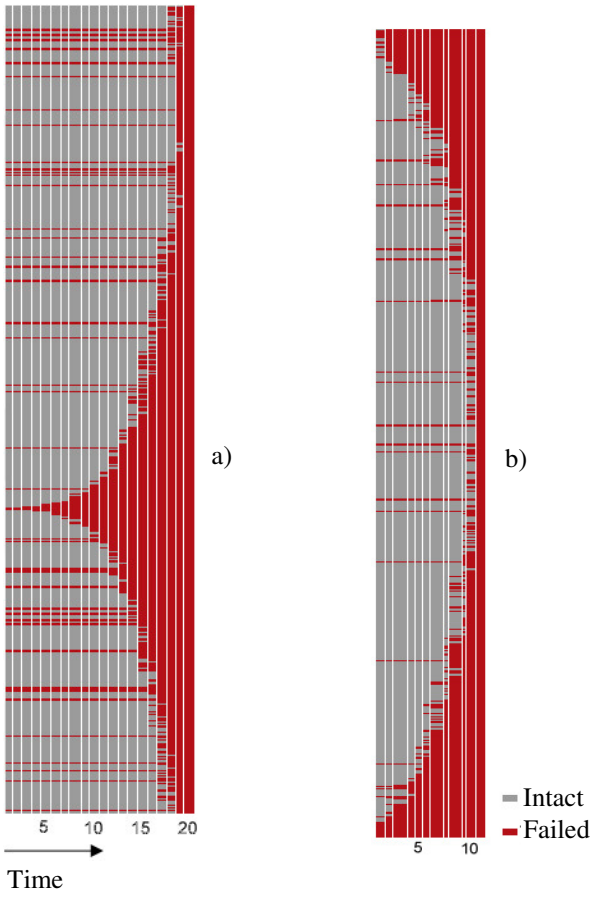

Fig. 4.5 Progression of the one dimensional array with time. Intact cells are grey, failed cells red. (a) Failure dominated by one primary fracture produced the exponential trend in seismicity shown in Fig. 4.4a. (b) Event rate produced is exponential initially, but becomes hyperbolic prior to failure (Fig. 4.4b). Results represent typical examples from multiple runs of the model.

Figure 4.6 shows an additional example of the progression of the model array, and the resulting linear inverse event rate. In this particular case a greater number of primary cracks grow throughout the model, allowing for greater crack interaction effects.

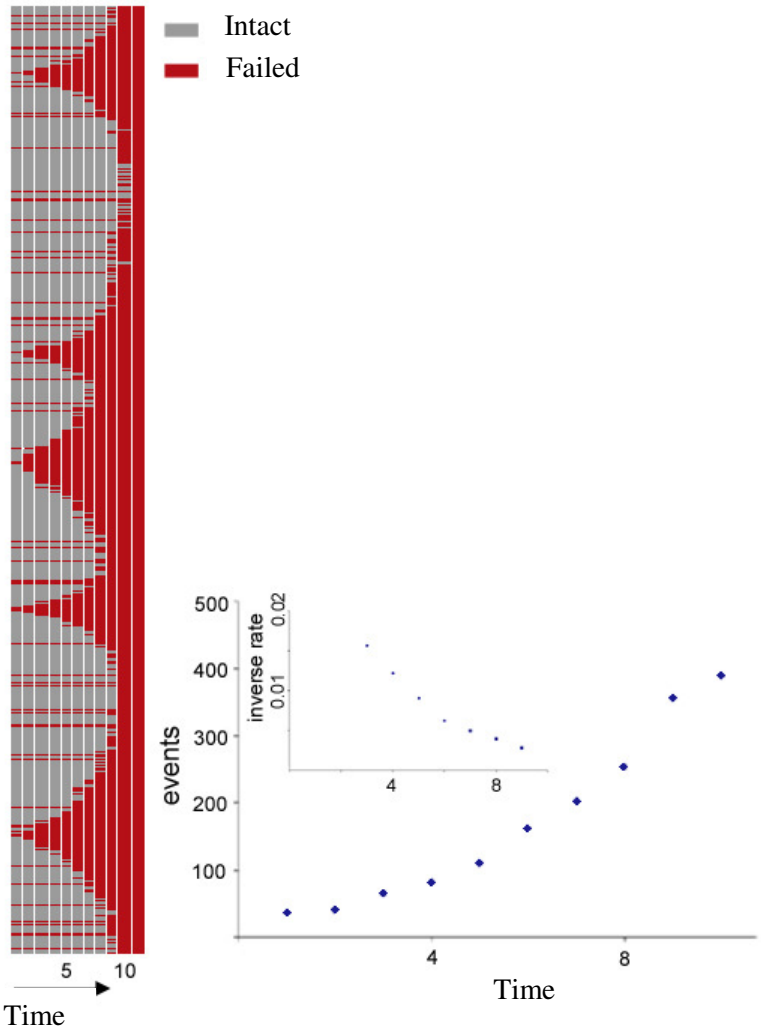

Fig. 4.6 Progression of one-dimensional array with time, showing simultaneous growth and interaction of multiple cracks, and the resulting event-rate and inverse-rate trends. This represents a typical such result from multiple runs of the model.

4.4.2 Effect of fracture distribution

To gain some understanding of the influence or importance of the distribution of initial cracks on the evolution of failure, the model was run three times, with the same distribution of fracture toughness but different arrangements of initial cracks. In each case 20 out of 1,000 cells were assigned a starting state of failure. In each of the three cases, these 20 cells were arranged as 10 uniformly separated cracks of length two, one single, central crack of length 20, and completely at random throughout the array. When subjected to a uniform load each case produced a seismic event rate with a good fit to an exponential curve ($R^2 > 0.94$). The magnitude of the applied stress was

chosen to be the minimum value that would lead to complete failure. The rate of exponential growth was slower in the case with one single crack, with a rate constant of 0.16, compared to values of 0.31 and 0.25 in the uniform and random case respectively. This may be due to the activity being driven by the growth of a single crack. If multiple cracks exist, interaction between these cracks further increases stress intensity, and the coalescence of cracks provides a mechanism for rapid crack growth.

Despite cells having the same fracture toughness value in all three cases, extensive failure initiates in different regions in each run (Fig. 4.7), implying that low fracture toughness alone does not determine which areas will fail most readily. The location of fractures is also important in determining the evolution of a fracture network.

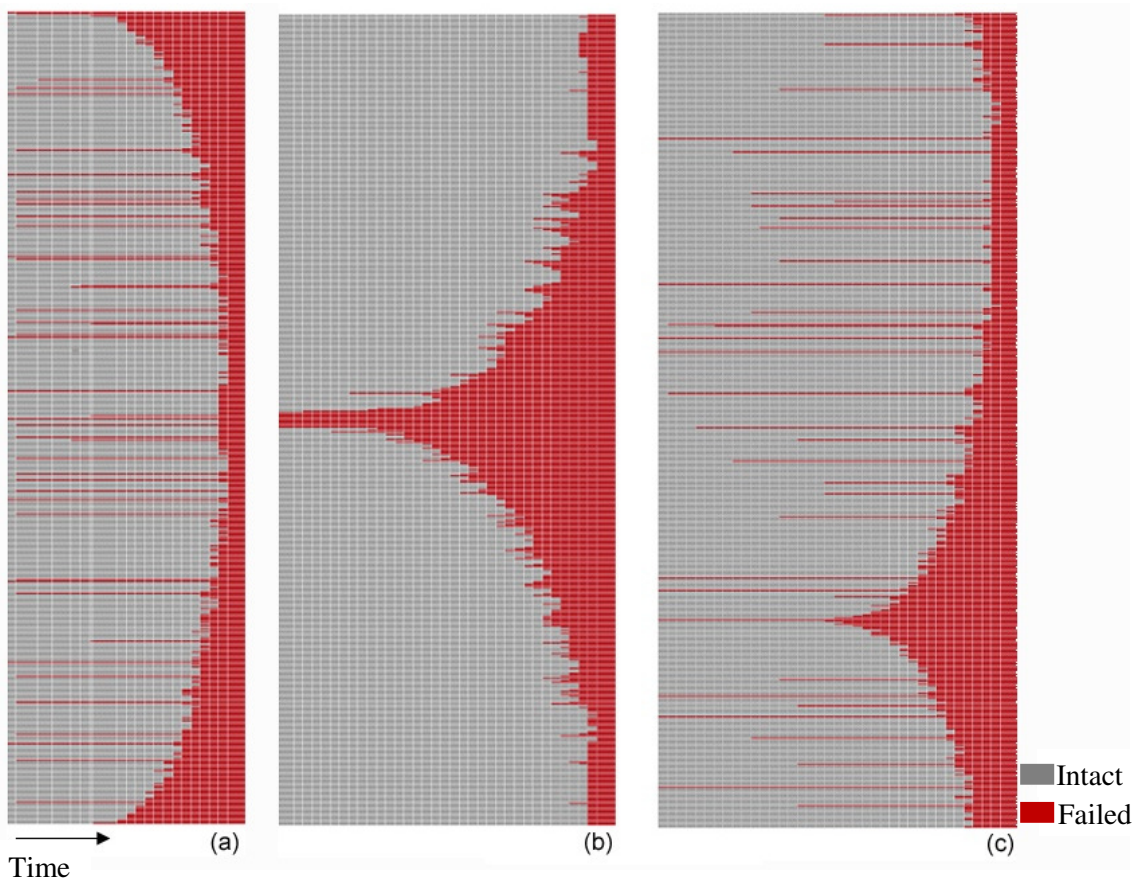

Fig. 4.7 Progression of cracks with time for three simulations of the one-dimensional model, with identical fracture toughness distribution. Each run has 20 initially failed cells, with a different spatial distribution of the failed cells in each case. (a) Failed cells are

distributed uniformally along the array, as 10 cracks of length 2 with an inter-crack distance of 98 cells. (b) Failed cells produce one single, central crack of length 20. (c) Failed cells are distributed at random along the array.

4.4.3 Effect of fracture toughness distribution

Given uniform fracture toughness, the event rate will be controlled by the stress intensity distribution and the location of initial cracks. Aside from interaction effects, two cracks of the same length will extend at the same rate. Under a constant load, the model will fail if the remotely applied stress is greater than that necessary to cause the largest crack to extend, as there will be no region of greater fracture toughness to halt crack growth. This crack, or multiple cracks if there are several of the same length, can then freely extend throughout the entire array (Fig. 4.8).

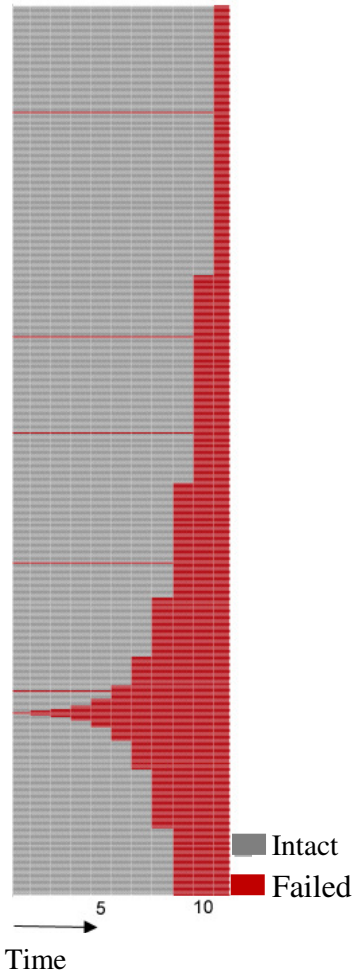

Fig. 4.8 Progression of a one dimensional array with uniform fracture toughness. The largest initial crack dominates activity entirely and growth spreads evenly while the model boundaries allow. Growth rate slows slightly once the dominating crack can grow in one direction only.

Under uniform fracture toughness, the model again provides a good fit to exponential growth in seismic event rate. When the model is run with the same initial cracks and the minimum stress that produces failure, but with an entirely random fracture toughness, exponential growth is still observed but the rate constant is generally lower, with exact magnitudes dependent on the distribution. In other words, the variable fracture toughness acts to slow down the process somewhat. Once a variable fracture toughness is introduced, rather than the pure extension of existing cracks, cracks tend to grow by the development of smaller cracks around its tip, which then coalesce to create extension of the original crack. This process leads to a damage zone around an advancing fracture.

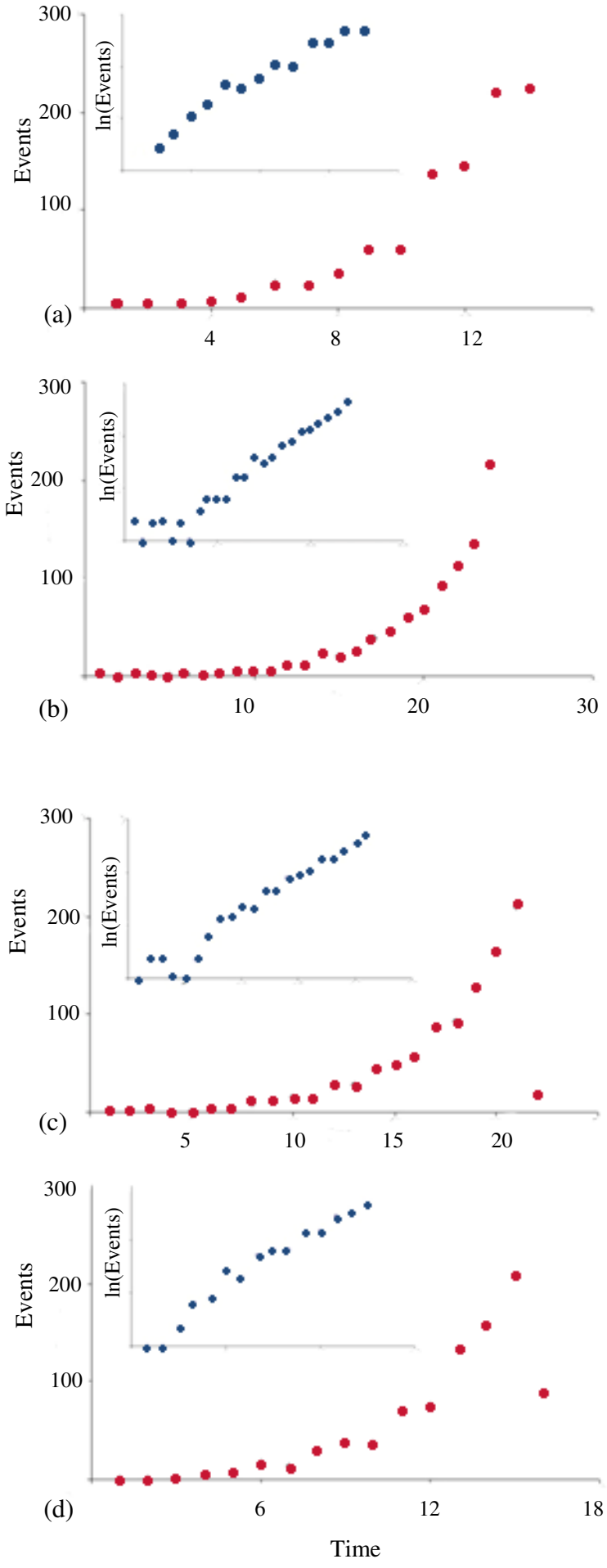

Fig. 4.9 Event rate and log event rate with time for four runs of the model with an identical distribution of initial flaws, and fracture toughness values assigned from different distributions. Fracture toughness values are selected at random from a rectangular distribution with a range of (a) 5 (b) 20 and (c) 10 units. Values are assigned randomly along the array. (d) The final run has toughness values selected at random from a rectangular distribution with a range of 20 units, which are applied to the array with clusters of similar magnitude values. All runs produce a roughly exponential increase in event rate. The exponential rate constant reduces with the increase in range of the fracture toughness distribution, λ = 0.4, 0.24, 0.28 respectively for ranges 5, 20 and 10 (Figs. (a) to (c)) respectively. A clustered distribution produced the rate λ = 0.39. For the case of a constant fracture toughness (Fig. 4.8) λ = 0.57.

The effect of the degree of variability in fracture toughness can also be considered. The model was run four times, each time with the same initial failures and the minimum load necessary to ensure failure. A random fracture toughness distribution is assigned with a range of 5, 10 and 20 units for the first three runs respectively. Values are selected from a rectangular distribution with ranges described above. These values are then distributed randomly over the cells. All three distributions are centred about the same mean, and the increase in range equates to over a 400% increase in the standard deviation from 1.4 to 5.8. As the variability increases, the exponential rate constant decreases (Fig. 4.9). For the final run of the model, a variability range of 20 is again used, but the values are clustered spatially. For example, cells with a high fracture toughness are more likely to be surrounded by other cells with a high fracture toughness. This has the effect of increasing the exponential rate of growth.

4.4.4 Monte Carlo sampling

The range of outputs from the model can be seen to be simultaneously dependent on the distribution of fractures, the distribution and variability of fracture toughness and the loading conditions. A Monte Carlo method was used to explore the outcomes of repeated samplings for combinations of these factors. Clearly a large degree of uncertainty exists concerning the appropriate inputs to use for any specific volcano under study. A Monte Carlo simulation provides not only a useful means of assessing how a variety of conditions may affect seismic event rate, but also the range of observations which might be expected prior to an eruption.

A separate simulation was run for constant load and constant load rate as the disparate time scales for these conditions makes comparison difficult. In each case, the model was run numerous times with different initial conditions chosen at random for each separate run. The variables selected are the shape and scale parameters used to describe the Weibull distribution of the fracture toughness values; the number, respective size and variability of layers for the fracture toughness values; and the number, length-frequency distribution and the degree of randomness or uniformity to the location of initially failed cells.

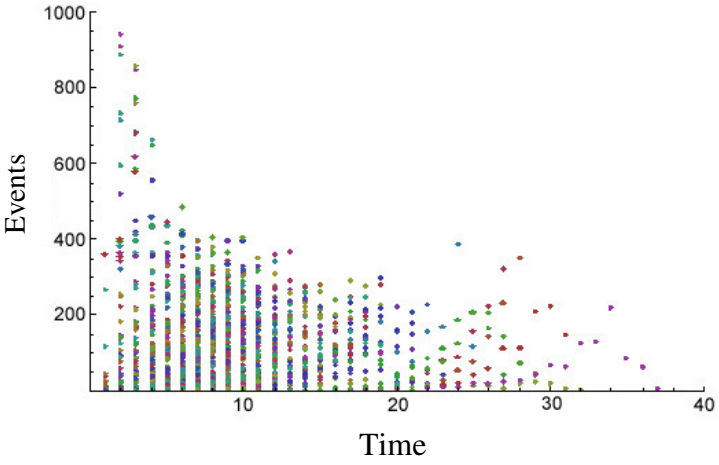

Fig. 4.10 Event rate with time for 200 individual runs of the one dimensional model under increasing stress. Input parameters are chosen at random from the distributions described in Table 4.1. Time is measured from the start of each model run.

Under constant loading rate, the same stress increase of 0.1 MPa/unit time was used in 200 separate runs (Fig. 4.10). This was a value found to be generally large enough to induce further fracturing, but sufficiently small to allow gradual rather than large scale failure. Of 200 outputs, 138 showed a significant fit ($R^2 > 0.9$) to a continuous exponential trend and 4 produced a better fit to an exponential growth that became hyperbolic prior to failure. The exponential rate constants and inverse gradients for these observations were also recorded (Fig. 4.11). The exponential constants range from 0.24 to 3.38, with approximately 80% of the trends having a rate constant less than 0.8. The 4 trends showing hyperbolic growth have inverse gradients of $(2.0, 4.1) \times 10^{-3}$.

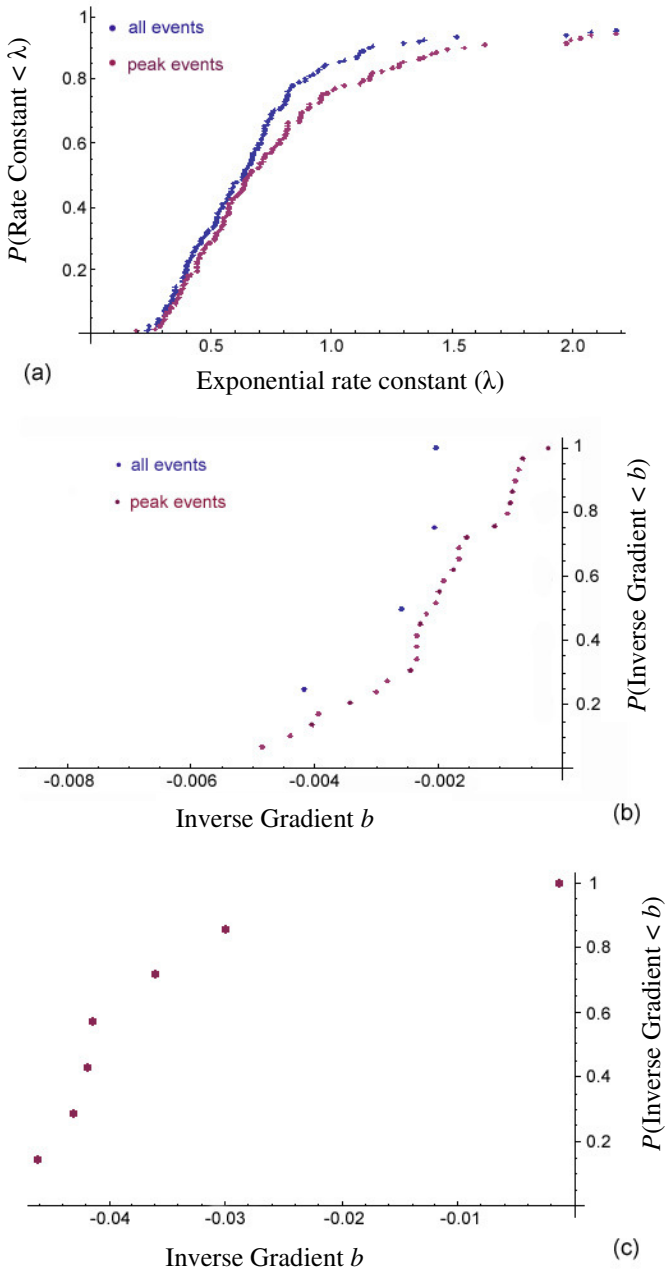

Fig. 4.11 Cumulative probability function for (a) the exponential rate constants from 138 Monte Carlo runs producing an expoential increase in event rate, and (b) the gradient of inverse seismic event rate for the 4 Monte Carlo runs producing an exponential followed by hyperbolic increase in event rate. The peak event distributions describe the exponential rate constants and inverse gradients for the Monte Carlo runs when only the local peaks in event rate were used in analysis, as described in Section 3.2.2. When only peak events are included, 29 of the Monte Carlo runs produce an exponential event rate that becomes hyperbolic prior to failure (b), and 7 produce a purely hyperbolic increase. Figure (c) shows the cumulative probability function for the gradient of the inverse event rate in these 7 cases. Event rate trends are the output from 200 individual runs of the one dimensional model subjected to increasing stress.

Many of the observed event rate patterns show an overall exponential or hyperbolic growth, but due to a greater degree or variability within this trend do not give a statistically significant fit. To look at the extent of these general trends, a similar analysis was done for the peak event rates only. Kilburn (2003) demonstrated that the failure forecast method could be applied to activity occurring on different scales at Pinatubo and Soufrière Hills. Using only peaks in the model event rate, the 200 runs produce 133 continuous exponential trends, 29 exponential to hyperbolic trends and 7

showing just the hyperbolic section of growth. Exponential rate constants are similarly distributed as in the case of all events. However, inverse gradients for the purely hyperbolic growth are in general an order of magnitude greater than those trends that become hyperbolic following an exponential increase. These purely hyperbolic cases are, by definition, examples which show rapid growth immediately and this is likely to occur when the selection of parameters gives relatively homogeneous and low fracture toughness values. Combined with a distribution of initial flaws that optimises interaction, this will lead to very rapid bulk failure, with little to slow the process. The small number of such cases in the simulation suggests that this combination of factors is statistically uncommon.

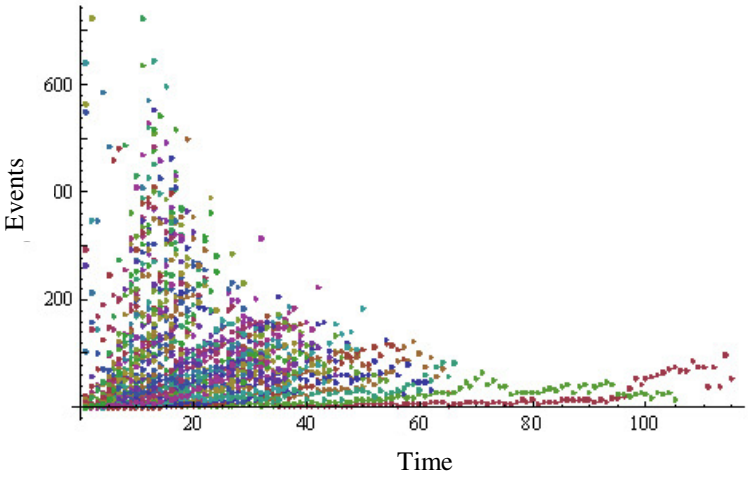

Fig. 4.12 Event rate with time for 100 individual runs of the one dimensional model under constant load. Input parameters are chosen at random from a range of possible values and distributions. Time is measured from the start of each model run.

Figure 4.12 shows the results of 100 runs of the model under constant load, where the level of stress chosen was the minimum required to produce complete failure. The average failure time under constant stress is longer than that with increasing stress. Stress intensity is an increasing function of crack length, proximity to a crack and also external stress. With all factors equal, an array that is subjected to a higher applied stress will fail more rapidly than that subjected to a lower stress. From the 100 runs, there were 77 significant ($R^2 > 0.9$) continuous exponential trends, and 9 that became

hyperbolic after an initial exponential increase. The number of significant exponential to hyperbolic trends increased to 27 when only peak events were considered, with 71 following continuous exponential growth. Exponential rate constants are significantly lower on average than for the increasing stress case, with values in the range of 0.03 to 0.7 (Fig. 4.13a). Inverse gradients have a similar lower limit to the increasing stress case, but increase to a lesser maximum of 2.0×10^{-3} (Fig. 4.13b), again with the peak event cases showing a wider range of values.

Looking directly at the initial conditions for the different runs, those that produce an exponential developing into hyperbolic trend appear to have a generally more homogeneous fracture toughness distribution, and initial flaws that are more clustered. As described in Section 4.2.1, the shape parameter b of the Weibull distribution controls the shape of distribution. The mean value for this parameter from the Monte Carlo runs producing an exponential trend was 1.7. For the exponential to hyperbolic trends the mean value was 0.8. Lower values of b produce a distribution closer to an exponential distribution, with a smaller range, and therefore more similar values than a normal distribution, which is more closely resembled with larger values of b. Both the exponential and exponential to hyperbolic trends had similar initial conditions in terms of crack length distribution, with average mean lengths of 1.5 and 1.4 respectively. However, a greater difference was observed in the initial inter-crack distance distribution. A mean value of 134 was recorded for the runs producing exponential trends, and 94 for those that progressed into hyperbolic trends.

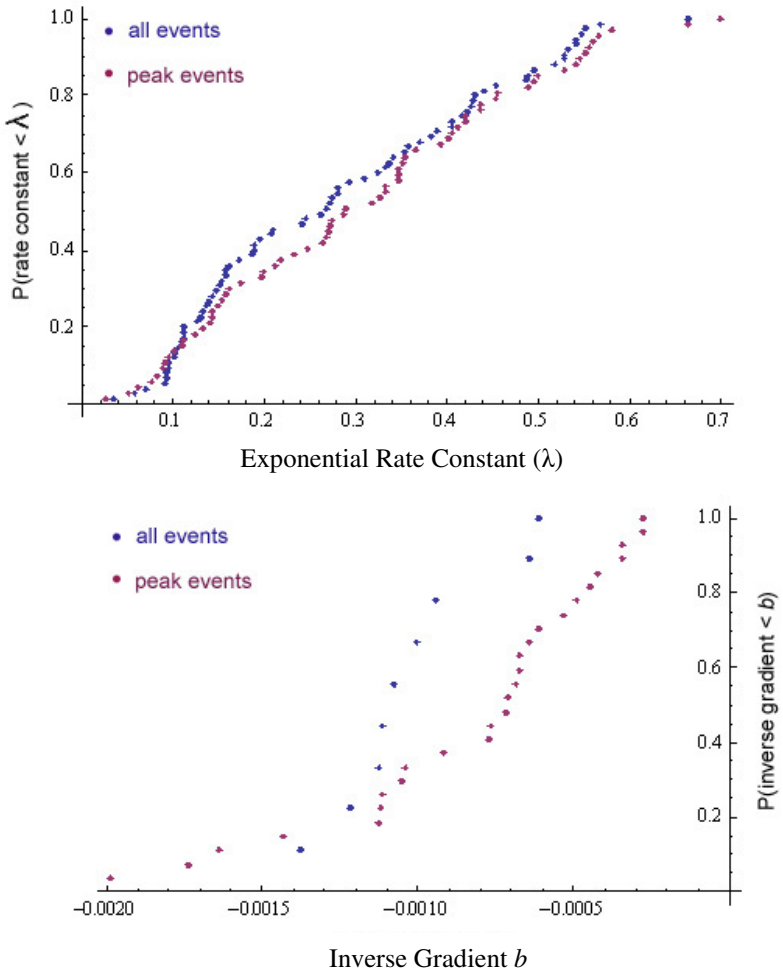

Fig. 4.13 Cumulative probability function for (a) the exponential rate constant from the 77 Monte Carlo runs producing an exponential increase in event rate prior to failure, and (b) the gradient of inverse number of events with time for the 9 Monte Carlo runs producing an exponential trend that becomes hyperbolic prior to failure. The peak event distributions describe the exponential rate constants and inverse gradients for the Monte Carlo runs when only the local peaks in event rate were used in analysis, as described in Section 3.2.2. When only peak events are included, 27 of the Monte Carlo runs produce an exponential event rate that becomes hyperbolic prior to failure (b). Event rate trends are the output from 100 individual runs of the one dimensional model under constant load.

These two types of trend, namely exponential and exponential to hyperbolic, clearly provide a good description for the majority of outputs from the one dimensional model, especially when run under a constant stress. In the constant load simulation they account for 86% of outputs, rising to 98% when only peak events are considered, compared to values of 71% and 85% respectively when run under an increasing stress. These two trends are discussed in more detail in Chapter 5. Figure 4.14 shows two examples of typical alternative outputs that do not fit either of these trends. Some such outputs show a marked increase in event rate leading up to failure, but a long tail of

much steadier increase prior to this prevents the growth from being described as exponential or hyperbolic (Fig. 4.14a). Another relatively common pattern is periods of exponential growth within a more disordered overall trend (Fig. 4.14b).

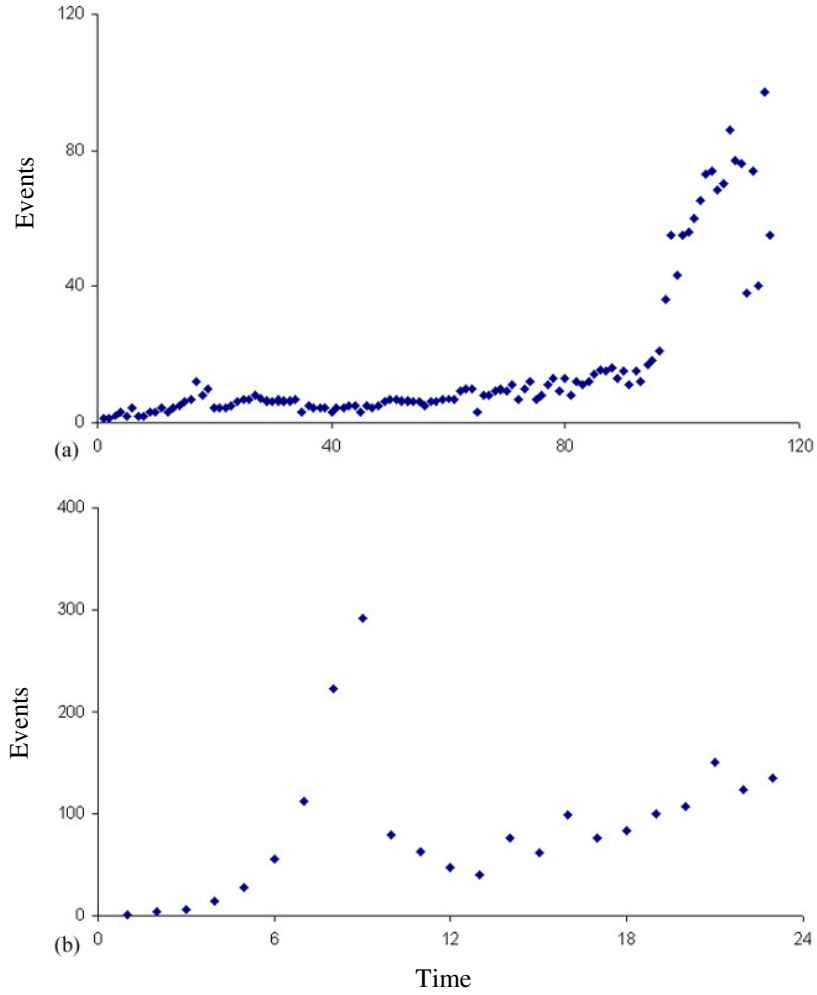

Fig. 4.14 Examples of alternative event rate trends, produced by the Monte Carlo run, which do not show an exponential or hyperbolic growth.

For completeness, a sampling of 550 runs where loading conditions also differed was performed (Fig. 4.15). Within each run of the model, the time between successive stress changes, and the extent of that change was non-uniform. However, to ensure that the model would always eventually progress to failure, no negative stress changes were applied. The time scale of failure covers a large range, with some cases in which arrays failed almost instantly and therefore with very high event rate, or a much longer failure time associated with a lower general event rate. However, even in these longer, drawn out trends some degree of increase in event rate can still be seen prior to failure. These

two extremes in output data may be due to the coupling of relatively homogeneous fracture toughness and a significant increase in stress for early, rapid failure, and diverse fracture toughness under a constant or very steadily increasing load, leading to the more gradual development of failure. The model has the same number of cells in each run and therefore in general, the shorter failure times will be associated with the larger event rates.

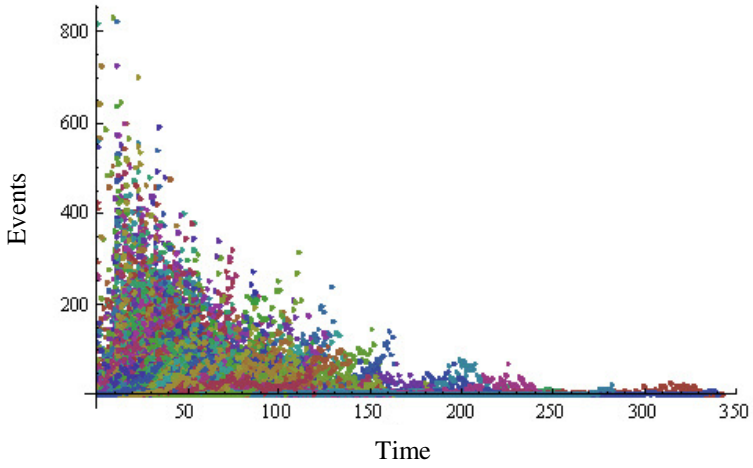

Fig. 4.15 Event rate with time for 550 individual runs of the one dimensional model. Varying input parameters are fracture toughness and initial flaw distributions, as well as external loading conditions.

4.5 Chapter summary

The one-dimensional model is based on physical principles of the concentration of stress due to the presence of cracks in a material. Mechanical properties of the host rock making up a volcanic edifice can be varied within the model, as well as the surrounding stress field. The distribution of initial cracks in the array, and the variability of fracture toughness of cells, both affect the failure rate of the model. The model produces exponential accelerations of failure rate, which in some cases become hyperbolic prior to bulk failure of the array. A Monte Carlo simulation highlights the relative probability of each style of precursor as well as providing a possible range of parameter values.

5. Analysis and discussion from 1D model: Accelerations of seismicity

5.1 Introduction

The Monte Carlo simulation described in the previous chapter showed that, when run from a suitable range of initial conditions, the one dimensional model will produce a definite, quantifiable pattern of precursory events. This chapter will consider in more detail the two predominant trends identified, exponential and hyperbolic, and the processes that may be responsible for these trends. The precursory sequences are consistent with the material failure forecast model (Voight, 1988) and crack interaction model (Kilburn and Voight, 1998) described in Chapter 3, as well as field data and laboratory observations.

Exponential rates of failure are commonly observed at volcanoes (e.g. Bell, 2008; Kilburn, 2003), and also in compression tests in the laboratory (e.g. Meredith et al., 1990). In addition, for both field and laboratory data, the emergence of subsequent faster than exponential trends have also been observed. Field observations from subduction zone volcanoes show a hyperbolic acceleration in seismicity in the final weeks prior to eruption (e.g. Kilburn & Voight, 1998; Kilburn, 2003). Tests in the laboratory show step increases in acoustic emission rates immediately prior to failure (Meredith et al., 1990). Similarly, the most common trend emerging from the one-dimensional model is an exponential rate of failure. Under certain conditions, this exponential trend then switches to become hyperbolic before bulk failure of the array.

In the following sections the exponential and hyperbolic sequences produced by the one-dimensional model are analysed in an attempt to understand further the processes creating these particular styles of precursory activity, and the emergence of a faster than exponential sequence. Aspects of the precursory trend such as duration and rate are considered, as well as the mechanisms and properties of failure and crack growth creating the trends.

In the remainder of this chapter, precursory trends produced by the model that remain exponential to failure are described as Type I trends. Exponential sequences that become hyperbolic prior to failure are described as Type II trends. Representative examples of each of these cases are used to illustrate the various analyses described in the chapter.

5.2 Controls on seismic event rate: constraints from field data

Predominantly exponential increases in seismic event rate (Type I) have been observed weeks to months before magmatic events at basaltic volcanoes, notably at Kilauea and Mauna Loa, Hawaii, and at Mt. Etna in Italy (Bell, 2007). Intrusive events at the same volcanoes have shown similar exponential seismic precursors (Bell, 2007), a feature that will be discussed in Chapter 8. In both cases, any faster-than-exponential trends appear as step-like increases in seismic event rate that continue for about a day or less.

More generally, exponential trends are observed in many natural processes that evolve through a mechanism of self-propagation. Applied to fracture growth, self-propagation is favoured because the stress intensity ahead of a crack increases with crack length. Thus, as a crack grows, the stress intensity at its tips becomes progressively larger, so favouring further growth. Once a crack begins to extend, therefore, the positive feedback between crack length and stress intensity will encourage an accelerating rate of growth. This behaviour may be altered by interactions with other cracks, or by the extending crack entering a region of unbroken material with mechanical properties, such as toughness, that vary significantly from those of the material through which the crack has just propagated. Such conditions may operate to increase (e.g., entrance into weaker rock) or to decrease (e.g., entrance into stronger rock) the observed rate of growth compared with that expected from the ideal model of a single crack growing in a homogeneous medium. Hence, given the heterogeneous nature of natural rock, it is remarkable that exponential increases in fracture event rate are commonly observed. It thus appears that most natural heterogeneities in rock have a secondary influence on rates of fracture propagation. Such a conclusion appears to contradict the discussion in Section 3.2.3 that fractures can be arrested by local rock structures. This contradiction can be resolved if the conditions arresting a fracture involve heterogeneities of a larger length scale or of a greater contrast in mechanical properties than those prevailing throughout most of a rock mass.

In contrast to precursors at basaltic volcanoes, pre-eruptive seismic trends at subduction-zone volcanoes may evolve from an exponential to hyperbolic (faster-than-exponential) increase with time (Type II trend; Kilburn & Voight, 1998; Kilburn, 2003; Kilburn & Sammonds, 2006). The hyperbolic trend evolves over days and has been interpreted to reflect the increasing rate of coalescence of fractures into a magmatic pathway (Kilburn, 2003). Because the hyperbolic trend has to date only been recognised

before andesitic-dacitic eruptions at subduction-zone volcanoes, it is possible that it reflects the influence of a compressional regional stress field, compared with the extensional regional stress field typical at basaltic volcanoes. However, no such constraints have been applied to the 1-D model. Hence, the fact that the 1-D model can produce both Type I and Type II trends suggests that, even if it should favour a particular sequence of precursors, the external stress field cannot guarantee that such a sequence will be observed.

5.2.1 Characteristic time scale of exponential trends

By definition, exponential changes with time are defined by a characteristic timescale that describes the specific shape of the exponential trend. In terms of physical processes, the characteristic timescale describes the time over which the controlling self-propagating mechanism becomes significant. Thus, similar characteristic timescales suggest a similar controlling mechanism, whereas significantly different timescales suggest that more than one mechanism may be important.

The characteristic timescales (equivalent to $1/A$ for the exponential limit of Voight's relation; Eq. (3.3)) for the 86 trends produced in the constant-stress Monte Carlo simulations (Chapter 4) yielded values of 0.04 – 0.66 for Type I precursors and 0.28 – 0.76 for the exponential portions of the Type II trends (77 and 9 runs, respectively; Fig. 5.1). A Mann Whitney Test was performed to assess whether the two sets of constants come from the same distribution. Both are assumed to follow a normal distribution. The results give a statistic value of $z = -2.89$. This lies outside the critical value of $z_{crit} = -2.58$ at the 0.1% level, leading to rejection of the null hypothesis that the two samples are drawn from a single distribution. However it should be noted that the relatively small size of the Type II data set means that the approximation to a normal distribution is less robust, and the fact that all observations were produced by the same numerical model means the sample sets may not be strictly independent. Hence, although the preliminary analysis suggests that the Type II trend tends to have larger characteristic exponential timescales than the Type I trend, further analysis is required to confirm the distinction. In any case, as is clear from Fig. 5.1, even if the distributions are different, they are close enough to provide a major overlap in characteristic timescale. Hence, unless the timescales are extremely high or low, it may not be possible to use their value to distinguish between Type I and II behaviour. In

practical terms, the characteristic exponential timescale cannot yet be used to anticipate whether a hyperbolic final trend will be observed.

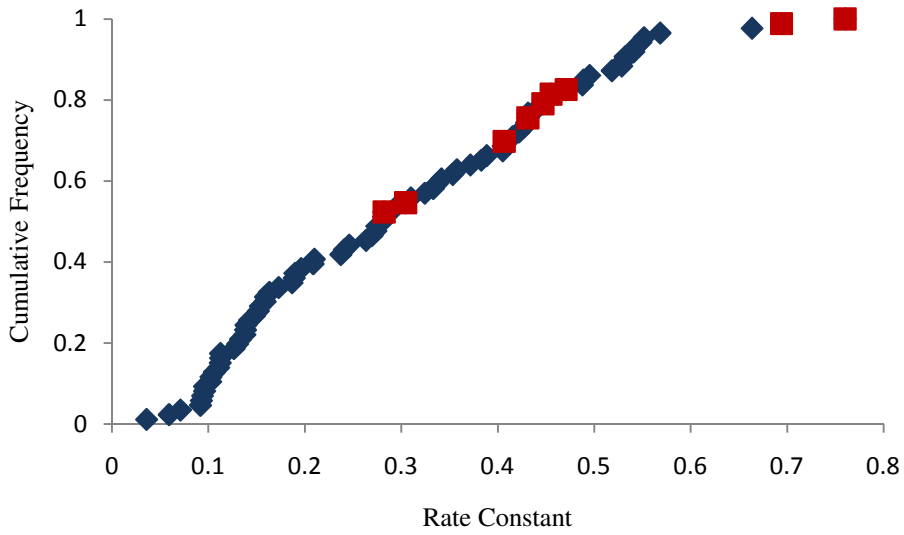

Fig. 5.1 Exponential rate constant for 77 Type I (blue diamonds) and 8 Type II (red squares) exponential trends recorded in 100 runs of the 1D model, for varying distributions of fracture toughness and initial flaws (Table 4.1).

The exponential precursory trend can be expressed in terms of the cumulative number of events N:

$$N = N_0 e^{(t-t_0)/\tau} \qquad (5.1)$$

where N_0 is the number of events recorded at time t_0 and represents the background rate of seismicity in the field or the number of initially failed cells in the one –dimensional model, and $\tau = 1/A$ is the characteristic timescale. Therefore a greater magnitude exponential rate corresponds to a shorter characteristic timescale of precursory trend. Setting $t_0 = 0$ and defining t_f to be the time of failure, and therefore the duration of the exponential sequence, (5.1) gives an expression for the total number of events by the

end of the sequence, N_f. Rearranging this expression gives a relationship describing the increase of an exponential sequence duration with the characteristic timescale:

$$t_f = \tau \ln\left(\frac{N_f}{N_0}\right) \tag{5.2}$$

The relationship between sequence duration and characteristic timescale in (5.2) is clearly visible in the Monte Carlo output plots in Chapter 4 (Fig. 4.15). In contrast to the hyperbolic relation, for which the infinite event rate provides a well-defined time to failure, values for t_f are theoretically unconstrained for the exponential trend. In practice, it is possible to assume a nominal upper limit for the ratio N_f/N_0, based on physical constraints of the problem and properties of rock failure. Bell and Kilburn (in press) argue that for bulk failure from initially unbroken rock, N_f/N_0 is expected not to exceed ~10^2 – 10^3, or $\ln N_f/N_0$ between 4.6 and 6.9. Observations from the field of cumulative seismic events in the days to weeks leading up to an eruption are consistent with this range of 10^2- 10^3 (Bell and Kilburn, in press).

For model simulations yielding Type I exponential sequences, the durations of the increase are constrained by the size of array. The total number of events is fixed, as well as the relative, initial material damage, and therefore the ratio of duration to characteristic timescale, t_f/τ, will necessarily be constant. However, when the simulations produce a Type II trend, showing a progression from exponential to hyperbolic increase, the duration of the exponential sequence is constrained instead by attainment of the critical condition necessary for a transition to hyperbolic growth. The results in the second case can therefore be used to investigate the relation between duration and characteristic timescale for exponential increases in VT event number.

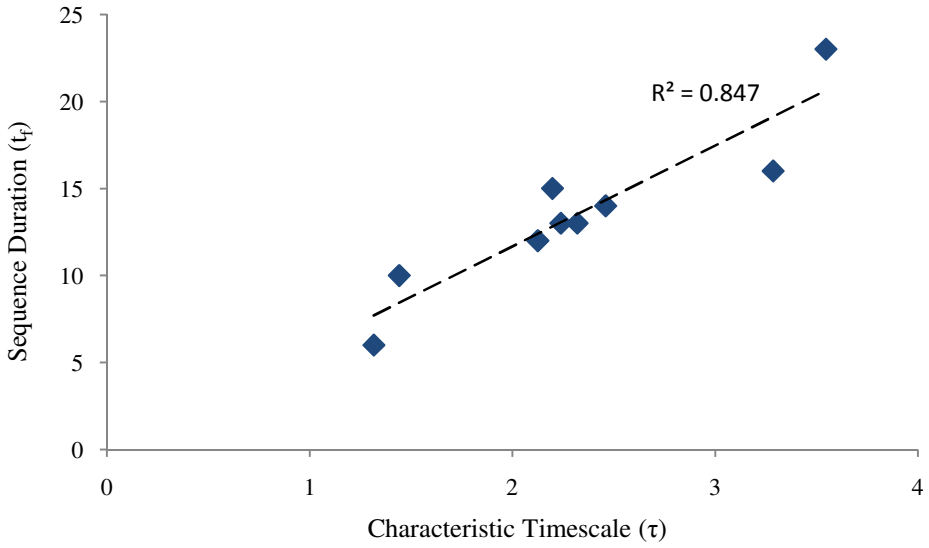

Fig. 5.2 Duration against characteristic timescale of Type II exponential sequences produced in Monte Carlo simulation.

The data from the nine recorded sequences show an approximately linear trend between duration and τ, with a gradient, equal to $\ln(N_f/N_0)$, of 5.8 (Fig. 5.2). This value lies within the range proposed for the duration-τ trend among exponential sequences for failure from initially unbroken rock. Here the duration, $t_{f,}$ is defined by the transition from exponential to hyperbolic increases in event rate, rather than by the end of the experiment. The full range of the exponential trend is therefore not limited by model constraints on the size of the model array.

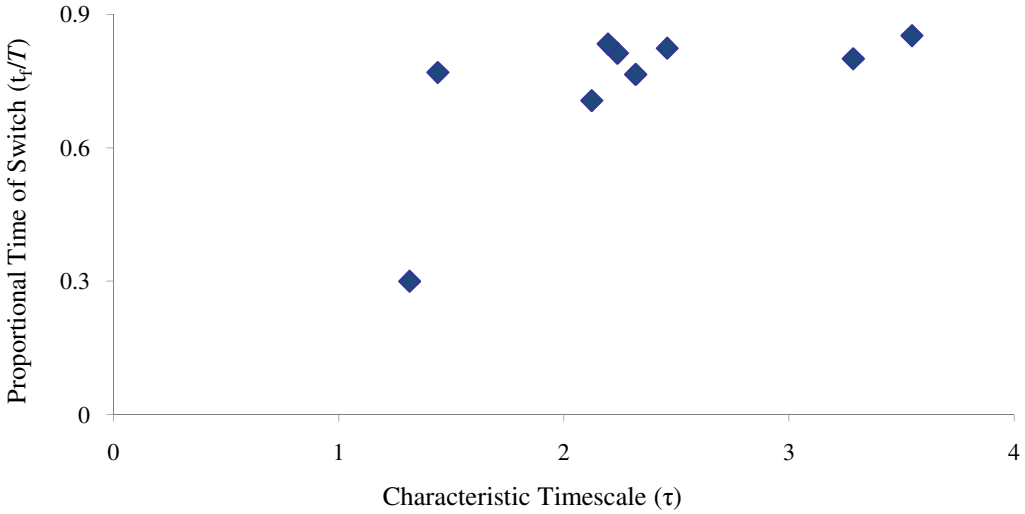

Fig. 5.3 Duration of exponential sequence t_f normalised against total length of pre-failure sequence, *T*, for Type I sequences produced by the Monte Carlo run, as a function of characteristic timescale.

When normalised against the duration of the entire pre-failure sequence, *T* (Fig. 5.3), the time of transition relative to the duration appears to be independent of the characteristic timescale, confirming that the characteristic timescale is not related to the duration of the experiment. One data point lies away from the main trend, at a proportional time of about 0.3, and represents both the shortest time scale and relative transition time. In this run there is a distinct scale change between the exponential and hyperbolic sections of the trend. The initial conditions of the array represent an extreme of the statistical possibilities, with a distinct layering of high and low fracture toughness. The initial exponential increase represents failure within the regions of low fracture toughness, which make up a relatively small proportion of the array. The hyperbolic portion of the sequence corresponds to the subsequent failure of the areas of a greater toughness.

The model conditions consider the development of a continuous fracture from the starting point of unbroken rock. In reality, a volcanic edifice will contain some fractures before the sequence of events that potentially leads to eruption. The greater the amount of initial fracturing, the shorter will be the time until bulk failure. Accordingly, observed values of $\ln N_f/N_0$ are expected to be less than the ideal values

of between 4.6 and 6 starting from unbroken rock. Indeed, data from Hawaii indicate values of $\ln N_f/N_0 \cong 1.5$ (Bell, 2007; Fig. 5.4). If such empirical limits are available for $\ln N_f/N_0$ at a particular volcano, then the characteristic timescale can be multiplied by this limit to estimate the time of bulk rock failure; if they are not available, then the ideal limits for $\ln N_f/N_0$ can be used to estimate the maximum time expected before bulk failure.

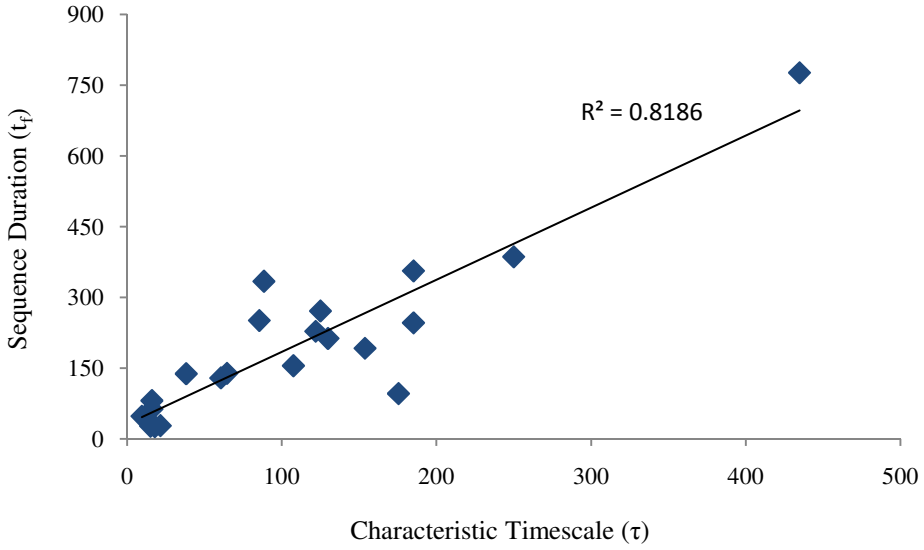

Fig. 5.4 Duration against characteristic timescale for 21 sequences prior to eruptions or intrusions at Mauna Loa, Kilauea and Mt. Etna (Bell, 2007).

5.3 Crack growth properties

Analysis of the characteristic timescales and rate parameters of precursory trends is important for identifying not only the time to bulk failure, or eruption, but also in attempting to establish any critical criteria for the transition of an exponential sequence to hyperbolic growth. Analysis of field and laboratory data is broadly restricted to evaluating these parameters. However, using the one dimensional numerical model it is possible to look in more depth at the physical processes causing the observed characteristic parameters, and the conditions for exponential or hyperbolic growth of seismic activity. In the field, features such as crack length distributions or the number of active cracks will be affected by an area much greater than that eventually forming the open conduit, and even if such parameters were measurable the existence of surrounding faults and fractures in an edifice would create very noisy data. By looking at these features in a one-dimensional array it may be possible to understand the cause of the observed trends; such understanding, in turn, may give some ideas of the controlling mechanisms that operate in a larger, more realistic setting. This section looks at a variety of crack growth properties, comparing observations from typical model outputs for precursory trends of both types I and II, for representative examples of each type of trend.

5.3.1 Active cracks

Detected seismicity is determined by the activation and growth of faults. Here, activation refers to when conditions around a fault first become favourable to allowing that fault to move, and growth refers to repeated movements along the same fault. At a molecular scale, the mechanism of creating a completely new discontinuity also becomes important, but such a process cannot be detected directly in the field.

As discussed in Section 3.2.2, the activation of new faults is expected to favour an exponential increase in event rate with time, whereas the growth and coalescence of faults is expected to yield a hyperbolic trend. Although the association is empirical, it is consistent with observations in the field (McGuire & Kilburn, 1997; Kilburn & Voight, 1998; Kilburn, 2003) and laboratory (Lockner et al., 1991; Main & Meredith, 1991). Thus the approach to bulk failure is expected to be dominated first by fault activation (yielding an exponential trend with time) and then by fault growth and coalescence (yielding a faster-than-exponential trend). Increasing beyond a critical number of faults

per unit volume is one possible condition that determines the change from activation-dominant to growth-dominant conditions (Kilburn & Sammonds, 2006). Such a possibility is investigated here by analysing the distribution of cracks at different stages within the model simulations.

In each simulation, the first cracks to become activated will be those in regions of lower general toughness. Additional cracks then become activated as either the applied stress increases, or local stress intensity increases due to growth of existing cracks. Two classes of new crack can be identified: (1) a newly activated crack, which appears as a failed cell, or collection of adjacent cells, that is isolated from any existing failed cells, and (2) a crack that occurs in a cell close to an existing crack and which can be related to crack growth.

Figures 5.5 and 5.6 show the number of newly-activated cracks as the model progresses for Type I and Type II precursory trends, model run 1 and run 2 respectively. In both cases, the rate of activation increases exponentially, before a significant drop occurs immediately before failure. The drop is favoured by the coalescence of cracks and, also, by the model constraint that as more of the cells in the array fail, so the opportunity decreases for new, isolated cracks to appear. At the present stage of development, it is not possible to distinguish the primary cause for the final drop-off in the 1D model. However, such a distinction might be possible in the future by implementing a two- or three-dimensional array, or incorporating a buffer zone into the one-dimensional model.

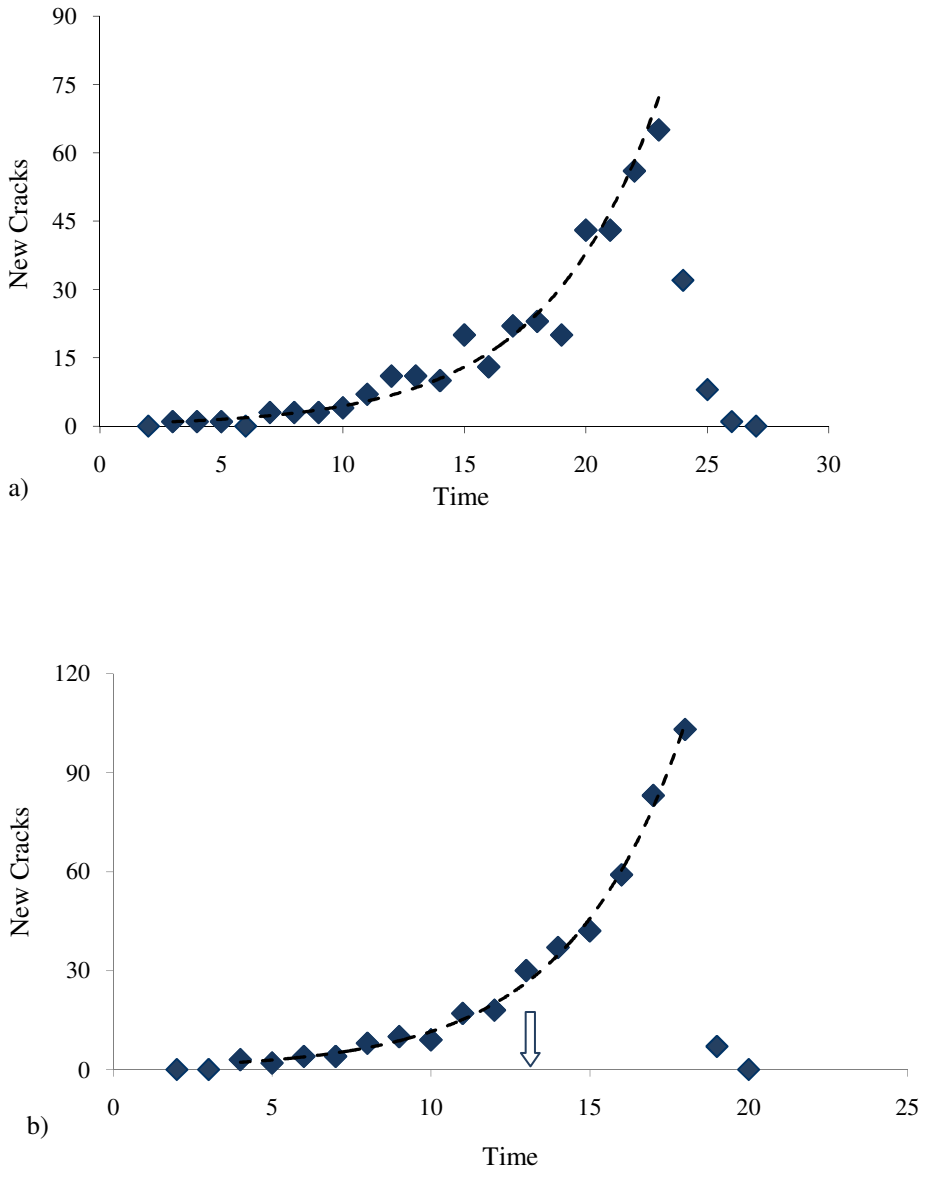

Fig. 5.5 Number of newly activated cracks per time step for model run 1 (a) and run 2 (b), Type I and Type II precursory trends respectively. The dashed lines show the best-fit exponential trends prior to the observed drop-off, and the arrow indicates the point at which the Type II trend becomes hyperbolic.

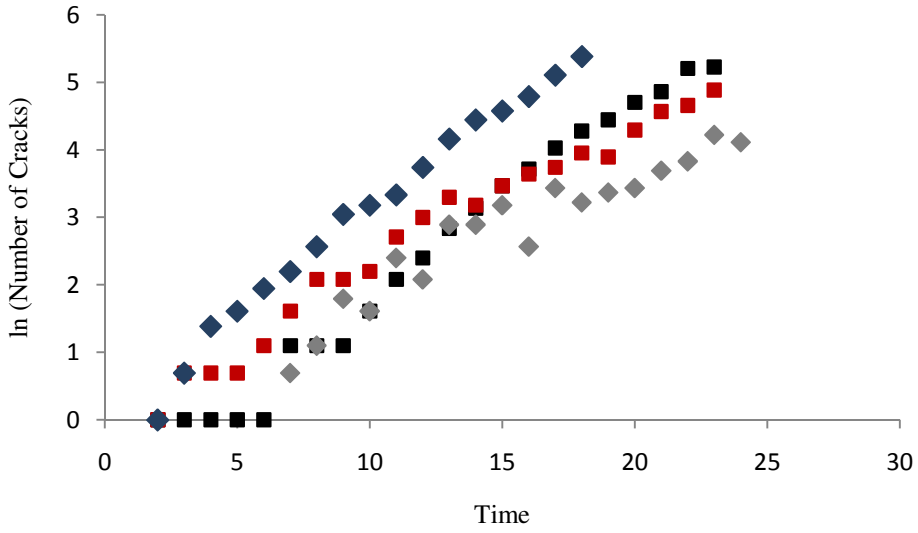

Fig. 5.6 Log plot of the number of newly activated cracks, before the pre-failure drop-off. Both Type I (red and black squares) and Type II (blue and grey diamonds) precursors show mean exponential activation rates, although each type may show second-order fluctuations about the mean (red squares and grey diamonds). The rate constants for both types cover a similar range of values (0.31 and 0.18 for blue and grey diamonds; 0.29 and 0.22 for black and red squares). The red squares and blue diamonds correspond to model runs 1 and 2 respectively, shown in Fig 5.5. The second Type I (black squares) and Type II (grey diamonds) trends were produced from model runs 3 and 4 respectively.

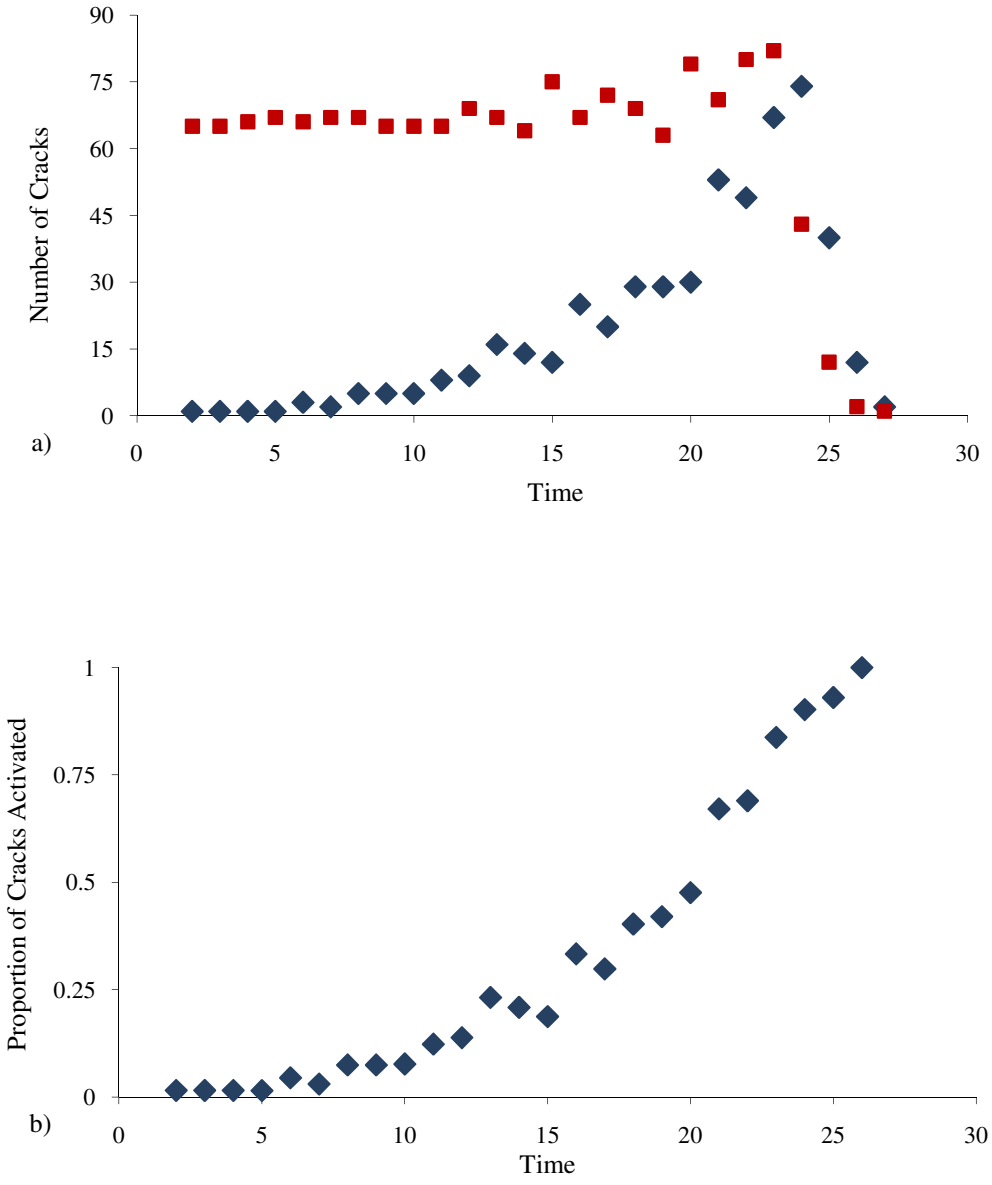

Fig. 5.7 (a) Number of active existing cracks (blue diamonds) and the resulting total number of cracks (red squares) with time, for a Type I trend (model run 1). An active existing crack is one that grows during a time step, but has also been active during the previous time step. The total number of cracks includes those that are present in the array but have not yet grown. (b) The proportion of the total number of cracks that grow during a time step.

While new cracks are being activated, existing cracks are also continuing to grow. The relative effect of crack growth can be inferred from Fig. 5.7 (a) and 5.9 for Type I precursors, and Figs 5.8 (a) and 5.9 for Type II precursors. The figures show the variation in the total number of cracks, n_T, present while the activation rate is increasing. In all four examples, the total number of cracks maintains a similar value during the first 50-65% of the increase in activation rate. At the start of a sequence, the approximately constant total value reflects the small proportion of new cracks being

formed. At longer times, however, the number of newly activated cracks becomes a significant proportion of the total number; at this stage the total number may increase (Fig. 5.7a) or begin to decrease (Fig. 5.8a). In the latter case, the increase in number of activated cracks is being offset by a decrease in total number due to the coalescence of existing cracks. Eventually, the effect of coalescence dominates until, just before bulk failure, the experimental array consists of only a small number of large cracks.

In the Type II examples (Figs 5.8 & 5.9), the transition from exponential to hyperbolic increases in event rate coincides with the onset of a sustained decrease in the total number of cracks. As expected, therefore, the hyperbolic sequence is characterised by the emerging dominance of crack growth and coalescence over crack activation.

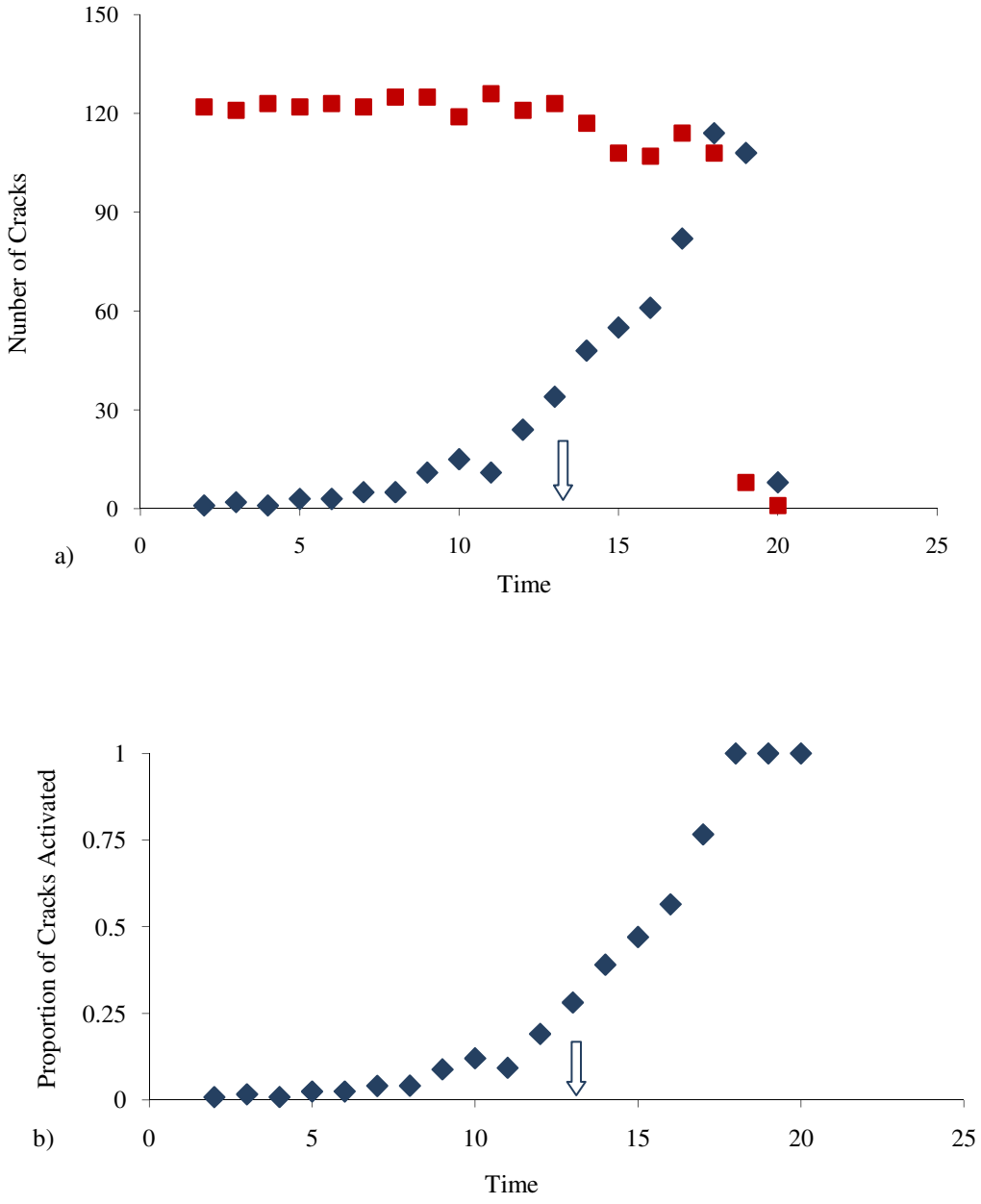

Fig. 5.8 (a) Number active existing cracks (blue diamonds) and the resulting total number of cracks (red squares) with time, for a Type II trend (model run 2). An active existing crack is one that grows during a time step, but has also been active during the previous time step. The total number of cracks includes those that are present in the array but have not yet grown. (b) The proportion of the total number of cracks that grow during a time step. Arrow indicates the point at which the event rate trend becomes hyperbolic.

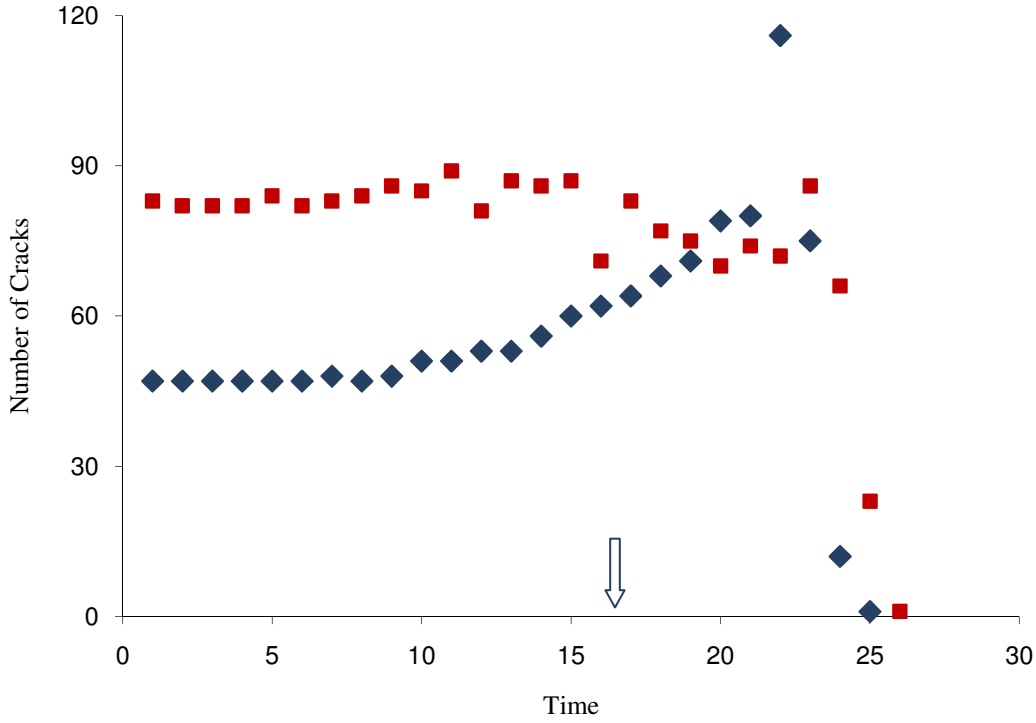

Fig. 5.9 Total number of cracks for model runs 3 (blue diamonds) and 4 (red squares), Type I and Type II precursory trends respectively. Arrow indicates the point at which the Type II trend becomes hyperbolic.

The change from activation-dominant to growth-dominant conditions may occur when the number density of cracks exceeds a critical value (Kilburn & Sammonds, 2006). The model results can be used to test this hypothesis because the number density of cracks is represented by the cumulative number of events. Due to the bounded nature of the model, the array must progress through the same density changes, resulting in 100% failure, whatever the pattern of event rate produced. The proportion of failed cells, or density of cracks, in the nine runs for which the exponential-hyperbolic transition occurred ranges from 4-70%. The single case below 10% corresponds to the outlier highlighted in Figure 5.3. The remaining, more representative, cases still cover a range of over 40%. This suggests that the actual density of cracks cannot by itself determine the mode of acceleration of seismic event rate, or certainly not one that can be identified from a closed model.

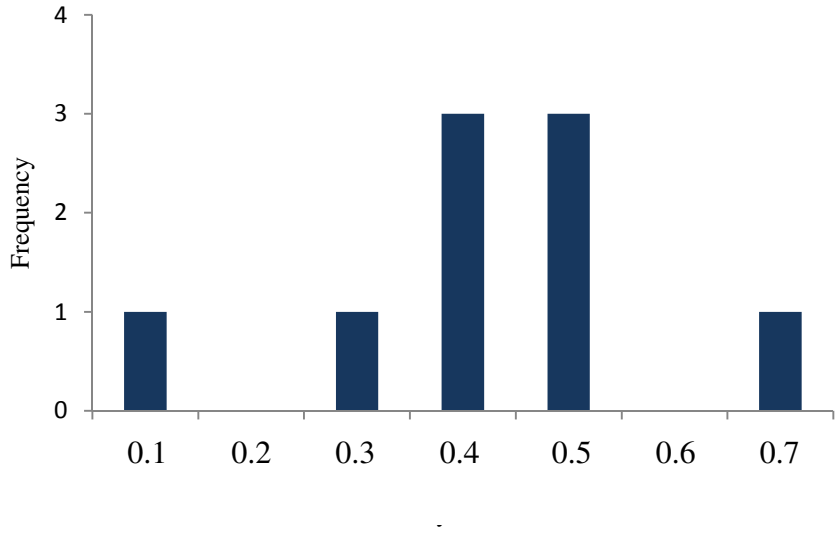

Fig. 5.10 Proportion of cells that have failed at the point of exponential-hyperbolic transition in nine runs from the Monte Carlo simulation.

5.3.2 Inter-crack distance

In the 1D model, interaction between cracks occurs once the inter-crack distance is on the order of the crack length. The interaction, in turn, governs the rate at which neighbouring cracks join up. The mechanism of crack coalescence is therefore dependent on crack length and inter-crack distance. In understanding the transition to this mechanism of failure it would be useful to identify any corresponding transitions in the geometry of cracks. As the model evolves, the distribution of crack lengths will naturally progress from numerous smaller cracks into, eventually, one large model-spanning crack at the point of bulk failure. Figure 5.11 shows the progression of mean crack length in the array for model runs 1 and 2 described in the previous section, producing Type I and II precursory trends. The model begins with almost entirely single cell cracks and progresses to a 2,000-cell crack that spans the array at the point of failure. The mean length in Type I event rate increases almost exponentially during the middle section of the model run. This precedes a rapid increase in the mean length in the final stages of the model as failed cells join up to form very large scale cracks (Fig. 5.11). The hyperbolic case appears to follow a similar trend (Fig. 5.11). Figure 5.12 shows the inverse mean crack length for the same two examples. Both inverse trends tend towards zero, corresponding to an infinitely long crack at the point of failure.

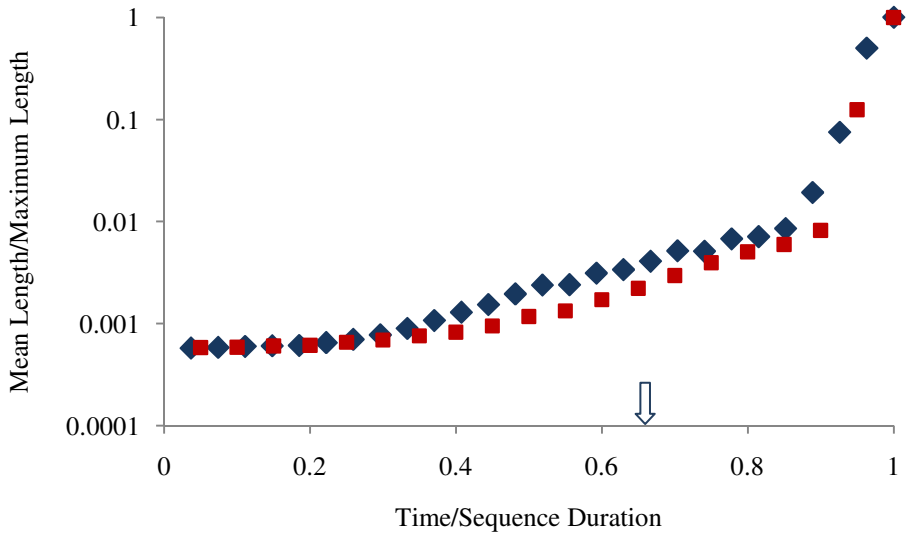

Fig. 5.11 Mean crack length with time, normalised for maximum length (equal to array size) and sequence duration respectively. The two cases show Type I (blue diamonds) and Type II (red squares) precursory trends. Arrow indicates the point at which the event rate trend becomes hyperbolic. Note the logarithmic scale for the vertical axis.

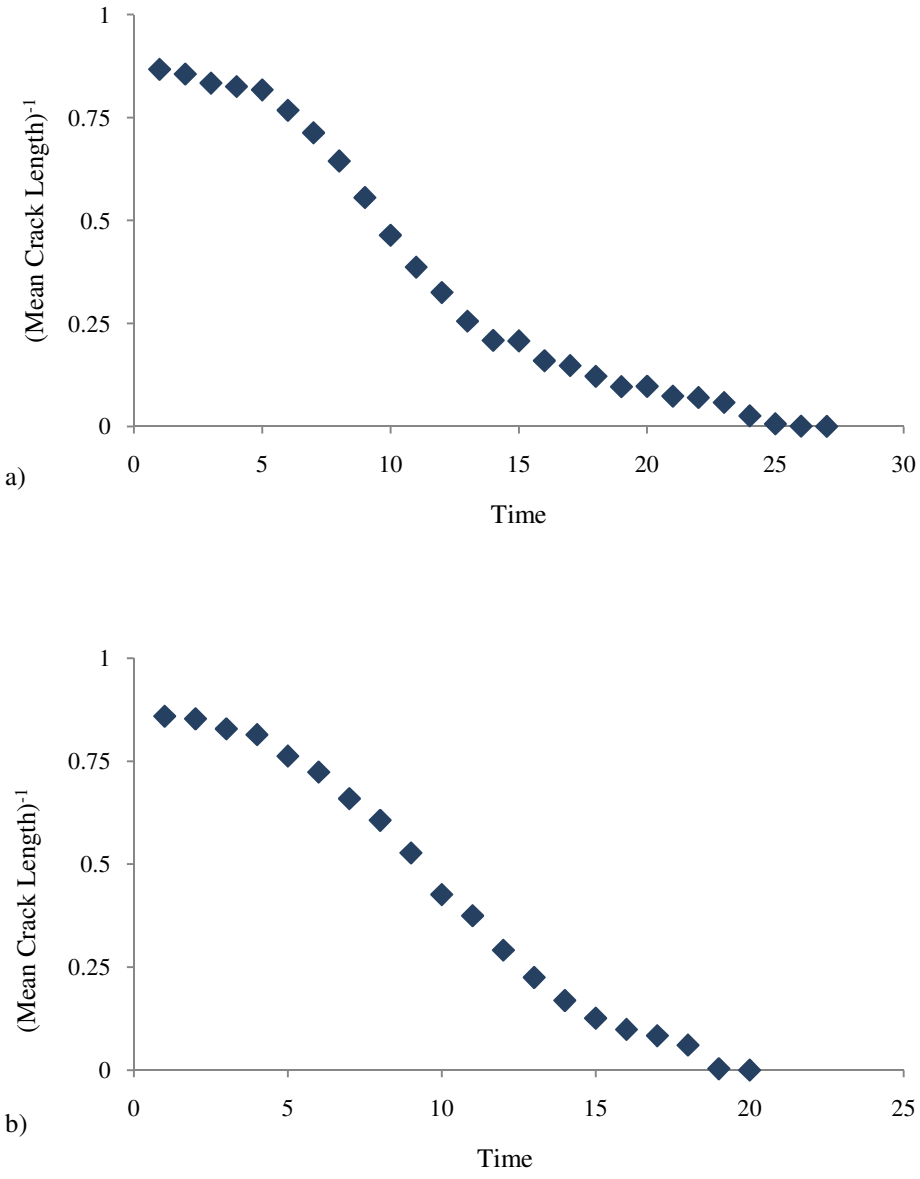

Fig. 5.12 Inverse mean crack length with time, for model runs 1 (a) and 2 (b), producing Type I and Type II precursory trends respectively.

Introducing the distribution of inter-crack distance allows for not only the magnitude but also the geometry of cracks to be considered. The idea of clustering, or avoidance within a set of cracks is discussed further in Chapter 6. The development of a fracture network will depend on whether cracks are more likely to grow where previous cracks exist or in isolation. The mean inter-crack distance decreases very gradually in the early stage of the model (Fig. 5.13). However, as the cracks grow in length and occupy a greater proportion of the array, the relative change in the mean with each incremental decrease in inter-crack distance will become greater.

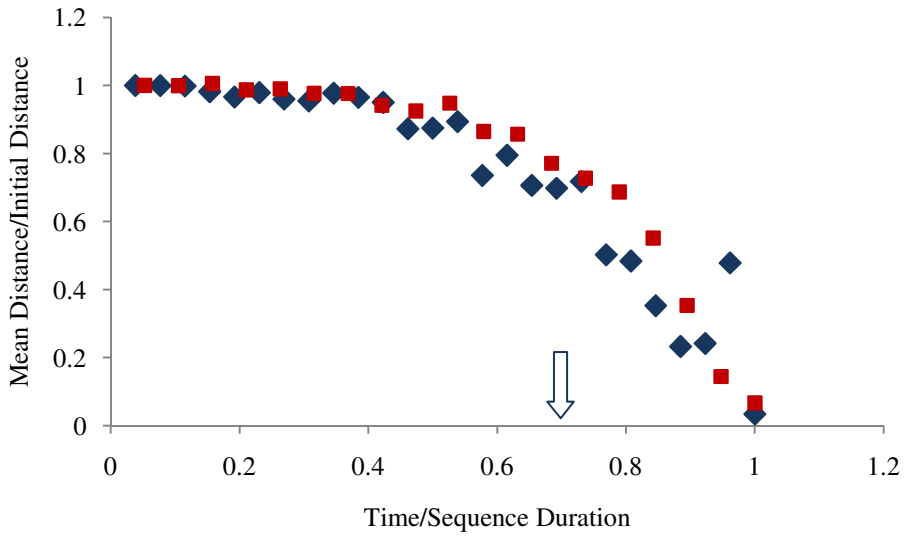

Fig. 5.13 Mean inter-crack distance with time, normalised for initial mean inter-crack distance and duration of sequence respectively. The two examples show a Type I (blue diamonds) and Type II (red squares) precursory trend. Arrow indicates the point at which the Type II trend becomes hyperbolic.

Both the Type I and II event-rate trends show a similar variation in mean inter-crack distance with time (Fig. 5.13). After a gradual decrease to about 75% of the starting mean distance after about 70% of the total duration, the rate of decrease becomes faster until a crack extends across the whole array (zero inter-crack distance) at bulk failure. The rate of decrease in the inter-crack distance is not affected by whether the event rate increases exponentially or hyperbolically, suggesting that the locality of fracturing is not dependent on the rate of fracturing. However, the initial mean value for the inter-crack distance in model run 1 was twice that for model run 2. The fact that initial cracks in the array for the Type II run have a shorter distance between them may lead to interaction between cracks occurring earlier in the model than in the Type I example. If this interaction is a mechanism that leads to hyperbolic growth in event rate, this would suggest that model size may be a limiting factor on the appearance of a hyperbolic trend, and that in many cases the model has reached bulk failure before the transition is made. However, the analysis of a greater number of both types of trend is necessary to investigate this idea further.

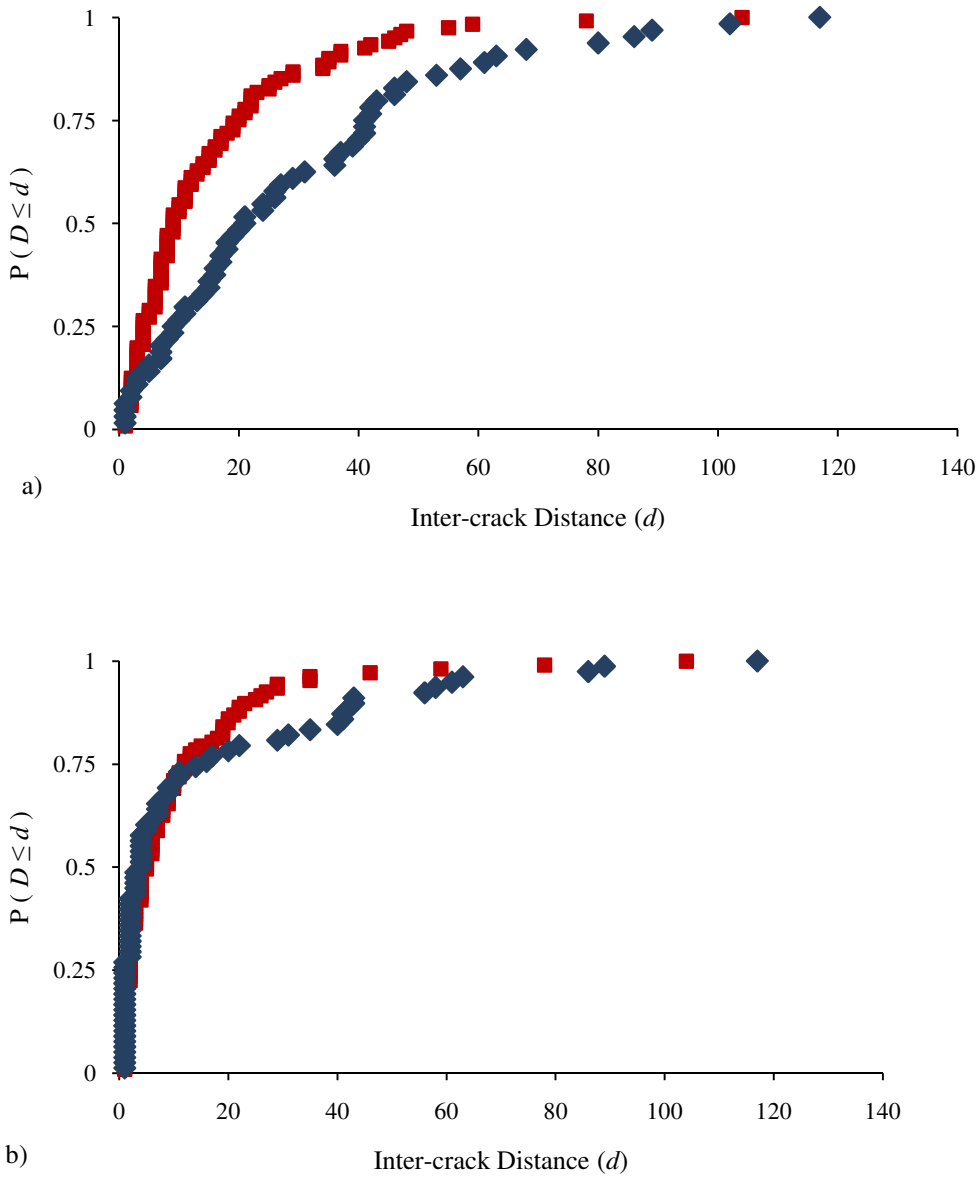

Fig. 5.14 Cumulative distribution function for the inter-crack distance at the (a) outset of the model run and (b) approximately three quarters through the total run time of the model for Type I (blue diamonds) Type II event-rate trends (red squares).

From Figure 5.14a it can be seen that initially the Type I and II examples have maximum inter-crack distances of a similar scale and that the smaller mean distance, in the Type II example, is a result of a higher proportion of cracks located close to each other. While for the Type I case only about 50% of cracks are located within 20 cells of a neighbouring crack, in the Type II instance this rises to almost 75%. This further supports the theory that interaction between neighbouring cracks may be the trigger for hyperbolic growth of event rate. The second plot of cumulative distribution function corresponds to the time instant 75% of the way through the total run time for each

model respectively (5.14b). By this stage both cases have a similar proportion of cracks within 20 cells of a neighbour.

Figure 5.15 illustrates one of the model runs that produced an event rate moving from exponential to hyperbolic prior to failure, model run five. Initially, the array breaks along isolated cells. As cracking proceeds, the originally isolated cracks grow and merge into two principal cracks that extend towards each other. The associated event rate changes from exponential to hyperbolic when the regions of influence ahead of each crack begin to overlap (Fig. 5.15). The process is highlighted when only changes in the number of newly failed cells at each time step are considered (Fig. 5.16). In this case, activity is clearly confined to an area surrounding the advancing main cracks.

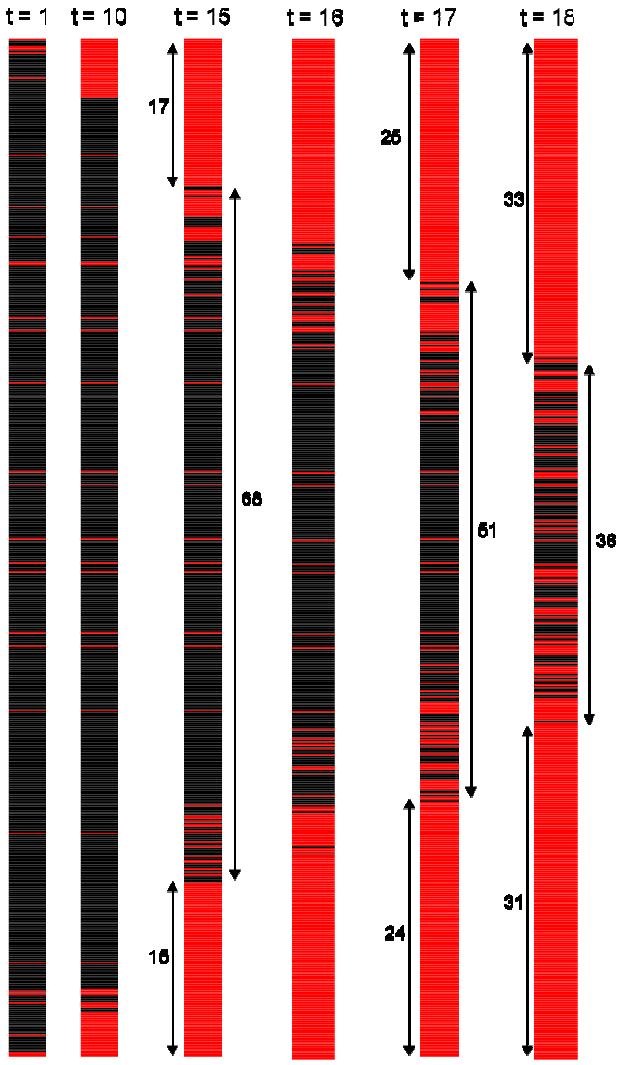

Fig. 5.15 Snapshots of the array at progressive time steps, from a model producing a Type II trend (model run 5). Cells that have failed are coloured red, intact cells are black. The hyperbolic trend emerged at t = 15.

The range of the active areas ahead of the crack tips appears to grow exponentially from t ~ 10-12 to failure at t = 18 (Fig. 5.17). The hyperbolic trend emerged at t = 15. This emergence of an exponential increase in the active area would explain the exponential event-rate trend, and the switch to a faster than exponential trend may be caused by a change in the density of failures within the active region. However, from Figure 5.18 it is difficult to define any consistent increase in the density of cracks within the regions of activity. A slight jump in the density is seen in the both the upper and lower sections at the emergence of the hyperbolic event rate. However,

this is only temporary and in fact the density fluctuates around a mean value for much of the run time of the model.

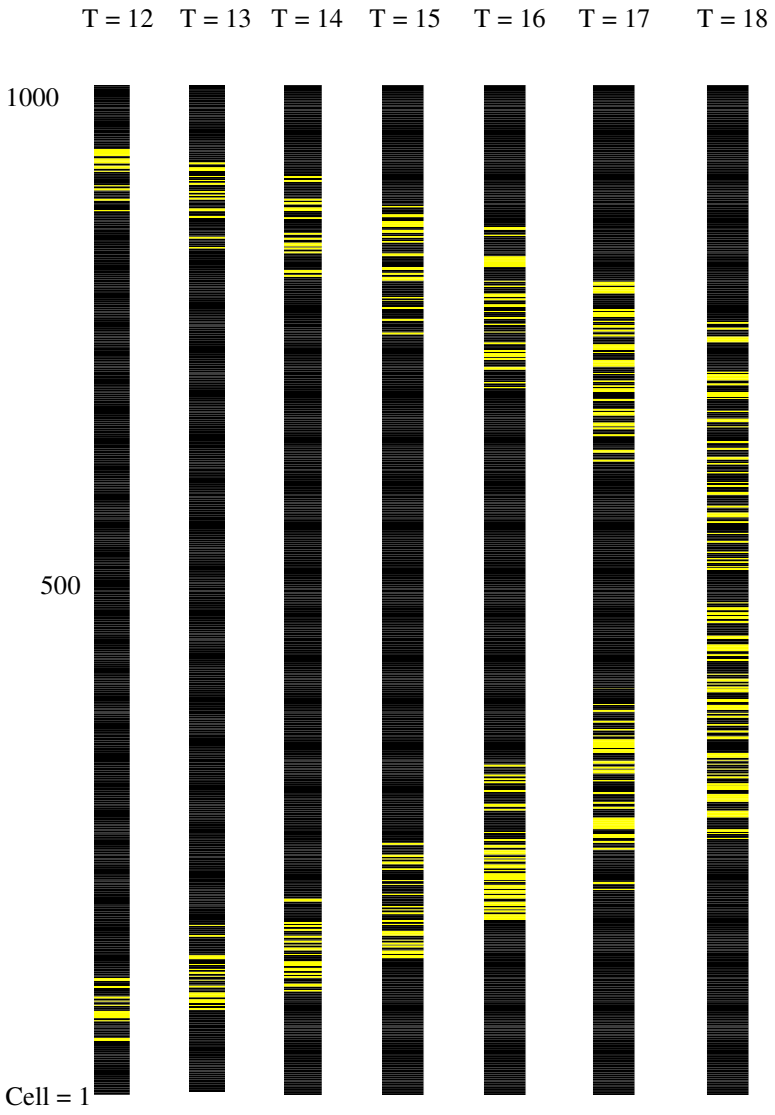

Fig. 5.16 New failures at progressive time steps in model run 5 (Fig. 5.15). Cells that have failed during the previous time step are coloured yellow.

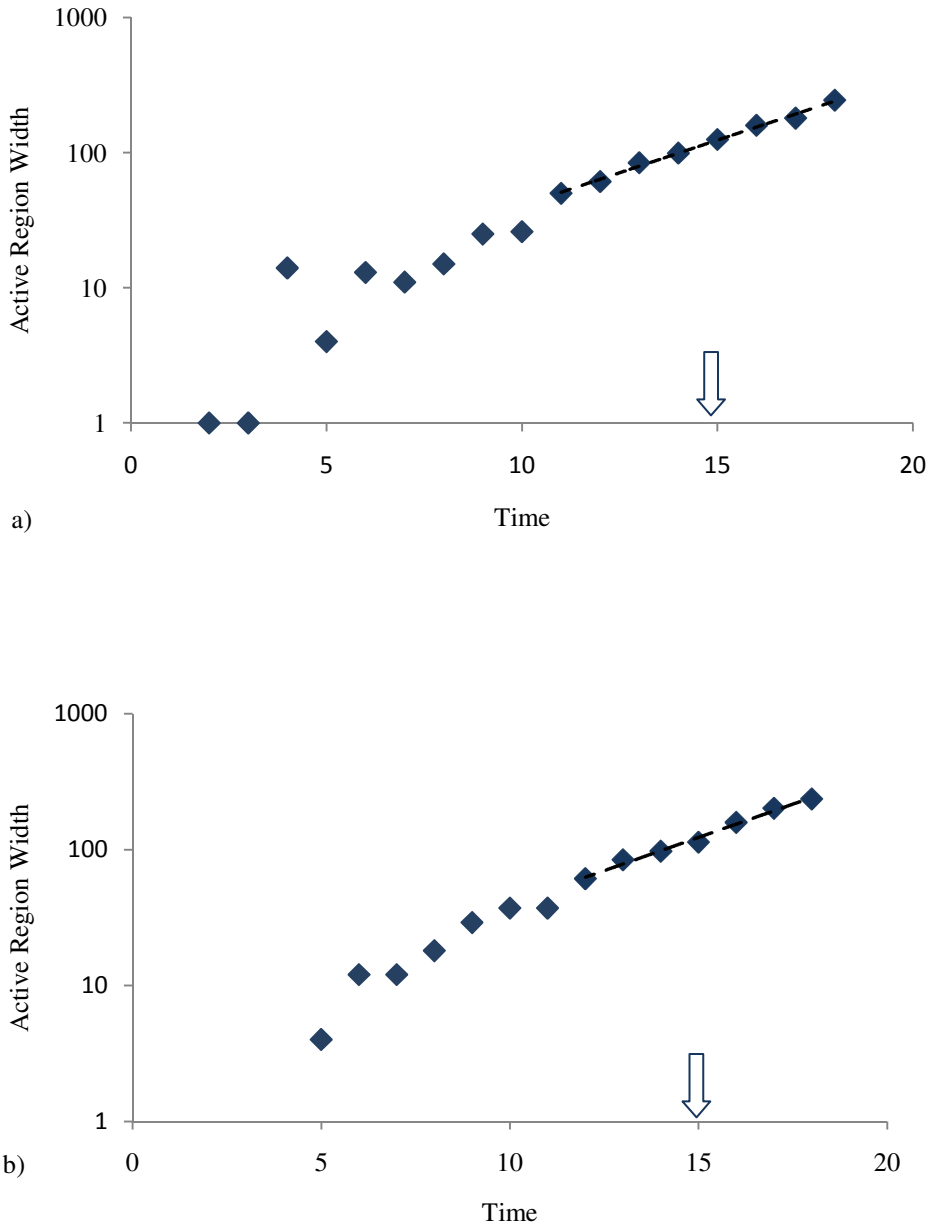

Fig. 5.17 Length of the active region ahead of advancing crack tips for model run 5, as shown in Figures 5.15 and 5.16. Length is measured as the total number of cells spanned. Plot (a) describes the upper region in Figure 5.16, 500 < cells < 1,000; plot (b) describes the lower region, 0 < cells < 500. Note the logarithmic scale for the vertical axis. Arrows indicate the point at which the event-rate trend becomes hyperbolic.

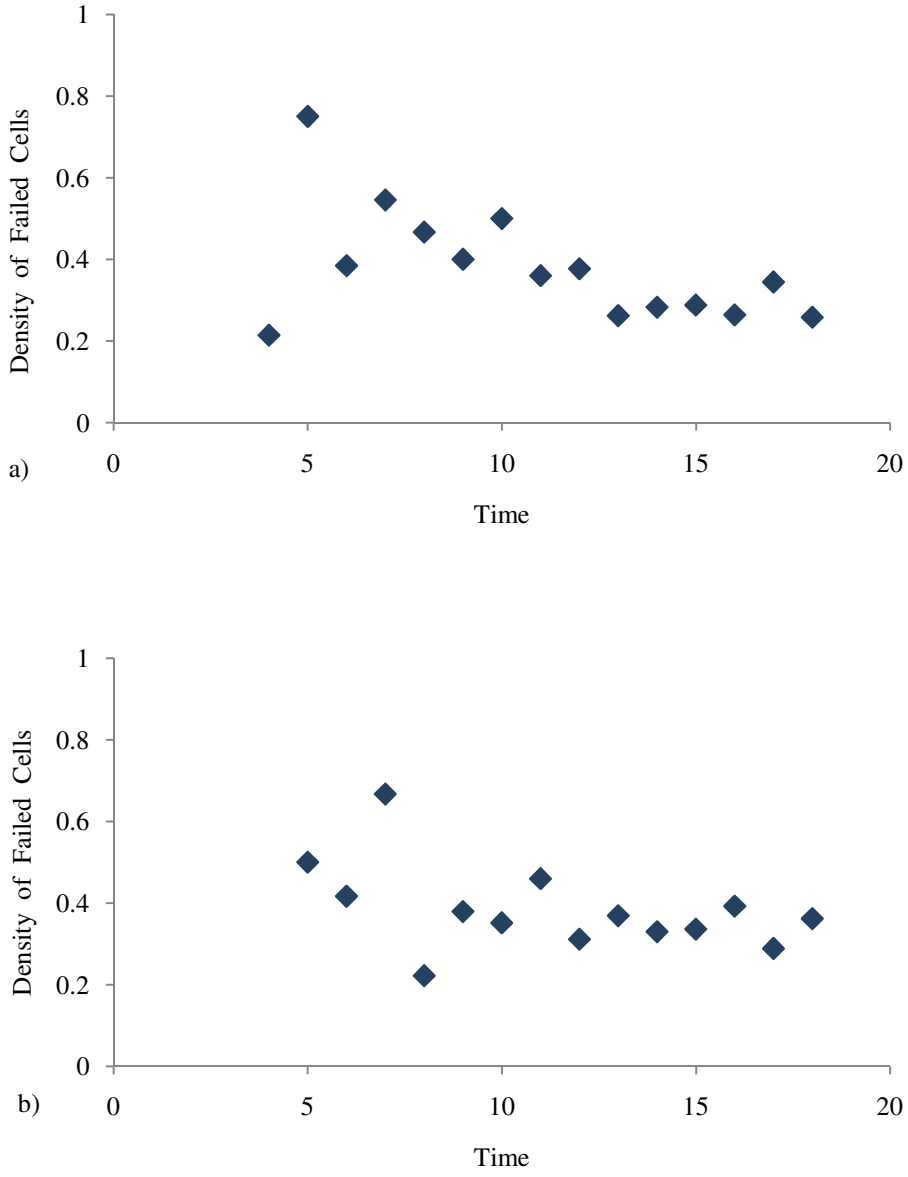

Fig. 5.18 Density of failed cells in the regions of activity ahead of advancing cracks for model run 5, as described in Figures 5.15 – 5.17. Plot (a) describes the upper region in Figure 5.16, 500 < cells < 1,000; plot (b) describes the lower region 0 < cells < 500.

5.4 Stress distribution

As the dominant failure mechanism changes from fault activation to fault growth, the relative influence of the remote and local stresses may change in the model. Initially failure is driven by the level of remotely applied stress and cells throughout the array would be equally likely to fail, dependent only their assigned fracture toughness. As the mechanism becomes dominated by crack growth, the concentration of stress around the larger cracks would exert a greater influence on the stress field and favour failure in already highly fractured areas. This assumption can be tested by looking at the distribution of stress intensity across the array as the model progresses. As described in Chapter 4, the stress intensity increases in cells around the tip of a crack depending on its length and the proximity of neighbouring cracks. The density distribution of stress intensity magnitude across the array is therefore an alternative measure of the variable geometry of cracks.

Figure 5.19 shows how the cumulative distribution function of stress intensity magnitude varies as the model evolves. For cells located outside the range of influence of failed cells, the stress intensity is just the remotely applied stress. Initially, there are relatively few cracks in the array and therefore this applies to the majority of cells (Fig. 5.19a). Initially, in both the Type I and Type II examples, over 80% of cells have this minimum magnitude of stress intensity, equal to the remotely applied stress. This minimum point is highlighted for each example in Figure 5.19 by a dashed line. As the model evolves and more cracks appear along the array, a greater number of cells will be within the range of influence of these cracks. This will cause the range of stress intensity magnitudes across the intact cells to increase. At two thirds through the duration of the model run, the isolated cells still account for the greatest proportion of stress intensity frequencies (Fig. 5.19b), and there are a high percentage of cells that remain isolated right up until the final stages of failure. This effect is more pronounced in the Type I event-rate case. The Type II example shows a faster decrease in the proportion of cells that are not affected by any neighbouring cracks. In other words, cells fall into the range of influence of cracks more quickly in this second case. This would be expected if the failure mechanism was dominated by the interaction and coalescence of exiting cracks, over the activation of new, isolated cracks.

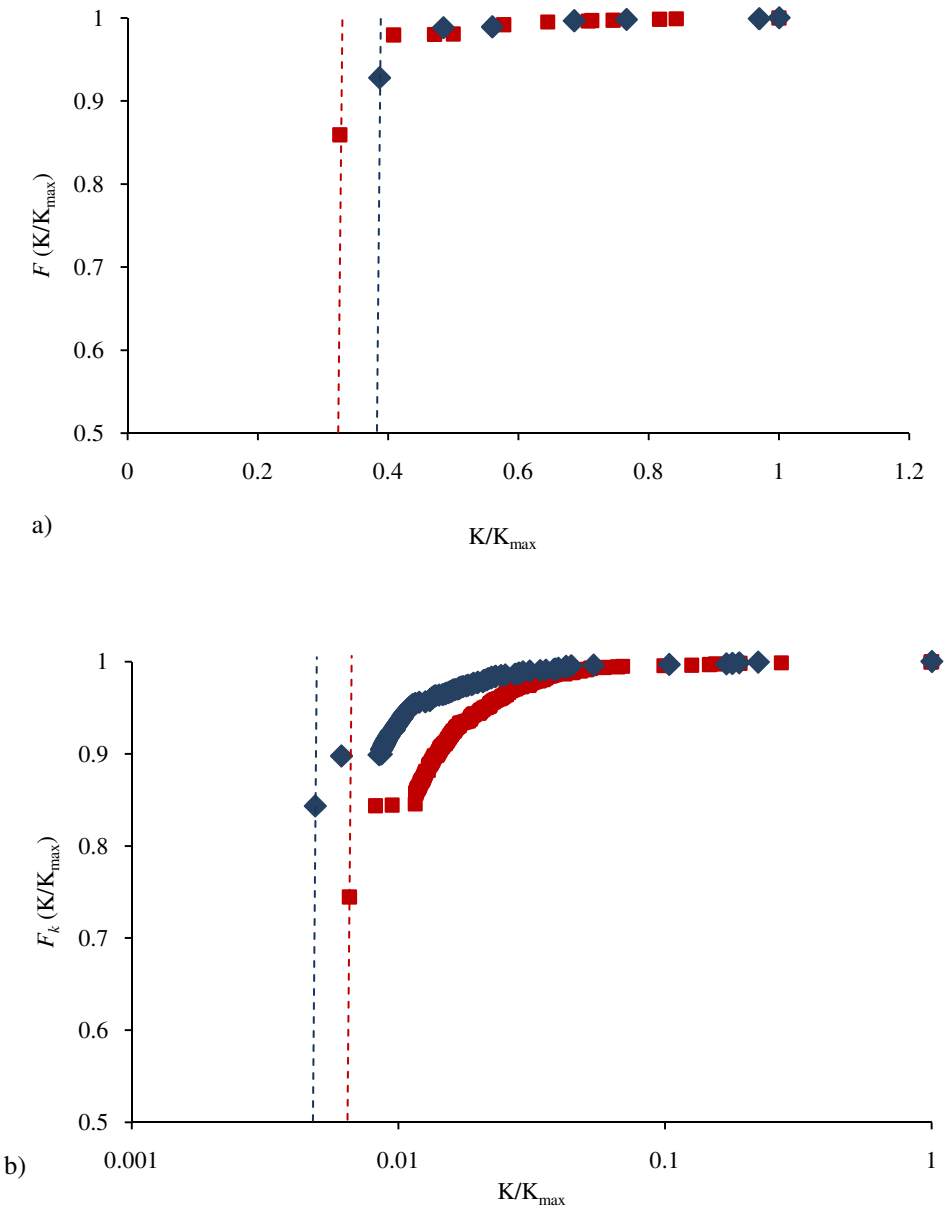

Fig. 5.19 Cumulative distribution function *F* for stress intensity factor, normalised for maximum stress intensity, over all cells at (a) the start of the model run and (b) approximately two thirds through the total run time of the model. $F(K/K_{max})$ describes the probability that the normalised stress intensity is less than or equal to the specified ratio. The two examples shown are for model run 1 (blue diamonds) and model run 2 (red squares), producing Type I and Type II event-rate trends respectively. Plot (b) shows *F* at the point at which the Type II trend becomes hyperbolic. The dashed lines show the value of the remotely applied stress, normalised for maximum stress intensity, and therefore represent the minimum stress intensity for each example. Note the logarithmic scale for the horizontal axis in plot (b).

5.4.1 Proximity to failure

The failure of cells in the array is controlled not only by stress intensity but also by the distribution of fracture toughness. The ratio of stress intensity to fracture toughness gives a measure of a cell's proximity to failure, with the limiting values of 0 and 1 corresponding to the conditions of no potential for failure and of imminent failure. Changes in the overall distribution of proximity to failure can highlight differences in the mechanism of failure Figure 5.20 shows the distribution function for this measure of proximity to failure at different stages throughout the run time of the example models 1 and 2. Figure 5.19a showed a near constant distribution of stress intensity at the start of the model runs. Due to the randomness of the fracture toughness across the array's cells, the initial distribution function shows more variety than the approximate step function that would otherwise be expected (Fig. 5.20a). However, with over 60% of intact cells having a ratio value between 0.3 and 0.5, there is still some regularity in the likelihood of failure across the array in both examples. As the model evolves there is a tendency to a more linear trend in the distribution function, highlighting a much greater difference in the proximity to failure across the remaining intact cells. The linearity is especially pronounced in the Type II example, with a fit of $R^2 > 0.99$ for the range of *K*/Toughness from 0.4 to 0.8. For the Type I example, the range from 0.7 – 1 also provides a linear fit with $R^2 > 0.99$.

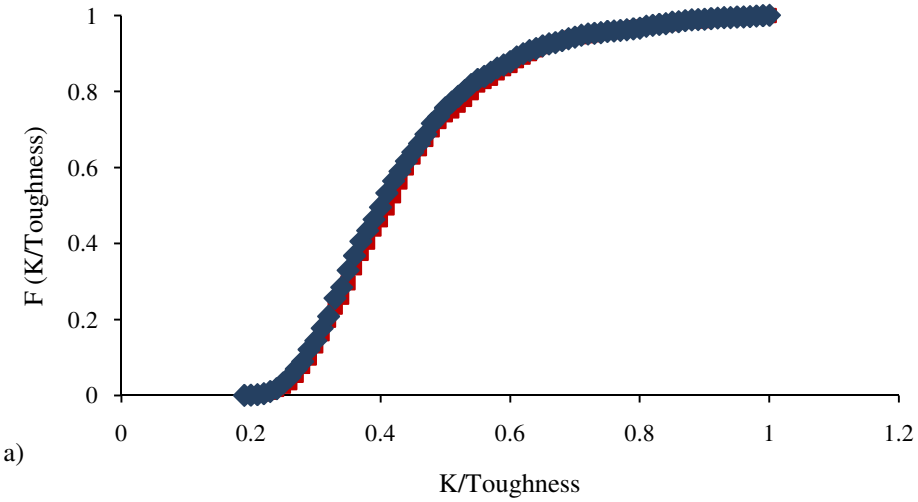
F (K/Toughness)
K/Toughness
0
0.2
0.4
0.6
0.8
1
1.2

a)

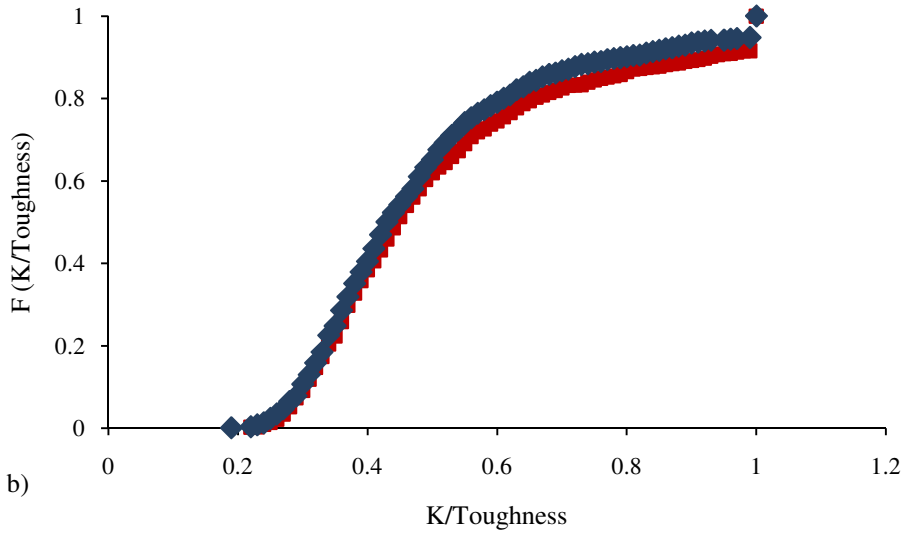
F (K/Toughness)
K/Toughness
0
0.2
0.4
0.6
0.8
1
1.2

b)

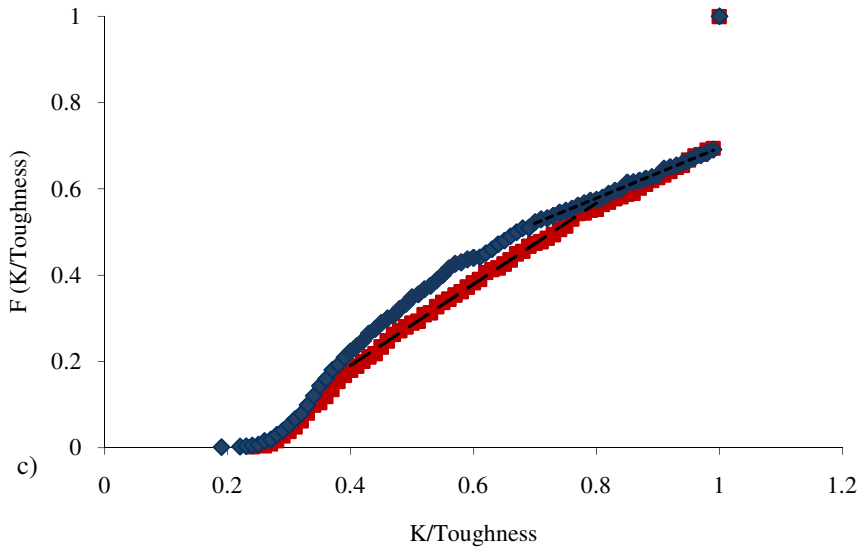

Fig. 5.20 Cumulative distribution function for the ratio of stress intensity to fracture toughness over all intact cells of the one-dimensional array for model runs 1 (blue diamonds) and two (red squares), producing Type I and Type II event-rate trends respectively. The distribution function is shown at: (a) the start of the run, (b) approximately two thirds through the total run time of the model, and (c) approximately 85% through the total run time of the model. Dashed lines show the range of linearity of the cumulative distribution function for each example. Plot (b) shows the point at which the Type II example switches to a hyperbolic event rate.

Failure dominated by the appearance of new cracks or newly activated cracks corresponds to randomness in the probability of failure across a domain. Any cell is just as likely as another to fail, and this corresponds to a random uniform proximity to failure for all cells across the array. However, once the mechanism of failure has switched to the extension and coalescence of existing cracks, this leads to a much greater variety in the proximity to failure across the array's intact cells. Regions surrounding extending cracks will be a lot more likely to fail than isolated cells, as the stress intensity in the former will be increased by the presence of neighbouring cracks. As these cracks grow larger, it becomes more and more likely that the intensity will exceed a cell's fracture toughness. Isolated cells maintain the same stress intensity until they eventually fall into the range of influence of an approaching crack. The change over the course of the model runs, from an initial, more uniform, proximity to failure to a final, almost linear, distribution function is therefore consistent with the theory of a change in failure mechanism from the appearance or activation of new isolated cracks to the extension of existing cracks.

5.5 Alternative precursory trends

The Monte Carlo simulation of the one-dimensional model captures the common behaviour of exponential and hyperbolic event-rate trends in the field. The simulations also produce alternative, less frequent trends, in which the faster than exponential sequence appears as a step like increase (Fig. 5.21). In the model this style of activity appears to correspond to a relatively homogeneous distribution of fracture toughness. At one extreme, with a low value of both the mean and variance of fracture toughness, a large number of cells fail almost instantly when stress is applied to the array (shown by the red squares in Figure 5.21). Remaining intact cells then tend to fail in quick succession due to the large number of surrounding cracks. At the other extreme, where fracture toughness again has a small variance but now with a much larger mean value, the model progresses with very few failing cells at each time step, creating a low background level of activity, and only once the applied stress has reached a critical point does the same effect occur of multiple cells, with similar fracture toughness values, failing simultaneously (blue diamonds in Figure 5.21). Although within the Monte Carlo simulation these two cases are seen as opposite extreme cases, they are in fact recording the same process. Whether stress has built up gradually or there is a rapid step like increase, the outcome of a large number of cells suddenly failing is the same.

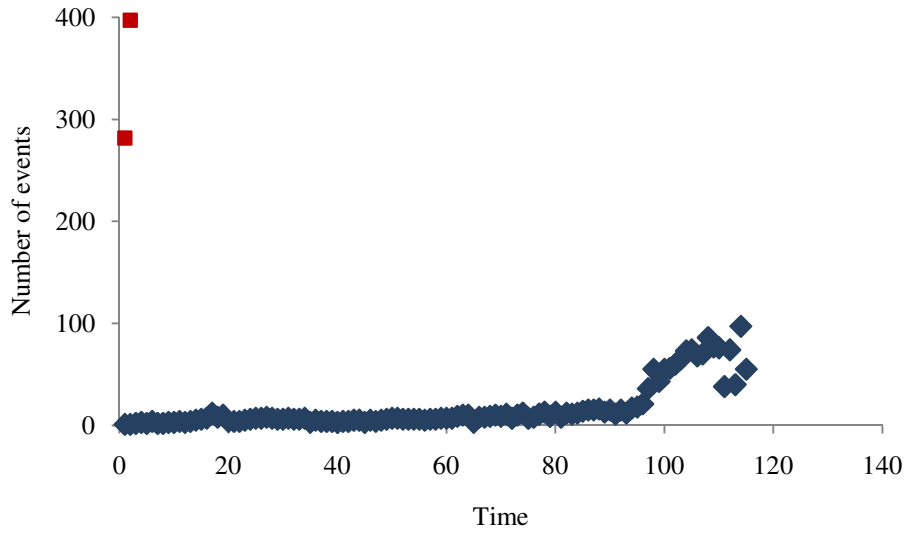

Fig. 5.21 Event rate plots from two model runs showing faster than exponential, step like increases in rate prior to failure.

An interesting future direction for this research would be to investigate the occurrence of these step-like increases in precursory activity in the field. A sharp increase in seismic energy and earthquake event rate was observed prior to the 1956 eruption of Bezymianny, Kamchatka (Tokarev, 1985), (Fig. 5.22). This explosive eruption followed 1,000 years quiescence, with a noticeable increase in seismic activity beginning approximately a month before the eruption. However, no further analysis on the nature of this trend was provided by the author, and it should be noted that activity leading up to the eruption may have been missed through lack of monitoring. A very sharp increase in earthquake numbers was also seen in the days prior to explosive dome eruptions in 1959 and 1960. Similar rapid increases in event rate were recorded prior to the 1964 eruption at Sheveluch, which ended 15 years of quiescence, and again prior to a later paroxysmal dome explosion in 1993 (Tokarev, 1985). In both cases seismic unrest was noted several weeks prior to eruption.

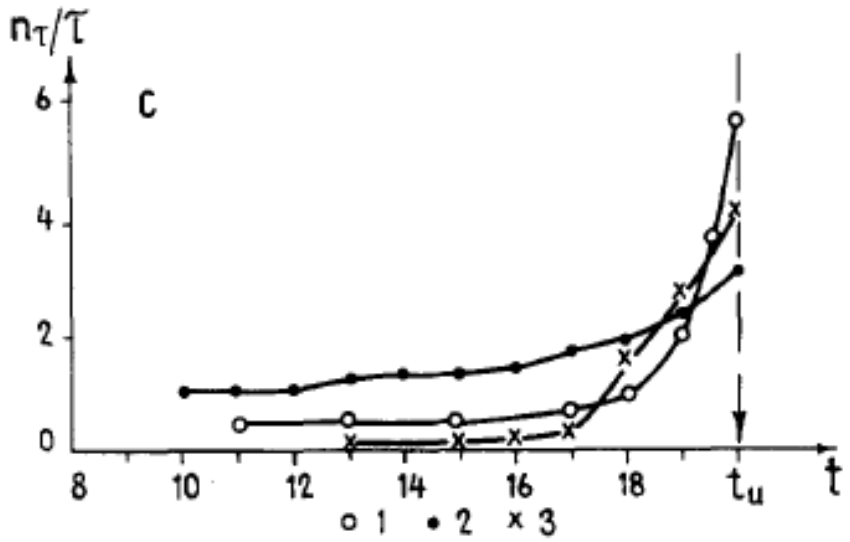

Fig. 5.22 The intensity of earthquakes per day prior to eruption (t_u) at Shiveluch, 1964 (1), Bezymianny, 1956 (2), and Mt. St. Helens, 1980 (3) (Tokarev, 1985). Intensity is measured as the average number of daily earthquakes.

The appearance of faster than exponential, step-like trends in the literature suggests that the one-dimensional model may also be utilised to anticipate alternative precursors in the future. In addition, occurrences in the field of a step increase in seismicity may be caused by a similar process to the model, implying the presence of a relatively homogeneous edifice.

5.6 Chapter summary

Exponential trends are commonly produced by the one-dimensional model, similarly to observations in the field and laboratory. In all three situations, examples of the emergence of a faster-than-exponential trend are also observed. Properties of crack growth in the model support the theory of a switch in dominating failure mechanism producing the two different trends. The exponential sequence is associated with the activation of new cracks. Once growth and coalescence of existing cracks becomes the favoured failure mechanism, the hyperbolic trend emerges. A second faster-than-exponential precursor is produced by the model, in the form of a step increase in seismicity. This type of activity has also been recorded prior to eruptions.

The exponential sequences produce a characteristic timescale for the precursory activity. This timescale can be related to the expected duration of the sequence, and therefore with the time to failure and eruption.

6. Spatial and temporal distribution of seismicity

6.1 Earthquake statistics

The statistics of earthquake magnitude distribution have been extensively studied. A key property is the frequency magnitude relation, because this describes the relative occurrence and expected recurrence time of earthquakes of different magnitudes. Additional information about the nature of the pressure source driving fracturing and the factors controlling fracture interaction can also be found from the statistics of the spatial distributions of seismicity. Spatial clustering can be measured by calculating a fractal dimension for earthquake hypocentres.

6.1.1 Earthquake magnitude

The magnitude of an earthquake has been measured both in terms of the maximum seismic wave amplitude and the energy released (Richter, 1935; Gutenberg & Richter, 1956; Hanks & Kanamori, 1979). In particular, Kanamori and Anderson (1975) described the relationship between earthquake magnitude and seismic moment, which is a measure of the energy released (Hanks & Kanamori, 1979) and depends on the area of the ruptured fault. The empirical relation between seismic energy E and fault area A is described by $E \propto A^{3/2}$ (Kanamori & Anderson, 1975). Following this relation the magnitude of events in the model, $m = \log E$, is calculated as proportional to the logarithm of the failed area A:

$$m \propto \log A \tag{6.1}$$

In the one-dimensional case failure occurs along a length only. However, due to the logarithmic relation in 6.1, the length of a fault is a still a suitable measure of magnitude. When failure occurs in the model, both the total length and additional length of the activated crack are recorded. Constants of proportionality were chosen such that the minimum possible area of a single cell failing corresponds to a magnitude $m = 1$ event.

6.1.2 Magnitude distribution: The Gutenberg-Richter Law

The frequency magnitude distribution for earthquakes has proven to be one of the most important statistics in the analysis of seismic activity. The distribution, which was first described by Ishimoto and Iida in Japan (Ishimoto and Iida, 1939) and then by Gutenberg and Richter in California (Gutenberg & Richter, 1944), is described by the relation:

$$\log N = a - bm \tag{6.2}$$

where N is the number of earthquakes with magnitude greater than or equal to m. The gradient b is known as the seismic b-value. This power law relation between the size and frequency of seismic events has become known as the Gutenberg-Richter Law. Figure 6.1 shows magnitudes and frequencies for earthquakes worldwide during 2007 (USGS, 2007). The cumulative number of earthquakes N can also be written in terms of seismic energy E, as $N \propto E^c$. The exponent c is a function of the seismic b-value.

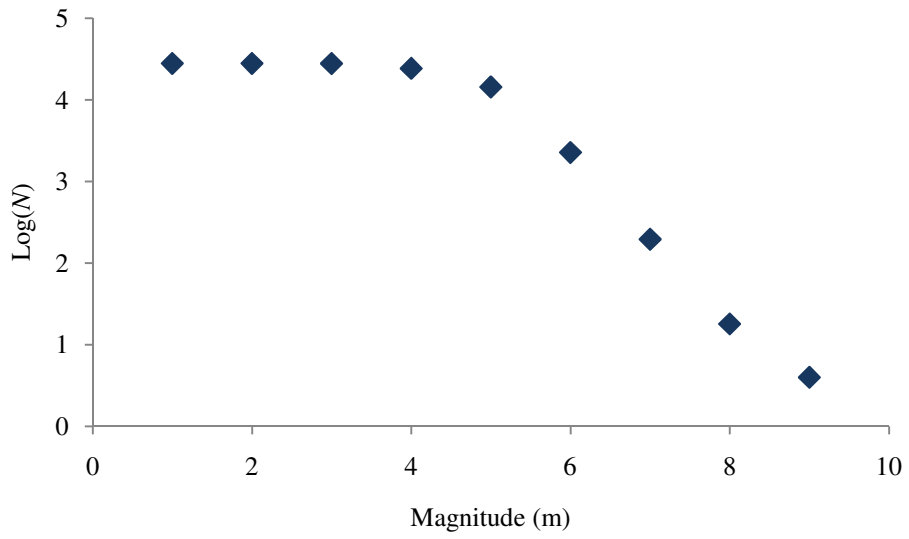

Fig. 6.1 Frequencies of global earthquakes in 2007 (www.usgs.com). N is the number of events with a magnitude greater than m. The linear log relationship for $m \geq 5$ is that described by the Gutenberg-Richter Law. Below $m = 5$ the catalogue of earthquakes is incomplete as the magnitudes become too low for observation.

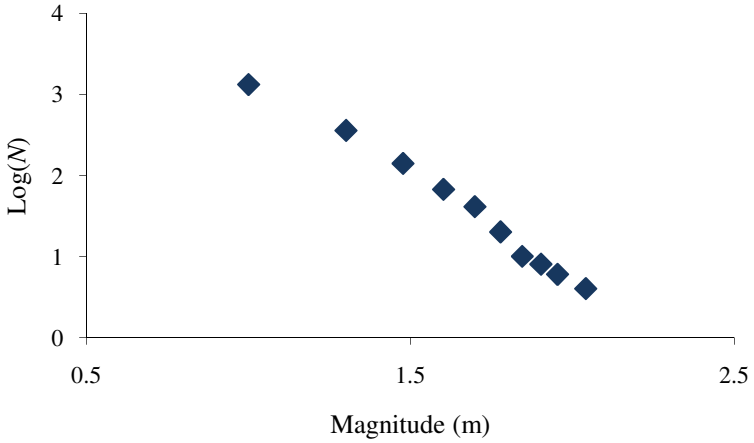

Fig. 6.2 Typical frequency-magnitude distribution for the one-dimensional model. N is the number of events with a magnitude greater than m. Lower magnitudes provide a good fit to the Gutenberg-Richter Law, with a deviation from a linear fit for $m > 1.7$.

The expression (6.2) describes a self-similar relationship and has been shown to describe both global and regional earthquake catalogues, as well as acoustic emissions produced by compressional rock fracture experiments in the laboratory (Scholz, 1968). Further supporting the universality of this relationship, the seismic *b*-value, shown as the linear slope of the logarithmic graph (Fig. 6.1) is typically found to be close to one at all scales of observation.

As with other examples of self-similarity in nature, limits of dimension prevent true scale invariance. In the case of earthquake magnitude, a finite limit to fault size provides an upper limit to possible earthquake magnitudes. Gutenberg and Richter (1949) observed a lack of events of magnitude 8 and greater. A deviation from large amplitude events in the laboratory has also been recorded (Scholz, 1968), as sample dimensions provide a limit to potential fracture size. A drop-off in the frequency-magnitude relation observed in volcanic settings (Qamar et al., 1983) has been attributed to inhomogeneous stress conditions. Observation becomes a problem at the lower scale range with events becoming too small for monitoring equipment to detect. There is therefore often a drop off away from the linear trend toward smaller magnitude values, which can be observed in the earthquake catalogue in Figure 6.1. The lower limit to the power law relation is defined as the magnitude of completeness m_c.

Figure 6.2 is a typical output from the one-dimensional model, run under constant stress, where magnitudes are recorded by the number of simultaneously failing

adjacent cells. The frequency-magnitude distribution provides a good fit to the Gutenberg-Richter Law, particularly at lower magnitudes. The fall-off from the linear trend at higher magnitudes implies a lack of large scale events. Similarly to the dimension limits in the laboratory, the number of cells in the model provides a theoretical upper limit to the possible event size. Previously failed cells distributed throughout the model restrict the potential length of adjacent simultaneous failures, leading to a much lower limit in practice.

The seismic b-value is inversely proportional to the mean magnitude. Therefore any variation in space or time of the *b*-value is also highlighting a variation in the mean magnitude. The measurement of magnitude can vary from location to location depending on coverage, instrumentation and analysis techniques. The seismic *b*-value therefore provides a more objective method of comparing magnitude distributions.

6.1.3 Seismic b-value

The Gutenberg-Richter Law is assumed to hold over all magnitudes where data are complete. However, it has been observed that the frequency-magnitude distribution can deviate from this linearity within the completeness range (Urbancic et al., 1992; Rydelek & Sacks, 1989; Taylor et al., 1990). This has been particularly noted in volcanic regions (Main, 1987). Earthquake swarms produced by magma movement may increase the number of small events or more importantly events of a similar magnitude and therefore create a bimodal frequency-magnitude distribution (Wiemer & Wyss, 2002). The *b*-value is a measure of the relative numbers of large and small magnitude events. A larger value describes a relative increase in the number of small events, and a smaller value a relative increase in the number of large events. Although *b* is generally found to lie close to one in the crust, it has often been observed closer to two and three, beneath volcanoes (Power et al., 1998; Wyss et al., 2001; Wiemer & McNutt, 1997). High *b*-values have been attributed to increased material heterogeneity (Mogi, 1962), increased local stress (Scholz, 1968; Huang & Turcotte, 1988), high pore pressure (Wyss, 1973), and large temperature gradients (Warren & Latham, 1970).

All of these properties can be associated with the presence of magma and high *b*-value anomalies at volcanoes have been used to provide constraints on the possible location of magma reservoirs or intrusions (e.g. Pinatubo, Sanchez et al., 2004; Makushin, Bridges & Gao, 2006; Etna, Murru et al., 2007). Fracturing around a body

of magma will lead to greater heterogeneity of the host rock, while interaction between magma and groundwater can lead to increased pore pressure (Wiemer & McNutt, 1997). An increase in pore pressure reduces effective stress, allowing for more slip on existing fractures, rather than the creation of new fractures (Murru et al., 2007). This creates a larger proportion of small events, leading to an increase in *b*-value. Larger events are more easily sustained in cooler, less fractured rock away from intruded regions (Power et al., 1998). Hence higher temperatures will favour a relative decrease in the number of larger events, so also producing an increase in *b*-value (Sánchez et al., 2004).

Spatial variations

Spatial variations in the seismic *b*-value have been studied at numerous volcanoes (McNutt, 2005). Studies show a high degree of spatial variation, with areas close to a normal value of $b \sim 1$ occurring adjacent to areas with anomalously high values in the range $1.5 < b < 3$. It is therefore now suggested that rather than volcanic regions as a whole having a high *b*-value, it may be more the case that pockets of high *b*-values exist in crustal rock producing otherwise normal or even low *b*-values (Wiemer & Wyss, 2002). The high anomaly values tend to occur at depths of less than 7km and are assumed to relate to the presence of magma bodies (McNutt, 2005). Weimer and Wyss (2002) suggest that a high *b*-value anomaly is a necessary but not sufficient condition for the presence of magma. Difficulties in building a clear representation of a spatial variation in *b* beneath a volcano are due to the high number of low magnitude events. Fewer are recorded, and therefore a large area or volume must be sampled in order to contain a large enough number of events to be statistically significant. Resolution may become too low, and any variation lost (Wiemer & Wyss, 2002).

At Montserrat a high *b*-value anomaly was found in the region about 2 km below the active crater area. During the period over which the study was conducted, increased fumarolic activity and ground cracks were observed in this region, suggesting again that increased heterogeneity or temperature may have caused the increase (Power et al., 1998). Two regions of high *b*-value at Pinatubo were situated next to the inferred location of a magma body derived from P-wave velocity analysis (Sánchez et al., 2004).

A high *b*-value anomaly beneath Mt. St. Helens was again found to correlate with an inferred shallow magma reservoir (Wiemer & McNutt, 1997). Areas of high *b*-value also coincided with regions of an increase in total number of events, and a

maximum magnitude approximately one unit smaller than surrounding areas with normal *b*-values.

The South flank of Kilauea is slipping seaward on a decollement plane. High *b*-values beneath the flank are recorded at a depth of approximately 6 km, decreasing to anomalously low values of $b = 0.4$ at depths greater than 8 km depth (Wyss et al., 2001). The high values are again associated with the presence of a magma body beneath the East Rift zone, whereas the low value at greater depth is thought to be an indication of the relatively homogeneous nature of the decollement plane and the potential for larger slips or ruptures (Wyss et al., 2001).

Temporal variations

Studying a temporal change in *b* in the field is inherently more difficult as consistent data sets are often not available. Any change in instrumentation or analysis procedures may influence the magnitude distribution and hence the *b*-value (Zuniga and Wyss, 1995). Hypocentre migration with time also makes temporal variation analysis difficult. A temporal shift can also coincide with a spatial shift, making it difficult to ascertain whether *b* is varying with time, space or both (Murru et al., 2007; McNutt, 2005).

A significant increase, followed by a sharp decrease in *b* is reported prior to two eruptions at Mt. Etna (Gresta & Patanè, 1983a; 1983b). An increase followed by a drop in *b*-value has also been observed leading up to large earthquakes (Smith, 1981). Under the stress regime hypothesis, this decrease would correspond to an increase in local stress leading up to an eruption. A sharp peak followed by a dip in *b*-value was observed before a phreatic eruption preceding the 18th May explosive eruption at Mt. St. Helens in 1980 (Main, 1987). However, no definitive precursory trend was noted leading up to the main 18th May eruption (Qamar, 1983). Similarly, no significant temporal change in *b* was found before or after the 1991 Pinatubo eruption (Sanchez et al., 2004).

As a precursory tool a similar problem exists as with measuring spatial variation in *b*. The resolution of time interval that must be sampled in order to include sufficient events for a statistically significant measurement may conceal any short-term variation in the *b*-value (Main, 1987).

Laboratory tests

Acoustic emissions produced during tensile fracture tests in the laboratory have amplitude correlated with crack length growth in a similar relation to earthquake source and magnitude (Lockner, 1993). Acoustic emissions during compression tests are linked to the propagation and interaction of microcrack arrays. Scholz (1968) demonstrated that microfracture events during rock deformation experiments also follow the Gutenberg-Richter Law and that b decreased as stress was increased. This relationship can be described by a statistical model of fracture growth (Scholz, 1968). A decrease in b is often observed before failure in both tension and compression tests in laboratory rock fracture experiments. It has been shown that the b-value is linearly related to stress intensity factor K:

$$b = p - qK \tag{6.3}$$

where p and q are constants (Meredith & Atkinson, 1983). Meredith et al. (1990) used relation (6.3) to explain and predict the decreases in b-value recorded prior to failure, which have been linked to an increase in stress intensity (Main et al., 1992; Sammonds et al., 1992). Stress intensity increases with fracture length, and therefore decreases in b-value arise when fractures lengthen and unite. This occurs just before bulk failure.

Compression tests carried out at temperatures up to 900^{oc} and 50MPa confining pressure found a minimum in b coincident with macroscopic failure (Smith, 2006).

6.1.4 Evolution of seismic *b*-value in the 1D model

Calculation of b-value

Given that the seismic *b*-value is such a widely analysed earthquake statistic, the methods used to estimate b are also important to consider. A simple least squares method can be used to calculate the slope of the linear relation (6.2). However, this method assumes a Gaussian distribution for residuals that leads to a disproportionate influence on the result by the few larger magnitude events (Page, 1968). Many studies therefore use a maximum likelihood estimate of *b*, as derived by Page (1968):

$$b = \log e \left[\bar{m} - \frac{m_{min} - m_{max} e^{-\beta(m_{max} - m_{min})}}{1 - e^{-\beta(m_{max} - m_{min})}} \right]^{-1} \tag{6.4}$$

where $\beta = b \ln 10$, $\bar{m}$ is the mean magnitude and m_{min} and m_{max} are the minimum and maximum magnitudes respectively. Equation (6.4) can be solved numerically for b. Alternatively, if the magnitude range is sufficiently large, for example $m_{max} - m_{min} > 2$ (Page, 1968), it can be approximated by (Aki, 1965):

$$b = \frac{\log e}{\bar{m} - m_{min}} \tag{6.5}$$

Due to the logarithmic form of the length to magnitude relation and the scale of the one-dimensional model, the model data will not cover a sufficiently large range of magnitudes. The minimum magnitude event, corresponding to the failure of a single cell, is $m = 1$. Occurrence of a $m = 3$ event requires the simultaneous failure of 100 adjacent cells. Damage zones around extending cracks and the distribution of microcracks throughout the model make this scale of event very improbable, as there is unlikely to be a fully intact section of this length. The lack of larger events results in a considerably high *b*-value. However, a comparison of values and overall trends can still provide a useful analysis, without concern of the absolute figures. It should also be noted that large magnitude events are in any case rarely observed in volcanic regions,

and due to factors previously discussed, *b*-values can be higher than average. In the model, *b*-values were calculated originally using a bisection method on Equation (6.4) to numerically solve for *b*. When derived to within a tolerance of 0.01 magnitude units, results were consistent with those produced by the approximation formula (6.5). For ease of computation, therefore, this approximation was used throughout.

The derivation of the maximum likelihood estimate also assumes a continuous range of magnitudes. As magnitude values correspond to the number of failed cells in the model, there is a discrete distribution of values. However, this is similar to the grouping of earthquake magnitudes in the field and for a group width, or resolution, of less than 0.1 magnitude units Equation (6.4) remains a good approximation (Bender, 1983). Due to the logarithmic relation in (6.2), magnitude group widths in the model are not equal, but become smaller with increasing magnitude, which makes the use of maximum likelihood estimates for grouped data inappropriate (Bender, 1983; Palacios et al., 2006). Because the group width is a maximum of 0.3, and rapidly falls below 0.1 units, Aki's continuous formula is used.

The minimum recorded magnitude in the model, m_{min}, is the failure of a single cell and corresponds to $m = 1$. The minimum magnitude used in calculating *b* should be the minimum value in the corresponding magnitude group (Palacios et al., 2006). Using $m_{min} = 1$ in calculating b may lead to considerably larger values, as the denominator in Equation (6.5) can be of the order of 10^{-2}. As with field data, and in accordance with the assumption of a continuous range of magnitudes, it is assumed that $m = 1$ is the midpoint of a magnitude group, and that $m_{min} < 1$. The group width is taken to be equal to the difference between the first two discrete magnitude values observed in the model, giving $m_{min} = 1 - \frac{\log 2}{2} \sim 0.85$. Choice of m_{min} modifies the scale of the *b*-value distribution but has no effect on the overall trend of the variation.

A least squares value was also estimated for each *b*-value calculation. Where no inconsistency was observed between the two estimators, the maximum likelihood estimate was the value reported. The standard error of b is calculated using the method of Shi and Bolt (1982). For a large sample size n, the standard error σ is given by:

$$\sigma = \frac{b^2}{\log e}\sqrt{\frac{\sum(m_i - \bar{m})^2}{n(n-1)}} \tag{6.6}$$

To produce a statistically significant *b*-value, the number of events in the catalogue used must be sufficiently large (e.g. $n > 100$, Wiemer & McNutt, 1997; Power et al., 1998). Events are selected within a moving window over time or space, with an overlap of events between successive windows.

Temporal variation

The variation of *b*-value with time was studied for both constant and increasing stress. A sliding window of 300-1,000 events was used, progressing by 50 events with each calculation. Event counts produced by the model provide a discrete rather than continuous time series, with no meaningful ordering of events within each time step. It was therefore important to include sufficient events in each calculation to avoid an arbitrary proportion of events within one time step creating an individual grouping of events. A minimum window size of 300 events was chosen as a good balance between exceeding the maximum number of events in one time step and producing enough *b*-values for a non-trivial analysis. To further mitigate the effect of a discrete time series, *b*-values were also calculated from data sets in which the order of events within each time step had been randomised. No significant variation in the results was observed. Using windows of equal time period also eliminated this problem. However, as event rate typically changes significantly during an individual run of the model, this leads to a considerable variation in the number of events per calculation. The same time interval towards the start of the model run will contain much fewer events than an equal time interval towards the end of the run. Nevertheless, consistency of results under different sampling techniques provides a useful test (Sanchez et al., 1994), and when this equal time window method was tested, again little qualitative difference was seen in the resulting *b*-value trend.

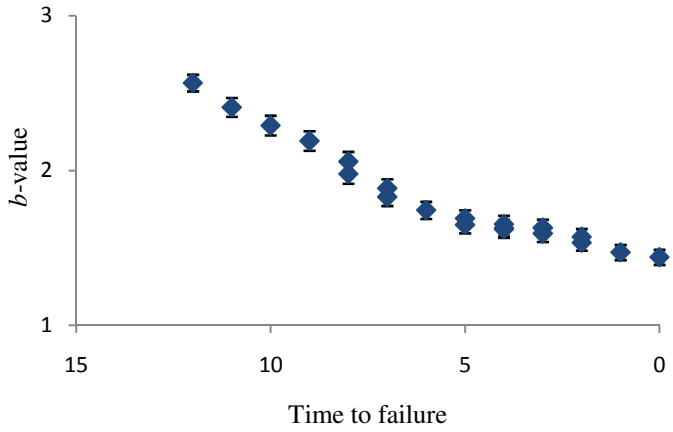

Fig. 6.3 Variation of *b*-value with time, under increasing stress conditions. A sliding window of 500 events is used for each calculation, advancing 50 events at a time. Vertical bars indicate the standard error.

Figure 6.3 shows a typical *b*-value trend with time until failure from a model run under increasing stress. The value tends to decline gradually over the entire time period, although fluctuations are also observed as seen in Figure 6.4, showing a model run under constant stress. However, independent of the style of decrease the *b*-value reaches a minimum at the point of failure. Both a gradual decrease and a minimum value at failure are consistent with deformation studies in the laboratory (e.g. Meredith & Atkinson, 1983; Smith, 2006; Scholz, 1968; Main et al., 1989).

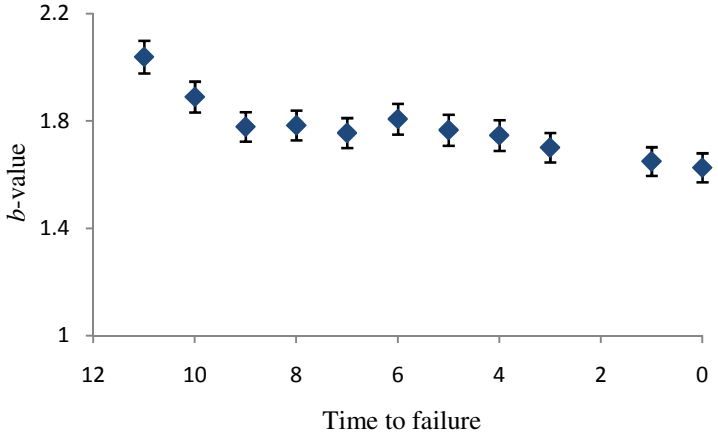

Fig. 6.4 Variation of *b*-value with time, under constant stress conditions. A sliding window of 500 events is used for each calculation, advancing 50 events at a time. Vertical bars indicate the standard error. Fluctuations occur in the gradual decline of *b*-value with time.

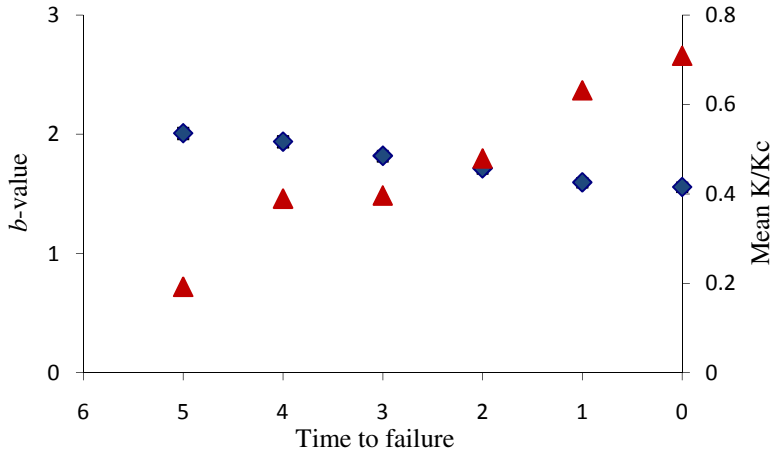

Fig. 6.5 Variation of *b*-value with time (blue diamonds) under increasing stress conditions. Red triangles show the average stress intensity over all intact cells, normalised for fracture toughness.

Figure 6.5 shows *b*-values for the same data set as used in Figure 6.3, but here each window contains 1,000 events. The triangles represent the average stress intensity factor over all intact cells in the model, normalised with fracture toughness at each cell. A gradual decrease can still be seen for the *b*-value, although some variation has been lost at this lower resolution. The decreasing *b*-value corresponds to a steadily

increasing value of K/K_c. The later section of the plot shows a quasi-linear relation between b-value and stress intensity, of the nature described by Main et al. (1989) in expression (6.3). However, the first three pairs of data points show a similar scale of decrease in b accompanied by first a large then very minor increase in stress intensity. This suggests that stress intensity may not be the sole factor affecting b-value variation.

The range of magnitudes produced by the model is small compared with earthquake catalogues from the field. Larger magnitude events in the model are rare partly due to the damage that builds up around extending fractures. The distribution of existing small cracks in these regions prevents a significant number of adjacent cells failing simultaneously. For example, while a major crack may appear to propagate a length on the order of 100 cells in a single iteration, producing a $m = 3$ event, this will in fact have been made up of numerous much smaller events linking up failed cells in the region around the tip of the major crack. However, this may be a similar mechanism to that which contributes to the b-value in volcanic settings higher than the expected $b \sim 1$ for tectonic earthquakes. Highly fractured material is likely at volcanoes due to the many processes occurring (Sánchez et al., 2004) and therefore in the same fashion, the host rock is not capable of sustaining a large event but instead produces many smaller events (Wiemer & McNutt, 1997).

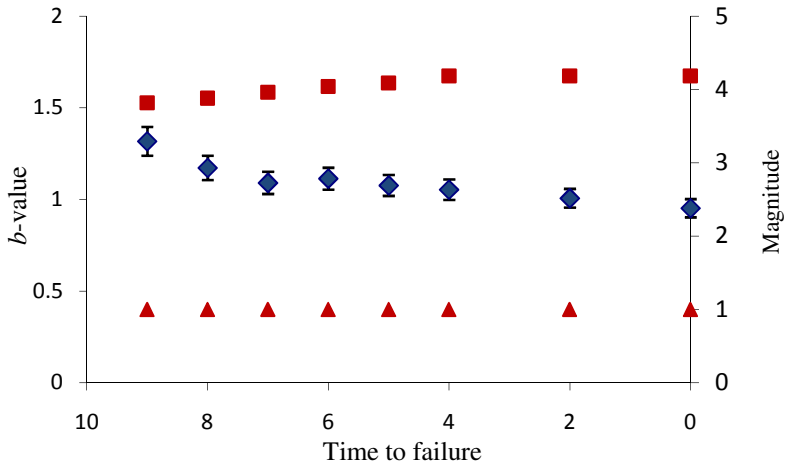

Fig. 6.6 Variation of b-value (blue diamonds) with time under constant stress conditions. 500 events were used for each calculation. The maximum (red squares) and minimum (red triangles) recorded magnitude for each window of events is also shown. Magnitudes are calculated using the total length of active cracks.

A second measure of magnitude is introduced that records the extension of a crack by the coalescence of numerous smaller cracks as a single event. A consequence of this method of measurement is the occurrence of larger magnitude events than were previously possible, the array dimensions providing the only limit on size. Figure 6.6 shows a typical *b*-value distribution calculated for this magnitude range, under constant stress conditions. The existence of larger magnitude events reduces *b*, but the overall trend of the distribution remains the same. A gradual decrease is observed, with the minimum *b*-value occurring at the time of failure. Whether it is assumed that magnitude measurements represent the joining together of adjacent fractures, or the extension of a single, major fracture, the *b*-value still decreases with time to a minimum before failure. Figure 6.6 also shows the maximum and minimum magnitudes observed in each window of events. From Equation (6.4), *b* is dependent on the mean magnitude rather than the spread, or range. This is highlighted by the continuing decrease in *b*-value, while the magnitude range remains constant.

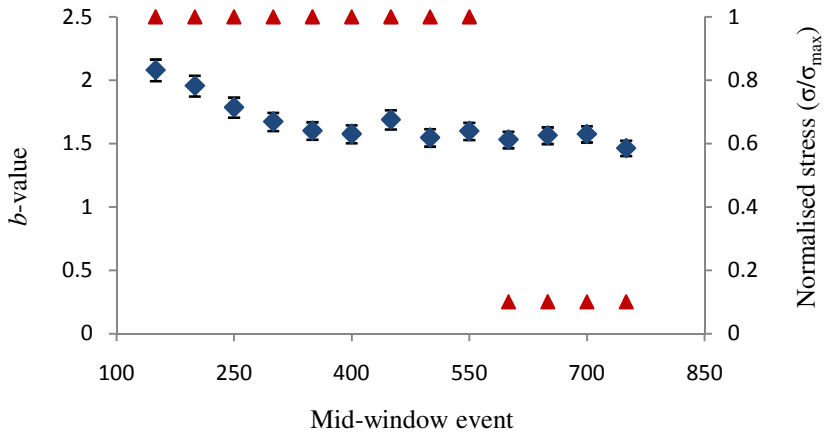

Fig. 6.7 Variation of *b*-value (blue diamonds) with time. Re triangles show applied stress, normalised by the maximum applied stress. The model reached equilibrium after the drop in stress with intact cells remaining.

No significant difference is seen in the *b*-value under constant or increasing stress. The range of *b* and the decrease with time are also consistent over different trends for event rate with time (e.g. Figs. 6.4 & 6.6). The resolution issue of including a sufficient number of events in each calculation window may mask any variations with different event rate trends. However the consistency in results implies that while the number of events may increase at various rates, the distribution of magnitudes of those

events does not change. Figure 6.7 shows that a similar trend is also seen when, after a drop in applied stress, the model does not fail, but reaches equilibrium with cells still intact. A significant reduction in applied stress appears to have no immediate effect on *b*, implying a greater dependence on fracture geometry rather than on background stress. Once fractures have formed in the model, they do not heal in the event of a stress drop. If the *b*-value depends on the size-frequency distribution of fractures then it would be expected for *b* to remain the same. The similarity of the trend observed when the model did not run to failure (Fig. 6.7) with those that did, implies a difficulty in using this as a method to forecast model behaviour.

While the observations from the model for temporal *b*-value variation are consistent with those produced in laboratory experiments and seen in field data, they suggest a limited useful function as a forecasting tool. Failure is generally coincident with a minimum in *b*. However, in real time analysis there would be no way to distinguish this data point from each previous minimum, without a known critical value for *b* (Main et al., 1993).

Spatial variation

For completeness, the spatial variation of the seismic *b*-value was also calculated. It has been suggested that regions of high *b*-value in volcanic regions correspond to the location of magma bodies. Processes caused by magma intrusions create greater material heterogeneity than in surrounding regions. In the model, a uniform remote stress is applied and the fracture mechanism is the same throughout the array.

Figure 6.8a shows the spatial variation of *b* calculated from windows of 300 events, with an overlap of 250 events, under increasing stress conditions. The location of an event is taken as the centre of adjacent failing cells. Magnitudes are measured using the length of new failing cells only. The slight increase in *b*-value toward the higher numbered cells may be due the greater extent of damage that builds up in this area before bulk failure. This can be seen as the increased density of red within grey cells on the right hand side of Figure 6.8b. The later fail time of the right hand region means that there is a greater opportunity for small cracks to form before bulk failure occurs. The numerous microcracks prevent larger magnitude events from occurring, and subsequently lead to a higher *b*-value. The observed increase in *b*-value is a consequence of the initial distribution of fractures.

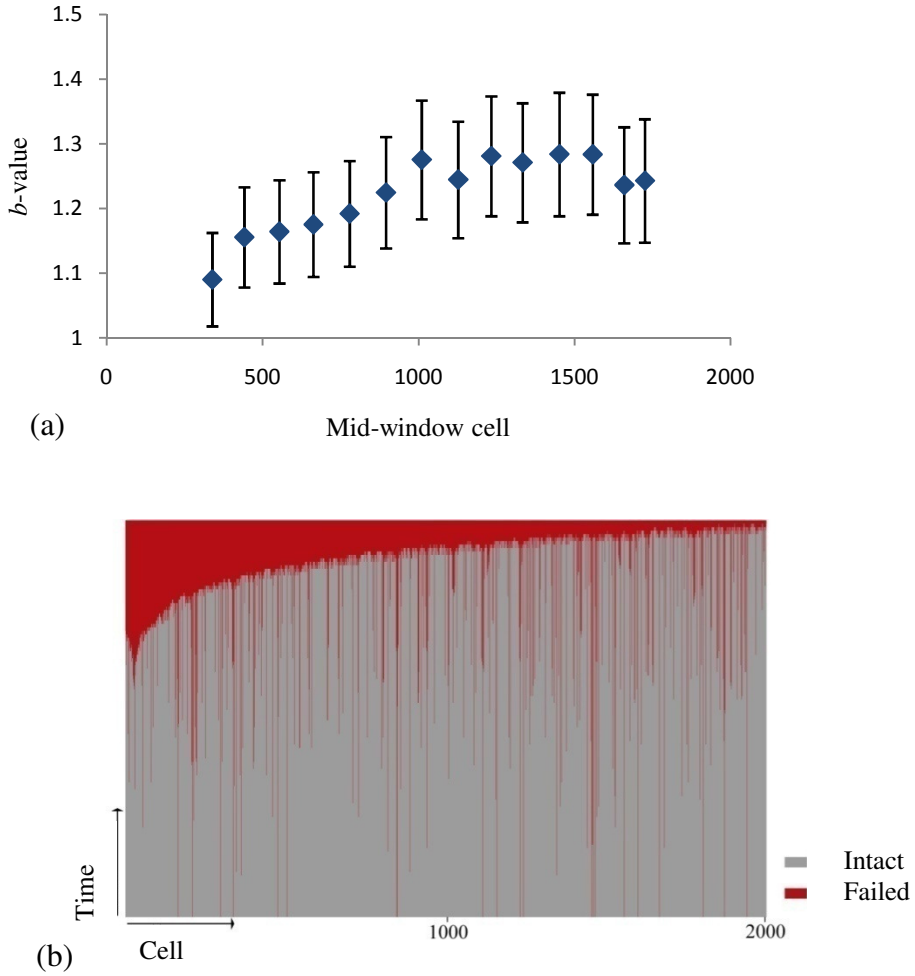

Fig. 6.8 (a) Spatial variation in *b*-value over an array of 2,000 cells, under increasing stress conditions. Vertical bars show the standard error. (b) Evolution of the array with time.

Figures 6.9a and 6.9b show the same results from a model run under constant stress. The values are consistently higher than for the increasing stress model in Figure 6.8. A higher *b*-value implies relatively fewer large magnitude events or more small magnitude events. When run under constant stress, a remote stress is applied that is just great enough to lead to failure of the model. Under increasing stress, applied stress exceeds this minimum level and therefore relatively larger magnitude events may be anticipated. Under constant stress, slow fracture is favoured and allows damage to build up around cracks before bulk failure occurs. Increased damage leads to an increased proportion of smaller events to large events and hence an increase in *b*.

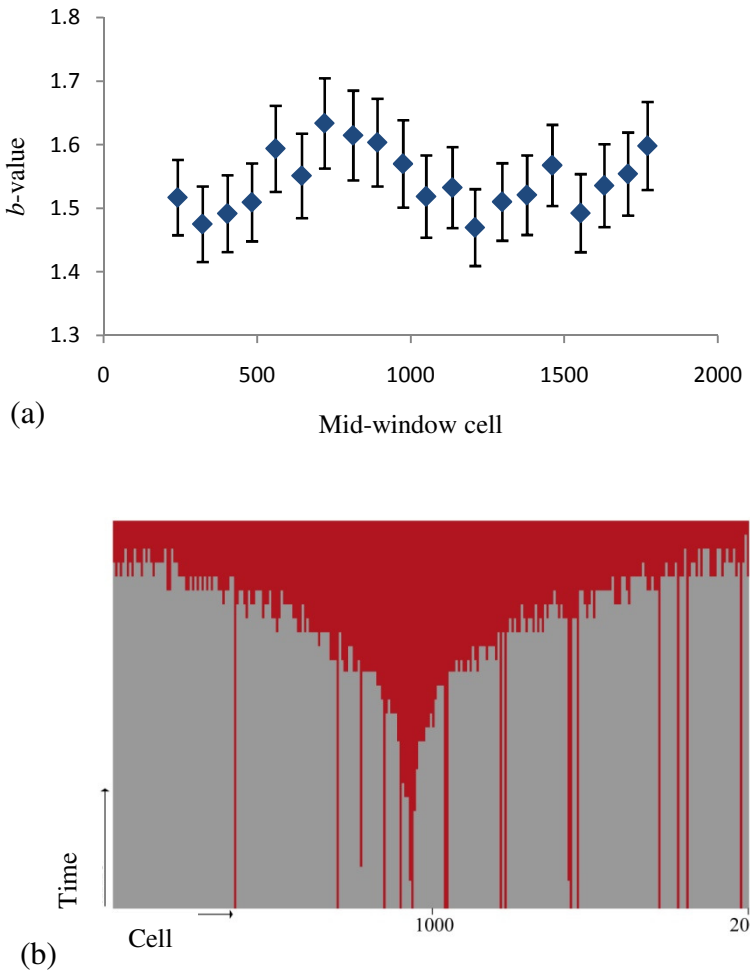

Fig. 6.9 (a) Spatial variation in *b*-value over an array of 2,000 cells, under constant stress conditions. Vertical bars show the standard error. (b) Evolution of the array with time.

There is no clear correlation between the calculated *b*-values and failure of the array in the constant stress example (Fig. 6.9). The relative increase in *b* at the end points of the array may be due in part to boundary effects preventing larger magnitude events. However, in the case of increasing stress, where the same effects would have been present, the end point *b*-values show a decrease. Both increasing (Fig. 6.8) and decreasing (Fig. 6.9) *b*-value trends are observed along a propagating fracture. The application of spatial analysis of *b*-values in the model appears to offer little potential in forecasting failure activity across the array.

6.1.5 Inter-occurrence statistics

The Gutenberg-Richter law can be written as a density function of the magnitude of events:

$$f(m) = \beta e^{-\beta(m-m_{min})} \tag{6.7}$$

thereby describing a very complex process by a simple statistical distribution. By describing the relative frequencies of different magnitude events, the Gutenberg-Richter law also tells us something of the expected recurrence time between events of a similar scale. The inter-event time of successive earthquakes in a region have been reported to follow universal scaling-laws (e.g. Saichev & Sornette, 2007; Corral, 2004) and have also been described by Poisson, power law and gamma distributions (Parsons, 2008; Bak et al., 2002; Corral, 2006). A Poisson distribution implies independence of the timing of an event with respect to previous events. Clustering of activity in time suggests a temporal correlation of events and a departure from independence. An established law for the expected inter-occurrence interval for certain magnitude events is valuable as a tool for forecasting anticipated frequencies of large scale earthquakes. Here, inter-event times between equal magnitude events are calculated to compare the statistics of events produced in the model with natural earthquake statistics.

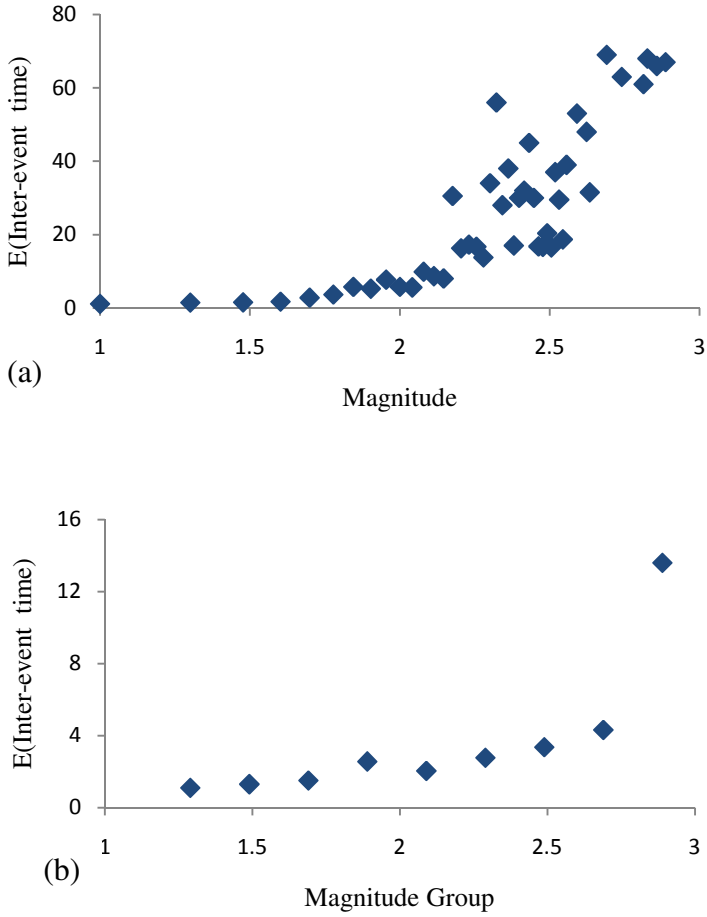

Fig. 6.10 (a)Average time interval between successive events of equal magnitude, for a typical run of the one-dimensional model. Events are grouped into nearest magnitude bins for the analysis in (b).

Mean inter-occurrence times were calculated for events in a model of 5,000 cells run under constant stress conditions. Figure 6.10a presents an expected time for each recorded magnitude, showing a large degree of scatter around a clear trend of increasing interval time with magnitude. Mean values for the larger magnitude events are necessarily based on fewer recorded inter-event times and therefore have a larger error associated with these expected intervals. In Figure 6.10b, the events have been placed in magnitude bins, incorporating much of the scatter. The discrete nature of time in the model again makes analysis of the series of events difficult. For example, many events of equal magnitude can occur at each time step but are not included in the calculation of inter-event time.

6.2 Fractal dimension

6.2.1 Fractals in nature

The scale invariance, or more accurately self-similarity, of nature has long been recognised and is exemplified by the need for a scale item in geological pictures. Self-similarity is a common characteristic of a fractal object. A coastline is a frequently used example of fractal geometry in nature which typifies this self-similarity. The observed length of a coastline will depend on the scale used to measure it. The smaller the measuring scale, the more fine detail of the coastline will be included in the measurement, and the longer the total length will become. Importantly, the measured length will increase without bound, rather than tending to a limit as would be expected for a Euclidean curve (Mandelbrot, 1977). The length of coastline increases as the measuring scale decreases, and can be described by:

$$N_i = \frac{C}{r_i^D} \tag{6.8}$$

where N_i is the length when measured by the characteristic linear dimension r_i, C is a constant and D is the fractal dimension. More generally, a fractal set is one made up of N_i objects of characteristic dimension r_i that follows the power law relation (6.8). Fault patterns also exhibit self-similarity and studies have explored the fractal nature of fault lengths (Hatton et al., 1993), geometry (King, 1983) and displacement (Walsh et al., 1991).

A fractal dimension can be calculated as a measure for the clustering of fractures in either space or time with a decreasing value indicating a move towards a more clustered structure. Therefore a significant shift in scaling parameter may indicate a change in controlling factors on a physical process (Caruso et al., 2006). Fractal analysis has been applied to various aspects of fracturing in the crust. The dimension D_l associated with the distribution of crack lengths is related to earthquake size and therefore to the *b*-value (e.g. Henderson et al., 1992). This relation is described in further detail in Section 6.3.2. Henderson et al. (1992) considered the distribution of earthquake epicentres, here described by exponent D_E. The variation in spatial

distribution of tectonic earthquakes was also studied by Hirata (1989), by estimating the fractal dimension of locations of earthquake epicentres in Japan over a period of approximately 40 years. This study also considered scaling exponents for fault surface traces, where fractal distributions were found over scale ranges of 2-20 km for areas of Japan and 1-100 km over the San Andreas fault (Aviles et al., 1987). This dimension, D_F is again measuring a different aspect of fracturing and seismicity. In a study of the seismicity in the Parkfield region of California, Henderson and Main (1992) developed a model that monitored the evolution of the *b*-value and fractal dimension of the fault trace, as single fault line fractures. Persistence is a measure of the similarity of future behaviour to current behaviour. Persistence is described by the Hurst exponent H. H lies between 0 and 1, with $H > 1/2$ indicating a persistent process, where future behaviour is more likely to be similar to current and past behaviour, and $H < 1/2$ implies anti-persistent behaviour (e.g. Telesca et al., 2002). Henderson and Main (1992) used the evolution of the *b*-value and fractal parameters monitored to distinguish between persistent and anti-persistent geometries of failure. They found a negative correlation between fractal dimension and *b*-value as the model advanced and neighbouring fractures coalesced.

Focusing on volcanic seismicity, Vinciguerra et al. (2001) calculated both the spatial and temporal fractal dimension for seismicity during periods before and after a major eruptive period at Mt Etna (1983-1988 and 1993-1996 respectively). They found a rise in temporal dimension, but a fall in spatial dimension between the two periods. This implies that the rate of seismic activity became less clustered, but that the activity occurred in more concentrated areas. Altering stress conditions within the volcano were proposed as the cause of the change in parameters. Vinciguerra (2002) also investigated the change in D, the scaling exponent measuring the relative proportions of small and large cracks, driving the seismic activity on Etna leading up to the 1989 flank eruption. Over several months prior to the eruption, the value of the exponent decreased. This was interpreted as evidence of a positive feedback process that favoured growth and coalescence of existing fractures over the nucleation of new cracks, thus increasing the number of fractures of greater length. Statistics of fracture length distributions are discussed in further detail in Section 6.3.2.

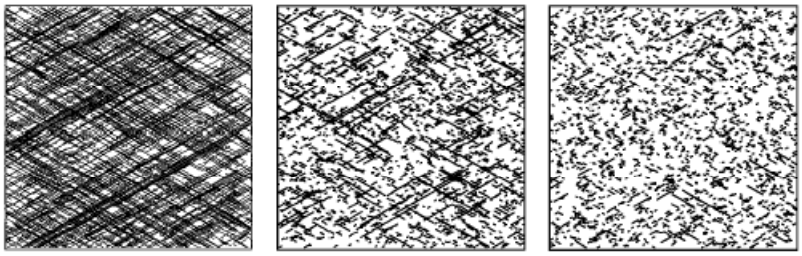

Fig. 6.11 Fracture networks with equal fractal dimension ($D = 2$), but with different fault length distributions. (After Bonnet et al., 2001). Sets with identical fractal dimension can exhibit very different fracture densities.

Caruso et al. (2006) looked at multifractal clustering of seismicity during dome building eruptions at Mt. St. Helens. Multifractal analysis allows for multiple scaling exponents, which may be necessary to fully characterise a fractal object. As seen in Figure 6.11, two sets with identical fractal dimension can have very different properties, and information such as density and orientation are also necessary to completely define a set (Sornette et al., 1993). Multifractal dimensions D_q can allow for this extra characterisation and are defined by:

$$D_q = \lim_{\varepsilon \to 0} \frac{1}{q-1} \frac{\ln\left(\sum_{i=1}^{N} p_i^q(\varepsilon)\right)}{\ln \varepsilon} \tag{6.9}$$

for $-\infty < q < \infty$ and partition size ε. $p_i(\varepsilon)$ can be thought of as a probability. If the fractal set contains M points, and the space occupied by the set is divided into N partitions of size ε:

$$p_i(\varepsilon) = \frac{M_i(\varepsilon)}{M} \tag{6.10}$$

where $M_i(\varepsilon)$ is the number of points in partition i. Objects may be monofractal, in which case D_q is equal for all values of q. D_0 gives the capacity dimension, which is the classic definition of a fractal described by (6.8), D_1 the information dimension, and D_2 the correlation dimension (Telesca et al., 2002). Multifractal analysis of seismic

activity during the eruptive period (1980-1986) at Mt. St. Helens shows D_q decreasing from 1 to 0.36 as q increases (Caruso et al., 2006). This implies clustering of seismic activity with time, but with different densities of activity in different regions. During non-eruptive periods, an almost constant value of $D_q \sim 1$ was calculated. The value of 1 indicates a random rather than clustered distribution of activity. When analysed spatially, decreases in the fractal dimension occurred at relatively smaller depths and may have been caused by magma intrusions in the shallow crust (Caruso et al., 2006).

6.2.2 Dimension measurements

The classical method for measuring the fractal dimension described by (6.8) is a box-counting technique (e.g. Bonnet et al., 2001). The numbers $N(l)$, of boxes of length l needed to cover the fractal set are counted. The fractal dimension D is then defined by:

$$D = -\lim_{l \to 0} \frac{\ln N(l)}{\ln l} \tag{6.11}$$

In practice, D can be calculated from the negative gradient of the log-log plot of number against size of boxes. An equivalent and often more straight forward method is to cover the area containing the fractal set F with a mesh of squares with side length δ. Then,

$$D = -\lim_{\delta \to 0} \frac{\ln N_\delta(F)}{\ln \delta} \tag{6.12}$$

where $N_\delta(F)$ is the number of δ-mesh partitions which contain or intersect F (Falconer, 1990). Again, D can be calculated from the gradient of the relevant log-log plot. This method of calculation can be derived from the multifractal definition (6.9) when $q = 0$. This provides a more simple calculation than (6.11) as it is not necessary to identify the optimal covering of boxes.

The correlation dimension was introduced by Grassberger and Procaccia (1983) and shown to be a good estimate for the fractal dimension *D* but with the advantage of a comparatively easy calculation. For a fractal distribution the relationship:

$$C(r) = \frac{N(r)}{n(n-1)} \tag{6.13}$$

where $N(r)$ is the number of data points a distance less than r apart, and n the total number of points, scales with r as r^D. This dimension is equivalent to (6.9) when $q = 2$.

Theoretically, fractal sets can be produced which remain self-similar over a large scale range. However, when observed in the field or laboratory the range over which a set exhibits fractal characteristics is generally very much reduced (Hamburger et al., 1996). When viewing data over less than one order of magnitude, distributions other than a power law, for example exponential, can appear linear on a log-log plot (Bonnet et al., 2001), which would result in classification of a Poisson process as fractal. Hamburger et al. (1996), showed that purely random distributions can appear fractal when observed over a limited range, similar to that often used in experimental measurements. In practice, obtaining a statistically large enough range can be difficult due to sampling difficulties at both upper and lower limits of scale. As always, the number of data points is also an issue in producing a statistically significant measurement. For example a minimum of 200 faults has been a suggested requirement for analysis of spatial and length distributions of fracture networks (e.g. Priest & Hudson, 1976; Bonnet et al., 2001).

6.3 Fractal analysis and fault statistics for one-dimensional model

6.3.1 Fractal and correlation dimensions

The spatial and temporal variations in fractal dimension were calculated for the model run under both increasing and constant stress conditions. Both a standard box-counting method and the mesh-cover method were used with no differences observed in the results. The outputs shown here were calculated by the box-counting method. As the model evolves there are two different patterns and fractal dimensions that may be considered, D_F and D_E. First is the distribution of all failed cells, which creates a fault trace pattern. Clearly, in the one-dimensional model this will always result in a single continuous line if the model fails. Second is the distribution of current failures or events with time. This is therefore looking at hypocentre location and represents a snapshot in time rather than the whole history of the model.

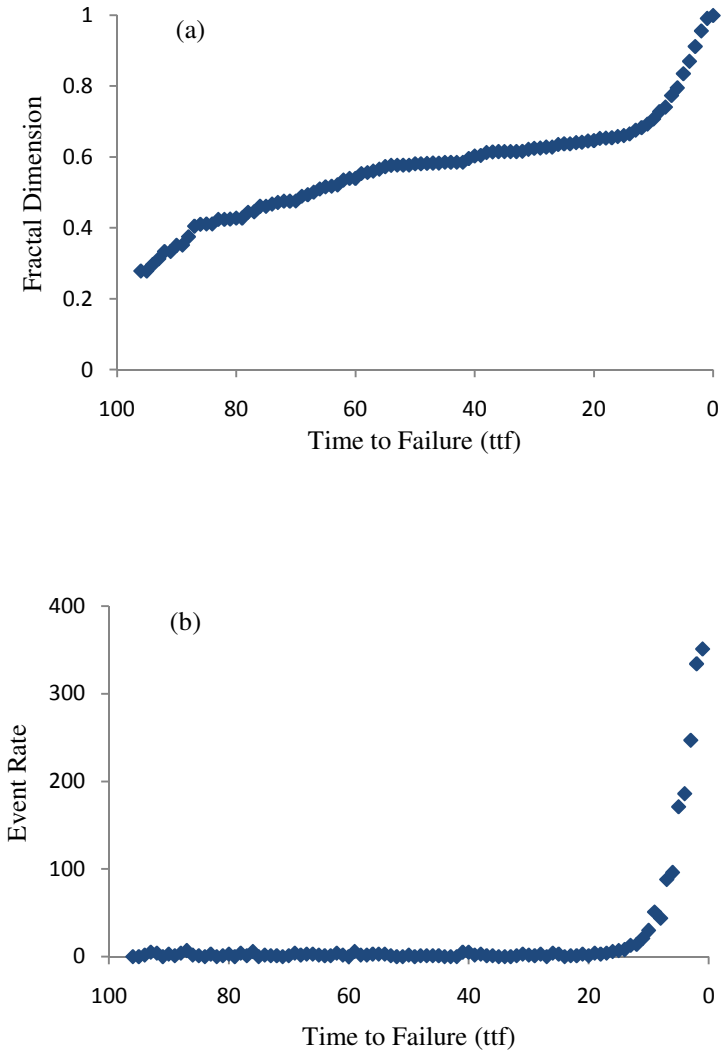

Fig. 6.12 (a) Variation of the fractal dimension D_F with time leading to failure, under increasing stress conditions. D_F will naturally tend to one as the failed cells eventually form a continuous line. The acceleration in D_F shortly before failure correlates with the exponential acceleration in event rate (b).

Calculating the fractal dimension of a continuous straight line will give $D_F = 1$. Figure 6.12a shows the trend towards this value when the fractal dimension was calculated over all failed cells with time. The increase in D_F becomes sharper once the event rate begins to accelerate (Fig. 6.12b), which may be due to the proportional increase in steps towards a continuous line which occurs once an increasing number of

cells are failing. The total number of failed cells increases monotonically and therefore the size of the fractal set, or the number of objects being analysed, will increase with time. Initially only 50 cells have failed, which is only 2.5% of the number at failure. This makes a direct comparison of the measured D_F values difficult. It is however constructive to observe the linearity and range of linearity of the box-counting calculations used to measure D_F. Figure 6.13 shows an example for the fractal dimension calculation at $ttf = 7$, at the start of the acceleration in event rate. At this stage 22% of cells have failed (Fig. 6.14). Although there is a slight deviation at the lower scale range, the linear trend covers at least one order of magnitude.

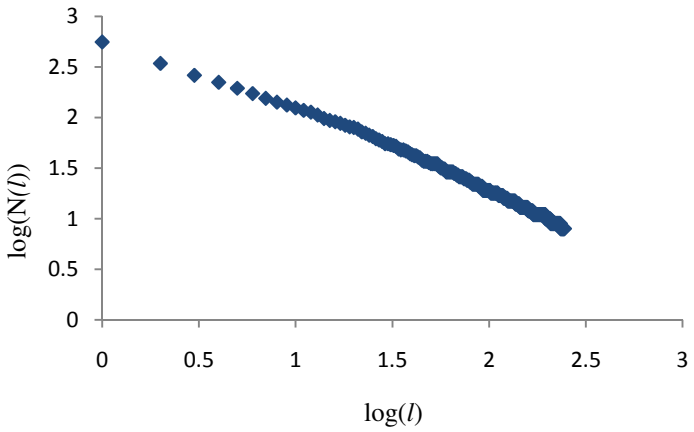

Fig. 6.13 Box-counting results used to calculate D_F. The fractal dimension is given by the negative gradient of the log-log plot of the number N(l) of boxes of size l needed to cover all failed cells.

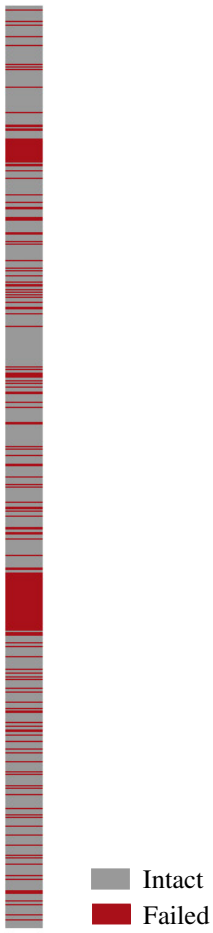

Fig. 6.14 Distribution of failed cells (red) used in the box-counting calculation plotted in figure 6.13. This shows a clear variety of crack densities along the array.

The distribution of events, or currently failing cells, provides analysis of the spatial location of seismic activity. The associated fractal dimension is defined as D_E. Event locations can be defined in several ways. Two methods were used to identify locations. Namely, each individual failing cell included as an event, regardless of any adjacent failures, and the central cell of adjacent failing cells only. In both cases moving windows of an equal number of events were used, with an overlap of events between consecutive windows. Similarly to the calculation of b-values, effects of the discrete time scale were checked by randomising events in a time step that was split between windows. This had no apparent influence on the calculated value of the dimension.

Figure 6.15 shows a typical trend of fractal dimension with time for a model run under increasing stress conditions. Error bars show the standard error for the slope of a least squares fit (e.g. Rice, 1995):

$$s = \sqrt{\frac{1}{n-2}\frac{\sum_{i=1}^{n}(y_i - \hat{y}_i)^2}{\sum_{i=1}^{n}(x_i - \bar{x})^2}} \tag{6.14}$$

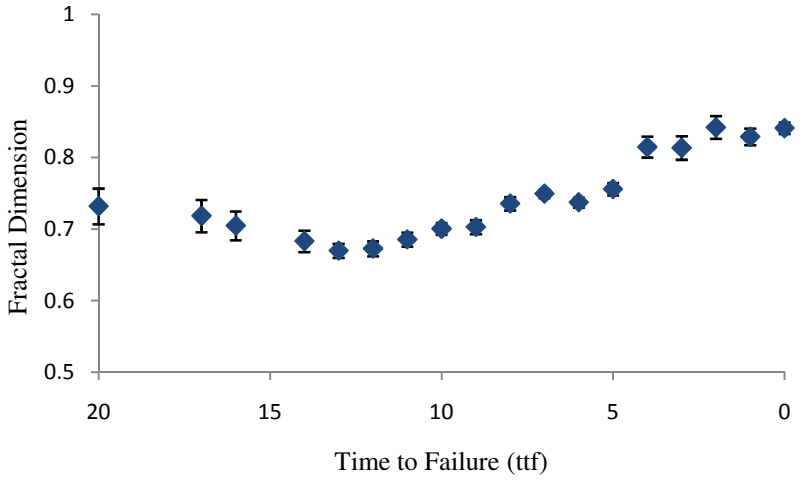

Fig. 6.15 Variation of fractal dimension D_E with time, under increasing stress conditions. A sliding window of 300 events is used for each calculation, advancing 50 events at a time. Vertical bars indicate the standard error.

The general increase in fractal dimension implies that events become less clustered with time, with values $D_E \sim 1$ signifying a random distribution of event locations. A lower initial applied stress, in addition to fewer failed cells causing stress concentrations, may result in more localised and clustered failures around the tips of existing cracks. As the stress and number of cracks increases, events become more widespread along the array, tending to a random uniform distribution. Leading up to failure, when event counts have become relatively large, the number of adjacent cells failing simultaneously is likely to increase. This leads to a larger proportion of continuous line segments, with a fractal dimension of one, making up the set of events. Taking only the central adjacently failing cells as event locations limits each element of the set to an equal size of one cell and prevents the occurrence of a continuous line.

However, when D_E was calculated for this alternative definition of location distribution, no significant difference was seen, especially in overall trend (Fig. 6.16).

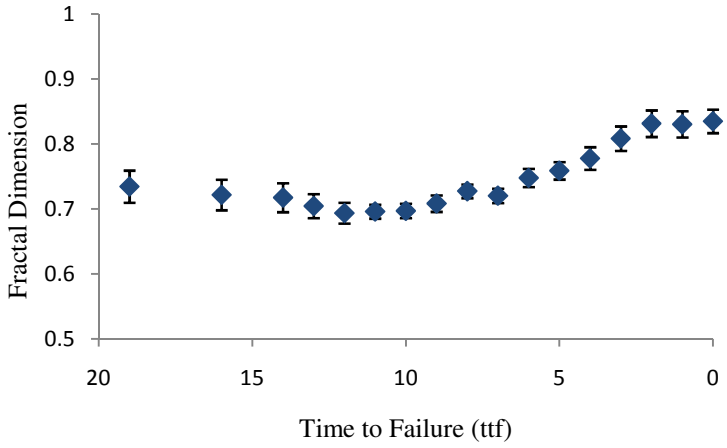

Fig. 6.16 Variation of fractal dimension D_E with time, under increasing stress conditions. A sliding window of 300 events is used for each calculation, advancing 50 events at a time. Events are defined as the central cell of adjacent simultaneously failing cells. Vertical bars indicate the standard error.

As with the calculation of *b*, the trade off between windows of a sufficient number of events for a significant value of D_E, and short enough time period to observe any variation presents a problem in this analysis. During the early stages of fracture there are very few events and a large time period must be incorporated to provide a set for testing which is of equal size to just a single time step much closer to failure. Therefore any temporal variation that may exist during this initial period is lost. When a sliding window of equal time period is used for the same data set, a much lower initial fractal dimension is observed (Fig. 6.17a). However the vast difference in set size makes comparison of the calculated dimension values difficult. The first window contains just 48 event locations while the final window contains over 1,700. This represents 85% of the entire array and will therefore naturally produce a very high fractal dimension as the set tends towards a continuous line. A smaller time window reduces this problem at the later time scale but reduces the number of events in early time windows even further. The first fractal dimension in Figure 6.17b is calculated from only 6 events. When a very small number of events is used, the possible range of cover numbers $N(l)$ in the box-counting calculation will be reduced, leading to less variation as box size l changes and hence a very low value for D. Although the range of fractal dimensions varies

considerably between the various methods of calculation (Figs. 6.15 – 6.17), the trend of an increasing D and a shift towards a random uniform distribution remains consistent across all cases.

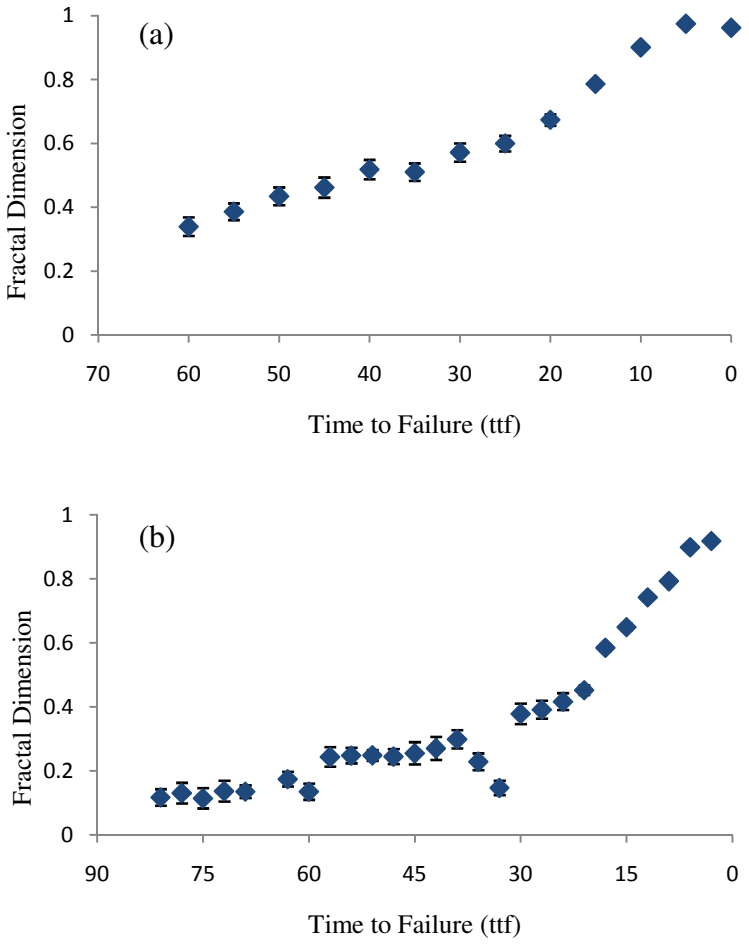

Fig. 6.17 Variation of fractal dimension D_E with time, under increasing stress conditions. A sliding window of equal time period is used for each calculation. Time periods of (a) 20 units and (b) 5 units advance (a) 5 and (b) 3 time steps each calculation. Vertical bars indicate the standard error.

The gradual increase in fractal dimension is generally less evident when models are run under constant stress conditions. The more typical trend in this case is a relatively consistent high D-value, showing small fluctuations with time (Fig. 6.18). This high measurement of D_E again closely approximates the non-fractal condition $D = 1$. Figure 6.19 shows the distribution of events in each window used to calculate the fractal dimensions. The active area shifts with time, but within this area the degree of clustering appears to remain the same. The concentration of events into localised

areas of activity, rather than distributed throughout the array, can result in a very dense distribution tending towards a continuous line and high fractal dimension.

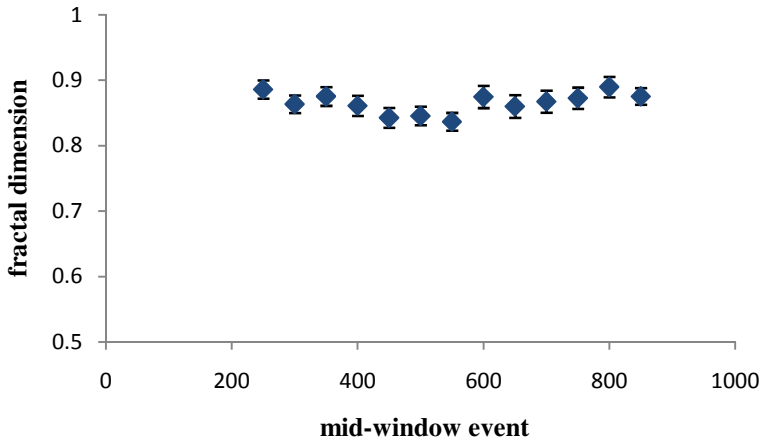

Fig. 6.18 Variation of fractal dimension with time, under constant stress conditions. A sliding window of 500 events is used for each calculation, advancing 50 events at a time. Events are defined as the central cell of adjacent simultaneously failing cells. Vertical bars indicate the standard error.

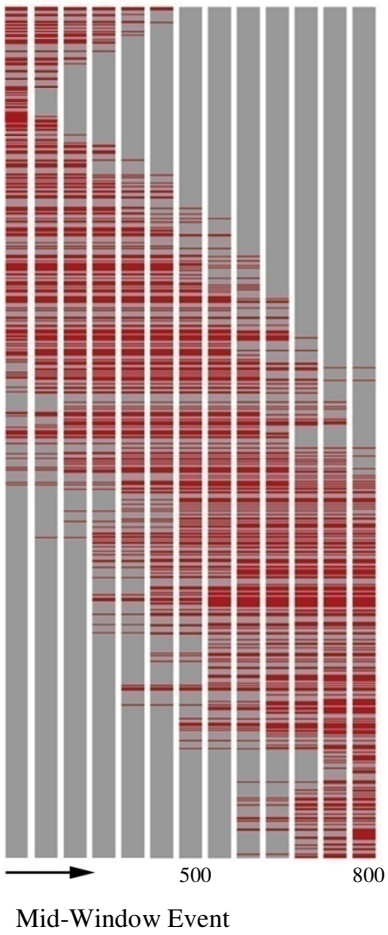

Fig. 6.19 Location of events (red) in windows used for calculation of fractal dimensions in Figure 6.18.

As would be expected for a non-fractal distribution, the correlation dimension also remains high (Fig 6.20). The correlation dimension is calculated as the negative gradient of the log-log plot of $C(r)$ against length scale r as defined in Equation (6.12). An example of this linear log-log plot, for the D-values in Figure 6.20 is shown in Figure 6.21. A good linear fit is observed, however limitations due to the model size restrict this analysis to only one order of magnitude of length scale r.

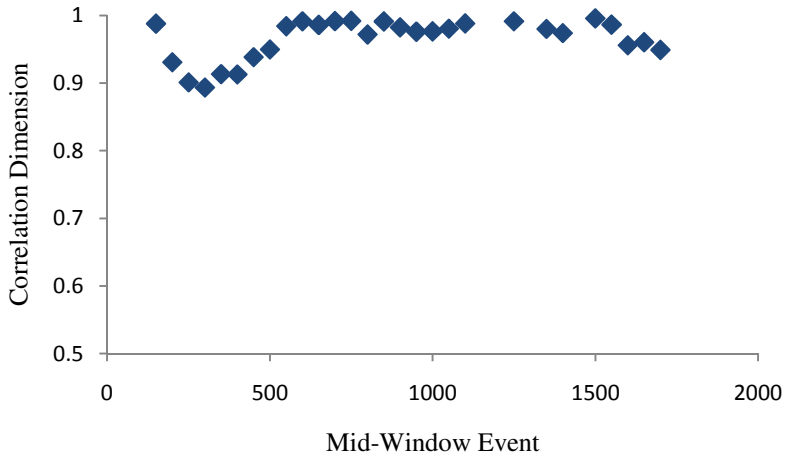

Fig. 6.20 Variation in correlation dimension with time (as described in (6.13)), under constant stress conditions. A sliding window of 300 events is used for each calculation, advancing 50 events at a time. All failed cells are included as event locations.

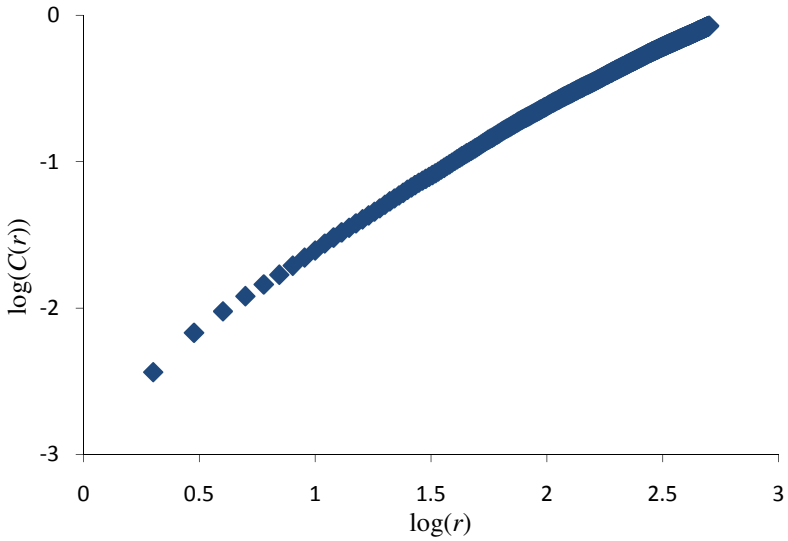

Fig. 6.21 Log-log plot of the proportion of data points within linear distance *r* of each other. The negative gradient gives the correlation dimension.

The evolution of events in Figure 6.19 appears to follow the trend of an advancing crack and this is frequently seen in the model. Assessing the effect of this migration of events on fractal dimension, D_E was calculated for two different cases; fracturing dominated by the growth of a single primary crack (Fig. 6.22a), and the development of multiple cracks throughout the array (Fig. 6.22b), which can also be observed in the model. Figure 6.23 shows the variation in fractal dimension for the two cases shown in 6.22. Both follow a similar, gradual increase to failure in D_E, but the values for the single crack growth are consistently greater than in the multiple crack case. This fits with the hypothesis that high fractal dimensions may be produced by the concentration of events around an advancing crack. However, the fact that both cases show values close to one implies approximately non-fractal distributions.

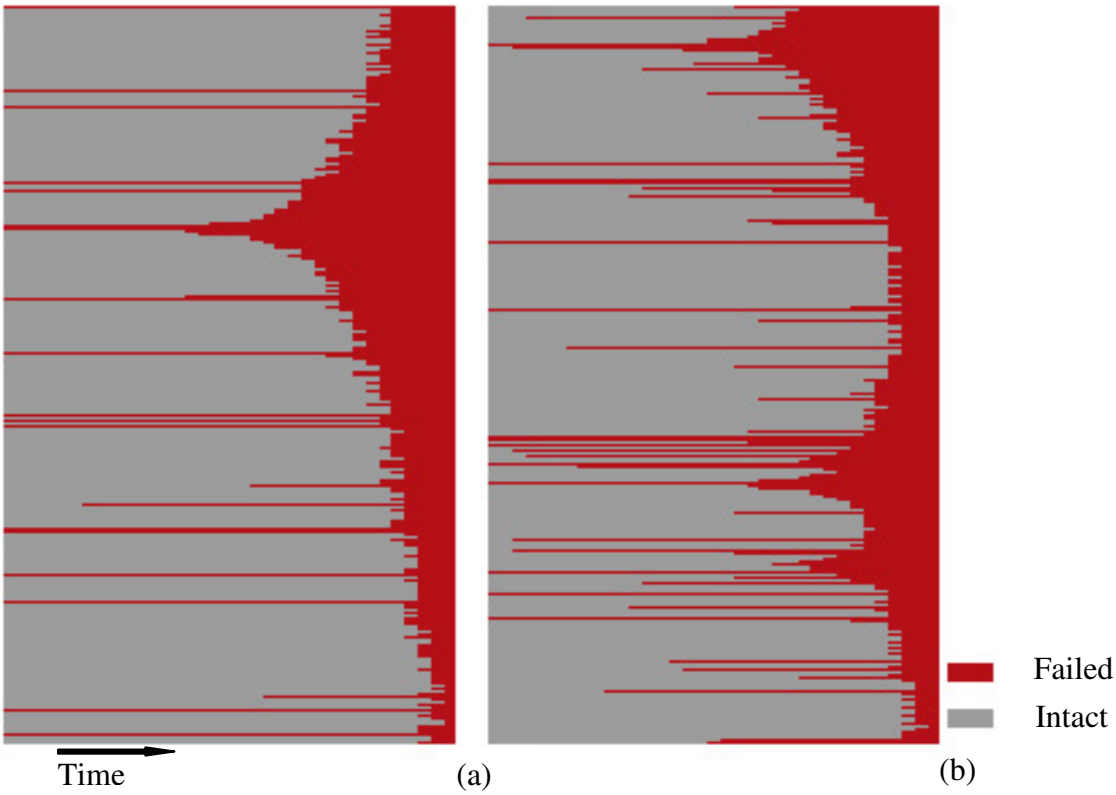

Fig. 6.22 Evolution of a one-dimensional array of 1,000 cells with time. (a) Failure is dominated by the growth of a single, primary fracture. (b) Multiple cracks grow simultaneously.

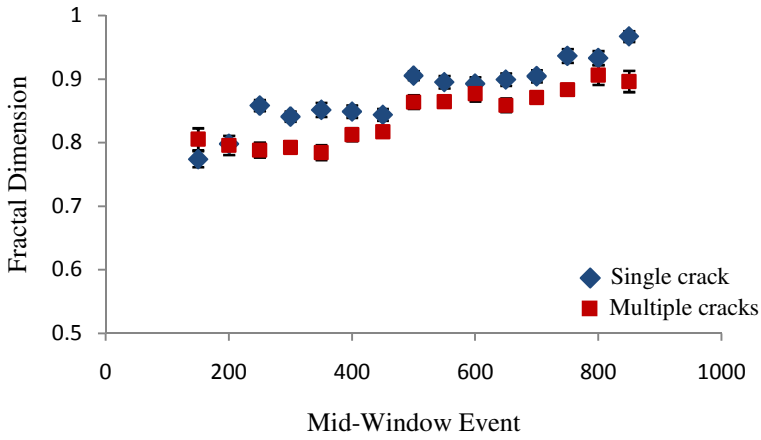

Fig. 6.23 Variation in fractal dimension D_E with time, under increasing stress conditions. The two data sets compare D_E for the growth of a single, dominant crack (blue diamonds) and multiple cracks (red squares). Vertical bars show standard errors.

The location of events will also clearly be affected by the geometry of initial cracks in the model. This can differ through the number, length distribution and location of failed cells. The results shown so far are from models with a random distribution of initial cracks. To assess the effect of this on the apparent trend of random uniform spatial distribution of events, D was also calculated for an initial array containing a fractal geometry of failed cells. Cracks were located using a Cantor dust set, which is developed through continually removing the middle third of a line segment (e.g. Falconer, 1990). This set, and therefore the initial trace of cracks in the model, has a fractal dimension of $\ln 2/\ln 3$, approximately 0.63. The fractal dimensions recorded remain high, generally in the range 0.7 – 1.0 (Fig. 6.24). A general increase in D leading up to failure is also often observed.

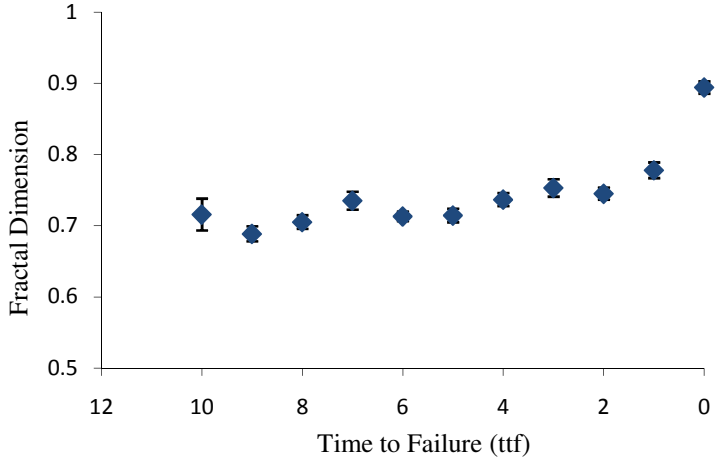

Fig. 6.24 Variation in fractal dimension D_E with time, under increasing stress conditions and a fractal geometry of initial cracks. Vertical bars show standard errors.

In addition to analysis of the spatial distribution of seismic events, studies have looked at the temporal clustering of earthquakes (e.g. Vinciguerra et al., 2001). Occurrence of data in discrete time periods prevents this type of analysis for the one-dimensional model, because there is no distinction of time lapse between individual events.

6.3.2 Fault length

As well as investigating the distribution of seismic events, many studies have also examined the geometry of fault lengths. Bonnet et al. (2001) contains a review of numerous experimental, numerical and field studies. Various factors have been

identified as affecting the distribution of lengths. In experiments, Krantz (1983) showed that an increase in applied stress increased the proportion of longer microcracks. The presence of fluid in specimens can also influence microcrack lengths (Hatton et al., 1993) with a higher fluid content leading to relatively more small cracks. Davy et al. (1995) found an exponential distribution of lengths in experiments where deformation was distributed uniformly, and power law during localised deformation. In numerical simulations an exponential distribution was observed during early deformation, becoming power law once fractures began to interact (Cowie et al., 1993). Power law distributions of fault lengths have also been observed in the field, including those from a fissure swarm in Iceland (Gudmundsson, 1987), and active surface faults in the United States (Hatton et al., 1993).

A power law fault length distribution can be described by:

$$N(l) \propto l^{-D_l} \tag{6.15}$$

where $N(l)$ is the number of faults of length greater than l. Fault length or area is related to seismic moment and magnitude (Kanamori & Anderson, 1975). Therefore this fractal dimension D_l for fault lengths can be related to the magnitude dependent *b*-value (e.g. King, 1983; Main 1988):

$$D_l = \frac{3b}{c} \tag{6.16}$$

c is a constant, usually given by $c = 3/2$ for tectonic events or $c = 3$ for small events such as acoustic emissions in the laboratory (Kanamori & Anderson, 1975). Main (1988) describes the reduction of D_l to a critical value of $D_l = 1$ as a method for failure forecast. A drop in the exponent is due to the natural tendency for larger cracks to grow more rapidly and have less chance of arrest. By Equation (6.16), this correlates with the drop in *b*-value reported before failure.

Crack length distribution was recorded in the model for both constant and increasing stress conditions, with similar results observed in both cases. Again, the geometry of initial cracks assigned in the model will have an effect on the development of the distribution. Figure 6.25 shows a typical log-log plot of the number of cracks $N(l)$ of length at least l, used for the calculation of fractal dimension D_l. Linearity generally holds over at least one order of magnitude even when the initially failed cells are assigned entirely at random. Relatively fast growing primary fractures may account for the departure from a linear trend at upper length scales although limits of scale in the model will ultimately restrict the number and magnitude of cracks of a medium to long length. Boundary problems are also an issue for fault length distributions studied in the field where the margins of a sampled region are more likely to intersect longer fault lines, causing censoring effects, or a biased choice of sample region in order to include or exclude large faults (Bonnet et al., 2001).

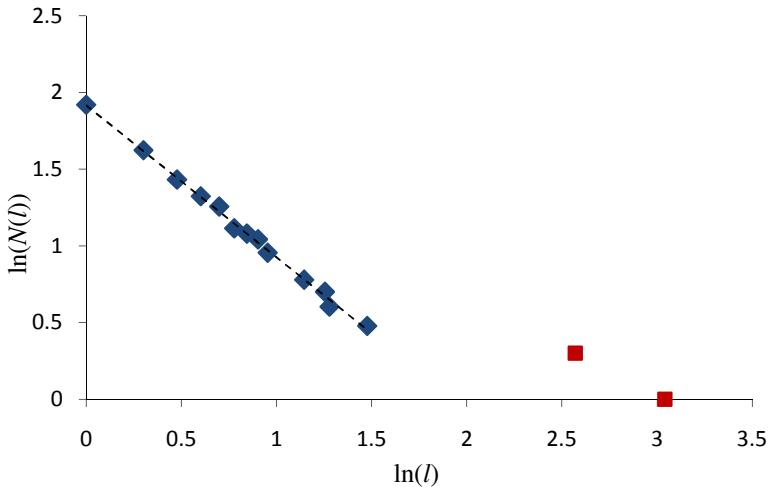

Fig. 6.25 Log-log plot of crack length distribution in a one-dimensional array subject to an increasing applied stress. $N(l)$ is the number of cracks greater than length l. The fractal dimension D_l is given by the negative gradient of the linear trend and is calculated over data points where linearity holds (blue diamonds). $D_l = 0.99$.

For the one-dimensional model, D_l was compared to the seismic b-value (Fig. 6.26), which was calculated for magnitudes measured both by the length of adjacent simultaneously failing cells and the length of adjacent current and existing failures, as described in Section 6.1.1. The length distribution exponent D_l appears to follow a general decreasing trend with time, falling to $D_l \sim 1$ just prior to failure. Where b is

measured by the length of adjacent failing cells (Fig. 6.26a), the two parameters vary in proportion, as Equation (6.16), until D_l shows a more marked decrease prior to failure. However, the constant of proportionality gives a value $c \sim 6$ in (6.16), significantly greater than the expected value of $c \sim 3$. A larger value of c reflects a relatively high b compared to field and laboratory values. D_l is calculated for all cracks in the model and therefore incorporates the entire history of activity as well as current failures while the b-value is measured for current events only. By corresponding magnitude values to the length of current failing cells adjacently linked by existing failures, this encompasses a measure of previous activity into the b-value and the two parameters b and D_l become more comparable. Prior to the pre-failure drop-off in the length dimension, $D_l \sim b$ as proposed for small scale faulting (Kanamori & Anderson, 1975).

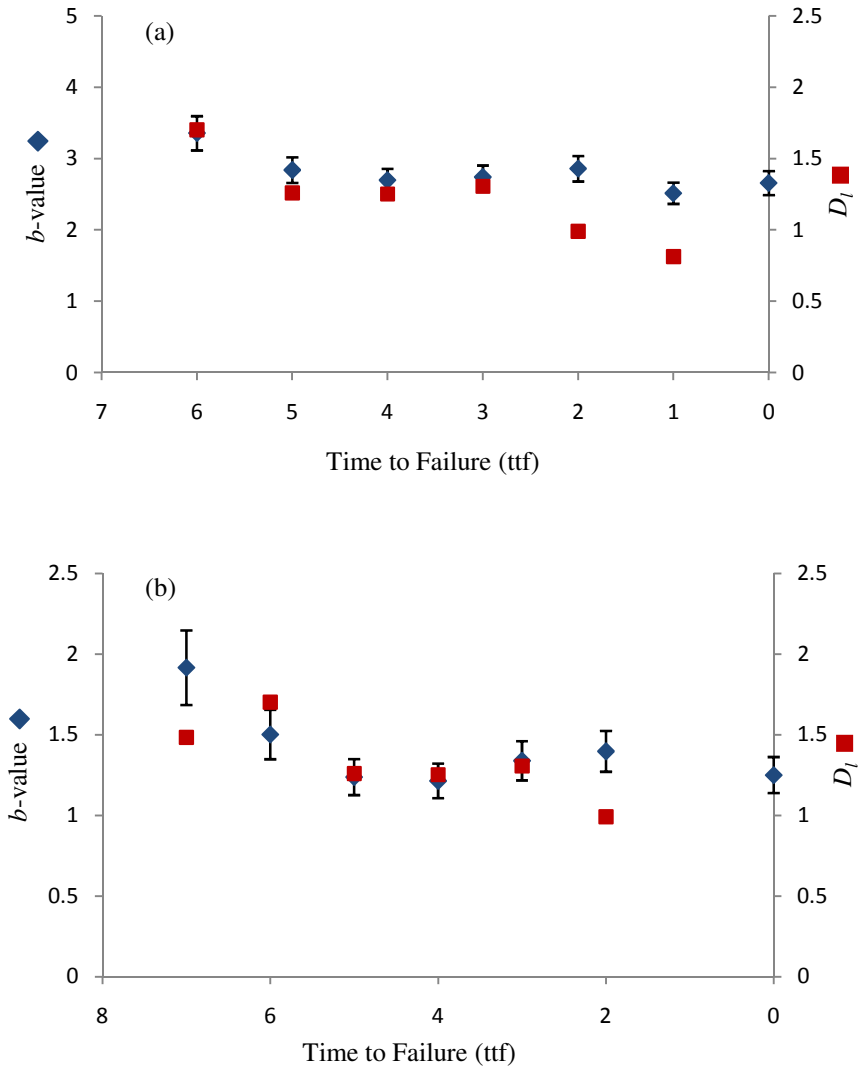

Fig. 6.26 Variation in seismic *b*-value (blue diamonds) and fractal dimension D_l (red squares) with time, under increasing stress conditions. Magnitude values used to calculate *b* are derived from (a) the number of adjacent simultaneously failing cells and (b) the number of adjacent current and existing failed cells. Note the change in scale for *b*.

6.4 Chapter Summary

The seismic *b*-value associated with tectonic earthquakes is generally found to lie close to one. The parameter is often observed to be greater than this, $b \sim 2$ or 3, in areas surrounding volcanoes. High material heterogeneity and high local stress may contribute to the anomalously high *b*-values. A minimum in *b*-value has been observed prior to failure at volcanoes and in fracture tests in the laboratory. In the one-dimensional model, b lies in the range $1 < b < 3$, and decreases towards the point of failure. A similar trend is observed for both increasing and constant stress conditions. Further work to identify a critical lower limit is necessary to fully utilise the *b*-value as a forecasting tool.

Fractal analysis is used to quantify the distribution of fault lengths or earthquake locations in the field. In the one-dimensional model a fractal dimension describing the location of all failed cells in the array, and a fractal dimension associated with the location of events with time were calculated. The former naturally tends to one at the point of failure. The latter also appears to increase towards a value of one prior to failure, although the trend can also start from a value as high as $D_E \sim 0.9$. The log-log plots used to calculate the dimensions show a good linear fit in all cases. The distribution of crack lengths in the model also follows a power-law relationship. The associated fractal dimension is proportional to the seismic *b*-value over a varying time interval in the model run. However, the constant of proportionality is greater than that expected from theoretical results.

7. Discussion and conclusions

The aim of this research was to improve understanding of the fracture processes occurring within a volcano and, thereby, to provide a physical basis for patterns of accelerating volcano-tectonic seismicity before eruptions. During an interval of weeks or more, the rate of VT events is commonly observed to increase exponentially with time and, at least at subduction-zone volcanoes reawakening after centuries of repose, this increase may evolve into a hyperbolic (faster-than-exponential) increase about two weeks before eruption (Kilburn, 2003; Kilburn & Sammonds, 2006). The prevalence of only two trends suggests that rates of crustal fracturing may occur under a small range of conditions and, consequently, may be amenable to analysis using a model that requires only a small number of key conditions to be satisfied.

As a result, a numerical model has been developed for which cracking is driven purely by stress concentration at crack tips, and interaction between neighbouring cracks. Different external loading conditions were considered, predominantly a constant applied load and a load that increased gradually with time. In addition, the material properties of the simulated rock mass could be considered as initially homogeneous or heterogeneous. Importantly, none of the simulations was required to end in bulk failure.

The simulation has been developed in a simple 1D setting. However, this simple model manages to capture the essential features of rock cracking and so remained the focus of this study.

Key results of the 1D simulation are that:

1. Event rates tend initially to increase exponentially with time.
2. Exponential increases in event rate can evolve into hyperbolic trends.
3. Exponential trends are controlled by the activation of an increasing number of cracks, whereas hyperbolic trends are determined by the interaction of major cracks that merge together.
4. Hyperbolic trends tend to emerge from a model with initial flaws more closely spaced than those that produce a purely exponential trend.
5. The preferred precursory trends remain the same, independent of loading conditions.
6. The magnitude-frequency distributions of model events follow a power-law relation, consistent with the Gutenberg-Richter law.

7. Event rates tend to decrease immediately prior to failure, due to limitations on remaining intact cells in the array.
8. A small proportion of simulated trends show precursory patterns that differ from the expected combination of exponential and hyperbolic increases.

The first six results are consistent with the common patterns of VT precursors observed in the field (Voight, 1988; McNutt, 2005). The agreement between model and field data supports the view that precursory VT event rates are determined by a combination of fault activation and of fault growth and linkage (Kilburn, 2003). It also suggests that the 1D simulation yields realistic results. Accordingly, the final two results, of a pre-failure drop in event-rate and alternative precursory trends, might yield insights into additional processes that may be occurring among potential VT precursors to eruption. Such processes are discussed below, together with their implications for making decisions during volcanic emergencies.

7.1 Model limitations

The 1D model itself has been subjected to a relatively broad sensitivity analysis. A large-scale analysis would require many more simulations of the model, and was therefore deemed too computationally expensive. Further work into establishing properties such as the linearity of output variables or the interaction of input factors may highlight possible interesting areas for further investigation. Identifying the most important factors is useful for establishing which commonalities between volcanoes may lead to similar precursory trends as well as the extent of these similarities. Information obtained on the sensitivity of the model to the various inputs will improve with the number of runs made. A Monte Carlo simulation would ideally involve running a model on the order of 10^4 - 10^6 times. Again however, in this case the model was too computationally expensive to produce such a large amount of data.

The discretisation involved in using a grid-based model for the fracture process is also an issue that arose in various parts of this research. Continuous modelling methods such as finite element analysis have seen wide applications across both engineering and geology problems (e.g. Manconi et al., 2007; Parsons et al., 2006). This type of approach brings with it numerous other complexities though and again a balance must be reached between the degree of accuracy required from a model and the relative simplicity. For the purpose of the research carried out here it was not necessary to produce an extremely accurate representation of the propagation of a crack, but more to establish the effects of interaction between two neighbouring cracks and the subsequent effect of this on an entire population of cracks. The discrete growth of cracks within the model also affected the analysis of seismic event magnitude distributions. A more varied distribution of magnitudes could be attained by dividing cells into smaller segments, and introducing a stochastic element of how many of these segments are to be used for a magnitude calculation. However, even though it gives a limited range, it is useful to have a measure of magnitude that can be directly linked to a physical parameter in the model. In addition, the grouping of recorded magnitudes in the field also leads to a discrete range of values.

The one-dimensional array used to represent the progressive failure of the edifice is of course a vast simplification of the modelled process. As described in Chapter 4, the interaction and coalescence of fractures and faults within host rock of a volcano will occur by shear faulting between neighbouring, non-aligned fractures rather

than simple tip-to-tip extension. Accordingly the model represents the development of failure within the edifice rather than the formation of a purely extensional fracture. The model assumes magma ascent as a passive action once the edifice is sufficiently fractured so as to no longer create a limitation on the movement of magma. However, little mention has been made of the proposed subsequent ascent of magma to the surface, and a much greater understanding of this must be developed in order to present a complete model of eruption mechanics. In particular, the feedback process between the propagating magma and host rock deformation is an important factor in the physics of magma ascent. Once magma begins its ascent, pressure in the magma chamber would be expected to fall. As a source of loading on the surrounding host rock, this may in turn lead to a reduction in the rate of cracking and seismicity. This drop-off in seismicity prior to eruption is observed in the field and is represented in the model by a redistribution, or loss of stress due to a limit on the number of remaining intact cells.

This model of edifice failure and magma ascent assumes that once a connected network of faults and cracks has formed, magma will follow its course to the surface. The creation of a fully connected conduit, linking a magma chamber to the surface is again a highly simplistic concept. Field observations suggest that magma-driven cracks propagate in a direction of principal stress and do not necessarily follow cracks and faults that already exist within the edifice. It must therefore be noted that while the 1D model reproduces recorded precursory seismicity by focusing on the interactions of a network of cracks, it cannot necessarily be assumed that this process leads directly to the creation of a conduit for magma ascent. Feedback and interplay between the two processes may instead be considered. Shear faulting and the coalescence of fracture networks may occur radially throughout the edifice, around a central axis of deformation, due to the loadings described previously. The 1D model then still represents a progression towards, and a measure of failure. However, the failure is representative of, rather than a direct cause of the creation of a pathway for magma ascent. Once the magma chamber ruptures, propagation of a magma-filled crack may still cause shear faulting or cracking within the surrounding rock due to redistribution of pressure or of geothermal fluids and volatiles. The interaction between fluid movement and fracturing is discussed in further detail in Section 7.2.3. Eventually this type of cracking and faulting, and therefore the related high-frequency earthquakes, falls away as pressure is released and the seismicity observed becomes lower in frequency, representative of the movement of magma through the volcano.

Further studies are required to explore this idea in more depth and would need to focus on details such as the utilisation of accurate location and source mechanisms of precursory volcano-tectonic earthquakes, and field, experimental and modelling approaches to understanding the interplay between faults and dykes within volcanoes.

7.2 Applications of the model to investigating the behaviour of volcanoes

The results of the 1D model are consistent with field observations that volcanic eruptions are commonly preceded by exponential increases in VT event rate with time. They also show that exponential trends can evolve naturally into hyperbolic increases in VT event rate. Such agreement between field and model results suggests that the model has captured the essential features of fracturing at volcanoes. An immediate practical implication is that the model supports interpretations of VT eruption precursors in terms of the activation and interaction of a population of fractures in subvolcanic crust and volcanic edifices. Two further implications are (1) that the less-common variations in model event rate that do not follow exponential or hyperbolic trends may also have analogues among the full spectrum of field precursors, and (2) that the model may be extended to investigate conditions for non-eruptive fracturing at volcanoes. The last two implications are of special interest at volcanoes that show unrest after long repose, because these are the volcanoes for which the least field data are available. Consequently, it is possible that some of the less-common trends in the model have yet to be identified in the field. The following sections therefore discuss how the numerical model might be used to guide future investigations into patterns of volcanic unrest.

7.2.1 Decreases in event rate before eruptions

A recurring feature in the model is the drop-off in event rate observed immediately prior to bulk failure. This has been attributed to the limit on remaining intact cells once the whole array is nearing failure. However, it is interesting to consider whether this kind of effect may be related to physical processes occurring in the field, due to release of magmatic pressures, either before eruptions or during false alarms. This section addresses pre-eruptive decreases; false alarms are considered in Section 7.1.2.

The 2000 eruption of Usu in Japan (Zobin et al., 2005) and the 1994 eruption at Popocatepetl in Mexico (De la Cruz-Reyna et al., 2008) provide two examples of pre-eruptive decreases in VT event rate. At Mt Usu, following an acceleration in seismic event rateover a period of approximately three days, the rate then began to decline, with the onset of eruptive activity occurring more than 12 hours after the peak in seismicity (Zobin et al., 2005). The model developed here presents the ascent of magma as an entirely passive process once an open pathway has been created. In addition to the

limits on intact cells, it is therefore also possible to imagine a time-lag between the formation of this open fracture network and the first emergence of magma at the surface determined by the rate of magma ascent. The failure forecasting methods described throughout this thesis suggest that the onset of activity coincides with the peak point of the observed precursor. However, it is also possible to imagine and to explain a scenario where although the forecasting method may correctly predict the time of failure, a decrease in the precursor may be observed prior to this.

A longer period between a swarm of seismic activity and the onset of eruption has been observed in the field. De la Cruz-Reyna et al. (2008) describe four phases of activity leading up the eruption of Popocatepetl in 1994, activity that followed almost 70 years of rest at the volcano. The increase in seismicity recorded in the years to months before the eruption are attributed to a series of magmatic injections, thermally-induced cracking and volumetric increase in the density of cracks and fractures caused by a concentration of stress. This latter process produced the type of acceleration in volcano tectonic activity analysed in this research. Extrapolation of a hyperbolic fit to the seismic energy released during the first three phases of activity provides a good forecast to the onset of the eruption. However, the observed acceleration in seismic activity shows a significant decline in the months prior to the eruption and the distribution of hypocentres becomes much more greatly dispersed. De la Cruz-Reyna et al. (2008) speculate that this final stage of activity may be indicative of a redistribution of built up stress throughout a greater volume of host rock as the effectively closed volume experiencing the acceleration in seismicity and fracturing is no longer able to maintain it. In essence this is similar to the process causing a drop in event rate in the one- and two-dimensional models, where there is a limit in the ability of the array to maintain the level of failing cells.

7.2.2 False alarms

The growth of cracks in the one-dimensional array, as well as in rock in the laboratory and field, creates a positive feedback. Stress intensity at the crack tip is an increasing function of the size of the crack. Therefore with nothing to prevent further growth, once a crack begins to extend, it grows rapidly until the entire array, block of material or volcanic edifice has failed. In nature however, this is clearly not the case. There are many more intrusion episodes at volcanoes that do not lead to the eruption of magma at the surface, than those that do (e.g. Gudmundsson and Philipp, 2006). Therefore for a

model to accurately describe the failure mechanism that occurs within a volcano, it must be possible for an extending crack to arrest before bulk failure is reached. This model may then help to explain the still poorly understood mechanism creating false alarms at volcanoes.

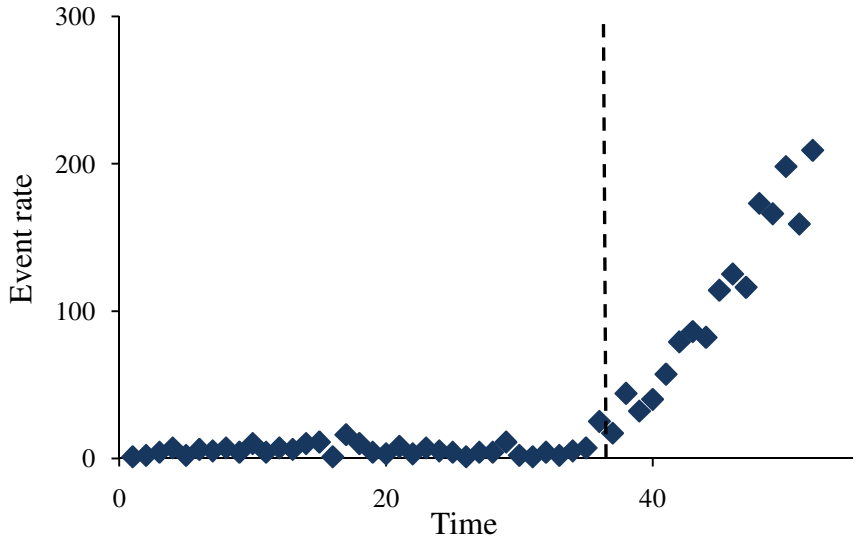

Fig. 7.1 Event rate with time for a one-dimensional array subjected initially to an increasing stress, which is then reduced by 50% and held constant. The dashed line shows the point at which stress is reduced. The event rate continues increasing until bulk failure of the array is reached.

Results shown in the thesis so far have focused on those cases when the model array fails. In the case of an increasing stress this will always eventually occur. For constant stress conditions, whether or not the array fails will depend on the chosen level of applied stress. In terms of improving understanding of false alarms at volcanoes, the cases when the model does not fail can also be of interest. In many cases, the location of initial cracks within areas of relatively high fracture toughness and a low level of applied stress results in a cessation of activity in just a few time steps. Under a randomly distributed fracture toughness, it was also observed that once a relatively large proportion of the cells had failed, it was likely that the array would progress to failure. Often, even if a drop in the applied stress was introduced, the density of fractures was sufficient to maintain the necessary degree of stress concentration at crack tips and to sustain the positive feedback of crack growth (Fig. 7.1). However, there are also a few cases when the event rate does die down after a drop in the applied stress. Figure 7.2 shows an example of two different model runs in which the applied stress is decreased

at the point indicated. In one case the model continued fracturing until the entire array had failed. In the second case, after an initial continuation of failing the event rate died down and finally stopped, with intact cells still remaining in the array. The similarity of the two trends, before one goes on to fail and one returns to equilibrium highlights the potential difficulty of distinguishing between these scenarios in the field. If the primary source of stressing in a volcano is the overpressure of a magma reservoir, the release of some of this pressure, for example in the form of an intrusion event, may lead to a relaxation, or at least redistribution of the regional stress. The one-dimensional model demonstrates that in such a scenario, increased seismic activity may eventually die down without the emergence of magma at the surface.

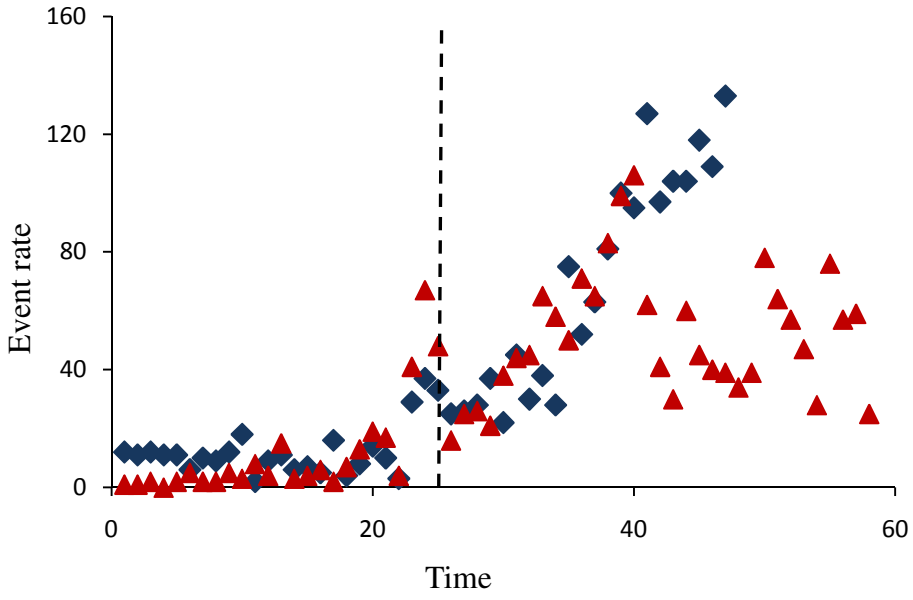

Fig. 7.2 Event rate with time for two separate runs of the one-dimensional model. The models are subjected initially to an increasing stress, which is then reduced by 50% and held constant. The dashed line indicates the point at which stress is reduced. After this drop, fracturing continued in one run of the model until bulk failure of the array (blue diamonds), while in the second run the event rate eventually died down and the model remained in an intact state (red triangles).

As well as a reduction in stress and therefore stress intensity, the second factor that may lead to the arrest of a propagating network is an increase of critical fracture toughness. A random fracture toughness distribution means that even if a propagating crack runs into a region of relatively high fracture toughness, it is likely that this region

will cover no more than one or two cells distance from the crack and therefore if the crack is long enough its range of influence may also reach to the less resistant cells beyond. Therefore once longer cracks have formed it is very difficult to prevent failure of the entire array. While mechanical properties of rock making up a volcano are likely to be highly heterogeneous, with stiffness of different rocks ranging over four or five orders of magnitude (Gudmundsson & Philipp, 2006), it is also reasonable to imagine that there will be some degree of local homogeneity in the layers making up the edifice. Gudmundsson and Philipp (2006) found that a dyke intrusion leads to an eruption only if a homogeneous stress field exists through the edifice. They used finite element analysis to investigate the effect of layers with various mechanical properties on the propagation of a dyke and found that while stiff layers favoured propagation, soft layers tended to arrest the dyke. Generally, a dyke reaches the surface by stress-field homogenisation, a process that reduces the stress difference between layers of host rock. When a dyke reaches the contact between adjacent layers it may become arrested or spread laterally to form a sill before either arresting or continuing its vertical propagation (Gudmundsson, 2003).

A layering of fracture toughness is a very simple constraint to build into the existing crack interaction model. In the one-dimensional case, the only option for a crack approaching a contact between two layers is to arrest or continue vertical propagation. However in two dimensions, with an adjustment of propagation rules within the array it would be possible to allow for horizontal spreading of a crack. In the case of a fluid filled crack, discussed below, this would then form a sill that in turn would alter the surrounding stress field further. This type of layered model could be developed into a stochastic tool for forecasting the proportion of intrusive to eruptive episodes at a volcano. Running numerous simulations, varying the distribution of initial cracks or external stress conditions provides a count of how many instances the array progresses to failure and how many times a swarm of activity occurs but then dies down without bulk failure. This type of study would give an indication of how often non-eruptive swarms might be expected at a volcano. It is also essential to be able to identify which these swarms are. Analysis of observable parameters such as earthquake locations or event rate trends may identify potential tools for such a forecasting capability. For example, with the potential for accurate event location it may be possible to identify a switch of location of concentrated activity as a major propagating crack becomes arrested.

7.2.3 Modelling intrusions

Failure of the one-dimensional model is based solely on fracture mechanics of a brittle material and assumes that it is this failure of a volcanic edifice that is the controlling factor on the ascent of magma to the surface (Kilburn, 2003). As discussed in Section 7.1, an interesting further development of the model would be to consider the effects of magma movement on the fracture network, once created, whether within or removed from the network. It is widely accepted that there are significantly more intrusion events at volcanoes, involving the propagation of a magma-filled dyke, than there are eruptions. This is therefore an important area of research and many numerical, empirical and theoretical studies have been carried out on the dynamics of fluid filled cracks and of dyke propagation. This section looks at the role of fluid within the fracture network, although this may be geothermal fluids rather than magma.

Allowing for fluid movement within the model is likely to introduce complex interactions with seismic activity. Rivalta and Dahm (2004) describe this interaction in a heavily fractured edifice. Dyke intrusion causes further cracking of the host rock, which in turn becomes weakened allowing for further propagation of the dyke. This type of positive feedback, leading eventually to bulk failure, has been previously described in terms of crack length dependent stress intensity factors. The effect of a propagating dyke on surrounding cracks is also akin to the interaction effects in the one- and two-dimensional models. Reaction of surrounding material to a fluid filled crack will depend on properties of both agents, such as the mechanical properties of the host rock and the buoyancy or volatile content of the magma. Roper and Lister (2007) described a fracture toughness parameter that incorporates the resistance to viscous flow as well as fracture. Along the length of a dyke, away from the tip, induced strains are on the order of the dyke's width to length ratio and are therefore generally small (Rubin, 1995).

If an intrusion of magma does not lead to enhanced fracturing of the host rock, it will still cause an increase in size of the channel it enters and can therefore result in observable ground deformation at the surface (Rubin, 1995). Two dimensions allow a factor of area change to be incorporated into the model, which can be extrapolated to look at volume change and deformation associated with failure in the edifice. Along with seismic activity, ground deformation is another promising tool for eruption forecasting and when taken in partnership with seismicity can help to create a clearer picture of activity beneath and surrounding a volcano. Technological advances in this

area have been great over the past few decades with many studies on volcanoes now using techniques involving InSAR (Interferometric Synthetic Aperture Radar) or GPS (e.g. Baer et al., 2008; Palano et al., 2008). Ground deformation studies can be useful in forecasting eruptions, identifying dyke intrusions and also for monitoring magma movement during an eruption (Kohno Y. et al., 2008).

Pressure source models translate volumetric change observed on the surface to sub-surface changes within the Earth's crust. Mogi's (Mogi, 1958) magma intrusion model is often used to correlate a volume change in a magma chamber to ground deformation. This model assumes a spherical magma body at depth, within an elastic body of country rock. It has also been suggested that mechanical properties of rock have a significant effect on displacements and deformation and that therefore heterogeneity is an important factor to allow in such a model (Manconi et al., 2007). The two-dimensional model described in chapter 7 was developed to consider the percolation of a damaged array and the properties of the resulting network. However, this model could be expanded further to also incorporate intrusions of magma into the fracture network and the subsequent increase in area of the array. The simplicity of the grid-like model allows for features such variation in area change with material properties. Clearly further complexities would also be necessary within such a model to incorporate local stress variation due to intrusions and pressure sources (Gudmundsson, 2002), and the effects of an expanding grid space. Intrusions may also have a more global effect across the grid. Toda et al. (2002) suggested a linear relationship between stressing rate induced by an intrusion event and remote seismic activity. A separate study on the same intrusion event in the Izu Islands, Japan uses this relationship to propose a method for establishing whether dyke expansion is occurring as a passive reaction to fracturing or due to the intrusion of magma (Rivalt & Dahm, 2004).

Modelling a fluid flow involves a much greater degree of complexity than is currently built into the fracture model. However, just by introducing additional stress perturbations brought about by magmatic intrusions and allowing these effects to propagate in such a way as to be representative of a viscous flow, the first order effects of dyke intrusions on a fracture network can be approximated. Allowing for volume change in the model as these intrusions occur could also be useful in providing a basic link between observed ground deformation and seismicity with activity caused by magma movement within a volcano.

7.2.4 Time-dependent rock failure

Greater complexity may also be built into the model by considering a time-dependent element, within the discrete time steps of stress redistribution. Currently each cell can exist in one of only two states, failed or intact. In theory a cell can remain at a very low level of stress right up until the time step during which it fails, as a major crack extends close enough to significantly increase the stress intensity of the cell. Alternatively, a cell adjacent to a crack tip may have a fracture toughness great enough to prevent the crack propagating until either an increase in remotely applied stress or a neighbouring crack advances close enough to cause interaction effects. In the latter case, although the cell does not fail immediately, it is nevertheless subject to a force that it would not feel if were completely isolated. Attempting to model if and when this cell may fail, and the crack propagate involves may introduce the concept of sub-critical crack propagation or use of a damage parameter. Sub-critical crack growth describes the extension of a crack at a stress intensity below its critical value and can be influenced by factors such as temperature, pressure as the presence of corrosive fluids (Atkinson, 1984), all of which can apply to a volcanic setting. Introducing the theory of damage mechanics allows the fracture of rock to be dealt with in a framework of continuum mechanics.

Main (2000) uses the concept of damage mechanics to look at time-dependent stages of creep in the Earth's crust, and to explain the foreshock and aftershock sequences of earthquakes described by Omori's law. Based on the constitutive equations of time-dependent crack growth, Main's model incorporates both a positive and negative feedback on rock failure, where local negative feedback occurs through strain hardening mechanisms. The occurrence of stress shadows will be discussed again in the following section. These various concepts of time-dependence can be built into the model by recording in essence a damage parameter for each intact cell. This may incorporate the number of time steps a cell is exposed to a stress intensity greater than the background remote stress, which would allow only cells surrounding a crack tip to experience any extent of damage, or a function of the ratio of stress intensity to fracture toughness thereby affecting all intact cells.

Modelling the host rock as a visco-elastic material would also create time dependent failure. The fracture mechanics currently applied to the model assumes brittle failure of rock is producing the volcano tectonic events recorded prior to eruption. Long period seismicity that becomes more common after the onset of eruption is associated with the movement of magma rather than brittle failure. Recent

studies suggest however that fracturing may not be confined to cool, brittle rock only. Tuffen at al. (2008) carried out high temperature fracture tests on lavas to investigate the possibility of seismogenic faulting along conduit walls, and within lava domes and erupting magma. Waveforms produced by the laboratory experiments showed both similar onset patterns and frequency content to volcano tectonic earthquakes. Looking instead at long period events, Neuberg et al. (2006) model the brittle-ductile transition of magma within the conduit where the low frequency seismicity is caused by the build up of shear stresses along the conduit wall as the magma ascends.

Seismogenic faulting of magma at shallow depths, either along the conduit walls or in lava domes, will generally only occur once a pathway to the surface has been largely created. It is therefore still reasonable to suppose that seismic activity used in the failure forecast methods described in this thesis can be assumed to come from the failure of host rock and the opening of a new fracture network. However as discussed above, the one-dimensional model of precursory seismicity produces a fall in volcano tectonic style events immediately prior to failure, and any attempts to improve the representation of the fracture and faulting development during this interval should take into account the possibility of high-frequency swarms produced by ascending magma itself. The effects of temperature on the fracture process at greater depths can also be incorporated into the existing model framework by looking at the effect of temperature change on fracture toughness.

It should also be noted at this point that many potential additions to the fracture model may become irrelevant when considering its ultimate function. The failure forecast method looks at the change in event rate and therefore requires data such as the number of events per hour or per day. Equally field data will often be presented in this way. Therefore the ability to model the time of events to a greater and greater accuracy becomes irrelevant. The discrete time scale used in the one-dimensional model reproduces observed data and is therefore essentially fit for purpose. Adding further complexities may not necessarily add any further utility to the model.

7.3 Modelling rapid changes in loading conditions

The fracture model has thus far been run under conditions of either a constant applied stress, using only the positive feedback created by the extension of cracks to induce further failure in the array, or a gradually increasing remote stress. When considering the mechanisms behind arrested failure and false alarms, a sudden decrease in stress was also applied. An area of potential future work would be to look at the application of a sudden, relatively large increase in ambient stress. Stress within a volcano is generally assumed to build up gradually by processes such as the increase in pressure within a magma chamber, or the exsolution of gases from ascending fluids. However, volcanoes can also react to dynamic and particularly static stress changes brought about by tectonic earthquakes. In recent years the idea of the transfer of stress during earthquakes, and the potential for the triggering of a volcanic eruption has been well publicised. It has been suggested that such triggering can cover time intervals from seconds to decades and distances from metres to thousands of kilometres (e.g. Freed, 2005). Static stress changes can lead to a triggered earthquake weeks or even years following an initial event. Effects diminish with distance from the slipped fault by some inverse function (Steacy et al., 2005). The one-dimensional model already incorporates a triggering mechanism in the sense that interaction between cracks can adjust local stress intensity. It is also possible to investigate the potential for interaction effects on a much larger scale.

It is very difficult to identify a definite causal relationship between a tectonic event and a subsequent volcanic eruption. There are several cases reported however where some correlation has been suggested between tectonic and volcanic activity (e.g. Cerro Negro, Nicaragua, La Femina et al., 2004; Vesuvius, Italy, Marzocchi et al., 1993; Merapi, Indonesia, Walter et al., 2007). A volcanic eruption may be induced by a variety of changes in the magma reservoir or conduit with, for example, both compression or dilation of a magma chamber capable of initiating volcanic unrest (Selva et al., 2004).

Coulomb stress transfer is often used as a measure of the increase or decrease in proximity to failure of a fault, following a change in regional stress (Toda et al., 1998). Studies using Coulomb stress change have been used to highlight potential risk areas for future earthquakes. McCloskey et al. (2005) calculated stress changes brought about by the magnitude 9.1 Sumatra-Andaman earthquake in December 2004. They highlighted

the contiguous Sunda trench as a real risk for future slip, with stress on the northern part of this segment calculated to have increased by 5 bars. Indeed this section did rupture in March 2005, creating a magnitude 8.7 earthquake and claiming the lives of about 2,000 people (Nalbant et al., 2005). This highlights the potential of stress triggering and in particular Coulomb stress forecasts in the area of seismic risk analysis. A similar style of forecasting tool, applicable to the effects of a tectonic earthquake on the increased probability of eruption at a volcano, would be a useful aid in disaster management.

Within the one-dimensional fracture interaction model it is possible to represent a step increase or decrease in the applied stress to represent a static stress change. Applying a Monte Carlo method, with parameters for mechanical properties suitable for the volcano in question, it is possible to model the conditions under which an earthquake may trigger an eruption, and the probability of this occurrence. With a more complex version of the model allowing for incorporation of magma and fluid movements, the effect of dynamic or static stress changes on the magma reservoir can also be modelled.

7.4 Decision-making during volcanic emergencies

A second aspect of the fracture model that could be developed is the investigation of potential warning times before an eruption. This would incorporate existing work on the characteristic time scales of exponential trends, the emergence of hyperbolic trends, and the relative probabilities of an eruption or false alarm. An important application is in the decision making procedure for civil authorities in the event of a volcanic crisis.

Probability plays a major role in eruption forecasting. This role has often proved to be quite controversial in terms of disaster mitigation and management. First is the problem of translating data such as observed precursors, historical knowledge and expert opinion into one figure representing the likelihood of the nature, location or time of the onset of activity. Once armed with this information, the next problem is what to do with it. For example, how high should the probability of activity be before an evacuation is called? This choice is ultimately weighted against the problem of how long a time interval is required for evacuation. If a large population lives on or around a volcano, it is vital that sufficient warning be given to allow a full and orderly evacuation. The overall decision in calling for an evacuation is therefore a trade-off between the relative certainty of an eruption occurring, and the time needed for a complete evacuation. Often this decision is made on a subjective basis, during the developing volcanic crisis. Such decisions may be aided by prior knowledge of the expected time scale of precursory activity.

Marzocchi and Woo (2007) proposed a probabilistic, cost-benefit strategy to provide a quantitative decision framework in a volcanic crisis. They look at a case study of an eruption at Vesuvius, Italy and the risk posed to the highly populated Bay of Naples, and the cost of mitigation measures against an acceptable level of risk for society. The decision is basically to evacuate or not to evacuate. In this economical framework this decision is made taking into account the potential cost of each action.

The discrete decision-making applied in this study assumes that sufficient time will be available to perform a full evacuation. An added complexity to the model is the more realistic continuous relationship between the loss risk and the time available for evacuation. A concept of the probable time frame available for evacuation is clearly also an important factor in the decision making process. Using theoretical models of time to failure forecasts can provide an upper limit on the potential time available for evacuation. If a hyperbolic increase is expected in precursory seismic event rate, an

upper and lower limit for time to failure is given by the proposed range in gradient limits, derived from physical and mechanical properties of a volcanic edifice. However, clearly this time interval must then be adjusted for the time already elapsed from the start of the increasing event rate to the point at which the trend is recognised. Similarly, the concept of the characteristic timescale in an exponentially increasing event rate can provide an estimate of time to eruption, again shortened by the time taken to identify the event rate trend and timescale. For the purpose of creating a decision making tool before the event of a potential crisis, it is useful to have some information on the probable chances of the various different timescales proposed by the theoretical models, and previous records of activity.

A Monte Carlo simulation of possible precursory activity would provide just that. The simulation of 300 runs described in Chapter 4 shows the range in output distributions from a variation in several different input factors. By allowing for different distributions of the various input factors, this type of simulation can be made as general or specific as required, and can show the potential variation in output trends even for a relatively constrained problem. As well as providing a range, the large number of runs also provides a valuable indication to the relative likelihood of occurrence of each of the outputs (Fig. 7.3). In particular, it can provide a probability distribution of the time to failure and this information could then be used to augment the respective cost and benefit associated with decision-making in the time of a crisis.

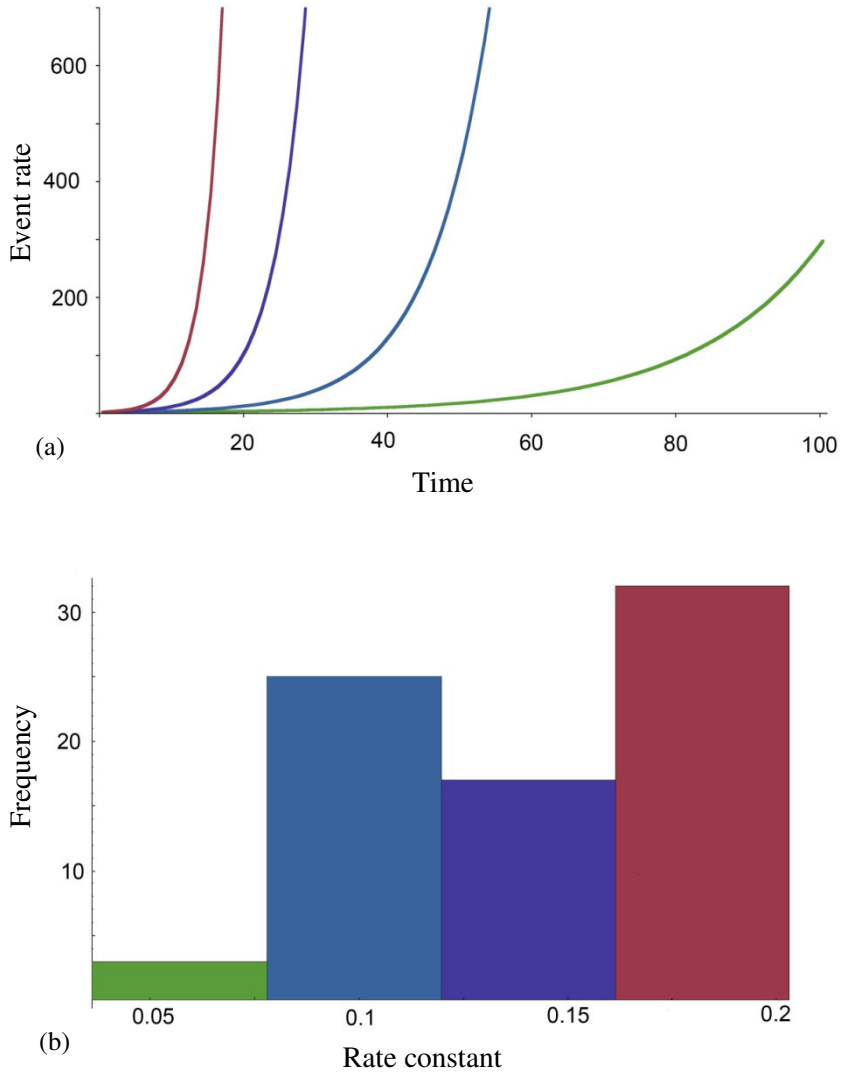

Fig. 7.3 (a) Four characteristic exponential trends and (b) the frequency of exponential sequences from the Monte Carlo simulation described in Chapter 4 when grouped with the closest characteristic trend.

7.5 Alternative methods for forecasting eruptions

Alternative forecasting methods can also be incorporated to aid in identifying between precursory accelerations in seismicity and non-eruptive swarms. In the event of an approaching volcanic crisis, applying a suite of techniques to accumulating observations will inevitably provide more information on which to base forecasts and decisions. In addition to seismic event rate, various other methods built from failure of the volcano have been developed. For example, the volume of rock that must be fractured for an eruption to occur can provide a characteristic threshold for the seismic energy released (De la Cruz-Reyna, 2008). Cumulative Benioff strain was used to forecast eruptions at Mount St. Helens following the cataclysmic May 1980 eruption (Malone et al., 1983). The longer the inter-eruption interval, the longer the precursory increase in seismic energy release. This relation was therefore suggested as a method for forecasting the time of approaching eruptions. Zobin and Jiménez (2008) suggested a relationship between the length of precursory seismicity and the magnitude of the eruption at volcanoes erupting after more than 100 years quiescence. A longer period of seismicity was associated with a lower VEI index at six different volcanoes studied.

Many methods that appear to provide a promising tool have only been tested in producing hindcasts, with few reports of successful, true forecasts of the onset of volcanic activity. It has also been suggested that in a time of crisis it would be very difficult to distinguish between the type of seismic signals incorporated into the failure forecast methods. By their very nature eruptions following a long repose interval happen relatively rarely. Their activity is often explosive in nature, producing eruptions of VEI ≥ 5. Eruptions of VEI 5 are expected roughly once a decade, while those with VEI 6 only slightly more often than once a century (Woo, 1999). Therefore there is a lack of field data to test such forecasting tools against and in this situation the use of empirical and numerical models, such as that developed here, becomes vital in order to identify the most plausible models to apply in forecasting these relatively infrequent, but highly hazardous eruptions.

7.6 Conclusions

The one-dimensional crack model is based on a fracture mechanics representation of failure within a volcano. It produces results consistent with field observations, especially before eruptions at subduction-zone volcanoes reawakening after long repose. Accordingly, the model supports interpretations of VT eruption precursors in terms of the activation and interaction of a population of fractures in subvolcanic crust and volcanic edifices. In particular, the model suggests that:

- Exponential trends are controlled by the activation of an increasing number of cracks, whereas hyperbolic trends are determined by the interaction of major cracks that merge together.
- Variations in the application of a remote stress field have a lesser effect on failure rate than the local ratios of stress intensity to fracture toughness.
- Failed eruptions may be caused by a redistribution of stresses, or by a heterogeneous edifice.
- Characteristic timescales associated with failure rate are indicative of the volume of rock to fracture. In the absence of definite criteria for failure forecasting, the characteristic timescale can provide a limit on the expected time to failure.
- A Monte Carlo simulation of the failure of a volcanic edifice can provide probabilistic data for an expected time to failure, as well as highlighting possible precursory trends to be observed before future eruptions.

To build on these results, future studies can extend the model to two and three dimensions, develop analyses of non-eruptive accelerations in VT event rate, and investigate the behaviour of deformation parameters in addition to event rate alone. In combination, such studies will help to improve interpretations of volcanic unrest and, as a result, will also enhance decision-making procedures during volcanic emergencies.

Appendices

Mathematica code to run 1D model of crack interaction:

```
<< Statistics`DescriptiveStatistics`
<< Statistics`ContinuousDistributions`
gaussdist = NormalDistribution[0, 1];

(* user input for length of array *)
n = Input["Enter number of elements"];

(* user input for initial stress and stress increase *)
initApp = Input["Enter initial value of remote applied stress"];
appStep = Input["Enter increment value for applied stress per step"];

(* user input for the area of each cell as used in the magnitude
calculations *)
area = Input["Enter the area of each element. Area of
    1/10,000 corresponds to the failure of a single element being a
zero magnitude event"];

(* Creates Random Walk of n elements *)
strengthinit = {};
For[i = 1, i ≤ n, i++,
      AppendTo[strengthinit, Apply[Plus, Table[Random[gaussdist],
{n}]]];
 ];
(*Shift values to make all toughnesses initially positive*)
strengthinit = strengthinit - Floor[Min[strengthinit]] + 1;
(* produces stiff and soft layers *)
(*topStiff = Take[Sort[strengthinit], -100];
  topSoft = Take[Sort[strengthinit], 50];
  For[i = 6, i ≤ 9, i++,
      strengthinit =
      ReplacePart[strengthinit, topStiff, Table[{x}, {x, i*100 +
      1, i*100 + 80}], Table[{Random[Integer, {1, 100}]}, {80}]];
      strengthinit = ReplacePart[strengthinit, topSoft, Table[{
            x}, {x, i*100 + 81, (i + 1)*100}], Table[{
          Random[Integer, {1, 50}]}, {20}]];
  ];*)

bvalEvolve = {};
dEvolve = {};
dErr = {};
maxScale = {};
dEvolveMesh = {};
dErrMesh = {};
maxScaleMesh = {};
eventEvolve = {};
eventEvolveEpicentre = {};
invEventEvolve = {};
crackEvolve = {};
eventListBnk = {};
eventListBnkJoin = {};
magLst = {};
magLstJoin = {};
magLoc = {};
magLocJoin = {};
newFailedLst = {};
lgthLst = {};
stressIntensityTipEvolve = {};
stressToughTipEvolve = {};
```

```
stressIntensityEvolve = {};
stressToughEvolve = {};
faultTrace = {};

time = 1;

(* module records length and mid - point of adjacent failed cells for
calculations *)
(* returns lists (lgth of new failures + midpoint, lgth of connected
new failures + midpoint, lgths of all failed cells *)
crackSites[{x_, y_}] := Module[{newFailed},
            newFailed = x;
            newFailedJoin = x;
            allFailed = y;
            allFailedCalc = y;
            totList = {};
            totListJoin = {};
            totListAll = {};

            crackSt = Min[Position[newFailed, 0]];
            relLoc = crackSt;
            For[i = 0, crackSt ≠ Infinity, i++,
                  newFailed = Drop[newFailed, crackSt - 1];
                  crackEnd = If[Min[Position[newFailed, 1]] ==
Infinity, Length[newFailed] + 1, Min[Position[newFailed, 1]]];
                  crackLgth = crackEnd - 1;
                  AppendTo[totList, {crackLgth, relLoc + (crackLgth -
1)*0.5}];
                  newFailed = Drop[newFailed, crackLgth];
                  crackSt = Min[Position[newFailed, 0]];
                  relLoc = relLoc + crackLgth - 1 + crackSt;
            ];

            (* includes length of original crack if both tips
propagate, rather than two new growths *)
            crackStJoin = Min[Position[newFailedJoin, 0]];
            relLocJoin = crackStJoin;
            For[i = 0, crackStJoin ≠ Infinity, i++,
                  newFailedJoin = Drop[newFailedJoin, crackStJoin -
1];
                  allFailed = Drop[allFailed, crackStJoin - 1];
                  crackEndJoin = If[Min[Position[newFailedJoin,
        1]] == Infinity, Length[newFailedJoin] + 1,
Min[Position[newFailedJoin, 1]]];
                  crackLgthTemp = crackEndJoin - 1;
                  newFailedJoin = Drop[newFailedJoin, crackLgthTemp];
                  allFailed = Drop[allFailed, crackLgthTemp];
                  endAll = If[Min[Position[allFailed, 1]] == Infinity,
Length[allFailed], Min[Position[allFailed, 1]]];
                  newFailedCovered = Max[Position[Take[newFailedJoin,
endAll], 0]];
                  If[newFailedCovered == -Infinity,
                        crackLgthJoin = crackLgthTemp;,
                        crackLgthJoin = crackLgthTemp +
newFailedCovered;
                        newFailedJoin = Drop[newFailedJoin,
newFailedCovered];
                        allFailed = Drop[allFailed, newFailedCovered];
                  ];
                  AppendTo[totListJoin, {crackLgthJoin, relLocJoin +
(crackLgthJoin - 1)*0.5}];
                  crackStJoin = Min[Position[newFailedJoin, 0]];
                  relLocJoin = relLocJoin + crackLgthJoin - 1 +
crackStJoin;
```

```
            ];

            (* records all crack lengths *)
            crackStAll = Min[Position[allFailedCalc, 0]];
            For[i = 0, crackStAll ≠ Infinity, i++,
                  allFailedCalc = Drop[allFailedCalc, crackStAll - 1];
                  allFailedEnd = If[Min[Position[allFailedCalc, 1]] ==
        Infinity, Length[allFailedCalc] + 1,in[Position[allFailedCalc,
1]]];
                  crackLgthAll = allFailedEnd - 1;
                  AppendTo[totListAll, crackLgthAll];
                  allFailedCalc = Drop[allFailedCalc, crackLgthAll];
                  crackStAll = Min[Position[allFailedCalc, 0]];
            ];

            Return[{totList, totListJoin, totListAll}]
      ];


(* module adjusts stress intensity around crack tips according to
crack length and distribution of surrounding cracks *)
(* returns (state, stress intensity, tghness) data with stress
intensity adjusted around crack tips *)
kfacInt[x__] := Module[{j, jBnk, lgth},
            data = x;
            For[s = 1, s ≤ n, s++,
                  AppendTo[data[[s]], {{}, {}}];
                  data[[s]] = Flatten[data[[s]], 1];
            ];
            j = 0;
            jBnk = {};
            lgth = 1;
            For[l = 1, Min[Position[Drop[data, Min[j + lgth - 1, n]],
{0, _, _, _, _}]] ≠ Infinity, l++,
                  j = j + lgth - 1 + Min[Position[Drop[data, j + lgth
- 1], {0, _, _, _, _}]];
                  If[MemberQ[jBnk, j], jInd = 1, jInd = 0];
                  lgth = 1;
                  For[i = 1, j + i ≤ n && MatchQ[data[[j + i]], {0, _,
_, _, _}] && i < n, i++,
                        lgth = lgth + 1;
                  ];

                  (* adds distance and length to all cells within half
- crack - length distance below current tip *)
                  For[k = 1, k ≤ Floor[lgth/2] + 1 && jInd == 0, k++,
                        If[j - k > 0,
                              If[data[[j - k, 1]] ≠ 0,
                                    AppendTo[data[[j - k,
4]], {k, lgth}];
                                          ];
                              ];
                  ];
                  (* adds distance and length to all cells within half
- crack - distance above current tip *)
                  For[m = 1, m ≤ Floor[lgth/2] + 1 && jInd == 0, m++,
                        If[j + lgth - 1 + m ≤ n,
                              If[data[[j + lgth - 1 + m, 1]] ≠
0,AppendTo[data[[j + lgth - 1 + m, 5]], {m, lgth}];
                                          ];
                              ];
                  ];
            ];
```

```
            (* adjusts stress intensity at intact cells *)
            For[u = 1, u ≤ n, u++,
                  Which[Length[data[[u, 4]]] ≥ 1 && Length[data[[u,
5]]] ≥ 1,
            (* within affected range of cracks above and below,
interaction formula applies *)
                        allCks = Flatten[{data[[u, 4]], data[[u, 5]]},
1];
                        data[[u, 2]] = 0;
                        For[v = 1, v ≤ Length[allCks], v++,
                                    data[[u, 2]] = data[[u, 2]] +
remStress*Sqrt[((allCks[[v, 1]] + allCks[[v, 2]])/allCks[[v,
1]])*Tan[Pi*allCks[[v, 2]]/(2*Apply[Plus, allCks[[v]]])]];
                              ];
                        data[[u, 2]] = 0.7*data[[u, 2]];,
                        Length[data[[u, 4]]] ≥ 1,
                        (* affected by crack above *)
                        data[[u, 2]] = 0;
                        For[v = 1, v ≤ Length[data[[u, 4]]], v++,
                                    data[[u, 2]] = data[[u, 2]] +
remStress*Sqrt[Pi*data[[u, 4, v, 2]]/(2*data[[u, 4, v, 1]])];
                              ];,
                        Length[data[[u, 5]]] ≥ 1,
                        (* affected by crack below *)
                        data[[u, 2]] = 0;
                        For[v = 1, v ≤ Length[data[[u, 5]]], v++,

                        data[[u, 2]] = data[[u, 2]] +
remStress*Sqrt[Pi*data[[u, 5, v, 2]]/(2*data[[u, 5, v, 1]])];
                              ];,
                        True,
                        data[[u, 2]] = remStress;
                  ];
                  data[[u]] = Drop[data[[u]], -2];
            ];
            Return[data]
      ];

(*checks for sites whose toughness is exceeded by remote applied
stress*)
failCheck[{1, a_, b_}] := {0, a, b} /; a ≥ b;
failCheck[{a_, b_, c_}] := {a, b, c};

(* builds initial (state,stress, fracture toughness) data, and checks
for initial failures *)
initData = Table[{1, initApp, strengthinit[[i]]}, {i, 1, n}];
initData = Map[failCheck, initData];
(* sets maximum of 20 or n/100 cells to failed *)
initData = If[Count[initData, {0, _, _}] < 20, ReplacePart[initData,
0, Table[{Random[Integer, {1, n}], 1}, {Max[Floor[n/100], 20] -
(Count[initData, {0, _, _}])}]], initData];

(* creates a fractal distribution of failed cells *)
(*fractalLst = Table[0, {n/3}];
sectionsLst = {{1, Length[fractalLst]}};
omitLgth = Floor[(sectionsLst[[1, 2]] - sectionsLst[[1, 1]] + 1)/3];

While[omitLgth ≥ 1,
      fractalLst = ReplacePart[fractalLst, 1, Partition[Table[x, {x,
sectionsLst[[1, 1]] + omitLgth, sectionsLst[[1, 2]] - omitLgth}], 1]];
      AppendTo[sectionsLst, {sectionsLst[[1, 1]], sectionsLst[[1, 1]]
+ omitLgth - 1}];
      AppendTo[sectionsLst, {sectionsLst[[1,2]] - omitLgth + 1,
sectionsLst[[1, 2]]}];
```

```
      sectionsLst = Delete[sectionsLst, 1];
      omitLgth = Floor[(sectionsLst[[1, 2]] - sectionsLst[[1, 1]] +
1)/3];
    ];

  initData = Table[{fractalLst[[If[Mod[xx, Length[fractalLst]] == 0,
Length[fractalLst], Mod[xx, Length[fractalLst]]]]], initData[[xx, 2]],
initData[[xx, 3]]}, {xx, n}];*)


AppendTo[crackEvolve, Flatten[Take[initData, n, 1]]];
remStress = initApp;
crackForm = initData;
intactSite = Count[initData, {1, _, _}];

(* loop continues until no intact cells remain *)
For[loop = 1, intactSite ≠ 0, loop++,
      numFailed = 1;

(* loop continues until no further failures occur at current stress,
or until no intact cells remain *)
(* remove (* *) for constant stress conditions *)
      (*For[k = 0, numFailed ≠ 0 && intactSite ≠ 0, k++,*)
            eventList = {};
            eventListJoin = {};

(* adjusts stress intensity around crack tips and checks for failures
*)

            initData = kfacInt[crackForm];
            failedElements = Flatten[Position[initData, {0, __}]];

            stressIntensityTip = {};
            stressIntensity = {};
            stressToughTip = {};
            stressTough = {};

 (* records stress intensity and stress intensity/toughness at cells
adjacent to crack tip *)
            For[ij = 1, ij ≤ Length[failedElements], ij++,
                        If[failedElements[[ij]] == 1,
                        (* remove (* *) for periodic boundaries *)

(*If[FreeQ[failedElements, n],
      AppendTo[stressIntensityTip, initData[[n, 2]]];


      AppendTo[stressToughTip, Min[initData[[n, 2]]/initData[[n, 3]],
1]];
                                    ];*),

                                    If[FreeQ[failedElements,
failedElements[[ij]] -
1],AppendTo[stressIntensityTip,initData[[failedElements[[ij]]
- 1, 2]]];
            AppendTo[stressToughTip,Min[initData[[failedElements[[ij]]
- 1, 2]]/initData[[failedElements[[ij]] - 1, 3]], 1]];
                                    ];
                        ];
            If[failedElements[[ij]] == n,
            (* remove (* *) for periodic boundaries *)
            (*If[FreeQ[failedElements, 1],
                  AppendTo[stressIntensityTip, initData[[1, 2]]];
```

```
                  AppendTo[stressToughTip,
Min[initData[[1,2]]/initData[[1,
                        3]], 1]];
                         ];*),
                         If[FreeQ[failedElements, failedElements[[ij]]
+ 1],
                         AppendTo[stressIntensityTip,
initData[[failedElements[[ij]] + 1, 2]]];
                         AppendTo[stressToughTip,
Min[initData[[failedElements[[ij]] + 1,
2]]/initData[[failedElements[[ij]] + 1, 3]], 1]];
                                    ];
                         ];
                  ];

            AppendTo[stressIntensityTipEvolve, stressIntensityTip];
            AppendTo[stressToughTipEvolve, stressToughTip];

(* records stress intensity and stress intensity/toughness at all
intact cells *)
            For[ij = 1, ij ≤ n, ij++,
                         If[FreeQ[failedElements, ij],
                               AppendTo[stressIntensity, initData[[ij,
2]]];
                               AppendTo[stressTough, Min[initData[[ij,
2]]/initData[[ij, 3]], 1]];
                         ];
                  ];

            AppendTo[stressIntensityEvolve, stressIntensity];
            AppendTo[stressToughEvolve, stressTough];

            (* checks for new failures *)
            crackForm = Map[failCheck, initData];
            newFailed = Flatten[Take[crackForm, n, 1]] - Flatten[
      Take[initData, n, 1]] + 1;
            allFailed = Flatten[Take[crackForm, n, 1]];
            AppendTo[newFailedLst, newFailed];
            numFailed = Count[newFailed, 0];

            (* records new crack lengths and total crack lengths *)
            bValLgths = crackSites[{newFailed, allFailed}];
            eventList = Flatten[AppendTo[eventList, bValLgths[[1]]],
1];
            eventListJoin = Flatten[AppendTo[eventListJoin,
bValLgths[[2]]], 1];
            AppendTo[lgthLst, bValLgths[[3]]];

            (* records state of each cell, failed or intact *)
            AppendTo[crackEvolve, Flatten[Take[crackForm, n, 1]]];
            eventCount = Apply[Plus, eventList[[All, 1]]];
            AppendTo[eventEvolve, eventCount];
            invEventEvolve = If[eventCount == 0, invEventEvolve,
AppendTo[invEventEvolve, 1/eventCount]];
            epicentreNew = {};
            eventLocs = Position[Flatten[newFailed], 0];

            (* records central location of adjacent failing cells *)
            For[jkl = 1, Length[eventLocs] > 0, jkl++,
                         endLoc = 0;
                         For[klm = 2, endLoc ≠ 1 && Length[eventLocs] >
klm - 1, klm++,
                  If[eventLocs[[klm]] == eventLocs[[klm - 1]] + 1,
                                          endLoc = 0;,
```

```
                                                endLoc = 1;
                                          ];
                              ];
                              If[Length[eventLocs] == klm - 1 && endLoc ==
0,
                                    klm = klm + 1;
                              ];
                              allLoc = Take[eventLocs, klm - 2];
                              epicentre =
allLoc[[Ceiling[Length[allLoc]/2]]];
                              AppendTo[epicentreNew, epicentre];
                              eventLocs = Drop[eventLocs, klm - 2];
                        ];

                  AppendTo[eventEvolveEpicentre, Length[epicentreNew]];

      (* increases time and returns stress intensity to remote stress *)
                  time = time + 1;

                  For[i = 1, i ≤ n, i++,
                              crackForm[[i, 2]] = remStress;
                        ];

                  (* calculates the magnitude of events *)
                  mags = Table[N[Log[10, eventList[[x, 1]]*area] + 4], {x,
1,Length[eventList]}];
                  mags = Delete[mags, Position[mags, 0]];
                  AppendTo[magLst, mags];
                  AppendTo[magLoc,Table[{mags[[y]], eventList[[y, 2]]}, {y,
1, Length[eventList]}]];
                  magsJoin = Table[N[Log[10, eventListJoin[[x, 1]]*area] +
               4], {x, 1, Length[eventListJoin]}];
                  magsJoin = Delete[magsJoin, Position[magsJoin, 0]];
                  AppendTo[magLstJoin, magsJoin];
                  AppendTo[magLocJoin, Table[{magsJoin[[y]],
eventListJoin[[y, 2]]}, {y,1, Length[eventListJoin]}]];

                  (* counts the number of cells remaining intact *)
                  intactSite = Count[crackForm, {1, _, _}];
            (*];*)

            (*calculates fractal dimension *)
            dimPos = 1 - Flatten[Take[crackForm, n, 1]];
            AppendTo[faultTrace, dimPos];
            dimPosBnk = dimPos;

            (*fractal dimension*)
            dimLstLgth = {};
            state = dimPos[[1]];
            stateEnd = state*Min[Position[dimPos, 0]] + (1 - state)*
                  Min[Position[dimPos, 1]];

            For[i = 0, stateEnd ≠ Infinity, i++,
                        stateLgth = stateEnd - 1;
                        AppendTo[dimLstLgth, {state, stateLgth}];
                        dimPos = Drop[dimPos, stateLgth];
                        state = dimPos[[1]];
                        stateEnd = state*Min[Position[dimPos, 0]] + (1 -
state)*Min[Position[dimPos, 1]];
                  ];

            dimLstLgth = AppendTo[dimLstLgth, {state, Length[dimPos]}];
            fractalDim = {};
            fractalDimMesh = {};
```

```
      For[k = 1, k ≤ 250, k += 1,
                  countBox = 0;
                  dimLst = dimLstLgth;
                  startBox = Min[Position[dimLst, {1, _}]] - 1;

                  For[i = 0,startBox≠Infinity&&dimLst[[1,2]] > 0, i++,
                        dimLst = Drop[dimLst, startBox];
                        boxSize = k - dimLst[[1, 2]];

                        For[j = 0,boxSize≥0&& Length[dimLst] > 1, j++,
                              dimLst = Drop[dimLst, 1];
                              boxSize = boxSize - dimLst[[1, 2]];
                        ];

                        countBox = countBox + 1;
                        dimLst[[1, 2]] = -boxSize;
                        startBox = Min[Position[dimLst, {1, _}]] - 1;
                  ];

                  AppendTo[fractalDim, {k, countBox}];
                  meshCover = Partition[dimPosBnk, k];
                  If[Mod[Length[dimPosBnk], k] ≠ 0,
                        AppendTo[meshCover, Take[dimPosBnk, -
Mod[Length[dimPosBnk], k]]];
                  ];
                  coverCheck = Table[If[MemberQ[meshCover[[x]], 1], 1,
0], {x, Length[meshCover]}];
                  countBoxMesh = Apply[Plus, coverCheck];
                  AppendTo[fractalDimMesh, {k, countBoxMesh}];
            ];

      For[m = 1, m ≤ Length[fractalDim], m++,
                  ind = 0;

                  For[p = 1, p < m, p++,
                        If[fractalDim[[m, 2]] == fractalDim[[p, 2]],
                                    ind = 1;
                                    Break[];
                              ];
                  ];

                  If[ind == 1,
                        fractalDim[[m, 1]] = 0;
                  ];
            ];

      For[m = 1, m ≤ Length[fractalDimMesh], m++,
                  ind = 0;

                  For[p = 1, p < m, p++,
                        If[fractalDimMesh[[m, 2]] ==
fractalDimMesh[[p, 2]],
                                    ind = 1;
                                    Break[];
                              ];
                  ];

                  If[ind == 1,
                        fractalDimMesh[[m, 1]] = 0;
                  ];
            ];

      fractalDim = Delete[fractalDim, Position[fractalDim, {0, _}]];
```

```
      fractalDim = Log[10, fractalDim];
      fractalDimMesh = Delete[fractalDimMesh, Position[fractalDimMesh,
{0, _}]];
      fractalDimMesh = Log[10, fractalDimMesh];
      fractalDimTemp = fractalDim;
      goodFit = 0;
      While[Length[fractalDimTemp] > 2 && Abs[goodFit] < 0.9,
                  Clear[x];
                  interp = Fit[fractalDimTemp, {1, x}, x];
                  sigX = Apply[Plus, fractalDimTemp[[All, 1]]];
                  sigXSq = Apply[Plus, fractalDimTemp[[All, 1]]^2];
                  sigY = Apply[Plus, fractalDimTemp[[All, 2]]];
                  sigYSq = Apply[Plus, fractalDimTemp[[All, 2]]^2];
                  sigXY = Apply[Plus,fractalDimTemp[[All,
1]]*fractalDimTemp[[All, 2]]];
                  noData = Length[fractalDimTemp];
                  goodFit =
        N[(noData*sigXY - sigX*sigY)/Sqrt[(noData*sigXSq -
sigX^2)*(noData*sigYSq - sigY^2)]];
                  fractalDimTemp = Drop[fractalDimTemp, -1];
            ];
      If[Abs[goodFit] > 0.9,

      AppendTo[fractalDimTemp,fractalDim[[Length[fractalDimTemp] +
1]]];
                  errD = noData*sigXSq - sigX^2;
                  calcY = {};

                  For[y = 1, y ≤ Length[fractalDimTemp], y++,
                        AppendTo[calcY, Coefficient[interp, x,
           0] + Coefficient[interp, x, 1]*fractalDimTemp[[y, 1]]];
                  ];
                  sumRes = Apply[Plus, (fractalDimTemp[[All, 2]] -
calcY)^2];
                  sdError = Sqrt[(sumRes/(noData - 2))*noData/errD];
                  AppendTo[maxScale, 10^fractalDimTemp[[-1, 1]]];
                  dvalue = -Coefficient[interp, x];
                  If[Length[dEvolve] > 0,
                        If[dvalue ≠ dEvolve[[Length[dEvolve], 2]],
                                    AppendTo[dEvolve, {remStress,
N[dvalue]}];
                                    AppendTo[dErr, sdError];
                              ];,
                        AppendTo[dEvolve, {remStress, N[dvalue]}];
                        AppendTo[dErr, sdError];
                  ];
            ];

      fractalDimTempMesh = fractalDimMesh;
      goodFit = 0;
      While[Length[fractalDimTempMesh] > 2 && Abs[goodFit] < 0.9,
                  Clear[x];
                  interp = Fit[fractalDimTempMesh, {1, x}, x];
                  sigX = Apply[Plus, fractalDimTempMesh[[All, 1]]];
                  sigXSq = Apply[Plus, fractalDimTempMesh[[All,
1]]^2];
                  sigY = Apply[Plus, fractalDimTempMesh[[All, 2]]];
                  sigYSq = Apply[Plus, fractalDimTempMesh[[All,
2]]^2];
                  sigXY = Apply[Plus, fractalDimTempMesh[[All,
1]]*fractalDimTempMesh[[All, 2]]];
                  noData = Length[fractalDimTempMesh];
                  goodFit = N[(noData*sigXY - sigX*sigY)/Sqrt[(noData*
              sigXSq - sigX^2)*(noData*sigYSq - sigY^2)]];
```

```
                  fractalDimTempMesh = Drop[fractalDimTempMesh, -1];
            ];
      If[Abs[goodFit] > 0.9,
                  AppendTo[fractalDimTempMesh,
fractalDimMesh[[Length[fractalDimTempMesh] + 1]]];
                  errD = noData*sigXSq - sigX^2;
                  calcY = {};

                  For[y = 1, y ≤ Length[fractalDimTempMesh], y++,
                        AppendTo[calcY, Coefficient[interp, x, 0] +
Coefficient[interp,x, 1]*fractalDimTempMesh[[y, 1]]];
                  ];

                  sumRes = Apply[Plus,(fractalDimTempMesh[[All,2]] -
calcY)^2];
                  sdError = Sqrt[(sumRes/(noData - 2))*noData/errD];
                  AppendTo[maxScaleMesh, 10^fractalDimTempMesh[[-1,
1]]];
                  dvalue = -Coefficient[interp, x];
                  If[Length[dEvolveMesh] > 0,
                        If[dvalue ≠ dEvolveMesh[[Length[dEvolveMesh],
2]],
                              AppendTo[dEvolveMesh, {remStress,
N[dvalue]}];
                              AppendTo[dErrMesh, sdError];
                        ];,
                        AppendTo[dEvolveMesh, {remStress, N[dvalue]}];
                        AppendTo[dErrMesh, sdError];
                  ];
            ];

  (*increases applied stress by increment value *)
      If[numFailed == 0,
                  nearFail = Min[Max[stressToughEvolve[[-1]]], 1];
                  remStress = remStress +
Ceiling[nearFail/appStep]*appStep;
                  time = time + Ceiling[nearFail/appStep] - 1;,
                  remStress = remStress + appStep;
            ];

      For[i = 1, i ≤ n, i++,
                  crackForm[[i, 2]] = remStress;
            ];

    ];

(* calculates b values *)
magLst = Flatten[magLst];
magLstJoin = Flatten[magLstJoin];
numEvents = Length[magLst];
numEventsJoin = Length[magLstJoin];
window = 300;
overlap = 100;
bValLst = {};
bValLstCut = {};
bValLstJoin = {};
bValLstJoinCut = {};

For[i = 1, Length[magLst] ≥ window, i++,
      currWindow = Take[magLst, {1, window}];
      avgMag = Apply[Plus, currWindow]/Length[currWindow];
      currB = N[Log[10, E]/avgMag];
      currBCut = If[avgMag - Log[10, area] + 4 == 0, Infinity, N[Log[
                10, E]/(avgMag - (Log[10, area] + 4))]];
```

```
      bValLst = AppendTo[bValLst, currB];
      bValLstCut = AppendTo[bValLstCut, currBCut];
      magLst = Drop[magLst, window - overlap];
    ];

bValLst = If[Length[
      magLst] == 0, bValLst, AppendTo[bValLst, N[Log[
        10, E]/(Apply[Plus, magLst]/Length[magLst])]]];
bValLstCut = If[Length[magLst] == 0, bValLstCut, AppendTo[bValLstCut,
N[Log[10, E]/(Apply[Plus, magLst]/Length[magLst] - (Log[10, area] +
4))]]];

For[i = 1, Length[magLstJoin] ≥ window, i++,
      currWindowJoin = Take[magLstJoin, {1, window}];
      avgMagJoin = Apply[Plus, currWindowJoin]/Length[currWindowJoin];
      currBJoin = N[Log[10, E]/avgMagJoin];
      currBCutJoin = If[avgMagJoin - Log[10, area] + 4 == 0, Infinity,
N[Log[10, E]/(avgMagJoin - (Log[10, area] + 4))]];
      bValLstJoin = AppendTo[bValLstJoin, currBJoin];
      bValLstJoinCut = AppendTo[bValLstJoinCut, currBCutJoin];
      magLstJoin = Drop[magLstJoin, window - overlap];
    ];

bValLstJoin =
              If[Length[magLstJoin] == 0, bValLstJoin,
AppendTo[bValLstJoin, N[Log[10, E]/(Apply[Plus,
magLstJoin]/Length[magLstJoin])]]];
bValLstJoinCut = If[Length[magLstJoin] == 0, bValLstJoinCut,
AppendTo[bValLstJoinCut, N[Log[10, E]/(Apply[Plus,
magLstJoin]/Length[magLstJoin] - (Log[10, area] + 4))]]];

For[i = 1, i ≤ Length[newFailedLst], i++,
      locs = Flatten[Position[newFailedLst[[i]], 0]];
      newFailedLst[[i]] = locs;
    ];
```

References

Abaimov S.G., Turcotte D.L., Rundle J.B. 2007, Recurrence-time and frequency-slip statistics of slip events on the creeping section of the San Andreas fault in central California, *Geophysical Journal International*, 170, 1289-1299.

Aki K. 1965, Maximum likelihood estimate of *b* in the formula $\log N = a - bm$ and its confidence limits, *Bulletin of the Earthquake Research Institute*, Tokyo University, 43, 237-238.

Albert R., Jeong H., Barabasi A.L. 1999, Diameter of the World-Wide Web, *Nature*, 401, 130-131.

Amitrano D. 2006, Rupture by damage accumulation in rocks, *International Journal of Fracture*, 139, 369-381.

Anderson E.M. 1936, The dynamics of the formation of cone-sheets, ring-dykes, and caldron-subsidences, *Royal Society of Edinburgh Proceedings*, 58, 242-251.

Ashby M.F., Hallam S.D. 1986, The failure of brittle solids containing small cracks under compressive stress states, *Acta Metallurgica*, 34, 3, 497-510.

Åström J.A., Timonen J. 2001, Fracture mechanics of snow avalanches, *Physical Review E*, 64, 011305.

Atkinson B.K. 1984, Subcritical crack growth in geological materials, *Journal of Geophysical Research*, 89, B6, 4077-4114.

Atkinson B.K. 1987, Introduction to fracture mechanics and its geophysical applications, *in* Fracture Mechanics of Rocks, ed. Atkinson B.K., *Academic Press*, London, UK.

Aviles C.A., Scholz C.H., Boatwright J. 1987, Fractal analysis applied to characteristic segments of the San Andreas fault, *Journal of Geophysical Research*, 92, 331-344.

Baer G., Hameil Y., Shamir G., Nof R. 2008, Evolution of a magma-driven earthquake swarm and triggering of the nearby Oldoinyo Lengai eruption, as resolved by InSAR, ground observations and elastic modeling, East African Rift, 2007, *Earth and Planetary Science Letters*, 272, 1-2, 339-352.

Bak P., Christensen K., Danon L., Scanlon T. 2002, Unified scaling law for earthquakes, *Physical Review Letters*, 88, 17, 178501.

Bak P., Tang C., Wiesenfeld K. 1987, Self-organized criticality: An explanation of the 1/*f* noise, *Physical Review Letters*, 59, 4, 381-384.

Balme M.R., Rocchi V., Jones C., Sammonds P.R., Meredith P.G., Boon S. 2004, Fracture toughness measurements on igneous rocks using a high-pressure, high-temperature rock fracture mechanics cell, *Journal of Volcanology and Geothermal Research*, 132, 159-172.

Balme M.R., Sammonds P.R., Vita-Finzi C., Couchman J.P. 2004, Experimental and theoretical fracture mechanics applied to fracture of the crust of Venus, *Journal of Geophysical Research*, 109, E03005.

Barabasi A.L., Albert R. 1999, Emergence of scaling in random networks, *Science*, 286, 509-512.

Barriere B., Turcotte D.L. 1994, Seismicity and self-organized criticality, *Physical Review E*, 49, 2, 1151-1160.

Bell A.F. 2007, Patterns of volcano-tectonic seismicity at basaltic volcanoes, *PhD Thesis*, University College London, UK.

Bonnet E., Bour O., Odling N.E., Davy P., Main I., Cowie P., Berkowitz B. 2001, Scaling of fracture systems in geological media, *Reviews of Geophysics*, 39, 3, 347-383.

Bridges D.L., Gao S.S. 2006, Spatial variation of seismic *b*-values beneath Makushin Volcano, Unalaska Island, Alaska, *Earth and Planetary Science Letters*, 245, 408-415.

Burlini L., Vinciguerra S., Di Toro G., De Natale G., Meredith P., Burg J.P. 2007, Seismicity preceding volcanic eruptions: New experimental insights, *Geology*, 35, 2, 183-186.

Caruso F., Vinciguerra S., Latora V., Rapisarda A., Malone S. 2006, Multifractal analysis of Mt. St. Helens seismicity as a tool for identifying eruptive activity, *Fractals*, 14, 3, 179-186.

Charles R.J. 1958, Dynamic fatigue of glass, *Journal of Applied Physics*, 29, 1657-1662.

Chelidze T.L. 1982, Percolation and fracture, *Physics of the Earth and Planetary Interiors*, 28, 93, 101.

Chelidze T., Kolesnikov Y., Matcharashvili T. 2006, Seismological criticality concept and percolation model of fracture, *Geophysical Journal International*, 164, 125-136.

Chen K., Bak P., Obukhov S.P. 1991, Self-organized criticality in a crack-propagation model of Earthquakes, *Physical Review A*, 43, 2, 625-630.

Chouet B.A. 1996, Long-period volcano seismicity: its source and use in eruption forecasting, *Nature* 380, 309-316.

Chan H.C.M., Li V., Einstein H.H. 1989, A hybridized displacement discontinuity and indirect boundary element method to model fracture propagation, *International Journal of Fracture*, 45, 263-282.

Corral A. 2004, Long-term clustering, scaling and universality in the temporal occurrence of earthquakes, *Physical Review Letters*, 92, 10, 108501.

Corral A. 2006, Dependence of earthquake recurrence times and independence of magnitudes on seismicity history, *Tectonophysics*, 424, 177-193.

Corazzato C., Tibaldi A. 2006, Fracture control on type, morphology and distribution of parasitic volcanic cones: An example from Mt. Etna, Italy, *Journal of Volcanology and Geothermal Research*, 158, 177-194.

Cornelius R.R., Scott P.A. 1993, A materials failure relation of accelerating creep as empirical description of damage accumulation, *Rock Mechanics and Rock Engineering*, 26, 3, 233-252.

Cornelius R.R., Voight B. 1995, Graphical and PC-software analysis of volcano eruption precursors according to the Materials Failure Forecast Method (FFM), *Journal of Volcanology and Geothermal Research*, 64, 295-320.

Costin L.S. 1983, A microcrack model for the deformation and failure of brittle rock, *Journal of Geophysical Research*, 88, B11, 9485-9492.

Cowie P.A., Vanneste C., Sornette D. 1993, Statistical physics model for the spatiotemporal evolution of faults, *Journal of Geophysical Research*, 98, 21809-21822.

Cox S.J.D., Scholz C.H. 1988, Rupture initiation in shear fracture of rocks: an experimental study, *Journal of Geophysical Research*, 93, 3307-3320.

Davy P., Hansen A., Bonnet E., Zhang S.Z. 1995, Localization and fault growth in layered brittle-ductile systems: Implications for deformation of the continental lithosphere, *Journal of Geophysical Research*, 100, 6281-6294.

De la Cruz-Reyna S., Reyes-Davila G.A. 2001, A model to describe precursory material-failure phenomena: applications to short-term forecasting at Colima volcano, Mexico, *Bulletin of Volcanology*, 63, 297-308.

De la Cruz-Reyna S., Yokoyama I., Martinez-Bringas A., Ramos E. 2008, Precursory seismicity of the 1994 eruption of Popocatépetl Volcano, Central Mexico, *Bulletin of Volcanology*, 70, 6, 753-767.

De Natale G., Petrazzuoli S.M., Troise C. 2000, Internal stress field at Mount Vesuvius: A model for background seismicity at a central volcano, *Journal of Geophysical Research*, 105, B7, 16,207-16,214.

De Natale G., Troise C., Pingue F., Zollo A. 1999, Earthquake dynamics during unrest episodes at Campi Flegrei Caldera (Italy): A comparison with Rabaul (New Guinea), *Physics and Chemistry of the Earth*, 24, 2, 97-100.

Diggle P. 2003, Statistical analysis of spatial point patterns, 2nd ed., *Pergamon Press*, Oxford.

Dingwell D.B. 1996, Volcanic dilemma: flow or blow?, *Science*, 273, 5278, 1054-1055.

Emmerich F.G. 2007, Tensile strength and fracture toughness of brittle materials, *Journal of Applied Physics*, 102, 7, 73504.

Erdos P., Renyi A. 1961, On the strength of connectedness of a random graph, Acta *Mathematica Hungarica*, 12, 1-2, 261-267.

Falconer K. 1990, *Fractal Geometry: Mathematical Foundations and Applications*, John Wiley & Sons, Chichester.

Freed A. 2005, Earthquake triggering by static, dynamic and postseismic stress transfer, *Annual Review of Earth and Planetary Sciences*, 33, 335-367.

Fukuzono T. 1985, A new method for predicting the failure time of a slope, *Proceedings of the 4th International Conference and Field Workshop on Landslides,* Tokyo.

Gargani J., Geoffroy L., Gac S., Cravoisier S. 2006, Fault slip and Coulomb stress variations around a pressured magma reservoir: consequences on seismicity and magma intrusion, *Terra Nova*, 18, 6, 403-411.

Grassberger P., Procaccia I. 1983, Measuring the strangeness of strange attractors, *Physica D*, 9, 189-208.

Green D.N., Neuberg J., Cayol V. 2006, Shear stress along the conduit wall as a plausible source of tilt at Soufrière Hills volcano, Montserrat, *Geophysical Research Letters*, 33, L10306.

Gresta S., Patanè G. 1983a, Changes in *b* Values before the Etnean eruption of March-August 1983, *Pure and Applied Geophysics*, 121, 903-912.

Gresta S., Patanè G. 1983b, Variation of *b* Values before the Etnean eruption of March 1981, *Pure and Applied Geophysics*, 121, 287-295.

Griffith A.A. 1920, The phenomena of rupture and flow in rocks, *Philosophical Transactions of the Royal Society of London*, 221**,** 163-198.

Gudmundsson A. 1986, Geometry, formation and development of tectonic fractures on the Reykjanes Peninsular, southwest Iceland, *Tectonophysics*, 139, 295-308.

Gudmundsson A. 1990, Emplacement of dikes, sills and crustal magma chambers at divergent plate boundaries, *Tectonophysics*, 176, 3-4, 257-275.

Gudmundsson A. 2002, Emplacement and arrest of sheets and dykes in central volcanoes, *Journal of Volcanology and Geothermal Research*, 116, 279-298.

Gudmundsson A. 2003, Surface stresses associated with arrested dykes in rift zones, *Bulletin of Volcanology*, 65, 606–619.

Gudmundsson A. 2005, The effects of layering and local stresses in composite volcanoes on dyke emplacement and volcanic hazards, *Comptes Rendus Geosciences*, 337, 13, 1216-1222.

Gudmundsson A. 2006, How local stresses control magma-chamber ruptures, dyke injections, and eruptions in composite volcanoes, *Earth-Science Reviews*, 79, 1-2, 1-31.

Gudmundsson A., Loetveit I.F. 2005, Dyke emplacement in a layered and faulted rift zone, *Journal of Volcanology and Geothermal Research*, 144, 311-327.

Gudmundsson A., Marti J., Turon E. 1997, Stress fields generating ring faults in volcanoes, *Geophysical Research Letters*, 24, 13, 1559-1562.

Gudmundsson A., Philipp S.L. 2006, How local stress fields prevent volcanic eruptions, *Journal of Volcanology and Geothermal Research*, 158, 3-4, 257-268.

Gutenberg B., Richter C.F. 1954, *Seismicity of the Earth and associated phenomena*, *Princeton University Press*, Princeton, New Jersey.

Gutenberg B., Richter C.F. 1956, Earthquake magnitude, intensity, energy, and acceleration: (Second paper), *Bulletin of the Seismological Society of America*, 46, 105-145.

Hamburger D., Biham O., Avnir D. 1996, Apparent fractality emerging from models of random distributions, *Physical Review E*, 53, 4, 3342, 3358.

Hanks T.C., Kanamori H. 1979, Moment magnitude scale, *Journal of Geophysical Research*, 84, 2348-2350.

Hatton C.G., Main I.G., Meredith P.G. 1993, A comparison of seismic and structural measurements of scaling exponents during tensile subcritical crack growth, *Journal of Structural Geology*, 15, 12, 1485-1495.

Havskov J., De la Cruz-Reyna S., Singh S.K., Medina F., Gutiérrez C. 1983, Seismic activity related to the March-April, 1982 eruptions of El Chichon volcano, Chiapas, Mexico, *Geophysical Research Letters*, 10, 4, 293-296.

Hazzard J.F., Young R.P., Maxwell S.C. 2000, Micromechanical modeling of cracking and failure in brittle rocks, *Journal of Geophysical Research*, 105, B7, 166683-166697.

Henderson J., Main I. 1992, A simple fracture-mechanical model for the evolution of seismicity, *Geophysical Research Letters*, 19, 4, 365-368.

Henderson J., Main I.G., Meredith P.G., Sammonds P.R. 1992, The evolution of seismicity at Parkfield: observation, experiment and a fracture-mechanical interpretation, *Journal of Structural Geology*, 14, 8/9, 905–913.

Herrmann H.J., Hansen A., Roux S. 1989, Fracture of disordered, elastic lattices in two dimensions, *Physical Review B*, 39, 1, 637-648.

Hirata T. (1989), Fractal dimension of fault systems in Japan: fractal structure in rock fracture geometry at various scales, *Pure and Applied Geophysics*, 131, 157-170.

Huang J., Turcotte D.L. 1988, Fractal distributions of stress and strength and variations of *b*-value, *Earth and Planetary Science Letters*, 91, 223, 230.

Inglis C.E. 1913, Stresses in a plate due to the presence of cracks and sharp corners, *Transactions Institute of Naval Architects*, 55, 219.

Irwin G. R. 1958, *Fracture in Handbuch der Physik 6*, Ed. Flugge S., Springer, Berlin, 551-590.

Jolly A.D., Page R.A., Power J.A. 1994, Seismicity and stress in the vicinity of Mt. Spurr volcano, south-central Alaska, *Journal of Geophysical Research*, 99, 15,305-15,318.

Kachanov M. 1987, Elastic solids with many cracks: A simple method of analysis, *International Journal of Solids and Structures*, 23, 1, 23-43.

Kamaya M., Totsuka N. 2002, Influence of interaction between multiple cracks on stress corrosion crack propagation, *Corrosion Science*, 44, 2333-2352.

Kanamori H., Anderson D.L. 1975, Theoretical basis of some empirical relations in seismology, *Bulletin of the Seismological Society of America*, 65, 5, 1073-1095.

Kesten H. 1980, The critical probability of bond percolation on the square lattice equals ½, *Communications in Mathematical Physics*, 74, 1, 41-59.

Kilburn C.R.J. 2003, Multiscale fracturing as a key to forecasting volcanic eruptions, *Journal of Volcanology and Geothermal Research*, 125, 271-289.

Kilburn C.R.J., Sammonds P.R. 2005, Maximum warning times for imminent volcanic eruptions, *Geophysical Research Letters*, 32, 24, L24313.

Kilburn C.R.J., Voight B. 1998, Slow rock fracture as eruption precursor at Soufriere Hills volcano, Montserrat, *Geophysical Research Letters*, 25, 19, 3665-3668

King G. 1983, The accommodation of large strains in the upper lithosphere of the Earth and other solids by self-similar fault systems: the geometrical origin of *b*-value, *Pure and Applied Geophysics*, 121, 761-815.

Kirkpatrick S. 1973, Percolation and conduction, *Reviews of Modern Physics*, 45, 4, 574-588.

Kohno Y., Matsushima T., Shimizu H. 2008, Pressure sources beneath Unzen Volcano inferred from leveling and GPS data, *Journal of Volcanology and Geothermal Research*, 175, 1-2, 100-109.

Konstantinou K.I., Schlindwein V. 2003, Nature, wavefield properties and source mechanism of volcanic tremor: a review, *Journal of Volcanology and Geothermal Research 119*, 1-4, 161-187.

Kranz R.L. 1983, Microcracks in rocks: A review, *Tectonophysics*, 100, 449-480.

Kueppers U., Perugini D., Dingwell D.B. 2006, "Explosive energy" during volcanic eruptions from fractal analysis of pyroclasts, *Earth and Planetary Science Letters*, 248, 800-807.

La Femina P.C., Connor C.B., Hill B.E., Strauch W., Saballos J.A. 2004, Magma-tectonic interactions in Nicaragua: the 1999 seismic swarm and eruption of Cerro Negro volcano, *Journal of Volcanology and Geothermal Research*, 137, 187-199.

Lam K.Y., Phua S.P. 1991, Multiple crack interaction and its effect on stress intensity factor, *Engineering Fracture Mechanics*, 40, 3, 585-592.

Latora V., Marchiori M. 2001, Efficient behavior of small-world networks, *Physical Review Letters*, 87, 1987011-1987014.

Latora V., Marchiori M. 2002, Is the Boston subway a small-world network?, *Physica A*, 314, 109-113.

Lawn B.R., Wilshaw T.R. 1975, *Fracture of Brittle Solids*, *Cambridge University Press*, Cambridge.

Liu H.Y., Kou S.Q., Lindqvist P.A., Tang C.A. 2007, Numerical modeling of the heterogeneous rock fracture process using various test techniques, *Rock Mechanics and Rock Engineering*, 40, 2, 107-144.

Lockner D. A. 1993, The role of acoustic emission in the study of rock, *International Journal of Rock Mechanics and Mining Sciences & Geomechanics Abstracts*, 30, 883-899.

Lockner D.A., Byerlee J.D., Kuksenko V., Ponomarev A., Sidorin A. 1991, Quasi-static fault growth and shear fracture energy in granite, *Nature*, 350, 39-42.

Lockner D.A., Madden T.R. 1991, A multiple crack model of brittle fracture: II Time-dependent simulations, *Journal of Geophysical Research*, 96, 19643-19654.

Luongo G., Mazzarella A., Palumbo A. 1996, On the self-organized critical state of Vesuvio volcano, *Journal of Volcanology and Geothermal Research*, 70, 67-73.

Main I.G. 1987, A characteristic earthquake model of the seismicity preceding the eruption of Mount St. Helens on 18 May 1980, *Physics of the Earth and Planetary Interiors*, 49, 283-293.

Main I. 1988, Prediction of failure times in the Earth for a time-varying stress, *Geophysical Journal*, 92, 455-464.

Main I.G. 1991, A modified Griffith criterion for the evolution of damage with a fractal distribution of crack lengths: application to seismic event rates and b-values, *Geophysical Journal International*, 107, 353-362.

Main I.G. 1999, Applicability of time-to-failure analysis to accelerated strain before earthquakes and volcanic eruptions, *Geophysical Journal International*, 139, F1-F6.

Main I.G. 2000, A damage mechanics model for power-law creep and earthquake aftershock and foreshock sequences, *Geophysical Journal International*, 142, 151-161.

Main I.G., Henderson J.R., Meredith P.G., Sammonds P.R. 1994, Self-organised criticality and fluid rock interactions in the brittle field, *Pure and Applied Geophysics*, 142, 3-4, 529.

Main I.G., Meredith P.G. 1991, Stress corrosion constitutive laws as a possible mechanism of intermediate-term and short-term seismic event rates and b-values, *Geophysical Journal International*, 107, 363-372.

Main I.G., Meredith P.G., Jones C. 1989, A reinterpretation of the precursory seismic *b*-value anomaly from fracture mechanics, *Geophysical Journal*, 96, 131-138.

Main I.G., Meredith P.G., and Sammonds P.R. 1992, Temporal variations in seismic event rate and *b*-values from stress corrosion constitutive laws, *Tectonophysics*, 211, 233-246.

Main I.G., Sammonds P.R., Meredith P.G. 1993, Application of a modified Griffith criterion to the evolution of fractal damage during compressional rock failure, *Geophysical Journal International*, 115, 2, 367-380.

Malakhovsky I., Michels M.A.J. 2007, Effect of disorder strength on the fracture pattern in heterogeneous networks, *Physical Review B*, 76, 144201.

Malone S.D., Boyko C., Weaver C.S. 1983, Seismic precursors to the Mount St-Helens eruptions in 1981 and 1982, *Science*, 221, 4618, 1376-1378.

Manconi A., Walter T.R., Arnelung F. 2007, Effects of mechanical layering on volcano deformation, *Geophysical Journal International*, 170, 2, 952-958.

Mandelbrot B.B. 1982, *The Fractal Geometry of Nature*, Freeman, San Francisco.

Marzocchi W., Scandone R., Mulargia F. 1993, The tectonic setting of Mount Vesuvius and the correlation between its eruptions and the earthquakes of the Southern Apennines, *Journal of Volcanology and Geothermal Research*, 58, 27-41.

Marzocchi W., Woo G. 2007, Probabilistic eruption forecasting and the call for an evacuation, *Geophysical Research Letters*, 34, 22, L22310.

Mavko G., Mukerji T., Dvorkin J. 1998, *The Rock Physics Handbook: Tools for Seismic Analysis in Porous Media*, Cambridge University Press, UK.

McCloskey J., Nalbant S.S., Steacy S. 2005, Earthquake risk from co-seismic stress, *Nature*, 434, 291.

McGuire W.J., Kilburn C.R.J 1997, Forecasting volcanic events: some contemporary issues, *Geologische Rundschau*, 86, 2, 439-455.

McNutt S.R. 2000, Volcanic seismology, in Sigurdsson H. et al eds., *Encyclopedia of volcanoes*, San Diego, California, Academic Press, 1015-1033.

McNutt S.R. 2005, Volcanic seismology, *Annual Review of Earth and Planetary Sciences*, 33, 461-491.

Meredith P.G., Atkinson B.K. 1983, Stress corrosion and acoustic emission during tensile crack propagation in Whin Sill dolerite and other basic rocks, *Geophysical Journal of the Royal Astronomical Society*, 75, 1-21.

Meredith P.G., Atkinson B.K. 1985, Fracture toughness and subcritical crack growth during high-temperature tensile deformation of Westerly granite and Black gabbro, *Physics of the Earth and Planetary Interiors*, 39, 33-51.

Meredith P.G., Main I.G., Jones C. 1990, Temporal variations in seismicity during quasi-static and dynamic rock failure, *Tectonophysics*, 175, 249-268.

Milgrim S. 1967, The small world problem, *Psychology Today*, 1, 1, 61-67.

Mogi K. 1958, Relations between the eruptions of various volcanoes and the deformations of the ground surfaces around them, *Bulletin of the Earthquake Research Institute*, 36, 99-134.

Mogi K. 1962, Magnitude-Frequency relation for elastic shocks accompanying fractures of various materials and some related problems in earthquakes, *Bulletin of the Earthquake Research Institute*, 40, 831-853.

Murray J.B., Ramirez Ruiz J.J. 2002, Long-term predictions of the time of eruptions using remote distance measurement at Volcan de Colima, Mexico, *Journal of Volcanology and Geothermal Research*, 117, 79-89.

Murru M., Console R., Falcone G., Montuori C., Sgroi T. 2007, Spatial mapping of the *b* value at Mount Etna, Italy, using earthquake data recorded from 1999 to 2005, *Journal of Geophysical Research*, 112, B12303.

Nalbant S.S., Steacy S., Sieh K., Natawidjaja D., McCloskey J. 2005, Earthquake risk on the Sunda trench, *Nature* 435, 7043, 756-757.

Neuberg J.W., Tuffen H., Collier L., Green D., Powell T., Dingwell D. 2006, The trigger mechanism of low-frequency earthquakes on Montserrat, *Journal of Volcanology and Geothermal research*, 153, 1-2, 37-50.

Neville D.J. 1987, A new statistical distribution function for fracture toughness, *Proceedings of the Royal Society of London A*, 410, 1839, 421-442.

Neville D.J., Knott J.F. 1986, Statistical distributions of toughness and fracture-stress for homogeneous and inhomogeneous materials, *Journal of the Mechanics and Physics of Solids*, 34, 3, 243-291.

Newhall C.G., Punongbayan R.S. 1996, *Fire and Mud: Eruptions and Lahars of Mount Pinatubo, Philippines*, University of Washington Press, Seattle.

Nishimura T., Chouet B. 2003, A numerical simulation of magma motion, crustal deformation, and seismic radiation associated with volcanic eruptions, *Geophysical Journal International*, 153, 699-718.

Page R. 1968, Aftershocks and microaftershocks of the great Alaska earthquake of 1964, *Bulletin of the Seismological Society of America*, 58, 3, 1131-1168.

Palano M., Pugisi G., Gresta S. 2008, Ground deformation patterns at Mt. Etna from 1993 to 2000 from joint use of InSAR and GPS techniques, *Journal of Volcanology and Geothermal Research*, 169, 3-4, 99-120.

Parsons T. 2008, Monte Carlo method for determining earthquake recurrence parameters from short paleoseismic catalogs: Example calculations for California, *Journal of Geophysical Research*, 113, B03302.

Parsons T., Thompson G.A., Cogbill A.H. 2006, Earthquake and volcano clustering via stress transfer at Yucca Mountain, Nevada, *Geology*, 34, 9, 785-788.

Peterson D.W. 1986, Volcanoes: tectonic setting and impact on society. In: Active Tectonics: Impact on Society, *National Academy Press*, Washington DC.

Petley D.N. 2004, The evolution of slope failures: mechanisms of rupture propagation, *Natural Hazards and Earth System Sciences*, 4, 147-152.

Pinel V., Jaupart C. 2000, The effect of edifice load on magma ascent beneath a volcano, *Philosophical Transactions of the Royal Society of London*, A, 358, 1515-1532.

Pinel V., Jaupart C. 2003, Magma chamber behaviour beneath a volcanic edifice, *Journal of Geophysical Research*, 108, B2, 2072.

Power J.A., Wyss M., Latchman J.L. 1998, Spatial variations in the frequency-magnitude distribution of earthquakes at Soufriere Hills Volcano, Montserrat, West Indies, *Geophysical Research Letters*, 25, 19, 3653-3656.

Qamar A., St. Lawrence W., Moore J.N., Kendrick G. 1983, Seismic signals preceding the explosive eruption of Mount St. Helens, Washington, on 18 May 1980, *Bulletin of the Seismological Society of America*, 73, 6, 1797-1813.

Renshaw C.E. 1996, Influence of subcritical fracture growth on the connectivity of fracture networks, *Water Resources Research*, 32, 6, 1519-1530.

Renshaw C.E., Pollard D.D. 1994, Numerical simulation of fracture set formation: A fracture mechanics model consistent with experimental observations, *Journal of Geophysical Research*, 99, B5, 9359-9372

Richter C.F. 1935, An instrumental earthquake magnitude scale, *Bulletin of the Seismological Society of America*, 25, 1-32.

Rice J.A. 1995, *Mathematical Statistics and Data Analysis: 2nd ed.*, Duxbery Press, Belmont, California.

Rice J.R. 1968, A path independent integral and the approximate analysis of strain concentration by notches and cracks, *Journal of Applied Mechanics*, 35, 379.

Ripley B.D. 1977, Modelling spatial patterns, *Journal of the Royal Statistical Society B*, 39, 172-212.

Rist M.A., Sammonds P.R., Oerter H., Doake C.S.M. 2002, Fracture of Antarctic shelf ice, *Journal of Geophysical Research*, 107, 2002.

Rivalta E., Dahm T. 2004, Dyke emplacement in fractured media: application to the 2000 intrusion at Izu Islands, Japan, *Geophysical Journal International*, 157, 283-292.

Rocchi V., Sammonds P.R., Kilburn C.R.J. 2003, Flow and fracture maps for basaltic rock deformation at high temperatures, *Journal of Volcanology and Geothermal Research*, 120, 1-2, 25-42.

Roman D.C., Cashman K.V. 2006, The origin of volcano-tectonic earthquake swarms, *Geology*, 34, 6, 457-460.

Roman D.C., De Angelis S., Latchman J.L., White R. 2008, Patterns of volcanotectonic seismicity and stress during the ongoing eruption of the Soufrière Hills Volcano, Montserrat (1995–2007*), Journal of Volcanology and Geothermal Research*, 173, 230-244.

Roman D.C., Moran S.C., Power J.A., Cashman K.V. 2004, Temporal and spatial variation of local stress fields before and after the 1992 eruptions of Crater Peak vent, Mount Spurr volcano, Alaska, *Bulletin of the Seismological Society of America*, 94, 6, 2366-2379.

Roper S.M., Lister J.R. 2007, Buoyancy-driven crack propagation: the limit of large fracture toughness, *The Journal of Fluid Mechanics*, 580, 359-380.

Rubin A.M. 1995, Propagation of magma-filled cracks, *Annual Review of Earth and Planetary Sciences*, 23, 287-336.

Rudnicki J.W. 1980, Fracture mechanics applied to the Earth's crust, Annual *Review of Earth and Planetary Sciences*, 8, 489-525.

Rudnicki J.W., Kanamori H. 1981, Effects of fault interaction on moment, stress drop, and strain energy release, *Journal of Geophysical Research*, 86, B3, 1785-1793.

Ruhla C. 1992, *The Physics of Chance*, Oxford University Press, Oxford.

Rydelek P.A., Sacks I.S. 1989, Testing the completeness of earthquake catalogues and the hypothesis of self-similarity, *Nature*, 337, 251-253.

Sahimi M. 1993, Flow phenomena in rocks: from continuum models to fractals, percolation, cellular automata, and simulated annealing, *Reviews of Modern Physics*, 65, 1393.

Sahimi M. 1994, *Applications of Percolation Theory*, Taylor & Francis Ltd, London.

Sahimi M., Arbabi S. 1993, Mechanics of disordered solids. III. Fracture properties, *Physical Review B*, 47, 2, 713-722.

Saichev A., Sornette D. 2007, Theory or earthquake recurrence times, *Journal of Geophysical Research*, 112, B4, B04313.

Sammis C.G. 2001, Materials science issues in the Earth and planetary sciences, *Progress in Materials Science*, 46, 231-247.

Sammonds P.R., Meredith P.G., Main I.G. 1992, Role of pore fluids in the generation of seismic precursors to shear failure, *Nature*, 359, 228-230.

Sammonds P., Ohnaka M. 1998, Evolution of microseismicity during frictional sliding, *Geophysical Research Letters*, 25, 5, 699-702.

Sánchez J.J., McNutt S.R., Power J.A., Wyss M. 2004, Spatial variations in the frequency-magnitude distribution of earthquakes at Mount Pinatubo volcano, *Bulletin of the Seismological Society of America*, 94, 2, 430-438.

Scandone R., Cashman K.V., Malone S.D. 2007, Magma supply, magma ascent and the style of volcanic eruptions, *Earth and Planetary Science Letters*, 253, 513-529.

Scholz C.H. 1968, The frequency-magnitude relation of microfracturing in rock and its relation to earthquakes, *Bulletin of the Seismological Society of America*, 58, 1, 399-415.

Selva J., Marzocchi W., Zencher F., Casarotti E., Piersanti A., Boschi E. 2004, A forward test for interaction between remote earthquakes and volcanic eruptions: the case of Sumatra (June 2000) and Denali (November 2002) earthquakes, *Earth and Planetary Science Letters*, 226, 383-395.

Shaw H.R. 1980, *The fracture mechanisms of magma transport from the mantle to the surface in Physics of Magmatic Processes*, Ed. Hargreaves R.B., Princeton University Press, Princeton, 201-264.

Shi Y., Bolt B.A. 1982, The standard error of the magnitude-frequency *b* value, *Bulletin of the Seismological Society of America,* 72, 5, 1677, 1687.

Sornette A., Davy P., Sornette D. 1993, Fault growth in brittle-ductile experiments and the mechanics of continental collisions, *Journal of Geophysical Research*, 98, 12,111-12,139.

Smith R. 2007, *Rates of rock fracturing as a tool for forecasting eruptions at andesitic-dacitic Stratovolcanoes*, PhD Thesis, University College London, UK.

Smith R., Kilburn C.R.J., Sammonds P.R. 2007, Rock fracture as a precursor to lave dome eruptions at Mount St Helens from June 1980 to October 1986, *Bulletin of Volcanology*, 69, 681-693.

Smith W.D. 1981, The *b*-value as an earthquake precursor, *Nature*, 289, 136-139.

Sneddon I.N. 1946, The distribution of stress in the neighborhood of a crack in an elastic solid, *Proceedings of the Royal Society of London, Series A*, 187, 229–260.

Sneddon I.N. 1958, *The classical theory of elasticity*, in Encyclopedia of Physics, Vol. 6, Elasticity and Plasticity, Ed. Flüge S., Springer-Verlag, Germany.

Sparks R.S.J. 1997, Causes and consequences of pressurisation in lava dome eruptions, *Earth and Planetary Science Letters*, 150, 177-189.

Stauffer D., Aharony A. 1992, *Introduction to Percolation Theory*, 2nd ed., Taylor & Francis, London, UK.

Steacy S., Nalbant S.S., McCloskey J., Nostro C., Scotti O., Baumont D. 2005, Onto what planes should Coumlomb stress perturbations be resolved? *Journal of Geophysical Research*, 110, B5, B05S15.

Steacy S.J., Sammis C.G. 1992, A damage mechanics model for fault zone friction, *Journal of Geophysical Research*, 97, B1, 587-594.

Swanson D.A., Casadevall T.J., Dzurisin D., Malone S.D., Newhall C.G., Weaver C.S. 1983, Predicting eruptions at Mount St-Helens, June 1980 through December 1982, *Science*, 221, 4618, 1369-1376.

Tada H., Paris P.C., Irwin G.R. 1973, *The Stress Analysis of Cracks Handbook, American Society of Mechanical Engineers*, Professional Engineering Publishing, New York, USA.

Tang C. 1997, Numerical simulation of progressive rock failure and associated seismicity, *International Journal of Rock Mechanics and Mining Sciences*, 34, 2, 249-261.

Taylor D.W.A., Snoke J.A., Sacks I.S., Takanami T. 1990, Nonlinear frequency-magnitude relationships for the Hokkaido corner, Japan, *Bulletin of the Seismological Society of America*, 80, 2, 340-353.

Telesca L., Cuomo V., Lapenna V., Macchiato M. 2002, On the methods to identify clustering properties in sequences of seismic time-occurrences, *Journal of Seismology*, 6, 125-134.

Telesca L., Lapenna V., Vallianatos F. 2002, Monofractal and multifractal approaches in investigating scaling properties in temporal patterns of the 1983-2000 seismicity in the western Corinth graben, Greece, *Physics of the Earth and Planetary Interiors*, 131, 63-79.

Tilling R.I. 1988, Lessons from materials science, *Nature*, 332, 108-109.

Toda S., Stein R.S., Reasenberg P.A., Dieterich J.H., Yoshida A. 1998, Stress transferred by the 1995 M_w = 6.9 Kobe, Japan shock: Effect on aftershocks and future earthquake probabilities, *Journal of Geophysical Research*, 103, B10, 24,543-24,565.

Toda S., Stein R.S., Sagiya T. 2002, Evidence from the AD 2000 Izu islands earthquake swarm that stressing rate governs seismicity, *Nature*, 419, 58-61.

Tokarev P.I. 1971, Forecasting volcanic eruptions from seismic data, *Bulletin of Volcanology*, 35, 1, 243, 250.

Tokarev P.I. 1985, The prediction of large explosions of andesitic volcanoes, *Journal of Geodynamics*, 3, 219-244.

Tuckwell G.W., Lonergan L., Jolly R.J.H. 2003, The control of stress history and flaw distribution on the evolution of polygonal fracture networks, *Journal of Structural Geology*, 25, 1241-1250.

Tuffen H., Dingwell D. 2005, Fault textures in volcanic conduits: evidence for seismic trigger mechanisms during silicic eruptions, *Bulletin of Volcanology*, 67, 370-387.

Tuffen H., Dingwell D.B., Pinkerton H. 2003, Repeated fracture and healing of silicic magma generate flow banding and earthquakes?, *Geology*, 31, 12, 1089-1092.

Tuffen H., Smith R., Sammonds P.R. 2008, Evidence for seismogenic fracture of silicic magma, *Nature*, 453, 7194, 511-514.

Ukawa M. 2005, Deep low-frequency earthquake swarm in the mid crust below Mount Fuji (Japan) in 2000 and 2001, *Bulletin of Volcanology*, 68, 47-56.

Umakoshi K., Shimizu H., Matsuwo N. 2001, Volcano-tectonic seismicity at Unzen Volcano, Japan, 1985-1999, *Journal of Volcanology and Geothermal Research*, 112, 117-131.

Urbancic T.I., Trifu C.I., Long J.M., Young R.P. 1992, Space-time correlations of *b* values with stress release, *Pure and Applied Geophysics*, 139, 449-462.

Valentini L., Perugini D., Poli G. 2007a, The ”small-world” topology of rock fracture networks, *Physica A*, 377, 323 –328.

Valentini L., Perugini D., Poli G. 2007b, The ‘small-world’ nature of fracture/conduit networks: Possible implications for disequilibrium transport of magmas beneath mid-ocean ridges, *Journal of Volcanology and Geothermal Research*, 159, 355-365.

Vinciguerra S. (2002), Damage mechanics preceding the September-October 1989 flank eruption at Mount Etna volcano inferred by seismic scaling exponents, *Journal of Volcanology and Geothermal Research*, 113, 391-397.

Vinciguerra S., Gresta S., Barbano M.S., Distefano G. (2001), The two behaviours of Mt. Etna volcano before and after a large intrusive episode: evidences from *b* value and fractal dimension of seismicity, *Geophysical Research Letters*, 28, 11, 2257-2260.

Voight B. 1988, A method for prediction of volcanic eruptions, *Nature*, 332, 123-130.

Voight B. 1989, A relation to describe rate-dependent material failure, *Science*, 243, 4888, 200-203.

Voight B., Cornelius R.R. 1991, Prospects for eruption prediction in near real-time, *Nature*, 350, 695-698.

Walsh J., Watterson J., Yielding G. 1991, The importance of small-scale faulting in regional extension, *Nature*, 351, 391-393.

Walter T.R., Wang R., Zimmer M., Grosser H., Luhr B., Ratdomopurbo A. 2007, Volcanic activity influenced by tectonic earthquakes: Static and dynamic stress triggering at Mt. Merapi, *Geophysical Research Letters*, 34, L05304.

Warren N.W., Latham G.V. 1970, An experimental study of thermally induced microfracturing and its realtion to volcanic seismicity, *Journal of Geophysical Research*, 75, 4455-4464.

Watts D.J., Strogatz S.H. 1998, Collective dynamics of “small-world” networks, *Nature*, 393, 440-442.

Weibull W. 1951, A statistical distribution function of wide applicability, *Journal of Applied Mechanics*, 18, 3, 293-297.

Wiemer S., McNutt S.R. 1997, Variations in the frequency-magnitude distribution with depth in two volcanic areas: Mount St. Helens, Washington, and Mt. Spurr, Alaska, *Geophysical Research Letters*, 24, 2, 189-192.

Wiemer S., Wyss M. 2002, Mapping spatial variability of the frequency-magnitude distribution of earthquakes, *Advances in Geophysics*, 45, 259-302.

Wong T-F., Wong R.H.C., Chau K.T., Tang C.A. 2006, Microcrack statistics, Weibull distribution and micromechanical modeling of compressive failure in rock, 38, 664-681.

Woo G. 1999, *The Mathematics of Natural Catastrophes*, Imperial College Press, London, UK.

Wyss M. 1973, Towards a physical understanding of the earthquake frequency distribution, *Geophysical Journal of the Royal Astronomical Society*, 31, 341-359.

Wyss M., Klein F., Nagamine K., Wiemer S. 2001, Anomalously high *b*-values in the South Flank of Kilauea volcano, Hawaii: evidence for the distribution of magma below Kilauea's East rift zone, *Journal of Volcanology and Geothermal Research*, 106, 23-37.

Xie H. 1993, *Fractals in rock mechanics*, A. A. Balkema, Rotterdam.

Xing X.S., Jeulin D., Pineau A. 1993, Derivation of statistical distribution of toughness from statistical distribution of strength, *International Journal of Fracture*, 61, 1, R11-R17.

Xu C., Dowd P.A., Mardia K.V., Fowell R.J. 2006, A connectivity index for discrete fracture networks, *Mathematical Geology*, 38, 5, 611-634.

Zobin V.M. 2003, *Introduction to Volcanic Seismology*, Elsevier Science B.V., Amsterdam, The Netherlands.

Zobin V.M., Jiménez Z. 2008, Some regularity in the process of re-awakening of andesite and dacite volcanoes: specific features of the 1982 El Chichón volcano, México reactivation, *Journal of Volcanology and Geothermal Research*, 175, 482-487.

Zobin V.M., Nishimura Y., Miyamura J. 2005, The nature of volcanic earthquake swarm preceding the 2000 flank eruption at Usu volcano, Hokkaido, Japan, *Geophysical Journal International*, 163, 265-275.

Zuniga F.R., Wyss M. 1995, Inadvertent changes in magnitude reported in earthquake catalogues: Their evaluation through *b*-value estimates, *Bulletin of the Seismological Society of America*, 85, 6, 1858-1866.

http://neic.usgs.gov/neis/eqlists/eqstats.html